Studies on Cement Design and Steel Corrosion towards Sustainable Reinforced Concrete

Guo, Peng

2017

UNIVERSITY OF CALIFORNIA

Los Angeles

Studies on Cement Design and Steel Corrosion towards Sustainable Reinforced Concrete

A dissertation submitted in partial satisfaction of the

requirements for the degree of Doctor of Philosophy

in Civil Engineering

by

Peng Guo

2017

ABSTRACT OF THE DISSERTATION

Studies on Cement Design and Steel Corrosion towards Sustainable Reinforced Concrete

by

Peng Guo
Doctor of Philosophy in Civil Engineering
University of California, Los Angeles, 2017
Professor Gaurav Sant, Co-Chair
Professor Mathieu Bauchy, Co-Chair

The two major construction materials in civil engineering, cement, and steel, are studied using Density Functional Theories (DFT) simulation and empirical methods, respectively. In this thesis, DFT method is used for the study of cement material reactivity study to get access to the electronic-scale investigation; for steel corrosion research, 3-dimensional topography at high resolution is captured for nanoscale pitting evolution observation. The simulation work aims at understanding how to enhance Ordinary Portland Cement (OPC) reactivity and reduce energy consumption as well as reduce CO_2 emission from cement industry. Ca_2SiO_4 (C_2S) is the second major phase in OPC clinker, however, it reacts with water at a slow rate and does not contribute early-age strength to concrete structures. To uncover the nature of this low reactivity, 3 major polymorphs of C_2S naming γ-, β- and α'_L-C_2S crystal structures are calculated to determine the least stable phase, revealing that the stability of three C_2S ranks in the sequence of γ- > β- > α'_L-C_2S. As β-phase is the dominant C_2S, points defects with foreign ions (K+, Na+, Mg^{2+}, Sr^{2+}, B^{3+}, Al^{3+}, Fe^{3+}, Ge^{4+}) have been introduced into β- C_2S crystal structure in order to improve the instability and potentially reactivity. From the doped β- C_2S structure, at the same molar concentration, B element shows the highest instability, following by Al element; Na and Mg elements exhibit little trend to

activate β- C_2S. Ionic size and doping preference have been further studied to uncover the rule of doping in β- C_2S as well as future doped structure design. The doping preference in β- C_2S crystal structure highly correlates to the ionic size difference between the foreign ion and the substituted ion. Ions with smaller ionic size difference from foreign ions are easy to be replaced. The investigated aspects include lattice parameter, mechanical performance, DOS, PDOS, liner charge distribution, coordination number with oxygen atoms, formation enthalpy as well as vacancy formation enthalpy. Results show that Mg atoms introduced the most instability to doped structures at the same oxide concentration (in mass).

Steel corrosion, specifically, rebar in the concrete structures, has aroused increasingly research interest in order to improve the understanding its nature as well as to protect steel from rapid failure. For steel corrosion study, AISI 1045 medium carbon steel has been selected to conduct pitting corrosion initiation and propagation observation using Vertical Scanning Interferometry (VSI). The corrosion environments are at neutral pH with/without 100 mM NaCl for comparison. Over time, the 3D steel surface morphology is captured with VSI for pitting corrosion analysis at the nanoscale. The comparing items include corrosion product chemical composition, pit initiation mechanism, pit density, average pit depth, and surface height change frequency distribution. Evolution of pitting corrosion over large surface areas has been examined. Special efforts have been paid to quantify the pitting nucleation, growth, and propagation rate. Chloride ions enhance the corrosion rate significantly by shortening the initiation time as well as increase the pit density, pit depth as well as steel surface height retreat. For both with and without chloride ion cases, the surface defects, e.g., MnS inclusions initiate pitting corrosion. Initial pits remove passivation film around themselves, where more pits will generate and propagate. In this study, the pitting corrosion follows the adsorption mechanism. This study provides new insights into steel corrosion at neutral pH environment and extends the understanding of the nature pitting corrosion process.

In sum, from the results of DFT simulation of doped C_2S structures, it can be concluded that the introduced instability highly depends on the ionic size mismatch between dopants and the ions being replaced. In steel corrosion study, it is found Cl- ions accelerate pitting corrosion by such factors: (i) destabilization of passivation films, (ii) prevention of repassivation, and, (iii) preservation of aggressive microenvironments within the pits. Both of the studies can be helpful to enhance the performance of reinforced concrete structures.

Key Words: concrete, DFT, dicalcium silicate, doping, steel, pitting corrosion, chloride

The Dissertation of Peng Guo is approved.

Scott Joseph Brandenberg
Mark S. Goorsky
Gaurav Sant, Committee Co-Chair
Mathieu Bauchy, Committee Co-Chair

University of California, Los Angeles
2017

Dedication

This work is dedicated to my parents Zhaohui Guo and Xuefeng Sun. I can finish my Ph.D. degree because of their endless love, sacrifices, and support. I love them so much.

Table of Contents

Acknowledgements

I would express my sincere appreciation to Professor Gaurav Sant for offering me the opportunity to pursue my Ph.D. degree at UCLA , for supporting me over the past 4 years and a quarter, as well as advising me during my research.

I would extend my appreciation to Professor Mathieu Bauchy who has been advising me on simulation work with insightful thoughts, profound knowledge, and patience.

I would like to thank my committee members Professor Scott J. Brandenberg and Professor Mark S. Goorsky who have been providing supports throughout my Ph.D. life.

I express my appreciation to Dr. Jian Huang, Dr. Bu Wang, and Dr. Erika Callagon La Plante for their help in my Ph.D. period. I appreciate the help of members in Laboratory for the Chemistry of Construction Materials and Physics of AmoRphous and Inorganic Solids Lab.

Finally, I am so grateful for my parents. They support and sacrifice so much for me in raising me up. I could not find more words to express my love to them. I want to thank the love of my life Dr. Yuchen Ding who always has my back whenever I encounter difficulties. I am so lucky to have her with me for the rest of my life.

Peng Guo

Los Angeles

December 2017

Biographical Sketch

Peng Guo finished his bachelor's degree in materials science and engineering from Wuhan University of Technology in China. After that, he went to Beihang University in 2010 and spent 3 years there for his master's degree in applied chemistry. His interests of study during the master period included functional surfaces and interfaces, as well as micro-/nano- scale structure fabrication on material surfaces. Then he continued his education at University of California at Los Angeles towards his Ph.D. degree of Civil Engineering. His focus was on study of construction materials using both computational and experimental methods. He has 5 papers published on academic journals and 2 patents by this time.

1. Background and Motivation

Reinforced concrete structures have been utilized extensively for modern society construction because of its high strength, affordable price, as well as well-developed techniques.[1], [2] Despite of those benefits, significant issues such as CO_2 emission [3]–[5] , concrete waste [6]–[8], reliability issues [9]–[11], as well as economic issues [12], [13], have been long existing with concrete structures and those issues can be categorized by materials. In this study, issues regarding the most vastly used construction materials are considered, namely, *cement* and *steel* and the goal of my work is to understand the principles behind existing problems and to improve the performance of those materials.

Cement

The production of ordinary Portland cement (OPC) is at this time, responsible for 6-to-9% of global CO_2 emissions [14]–[18]. These emissions are a consequence of: (i) process-related emission, the decarbonation of limestone ($CaCO_3$) during the high-temperature clinkering process (54%), (ii) combustion-related emission, required for heating the kiln and grinding cement clinker (46%) [19]. For these reasons, it is critical that the production and use of OPC be rationalized, so as to improve the environmental impact metrics associated with this material. Cement is composed of alite (Ca_3SiO_5 = C_3S), belite (Ca_2SiO_4 = C_2S), and tricalcium aluminate ($Ca_3Al_2O_6$ = C_3A) and tetracalcium aluminoferrite ($Ca_4Al_2Fe_2O_{10}$ = C_4AF) which are interground with gypsum ($CaSO_4{\cdot}2H_2O$ = CSH_2). Of these phases, alite (about 50%, by mass) and belite (about 20%, by mass) compose 70-to-75 mass% of OPC [20]. Furthermore, on account of their CaO-rich nature, the majority of limestone decomposed, is utilized in their formation.

Of the phases alite and belite, alite has a substantially higher "environmental impact" as (a) compared to C_2S, C_3S requires an additional molar unit of CaO for its formation and (b) C_3S forms only at temperatures in excess of 1300°C, as compared to C_2S which begins to form at around 1000°C [18]. While these attributes make C_2S far more desirable from a sustainability viewpoint, from an engineering performance perspective, this is not so. This is because, when compared to C_3S which reacts rapidly with water, the hydraulic reactivity of C_2S is substantially lower. As a result, C_2S does not contribute to (required) early-strength gain, with its benefits only being realized by 28 days, and later. It should be noted, however, that by an age of 1 year, pure C_3S and C_2S when mixed with water, separately, result in materials which demonstrate equivalent strengths. This is because, C_3S and C_2S, in reaction with water, both produce similar reaction products, with similar properties [20].

The discussion above suggests that if the reactivity of C_2S could be improved, this would be a significant direction towards the production of *belite-rich cement*, as opposed to the alite-rich cement chemistries which are produced today. Significantly, this would also exert a substantial impact on improving the sustainability metrics of OPC as a construction material. The reactivity of C_2S is sensitive to (a) the polymorph considered, i.e., α'_L, β, γ and (b) the nature of impurities contained in the native crystal structure, i.e., in the form of substitutional impurities at limits inferior to the formation of solid solutions. In general, both of these issues are related to the alterations of crystallochemical configurations, in relation to the polymorph considered, or the insertion of impurity ions. This is significant as it suggests that in relation to the polymorph that is formed, and the nature of impurities substituted, it may be possible to elevate the reactivity of C_2S to desirable levels, as relevant to OPC systems.

To better understand these aspects, the studies in this thesis seek to uncover:

- The nature of similarities and differences amongst the different C_2S polymorphs, namely, α'_L-C_2S, β-C_2S, γ-C_2S, from a structural, mechanical and electronic viewpoint

- The influences of impurities on the structural, mechanical and electronic properties of a given polymorph, in relation to (a) the impurity type and (b) the impurity dosage. Special focus is placed on considering the impurity species (K, Na, Mg, Sr, Al, Fe, Ge, and B), as this span the differences in valence, and magnetic properties, and are geologically common, and hence prominent in the raw feed used to produce cement

- The influences of polymorph type, and impurity insertion on polymorph instability in terms of the energetics of formation. This seeks to unravel, how doped structures may be altered in relation to the crystallochemical configuration, i.e., polymorph type and/or the type and dosage of impurity substituted.

As such, in broad scope, the outcomes of the work seek to provide guidance relevant towards increasing the reactivity, and hence the quantity of belite contained in OPC.

While there has been substantial inquiry into the influence of impurities, on especially the reactivity of the β-C_2S phase that is common to OPC [20]–[36], these studies have been parametric, and due to lack of equivalences across studies, e.g., in methods of synthesis, or investigation; the outcomes are not generic. Moreover, typical experimental methods are often incapable of revealing mechanistic details, of how impurities alter stability (reactivity). As such, it is not yet clear as to how impurity types/dosages influence phase reactivity. Obviously, due to the number and combinations of elements that may be substituted across options provided by the periodic table, investigations of this nature, by experimental methods alone, remain intractable. Therefore, to develop: (a) quantitative chemical/electronic scale understanding, (b) linkages between the nature of substituents and reactivity, and (c) to fully consider the role of the polymorph involved, this thesis interrogates such influences using electronic structure calculations implemented at the density functional level of theory (DFT). By detailed analysis of C_2S crystal structures, new insights are developed to inform the synthesis of *green belite-rich OPCs*.

Steel

Concrete is no doubt the most widely used artificial material in modern society construction, such as in building skyscrapers, bridges, highways, as well as dams. However, concrete is a material with high compressive but its tensile strength is usually lower than 10% of the compressive strength [37]–[39]. To compensate this weakness, reinforced steel rebar has been embedded into concrete structures and provide the tensile strength. [40], [41] Besides acting as reinforced material in concrete structures, steel has also been utilized to build structures on its own with the typical examples Eiffel Tower and Golden Gate Bridge. As steel provides so many benefits to construction engineering, almost all of the structures with steel are exposed to corrosion problems. [42]–[45] According to a study of National Association of Corrosion Engineers (NACE), the global annual cost from corrosion in 2016 is about 3.4 % of the global Gross Domestic Product (GDP) reaching 2.5 trillion US dollars. [46]

Corrosion is a thermodynamically irreversible electrochemical reaction process with metal elements being oxidized into their higher valent states as exists in corrosion products.[47] Although corrosion reaction happens spontaneously, this process could be accelerated many factors such as intrinsic defect in metal materials [48]–[51], microorganisms [52]–[54], aggressive agents [44], [55], [56], temperature effect [57]–[60], and so on. Among all those factors, halide ions, especially chloride ions have been considered to be one of them most important factors causing/accelerating the metallic corrosion process. [61]–[65] This is because chloride ions exist commonly in metal-serving environments. For example, in cold area, people use chloride salt as a deicing agent when chloride ions have a chance to penetrate inside concrete structures and initiate rebar corrosion. [66]–[68] Chloride ions have a strong ability to both initiate and accelerate steel corrosion despite of many attempts to prevent or retard this process, however, the problem is still not well-solved and highly on agenda.

A lot of efforts have been paid in investigating the nature of chloride-induced corrosion and methods to alleviate the damage from this kind of corrosion. Pitting corrosion has been found to be one of the most important corrosion forms with the following features:

- Pitting corrosion is an extremely localized corrosion form: Despite that pitting corrosion would not cause the loss of a large amount of metal, it introduced threats to the reliability of the system and even total failure. For example, stress usually concentrates at pitting sites, where cracks used to initiate and develop. [69]
- Pits are difficult to be found: At the initiation period, the pits could be as small as micrometers, and pits are usually covered by corrosion product or wrapped up by cover materials, e.g., painting or concrete, as a result pitting corrosion is not able to be visualized. Pitting corrosion is difficult to track: The initiation of pitting corrosion could occur within a few minutes and the pitting corrosion process could last for months [70], [71] until a critical failure occurs. Although there could be methods such as Electrochemical Impedance Spectroscopy (EIS) [72], [73] and Voltage-Current (VC) [74], [75] measurement for measuring the characterization pitting signals, the noises from other signal sources make it inaccurate to identify corrosion. Moreover, the pitting initiation and evolution process with these methods are usually indistinguishable from the noises.[76]
- Pitting corrosion is basically unavoidable: The pitting initiation is found to usually starts from intrinsic defects of metal materials such as second-phase inclusions or grain boundaries [77],

however, in the field of engineering, in order to keep the economic efficiency low corrosion-resistance metals have to be used. As a result, corrosion of such types of metals, especially in aggressive environments, is unavoidable. There have to be other protection methods instead of using expensive metallic materials against corrosion.

Considering the significance of pitting corrosion, a series of methods have been applied to uncover the nature of pitting corrosion initiation and propagation. These methods could be divided into two groups, namely overall performance methods and microscope investigation methods. The overall performance methods include those relatively traditional ones such as electrochemical polarization technique[78], EIS [72], [73], potentiometric methods [79], electrical resistance techniques [80], and so on. However, as mentioned above, these methods only offer the overall performance of corrosion without detailed information regarding individual pit initiation and evolution. The microscope investigation methods include Scanning Electronic Microscopy (SEM) [81], [82], Atomic Force Microscopy (AFM) [83]–[86], Scanning Electrochemical Microscopy (SECM) [83], [87], [88], Scanning Tunneling Microscopy (STM) [50], [89], Microelectrochemical measurement [90], [91] etc. More instruction will be discussed in chapter 7 and 8 regarding the techniques of corrosion study.

In order to obtain detailed information of pitting corrosion, microscale investigation methods are getting increasingly popular. But these methods also have their shortcomings. SEM can only provide 2-dimensional information; SECM and STM have low resolutions of a few micrometers; AFM cannot detect sharp deep pits due to the size of its detecting pin. In this study, Vertical Scanning Interferometry (VSI) will be applied to offer both high lateral resolution of 1.63 μm and large field of view for sufficient statistical data. With this equipment, 3-dimensional ex-situ data of high resolution will be captured over time, so that the pitting initiation and propagation process will be fully studied and light will be shed on new understanding to pitting corrosion.

Overall Scope

In summary, the goal of this thesis is seeking new approaches to improve the sustainability and reliability of concrete structures, to improve the economic efficiency from reducing fuel consumption, cut CO_2 emission, as well as expand the service of the engineering structures. To achieve these goals, novel methods will be applied to address problems specific questions, which will be introduced in the following chapters.

2. Introduction to Ordinary Portland Cement (OPC)

Ordinary Portland cement (OPC) is a hydraulic binder which can react with water and bind the constituents of concrete, i.e., sand and stone, together into a dense matrix with low permeability. At a global level of production on the order of 3.8 billion tons, OPC is the dominant binding material used by the concrete construction industry, e.g., in the construction of buildings, freeways, dams etc. OPC is produced by reacting limestone, shale, quartz, clay and iron oxides at high temperature (1450°C) and at ambient pressure in a cement kiln [20]. Following "clinkering" (a synthesis process at high temperature) and cooling, a few percent of gypsum is added to the clinker, to regulate its setting behavior. In general, OPC is produced in 5 types (e.g., Type I-to-V, as per ASTM C150) as a function of its composition and physical properties [20]. Type I OPC is the most commonly used and produced a variant.

Cement clinker consists of four major phases, namely, alite, belite, the aluminate phase and the ferritic phase(s). Cement clinker constitutes about 67% CaO (C), 22% SiO_2 (S), 5% Al_2O_3 (A), 3% Fe_2O_3 (Fe) and 3% other components. [20] a) Alite is the dominant component of clinker (and OPC) and it comprises 50-70% of OPC. Alite is an impure tricalcium silicate (Ca_3SiO_5, C_3S), which is stabilized by foreign ions, e.g. Mg^{2+}, Al^{3+}, and Fe^{3+}. Alite demonstrates the high hydraulic reactivity and is responsible for early, and medium-term strength gain, i.e., from 1-until-90 days. b) Belite comprises 15-to-30% of OPC and it is an impure dicalcium silicate (Ca_2SiO_4, C_2S) that is once again stabilized by foreign ions. In OPC, C_2S is present largely as β-C_2S. Belite reacts slowly with water. As such, it only provides long-term strength, typically at ages greater than 28 days. c) The aluminate phase comprises 5-to-10% of OPC and it is a tricalcium aluminate ($Ca_3Al_2O_6$, C_3A) that contains foreign ions, such as Si^{4+}, Fe^{3+}, Na^{+}, and K^{+}. It reacts with water very rapidly and even faster than C_3S. d) The ferrite phase comprises 5-to-15% of OPC and it is a tetra-calcium aluminoferrite

(Ca_2AlFeO_5 or $Ca_4Al_2Fe_2O_{10}$, C_4AF) which once again contains foreign ions. The aqueous reaction rate of ferritic phase is variable and in between that of alite and belite.

Figure 2.1 shows the formation/existence of the different cement phases as a function of the kiln temperature [18]. In general, following the decomposition of calcite, phase formation initiates with the formation of the aluminate and belite phases around 700 ℃. The formation of alite initiates at a higher temperature, about 1100℃. Alite formation can occur by the direct combination of its constituents, or from belite, in which case belite (and additional CaO) serve as its precursors. It should be noted that the temperatures noted below correspond to the formation of the technical clinker phases, i.e., those containing minor impurities. In the case pure phases, these temperature relations alter, in general, shifting to slightly higher temperatures [92], [93].

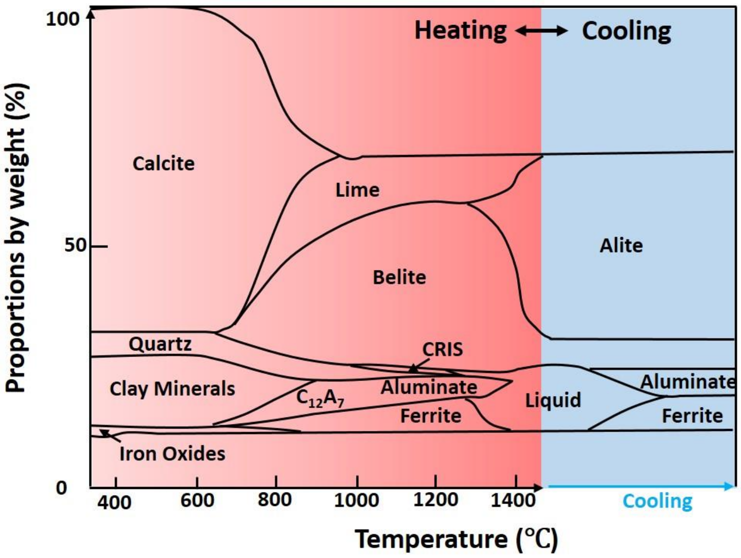

Figure 2.1 A schematic showing the variation of phase contents, and formation temperatures during the formation of cement clinker [20] during pyroprocessing.

2.1 The Dicalcium Silicate Phases ($C_2S = Ca_2SiO_4$) Crystal Structure

Ca_2SiO_4 exists dominantly in the form of the β (i.e., belite) form [20]. In general, C_2S have 5 polymorphs and these polymorphs transform as temperature changes [94]. The relationships between these polymorphs as a function of temperature is shown below, where "H" represents the "high temperature" variant and "L" represents the "lower temperature" variant.

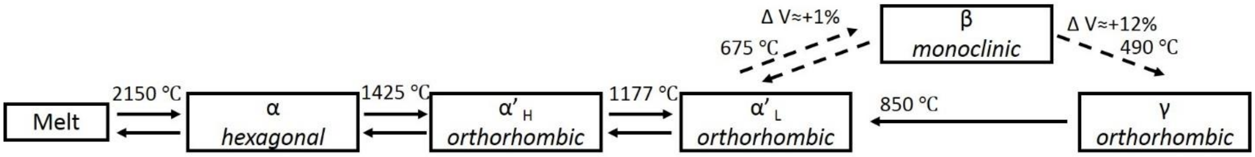

Figure 2.2 A schematic of the sequence of polymorphic transformations of C_2S [95]

Based on x-ray investigations the polymorphs (α, α'$_H$-, α'$_L$-, and β)-C_2S belong to a family of crystalline phases known as glaserite ($K_3Na(SO_4)_2$), while γ-C_2S being far less dense belongs to olivine ($(Mg, Fe)_2SO_4$) family. Exemplar crystallographic data for these polymorphs is noted below [20]:

Table 2.1 Crystal structure data of the C_2S polymorphs

Polymorph	a (nm)	b (nm)	c (nm)	Angle (°)	Space group	Axial relation	Z
α	0.5579		0.7150	γ= 120	P(-3)1c	-ac	2
α'$_H$	0.9490	0.5590	0.6850		Pcmn	abc	4
α'$_L$	2.0871	0.9496	0.5600		Pna21	bca	12
β	0.5502	0.6745	0.9297	β= 94.59	P21/n	cab	4
γ	0.5081	1.1224	0.6778		Pbnm	bca	4

(α'$_H$-, α'$_L$- and β)-C_2S all form (transform) from α-C_2S by undergoing slight changes in lattice parameters enforced via changes in the positions of Ca atoms and orientations of Si-O tetrahedra (see Figure 2.2). The structure of α'$_L$-C_2S, on the other hand, is more complex because it shows a highly elongated dimension in the equivalent “c-axis”, 2.0871 nm, which is about three times of those in other polymorphs. Finally, γ-C_2S shows a crystal structure similar to olivine’s ($(Mg, Fe)_2SO_4$) and shows little if any reactivity with water at room temperature [96].

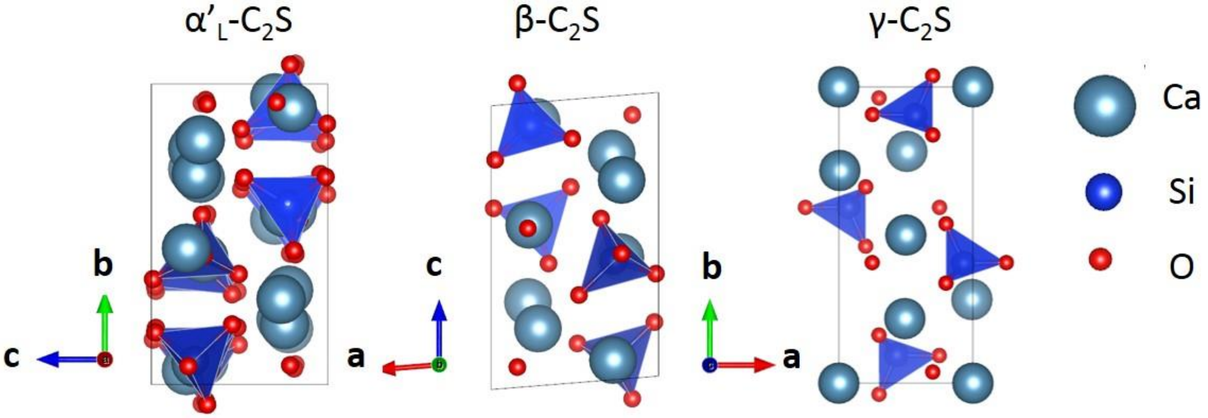

Figure 2.2 A schematic illustrations of the unit cells of most common C_2S polymorphs [20]

The sequence of polymorphic transformation and modulations within the C_2S phases has been elucidated by Chan [95] as shown in Figure 2.1. They reported that the structural changes are induced by accumulated strains in the crystal lattice during a rapid quenching. In general, starting from the melt (2150℃), as the temperature decreases the hexagonal α-C_2S polymorph is first to form. It should be noted due to the typical conditions as relevant to a cement kiln, this phase is unlikely to form during OPC production (T ≈ 1400℃). As the temperature decreases to 1425℃, the hexagonal α-C_2S phase transforms to orthorhombic α’$_H$-C_2S. When temperature reduces to 1177℃, the orthorhombic α’$_H$-C_2S transforms to orthorhombic α’$_L$-C_2S. This transformation involves the expansion of the “*a*, *b*” axes of α’$_H$-C_2S while the “*c*” dimension remains fixed. This transformation has been explained by Saalfeld and Udagawa as well as Urabe as being on account of tripling the “*c* axis” of α’$_H$-C_2S; based on single crystal determinations [97], [98]. As the temperature reduces to 675℃, orthorhombic α’$_L$-C_2S transforms to monoclinic β-C_2S with an associated unit cell volume change (increase) around 1%. Finally, as the temperature is reduced yet further to 490℃, monoclinic β-C_2S transforms to orthorhombic γ-C_2S with an associated volume increase of 12%. It should be noted that if the temperature is increased from below 490℃ to 850℃, γ-C_2S transforms to α'$_L$- C_2S directly and bypasses the intermediate formation of the β-C_2S phase.

2.2 C_2S: Hydration and Reactivity with Water and the Influences of Impurities

C_2S reacts with water and forms the binding calcium silicate hydrate as well as calcium hydroxide (CH). The kinetics of the reaction is slow and described as [99], [100]:

$$C_2S + 4.3H_2O \rightarrow C_{1.7}SH_4 + 0.3CH$$

The C_xSH_y phase has variable stoichiometry and shows poor long-range order [20]. In the case of typical reaction conditions, "x and y" take values of 1.7 and 4.0 (molar units) respectively. The kinetics of the reaction is slow, ensuring that long periods of time need to pass before C_2S is able to reasonably contribute to strength development [20].

To improve its (C_2S) reactivity, several pathways have been followed including: (i) the insertion of foreign ions into the C_2S structure, (ii) the use of hydrothermal processing methods and (iii) increased grinding, to enhance the surface area available for reactions. Georgescu et al. prepared highly reactive dicalcium silicate by hydrothermal processing using calcium silicate hydrates as precursors [21]. Singh et al. prepared calcium silicate hydrate by hydrothermal reaction of calcium oxide and silica at 205-215℃ and 17-19 bar and then decomposed the product to obtain highly reactive β-C_2S [22]. On the other hand, Kantro et al. systematically doped β-C_2S with foreign oxides including Al_2O_3, MgO, SO_3, B_2O_3, and Na_2O highlighted dopant dependent reactivity [23]. Sasaki et al. correlated surface area and reactivity, and then expectedly concluded that finer the β-C_2S particulates, the higher their reactivity [101]. The doping limits for Al_2O_3 and Fe_2O_3 are reported to be 4~6 wt% and for K_2O is 1.2 wt%. [20], [33]

Romano et al. synthesized C_2S variants containing cationic dopants of barium and manganese [24]. C_2S exhibits only β-phase at barium dosages around 5 % (molar ratio) while both the β- and α'_L-forms are observed at manganese dosages on the order of 10 % (molar ratio). Interestingly, in spite of the use of 5 % (molar ratio) barium dopants, the reactivity of the synthesized-C_2S and pure C_2S are similar. Fierens and Tirlocq synthesized doped C_2S variants wherein silicon was substituted with boron, vanadium, phosphorus, arsenic or chromium at dosages of 0.50% and 3.0% (mass basis [25]; general formula: $2CaO\cdot(1-x)SiO_2\cdot xA$ where $x = 0.005$ or 0.030 and A is the impurity oxide. They concluded that at lower dopant concentration the order of reactivity scaled as V>P>B>Cr>As while at the higher concentration the order followed as Cr>P>B>As>V. This suggests that while boron and phosphorus broadly do not (or very slightly) influence phase reactivity, the other species display a dosage based impact on mineral reactivity.

Xiuji and Shizong doped β-C_2S with Na_2O and P_2O_5 where Na atoms substitutes Ca atoms and P atoms substitute Si atoms [26]. Significantly, doping altered phase equilibria, with the formation of doped C_2S being more favorable than the undoped variants. For example, doped C_2S formed at temperatures 100-200℃ lower than the undoped form which formed around 1300℃. The authors also observed hydration behavior by testing the chemically combined water. They found that increasing Na into β-C_2S resulted in anionic vacancies as well as crystal boundary enrichment, which was the domain factor for β- C_2S hydration. The more quantities of Na atoms were added, the larger area of crystal boundary will be enriched, correspondingly, the lower surface energy of the doped crystal was and the lower hydration speed was. In addition, Gajbhiye and Singh

[27] reported that 5% Fe^{3+}-doped β-C_2S (doping on a mass basis) are more reactive that undoped C_2S based on determinations using powder X-ray diffraction, FTIR spectra, SEM, magnetic measurements, specific surface area measurements and hydration test. They concluded that significant distortion of the silicate tetrahedra caused by Fe-doping destabilized the C_2S structure, and hence enhanced its hydration rate. In general, while a wide range of dopants has been considered, a comprehensive understanding of impurities, and their influences remains unclear. Significantly, it is unclear how impurities for equivalent dosages may alter phase equilibria, or how the reactivity of even the phase pureC_2S polymorphs may scale. As such, a clear direction of inquiry is needed to resolve and understand these aspects on a mechanistic basis.

3. State-of-the-art: Stabilization and Insertion of Impurities in Ca_2SiO_4 (C_2S)

3.1 Experimental Investigations on the Structure and Reactivity of Ca_2SiO_4

Ghose et al. [28] reported that the hydraulic activity of doped C_2S polymorphs scaled as α'$_H$-C_2S (BaO)>β-C_2S (BaO)>α'$_L$-C_2S (P_2O_5)>β-C_2S (P_2O_5). They concluded that, in the case of β-C_2S, an amorphous grain boundary exists and dopant does not necessarily concentrate in β-C_2S. Barium enriched in the boundary whether or not there is phosphorus, while aluminum also concentrated in the grain boundary. In the case of α'-C_2S, only the BaO-doped phase showed a distinct grain boundary and dislocations in the boundary. B_2O_3-doped α'-C_2S also showed dislocations in the grain boundary, though with a lower density than the BaO-doped phase. P_2O_5-doped α'-C_2S showed neither boundary enrichment nor dislocations. The trends in dopant concentration in the grain boundary and the density of dislocations therein appear to explain reactivity correlations.

Saraswat et al. evaluated the influences of alkaline earth metal dopants (Mg, Sr, and Ba) on C_2S formation [29]. The concluded that none of these dopants influence the reaction temperature at dosages in the range of 0.1-to-1wt%. However, when the dosage was increased to 5 wt%, MgO and $BaCO_3$ significantly decreased formation temperatures, while $SrCO_3$ had no effect. Li et al. showed that P^{5+}, Ba^{2+}, and Zn^{2+} can stabilize and enhance the reactivity of β-C_2S while B^{2+} cannot [102]. The reactivity in relation to the dopant type scaled in decreasing order as Ba^{2+}> P^{5+}> pure β-C_2S >Zn^{2+}>B^{3+}.

Bonafous et al. studied the effects of Al^{3+} and S^{6+}, separately and together, as stabilization agents for β-C_2S by three different processes: 1) a sol-gel route, 2) classical wet process with laboratory-grade reagents and 3) a dry process using natural reagents [32]. They compared these belites to those with Fe^{3+} and Ti^{2+}. They concluded that Al^{3+} compensates the effect of S^{6+} and because of this synergy they can coexist in belite at high concentration (27 % of Si sites,). They also noted that the new structure by partial replacement of Si^{4+} by Al^{3+} and/or S^{6+} is still in continuous tetrahedral geometry and the mean geometry is similar to tetrahedral in pure β-C_2S.

Chan et al. synthesized doped belites doped with varying dosages, up to 1.5% (by mass) of K_2O and up to 4.5% (by mass) of Al_2O_3 [33]. The results showed that only Al_2O_3 dopant is found in lime-rich β-C_2S and up to 3 wt% concentration is found. At silica-rich conditions, 1.5 wt% K_2O or ≥3.0 wt% Al_2O_3 were found. The crystal structures were rankinite ($Ca_3Si_2O_7$) in the K_2O-doped case and gehlenite ($Ca_2Al_2SiO_7$) in Al_2O_3-doped case.

Cuesta et al. determined the mechanisms/nature of boron (and mixed Na/B) substitutions in C_2S [31]. They concluded that: 1) In the case of only boron doping, $Ca_{2-x}B_x(SiO_4)_{1-x}(BO_4)_x$ is preferred, 2) in the case of Na/B mixed doping $Ca_{2-x}Na_x(SiO_4)_{1-x}(BO_3)_x$ is preferred and when x>0.10, α'$_H$-C_2S forms as the dominant polymorph, while when x=0.25, α'$_H$-C_2S is the only polymorph that forms. From an atomistic perspective, in boron-doped C_2S, B substitutes Si and forms a new tetrahedron, $(BO_4)^{5-}$ as a means of ensuring charge balance. On the other hand, in the case of Na/B doping, B substitutes silicon to form a triangular-planar anion, $(BO_3)^{3-}$. It should be noted herein, that Na substitutes Ca atom.

Fukuda et al. studied SrO doped belites [30]. They concluded that: a) when x ≤ 0.08, the crystal structure of $(Sr_xCa_{1-x})_2SiO_4$ is β-C_2S but when x=0.10 the crystal structures of $(Sr_xCa_{1-x})_2SiO_4$ are β-C_2S and α'$_L$-C_2S (i.e., bimorphic), b) as x increases, the unit cell sides expand and the (β) bond angle decreases, consequently, the unit cell volume could increase or decrease; c) the Sr^{2+} ions only occupied seven-coordinated Ca^{2+} sites other than eight-coordinated sites; 4) the unit cell system could be changed because of dopant ions.

3.2 Computational Investigations of the Structure and Reactivity of Ca_2SiO_4

There are increasing interests in applying computational methods, including classical and *ab initio* simulations to study the crystal structure/reactivity of C_2S [34]–[36], [103], [104]. While powerful, the application of these methods is challenging. This is not only on account of computational demands but also on account of technical limitations. For example, in the case of doped C_2S variants [35], [36], [105], crystal structures resolved using x-ray diffraction (e.g., using "pattern fitting" type Rietveld methods) do not indicate the atomic positions of impurities, especially when their abundance is low (<5%, mass basis). As a result, there is substantial ambiguity/imprecision in the crystal structure inputs provided for calculations [36]. This is significant, as deviations between the "computed" and "realistic" positions for impurity atoms, especially in relation to the element type, has the potential to widely influence the calculated properties [105]. Moreover, a resolved crystal structure for the α'_H structure is not yet available, as a result of which this phase has not yet been studied. Detailed below are the outcomes of recent computational investigations which attempt to better understand, explain and manipulate reactivity, of C_2S (and the C_3S phase) encountered in OPC systems [106].

Sakurada et al. studied β-C_2S variants in which Ba^{2+} replaced Ca^{2+} using first principles methods using VASP [34], [107]. They observed that following such substitutions: when Ba^{2+} occupies a seven-coordinated Ca^{2+} site, the Ba-O bond length increases more than when an eight-coordinated Ca^{2+} is occupied. Moreover, the total energy of Ba^{2+} doped β-C_2S is lower than pure β-C_2S suggesting that the doped structure is more stable than the phase pure variant. Wang et al.[34]

investigated the relationship between reactivity and electronic structure of α'$_L$-, β- and γ-C_2S at a DFT level of theory using CASTEP [108]. They noted that among the pure polymorphs, γ-C_2S displays the highest cohesive energy which explains its low reactivity with water, i.e., high stability. Via evaluations of the LDOS maps [35], they then concluded that density of states for O-2p and Ca-3d orbits scale from α'$_L$-to-β-to-γ forms an order which is broadly consistent with the reactivity of these polymorphs with water.

Manzano et al used atomistic and DFT simulations to understand the influence of impurities of (Mg, Al, and Fe) on alite and belite [35]. These impurities were considered as they are the most common type encountered in technical clinkers. From evaluations of a limited number of impurity substitution sites, atomic rearrangements, elastic properties and features of electronic structure they concluded that: (i) Al localized the VBM (valance band maximum) and CBM (conduction band minimum), which means the reactivity of some areas will be enhanced but the reaction sites will be decreased due to electron localization, (ii) Fe impurities reduce reactivity due to strong electron localization while (iii) Mg doping does not influence the reactivity of either phase. More detailed work by Durgun et al. showed that in general, strong electronic localization will decrease reactivity [36]. Based on this understanding they created plots of charge localization for single or multipoint substitutions, to identify optimal dopants to enhance C_2S (and C_3S) reactivity.

3.3 Research Objectives

Researchers tried to improve C_2S reactivity by doping with foreign ions, as discussed in sections 3.1 and 3.2 so that CO_2 emission and fuel consumption could be decreased. A lot of experiments have been operated to check reactivity influences from different types and different concentrations of dopants.[28]–[33] However, with experimental approaches, researchers can only examine the overall performance but it is difficult to prepare a doped crystal structure as designed.

This is because dopants are not always distributed in C_2S evenly and prefer to gather in clusters. With the computational approach, especially first principle calculation, desirable doped structures can be designed by replacing atoms. Several types of research have been conducted through computational approach [34]–[36], [103], as discussed in section 3.2, however, there is no systematic work with respect to a comprehensive knowledge of 1) the relations and differences among C_2S polymorphs, 2) how dopant ions influence C_2S micro-scope structure and material properties, 3) how much energy the doped structures could be saved, and 4) which structure is the optimized doped C_2S structure of high instability/reactivity. Hence, in this research, several researchers will be operated.

1) **Investigations on pure γ-, β-, α'$_L$ -C_2S.** Stabilized β- C_2S by foreign ions is the main phase in Portland cement clinker and in this research, the most closely related γ-, β-, α'$_L$ -C_2S will be studied. α'$_L$ -C_2S is reported to be the most reactive one among γ-, β-, α'$_L$ -C_2S and γ- C_2S is the most stable one. Consequently, it is essential to uncover the nature of γ-, β-, α'$_L$ -C_2S from macro-/micro- scope investigation.

2) **Doped C_2S structures study.** Once the most reactive phase is determined, several most common elements (Mg, Al, Fe and B etc.) existing in this phase will be studied and it will be studied which element (at which concentration) is the most effective one. This result can be examined with previous experimental results.

3) **A broader study scope of dopants.** After these work, another element in the periodic table can be taken into consideration so that a basic trend of how a dopant type as well as its concentration influence C_2S energy saving potential.

4. Theoretical Background and Methodology

4.1 Physical Background

4.1.1 Schrödinger's Equation

A general form (3D, time-dependent) of the Schrödinger equation describes the quantum state evolution of a system in space with respect to time. To simplify, 1D form Schrödinger equation is usually used.

$$-i\hbar \frac{\partial \psi(x,t)}{\partial t} = \hat{H} \psi(x,t) \tag{4.1}$$

where $\psi(x,t)$ is the wave-function relating to space x and time t. $\hat{H}$ is the Hamiltonian operator of the system and

$$\hat{H} = -\frac{\hbar^2}{2m}\nabla_x^2 + V(x,t) \tag{4.2}$$

The first term in the right side of Hamiltonian equation describes the kinetic energy and the second term represents the potential energy. To simplify the calculation of the Hamiltonian and give an approximate value, it can be determined by electrons and nuclei terms (5 terms in total), as shown in equation 4.3.

$$\hat{H} = \sum_{i=1}^{X} \frac{p_i^2}{2m} + \sum_{n=1}^{Y} \frac{p_n^2}{2M_n} + \frac{1}{8\pi\varepsilon_0} \sum_{i=1;i\neq j}^{X} \sum_{j=1}^{X} \frac{e^2}{|r_i - r_j|} + \frac{1}{8\pi\varepsilon_0} \sum_{n=1;n\neq n'}^{Y} \sum_{n'=1}^{Y} \frac{Z_n Z_{n'} e^2}{|R_n - R_{n'}|} - \frac{1}{4\pi\varepsilon_0} \sum_{n=1}^{Y} \sum_{i=1}^{X} \frac{Z_n e^2}{|r_i - R_n|} \tag{4.3}$$

Here X and Y are the total numbers of electrons and nuclei in the system, respectively. Z_n is the charge of the n^th^ nucleus, m is the mass of an electron, M_n is the mass of the n^{th} nucleus, p_i and p_n are momenta of the i^{th}-electron and the n^{th}-nucleus, respectively. e is the charge of the electron, and ε_0

is the permittivity of vacuum. The first two terms describe the kinetic energy of all the electrons and nuclei in the system, respectively, the third and fourth terms describe electronic and nuclei repulsion, respectively, and the last term describes the attractive potential energy between electrons and nuclei.

For a stationary system where time becomes an independent factor, the Schrödinger equation in 1D reduces to the form of

$$E\phi(x) = \hat{H}\,\phi(x) \tag{4.4}$$

and plugging the Hamiltonian term in 4.4, a final expression is

$$E\phi(x) = -\frac{\hbar^2}{2m}\frac{\partial^2\phi(x)}{\partial x^2} + V(x)\phi(x) \tag{4.5}$$

4.1.2 Born-Oppenheimer (BO) Approximation

For the calculation of this work, the time-independent variant of the Schrödinger equation is applied to investigate a stationary system. Given the dramatic difference in mass of the electrons with respect to the nuclei, the Born-Oppenheimer (BO) approximation [109] can be imposed where the second and fourth terms of Equation (4.3) can be neglected. Such an approximation allows considering the nuclei as stationary with respect to the electron which is about 1,000 times lighter. Thus, through the application of the BO approximation, the Schrödinger equation reduces to the form

$$H = \sum_{i=1}^{X}\frac{p_i^2}{2m} + \frac{1}{8\pi\varepsilon_0}\sum_{i=1;i\neq j}^{X}\sum_{j=1}^{X}\frac{e^2}{|r_i - r_j|} - \frac{1}{4\pi\varepsilon_0}\sum_{n=1}^{Y}\sum_{i=1}^{X}\frac{Z_n e^2}{|r_i - R_n|} \tag{4.6}$$

4.1.3 Hartree-Fock (HF) Approximation

Despite the formal simplification by BO approximation, the third term in Equation (4.6) is still challenging to be treated analytically. In the BO approximation, the wave-functions of an N-electron system belong to a 3^N dimensional space. As such, the high dimensionality of the problem is an obstacle in the search for the *exact solution* (eigenvalues, and eigenfunctions) of the (time-independent) Hamiltonian. In this regard, the HF approximation assumes that no correlation occurs between electrons and therefore it simplifies the multi-electron system problem into one-electron one. Slater determinants, which describes the expression of multiple electron wave-functions and obeys Pauli principle by changing sing of two electrons' exchange, are then used to decrease the dimensionality of the 3^N dimensional wave-functions to N-dimensional wave-functions. [110], [111]

4.1.4 Density Functional Theory (DFT)

Following the HF approximation, the correlations between electrons are ignored and this treatment may result in large errors between computational and experimental results of crystal structures. In DFT, the physical state of a system can be described with functions which depend on spatial electron density. As a result, the 3^N dimensional wave-function space is decreased to a 3-dimensional electron density space. Furthermore, DFT is a ground state theory because the ground state energy of a system is the lowest energy state that can be attained.

As discussed in 4.1.2, with BO approximation, the nuclei are treated as fixed, so there will be a static external potential as the electrons move. If the electrons keep "frozen", say a stationary state, the state of a multiple-electron system can be described with time-independent Schrödinger equation, writing

$$\hat{H}\Psi=[\hat{T}+\hat{V}+\hat{U}] \qquad (4.7)$$

Where $\hat{H}$ is Hamiltonian, Ψ is wave function, $\hat{T}$ is kinetic energy; $\hat{V}$ is potential energy of electrons from the nuclei field; $\hat{U}$ is electron-electron interaction energy; E is total energy.

$\hat{T}$ and $\hat{U}$ are taken as universal operators because they are identical for any n-electron system. $\hat{V}$ depends on a system. For the n-electron system, this function cannot be treated as a sum of n single electron wave because of interaction in $\hat{U}$. As discussed above, DFT systematically treats a multiple-electron to a simple system by taking the wave-function into a relation of electron density, hence the $\hat{U}$ can be eliminated. For a non-interacting system (ground state), the wave-function can be written as

$$\Psi_0 = \Psi(\rho_0) \tag{4.8}$$

and for an interacting system

$$\Psi = \Psi(\rho) \tag{4.9}$$

$\hat{T}$, $\hat{U}$ and $\hat{V}$ can then all be transferred to relations with electron density $\rho(\vec{r})$. For example, the potential term $\hat{V}$:

$$V(\rho) = \int V(\overset{\rightarrow}{\rho}) \bullet nd(\overset{\rightarrow}{\rho}) d^3 r \tag{4.10}$$

Consequently, the total energy of the ground state can be expressed by

$$E(\rho) = T(\rho) + U(\rho) + V(\rho) \tag{4.11}$$

$T(\rho)$ and $U(\rho)$, mentioned above, is the universal term and in a ground state, the sum of these two terms are included in interacting systems. At last, $V(\rho)$ should be determined with some approximations which will be discussed below.

4.1.5 Kohn-Sham (KS) Scheme

The KS scheme treats electrons in a system as a non-interacting system.[112] Nevertheless, it generates the same electron density as the one arising from an interacting-electron system. In the KS equation, the particles in a system, typically electrons, are assumed to move in a fictitiously local external field and those electrons in this field are assumed to be non-interacting. With this treatment, the potential can be divided into a non-interacting potential term and a field effect potential term. In DFT, the ground state energy of an *N*-electron system is given by:

$$E_0 = \min_{\rho \to N}(T[\rho(r)] + \int \rho(r) V_{Ne} dr \tag{4.12}$$

Where $T[\rho(r)]$ is the kinetic energy and $\int \rho(r) V_{Ne} dr$ is the potential energy. In a real system where there are interactions among electrons, the ground state electronic energy reads as:

$$E_0 = \min_{\rho \to N}(F[\rho(r)] + \int \rho(r) V_{Ne} dr \tag{4.13}$$

where $F[\rho(r)]$ is the new term

$$F[\rho(r)] = T[\rho(r)] + E_{ele}[\rho(r)] + E_{nele}[\rho(r)] \tag{4.14}$$

In equation (4.14) $E_{ele}[\rho(r)]$ is the electrostatic energy between electrons and $E_{nele}[\rho(r)]$ designates other forms of electronic interactions, such as the non-electrostatic energy. However, it is difficult to solve the kinetic energy $T[\rho(r)]$ accurately in an interacting system. Kohn and Sham applied the kinetic energy of non-interacting base $T_r[\rho(r)]$ and the term E_{XC} instead of $T[\rho(r)]$ to render solution. E_{XC}, the difference between $T[\varrho(r)]$ and $T_r[\varrho(r)]$, is defined the exchange-correlation term.

$$E_{XC}[\rho(r)] = T_{corr}[\rho(r)] + E_{nele}[\rho(r)] \tag{4.15}$$

where $T_{corr}[\rho(r)]$ is the correlation correction term.

In the KS equations

$$E\Phi^{KS}(x) = -\frac{\hbar^2}{2m}\frac{\partial^2\Phi^{KS}(x)}{\partial x^2} + V(x)\Phi^{KS}(x) \tag{4.16}$$

the term $V(x)$ for an interacting system also need exchange-correlation correction such that:

$$V(x) = V_{non\,\mathrm{i}}(x) + V_{XC}(r) \tag{4.17}$$

and

$$V_{XC}(r) = \frac{\partial E_{XC}[\rho(r)]}{\partial \rho(r)} \tag{4.18}$$

To solve the KS equations, some approximations for E_{XC} have been developed starting from the local density approximation (LDA), to the generalized gradient approximation (GGA) and to the use of hybrid functions.

a) Local Density Approximation (LDA)

Within LDA the electron distribution is assumed to be an ideal gas system of spatial isotropy where the system is charge balanced, therefore the electron charge density is uniform. [113]At LDA level, E_{XC} is written as

$$E_{XC}^{LDA}[\rho(r)] = \int \rho(r) \bullet \varepsilon_{XC}[\rho(r)]dr \tag{4.19}$$

where the term $\varepsilon_{XC}[\rho(r)]$ implies that the unit exchange-correlation energy is always divided into the exchange $\varepsilon_X[\rho(r)]$ and the correlation $\varepsilon_C[\rho(r)]$ part.

b) Generalized Gradient Approximation (GGA)

GGA represents the first improvement to LDA.[114] At GGA level the local charge density $\rho(r)$ is corrected by the gradient of electron charge density $\nabla\rho(r)$:

$$E_{XC}^{GGA}[\rho(r)] = \int \rho(r)\varepsilon_{XC}[\rho(r)]dr + \int F_{XC}[\rho(r), \nabla\rho(r)]dr \tag{4.20}$$

where $E_{XC}^{GGA}[\rho(r)]$ is again separated from the exchange and the correlation parts. Several forms of GGA exchange functionals have been developed, the most known and successful including: B [115] (by Becke in 1988), B86 (by Becke in 1986), P (by Perdew in 1986), PBE (by Perdew, Burke and Ernzerhof in 1996) [114] and correlation functionals such as: P86, PW91[116], LYP [117] (Li, Yang and Parr in 1988).

c) Hybrid Functionals

Hybrid functions are a combination of HF exchange functions and DFT correlation functions. At this time, B3LYP [118] is a popular hybrid functional in use. The hybrid function can be written as [119], [120]

$$E_{xc}^{B3LYP} = E_x^{LDA} + a_0(E_x^{HF} - E_x^{LDA}) + a_x(E_x^{GGA} - E_x^{LDA}) + E_c^{LDA} + a_c(E_c^{GGA} - E_c^{LDA}) \tag{4.21}$$

Here, a_0, a_x and a_c equal to 0.20, 0.72 and 0.81, respectively; E_x^{LDA} and E_c^{LDA} are the approximation to local-density exchange and correlation functional, respectively; E_x^{HF} is the approximation to Hartree-Fock exchange functional; E_x^{GGA} and E_c^{GGA} are the generalized gradient approximation of exchange and correlation functional, respectively.

4.2 Discretization Techniques

There are three major discretization techniques in DFT simulations, including a linear combination of atomic orbitals (LCAO), plane waves (PW), and real space mesh (RSM) techniques. The LCAO method considers atomic orbitals as linear combinations of all the partial atomic orbitals. Although this assumption increases calculation intensity, the accuracy is not always satisfactory. In the PW technique, atomic orbitals are simulated by non-local plane waves. Moreover, it is not easy for the consistent plane waves to converge to 0 outside the atom. Another issue with the PW technique is that a high cutoff energy is needed when the plane waves fluctuate. In the real space mesh technique, space is divided into meshes and in each mesh, the states will be calculated. This method is even more accurate than PW technique but mesh design can be problematic.

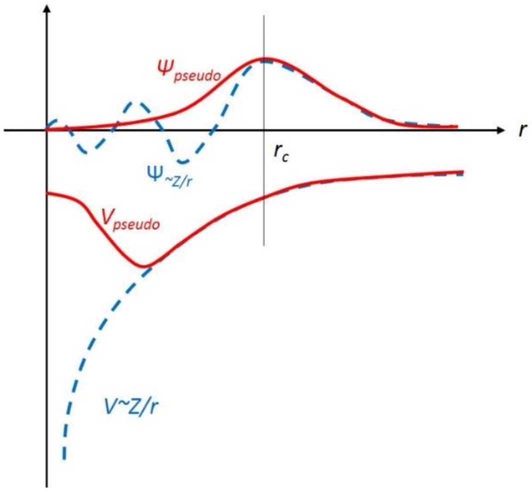

Figure 4.1 A comparison of a wave-function in the Coulomb potential of the nucleus (blue) to the one in the pseudopotential (red). In the figure, the real and the pseudo wave-function and potentials match perfectly above a certain cutoff radius r_c. [121]

Pseudopotentials are used to substitute the nucleus and core electrons with approximated potentials and only considering the valence electrons as participating in the chemical bonds. As such the Columbic potentials in Schrödinger equation can be replaced by known potentials. This approximation simplifies the problem, reducing its computational demand still providing reasonably satisfactory results. Wave-functions of ideal pseudopotentials are expected to be smooth when the distance between the atoms tends to zero (Figure 4.1) so that a small cutoff energy is sufficient. Empirical pseudopotentials (EPP) and *ab initio* pseudopotentials are the most common types of use. The EPP need experimental data for calculation, which is often not available. *Ab initio* pseudopotential requires no empirical results to simulate atomic states. Such calculations start from pseudopotentials and converge to the preset values by self-consistent-field (SCF)/HF (Hartree Fock) type calculation. The following pseudopotential is often used: (a) Vanderbilts's Ultra-Soft pseudopotential (US-PP) [122] and (b) Projector Augmented Wave potential (PAW). [123]

4.3 Calculation Details and Input Crystal Structures: Calculations Rational, Selection of Parameters, and Calculated Properties

The initial crystal structures of γ-C_2S, β-C_2S, and α'_L-C_2S were sourced from Mumme's work [94], [124], and these structures belong to the following space groups: Pbnm (orthorhombic), $P2_1/n$ (orthorhombic) and $Pna2_1$ (monoclinic), respectively. The unit cells of γ- C_2S and β-C_2S contain 28 atoms with 8 Ca atoms, 4 Si atoms and 16 O atoms; the unit cell of α'_L-C_2 is expanded threefold along the c-axis of the α'_H-C_2S unit cell (see Table 2.1), so it consists of 24 Ca atoms, 12 Si atoms and 48 O atoms with a total of 84 atoms. All the Si and O atoms coordinatively configure as Si-O tetrahedra with no leftover interstitial O sites.

The calculations are performed using DFT packages such as Quantum ESPRESSO (QE) package and Vienna Ab initio Simulation Package (VASP). [104] A plane wave basis combined with Vanderbilt ultrasoft pseudopotentials is applied. [122] To treat the effects of exchange-correlation (XC) part of the potential the Perdew-Wang (PW91) GGA functional is adopted.

Starting from the input crystal structure, the sequence of calculations can be illustrated through the flow chart reported in Figure 4.2.

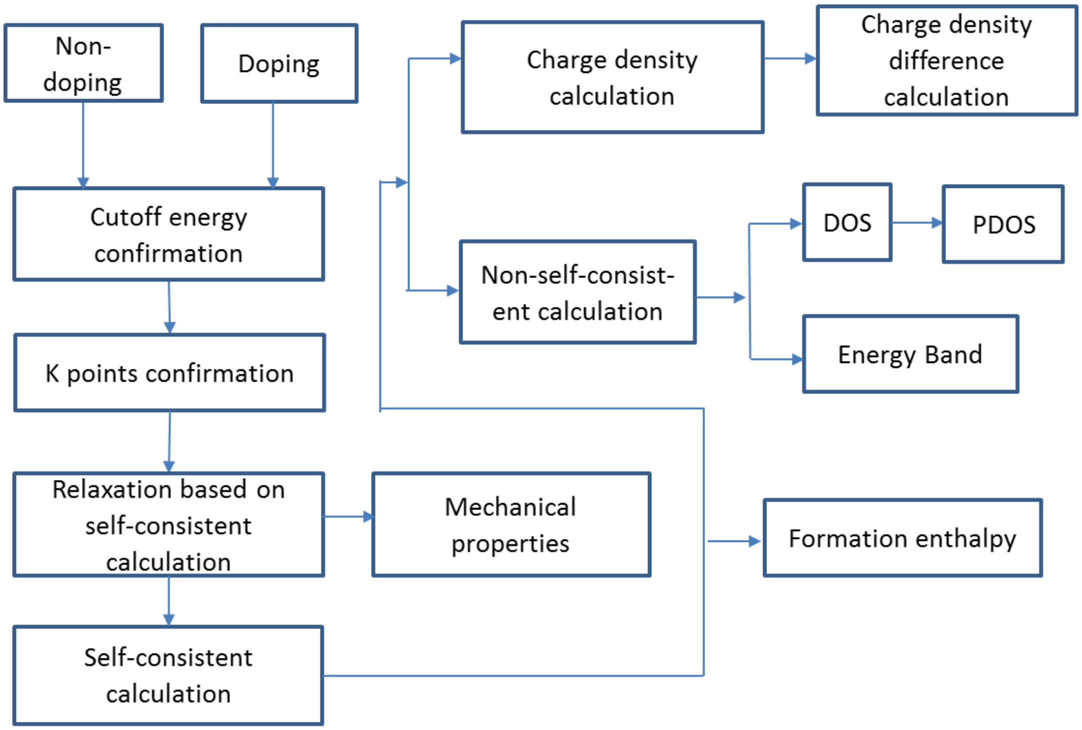

Figure 4.2 A flow chart illustrating the sequence of calculations applied in this research. The selection of parameters and properties were chosen for calculations is described as follows:

a) **<u>Cutoff energy:</u>** The cutoff energy refers to the kinetic energy cutoff for the wave-function and charge density. It is important to choose a proper energy cutoff in the interest of computational accuracy. Kinetic energy cutoffs for wave-functions should be selected to match r_c (Fig 4.3) because the real and the pseudo wave-function and potentials match at this point. An example of how the cutoff energy influences the total energy of a methane molecule is shown in Fig 3.1 where with the increasing of the energy cutoff the total energy tends, as expected, to plateau.

The kinetic energy cutoff for the charge density was in turn set to be 10 times that of wave-functions. In this study, the cutoffs for kinetic energy and charge density for pure phase crystal structure calculations are set as 816 eV and 8160 eV, respectively for pure phase calculation. The convergence accuracy of the total energy and force are set as 10^{-5} eV and 10^{-5} a.u, respectively. For doping systems, e.g., a β-C_2S supercell with 268 atoms, the cutoff energy is changed to 420 eV for calculation efficiency. This selection was verified by trial calculation. Furthermore, ultrasoft pseudopotentials are employed.

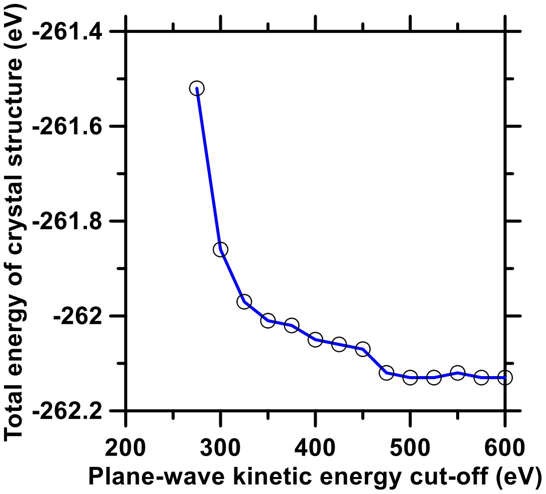

Figure 4.3 An example of total energy as a function of planewave cut-off energy. [125] The plane-wave energy is calculated with LDA|CA|PAW approximations. The system ZnS crystal structure with the k-point mesh 8 × 8 ×8.

b) ***k*-points selection:** For a periodic (3D) crystalline system, the integrals in the real space over the infinite space are replaced by integrals in the finite reciprocal space. According to Bloch's theorem, the finite reciprocal space can be determined by the first Brillouin zone. The k-point mesh allows building a discrete grid of points in the first Brillouin zone (BZ) where the electron density is determined at each point, to be subsequently continuously summed to obtain its integrated value. A dense k-point mesh is needed for calculation convergence. Figure 4.4 shows a Na-doped graphene example of the change of the total energy as a function of the number of k-points. A general trend is that the higher the number of k-points, the more accurate the result until numerical converge is reached. However, a denser *k*-point mesh implies more expensive calculations, so both simulation accuracy and computational cost should be taken into consideration. For those lattice sides with larger values, e.g., *c* = 2.0871 nm in α'$_L$-C_2S, the number of k-points could be smaller because in the reciprocal space longer lattice dimensions turns to be shorter. As per the lattice parameters of C_2S polymorphs, k-point meshes for γ-, β- and α'_L-C_2S are determined as 5×2×4, 5×4×3 and 1×2×3, respectively. It should be noted that for non-self-consistent calculations, *k*-point meshes should be denser and this will be further discussed in the corresponding simulation sections. For doped systems with more atoms, *k*-points are set to be smaller, which will be discussed in doping section.

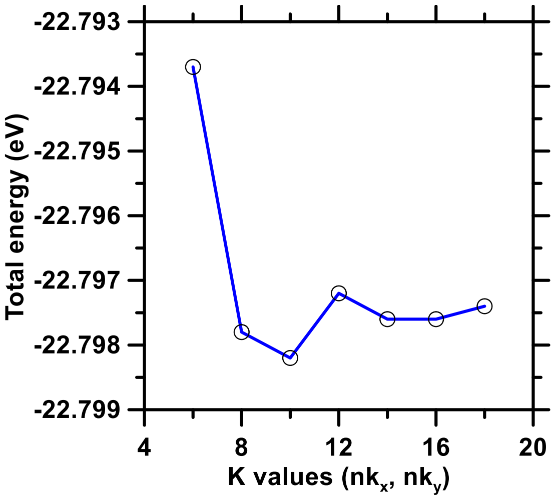

Figure 4.4 An example: the evolution of the total energy with increasing number of sampled "*k-points*" [126]. The system is Na-adsorbed graphene.

c) <u>Relaxation:</u> During structural relaxation, the crystal structures are turning to their optimized/stable configurations when minimizing the total energies and internal forces towards their convergence levels. For example, the convergence threshold for self-consistency is set to 10^{-9} eV for pure phase calculation. The relaxation could be conducted in two steps. The first one is a dynamic relation (in calculation noted with "vc-relax") which means during the relation process, both the atomic positions and the lattice parameters are optimized. After this relaxation, a "stationary" relation (in calculation noted with "relax") will be conducted and in this relaxation, only lattice parameters are optimized.

d) **Self-consistent calculation and total energy:** For optimized crystal structures, the total energy of each structure can be obtained by self-consistent field calculation (SCF, Hartree-Fock method). The whole calculation procedure is an approximation of the wave-function and system energy in a stationary state. It assumes the wave-function of a single configuration. In local approach, the states of a system can be demonstrated with wave-functions. PW method applies infinite periodical waves simulate local states. At the beginning of the calculation, an arbitrary state is set for a possible solution. Convergence is often reached after several iterations given as outcome the total energy of the system. The lower the energy the more stable the system. This approach, therefore, allows comparing the total energy of α'_L-, β- and γ-C_2S, to identify the most stable polymorph among the three.

e) **Non-self-consistent calculation:** Non-self-consistent calculation is also called Harris-Foulkes (H-F) functional calculation [127]. The outcomes of the SCF calculations are used to conduct the non-self-consistent calculation allowing to construct the corresponding charge density which is then used to calculate the band structure.

f) **Analysis of the unit cell structure:** α'_L-, β- and γ-C_2S demonstrate polymorphic transitions with respect to temperature changes. The following parameters are evaluated: i) lattice parameters, ii) unit cell volume, iii) density, iv) crystal space-group, v) Si-O bond lengths and bond angles and Si-O tetrahedral volumes, vi) Ca coordination number, vii) arrangement and orientation of the Si-O tetrahedra and Ca-O polyhedral. Through such a comparison, relations and differences amongst the three polymorphs are provided.

g) **Calculations of elastic constants and mechanical moduli:** Mechanical properties are of great interests for engineering materials. The calculation of the elastic constants allows determining its bulk, elastic, and shear moduli, and the Poisson's ratio. Two methods can be applied to determine the full set of elastic constants: (a) via the total energy calculation method and (b) via the stress-strain method. From a thermodynamics angle, $P = (\partial U / \partial V)_T$, where P is pressure, U is the internal energy and V is volume. Since first principle calculations are processed at constant temperature (0K), P can be obtained from the slope of the U-V curve and then the elastic constants could be derived from P-V curves. The second method is to directly apply a strain on the unit cell and then calculate the response of stress. Since mechanical properties can be expected to be related to both structural and compositional features of α'_L-, β- and γ-C_2S, the comparison of the elastic constants against the lattice parameters (and by extension, cell volumes), atomic (re)arrangements, and charge density, allows to investigate the differences in the response of the polymorphs to mechanical stress.

h) **<u>Calculation of charge density and charge density difference:</u>** The charge density distribution of the system can be represented either in 2-D or in 3-D. It is the charge density obtained by subtracting the atomic charge density of free-state from a complex charge distribution state in a crystalline bulk. From this distribution difference, one can tell the bonding preferences as well as bonding strength. It is also useful to investigate the charge density difference distribution versus the bond length curves. When a system is doped with guest ions, by observing the charge distribution in the vicinity of the dopants, electronic features, and possible chemical reaction trends can be better understood. Such an exploration is needed as chemical reactions involve charge density re-distribution. By knowing the charge distribution of a system, it is possible to predict its chemical behaviors.

i) **<u>The density of States (DOS), Partial Density of States (PDOS), and electronic band structure:</u>** The DOS describes the number of states per energy level that is possible to be occupied by electrons. It turns out that the electronic band structure describes the energy level populated by electrons. While DOS and the band structures both provide the information about the band gap of the material, from the DOS we can infer the most likely distribution of charge with respect to each energy level, while from the bands we can infer the electron energy level at specific k points that is along specific path in the reciprocal space. Furthermore, the VBM (valence band maximum) and CBM (conduction band minimum) around the Fermi level allow analyzing the band gap. A small, together with a large charge distribution on the VBM may indicate high reactivity. However, other factors like activation energy and temperature can also influence the correct determination of such property. The PDOS allow factorizing the contribution that each electronic orbital gives to the DOS. Therefore, a PDOS distribution can allow determining not only the contribution arising from each atom in the system but more specifically the electron orbital(s) which mostly contribute to the VBM. Such analyses can guide in identifying sites for *ad hoc* doping of ions (impurities) and the types of dopants to use.

j) **Enthalpy of formation:** The standard enthalpy of formation of a compound is the change in enthalpy that arises when one mole of a substance is produced starting from its elements at standard conditions (10^5 Pa and 298.15K). Note that for the purposes of this work, the control (formation enthalpy of pure phases) will be calculated from the oxides. In the case of *ab initio* calculations, the standard condition is 0 K and 0 Pa. Independently from this discrepancy, the enthalpy of formation computed at DFT level only gives the relative stability of the investigated polymorphs. In general, the more negative the enthalpy, the more stable the phase. The following reactions which can be used to calculate the enthalpy of formation of C_2S from its elements or its constituent simple oxides, respectively:

$$2Ca + Si + 2O_2 \rightarrow Ca_2SiO_4 \text{ (from elements)} \tag{4.22}$$

and

$$2CaO + SiO_2(\alpha - quartz) \rightarrow Ca_2SiO_4 \text{ (from oxides)} \tag{4.23}$$

k) Types of dopants and substitution sites: In reference to dopants, a few requirements need to be fullfilled: i) the charge balance of the unit cell should be maintained, in the case of iso/alio-valent doping, ii) the concentration of the dopants should be less than 4-to-6% which correspond to the maximum limits of impurity substitution in C_2S to prevent dopant clustering, iii) the dopants considered are common elements existing in practical such as Al^{3+}, Fe^{3+}, and Mg^{2+}, iv) dopant species should be well separated from each other so that inter-dopant interactions are minimized, v) doping sites should be selected to conform to high-symmetry positions. This requirement should uniformly be satisfied across the different polymorphs to ensure consistent comparisons.

5. Calculation of Pure C_2S

5.1 Simulation Parameters

A DFT plane-wave basis and Vanderbilt ultrasoft pseudopotentials [122] were used as implemented in the QUANTUM ESPRESSO distribution.[104] The exchange-correlation functional implemented within the generalized gradient approximation (GGA) in the form of the Perdew-Wang (PW91) functional is adopted. [116] Because β-C_2S is the dominated phase of belite in cement clinker [20], so we focus on it as well as the closely relating γ- and α'$_L$-C_2S. C_2S crystal structures refined by Mumme [94], [124] were used as the starting point for all periodic calculations. γ- and α'$_L$-C_2S are orthorhombic lattices (space group *Pna2₁* and *Pbnm*, respectively) while β-C_2S forms within a monoclinic crystal system (space group *P2₁/n*) (Figure 5.1). Both γ- and β-C_2S unit cells contain 28 atoms (4 Si, 8 Ca, and 16 O atoms). The unit cell of α'$_L$-C_2S is elongated approximately three times with respect to γ- and β-C_2S along the *c* axis, and contains a total of 84 atoms. The crystal structures were dynamically allowed to relax (*i.e.*, the lattice constants, and atomic positions were optimized simultaneously) as per the Broyden-Fletcher-Goldfarb-Shannon (BFGS) scheme.[128] A convergence threshold on forces of 2.57×10^{-4} eV/Å on each atom was imposed. The tolerance on the total energy was set to 1.36×10^{-7} eV. The k-meshes of points in the reciprocal space were set to 5×2×4, 5×4×3, and 1×2×3, for γ-, β-, and α'$_L$-C_2S structures, respectively.

The x-ray diffraction (XRD) patterns of the optimized C_2S polymorphs and doped structures were visualized using *CrystalDiffract* by simulating the powder diffraction patterns for particles with a size set to 1 μm. The x-ray structure factors and corresponding more interplane distances were obtained by setting the wavelength for the incident x-ray beam to 1.541 Å and the Gaussian type peak width to 0.05 corresponding to Cu-Kα radiation. The mechanical moduli (bulk (K), shear (G), and elastic (E)) of the three polymorphs were determined. The Reuss-Voigt-Hill (RVH) average based on the stress-strain method was applied [129] to evaluate the independent second order C_{ij} tensorial components (9 for α'$_L$- and γ-C_2S, and 13 for β-C_2S [130]). Uniform volumetric deformations were imposed on the unit cells for strain levels ranging from 0% to ±1% in 0.2% increments (for both tensile and compressive loads). The corresponding stresses were then retrieved by relaxing the atomic positions with the preset strains acting on the unit cells. The enthalpies of the formation with respect to the constituent elements (ΔH_e) and simple oxides (ΔH_o) were calculated to evaluate the thermodynamic stability of the three C_2S polymorphs, and the doped β-C_2S structures using Equation (1):

$$\Delta H_e = E_{tot} - 2E_{Ca} - E_{Si} - 2E_{O_2\,\mathrm{(g)}} \tag{5.1}$$

$$\Delta H_o = E_{tot} - 2E_{CaO} - E_{SiO_2\,(\alpha-quartz)} \tag{5.2}$$

where, E_{tot} (kJ/mol) is the calculated total energy of a given C_2S structure, and E_{Ca} (kJ/mol), E_{Si} (kJ/mol), E_{CaO} (kJ/mol), and $E_{SiO_2\,(\alpha-quartz)}$ (kJ/mol) are the total energies of the elements and simple oxides, respectively; $E_{O_2\,\mathrm{(g)}}$ (kJ/mol) is the total energy of O_2 in the gas phase treated by imposing periodic boundary conditions within a 15 × 15 × 15 Å^3 unit cell for the O_2 dimer.

5.2 C_2S Polymorph Crystal structures

5.2.1 Relaxed Structures

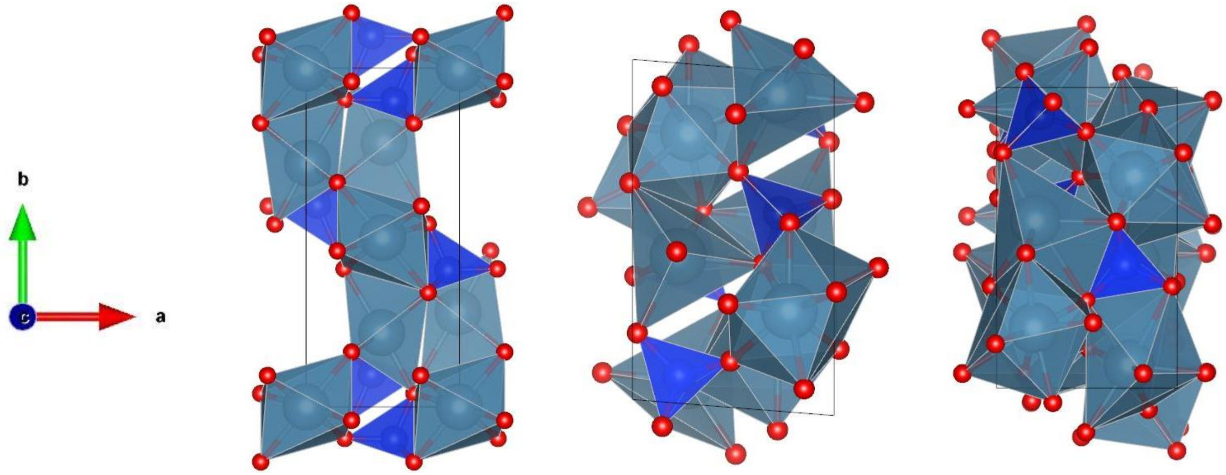

(a) *(b)* *(c)*

Figure 5.1 The relaxed unit cell's of **(a)** γ-C_2S**,** **(b)** β-C_2S, and **(c)** α'$_L$-C_2S. The blue, red, and grey spheres refer to Si, O, and Ca atoms, respectively. These structures are composed of Si-O tetrahedra and Ca-O polyhedra. All Si atoms are coordinated by four O, while the coordination number for Ca atoms in γ-, β-, and α'$_L$-C_2S are 6, 7/8, and 6/7/8, respectively.

Table 5.1 below reports the calculated and experimental results [97] for the lattice parameters and unit cell volumes of the different C_2S polymorphs. In general, the unit cell volumes are in good agreement with experimental results; within ±2% - for all polymorphs and are in good agreement with the values of Manzano et al. [131]

Table 5.1 The lattice parameters, and the unit cell volumes of the different C_2S polymorphs.

	Polymorph	**a (Å)**	**b (Å)**	**c (Å)**	**γ (°)**	**Volume (Å^3)**
DFT Calculation	γ	5.115	11.315	6.789		392.9
	β	5.568	9.356	6.798	94.557	353.0
	α'$_L$	5.592	9.310	20.500		1067.3
Experimental Data [94], [124]	γ	5.076	11.214	6.758		384.7
	β	5.512	9.314	6.758	94.580	345.8
	α'$_L$	5.590	9.496	20.527		1089.6

To further check the agreement between the calculated crystal structures and experimental data, XRD patterns and structure factors were obtained. Figure 5.2 shows comparisons of structure factors plot against the corresponding interplanar distance where each datapoint represents a reflective plane. While overall the calculated results are in reasonable good agreement with the experimental structure refinements, the results are improved for γ- and β- than for α'_L-C_2S. [94], [124].

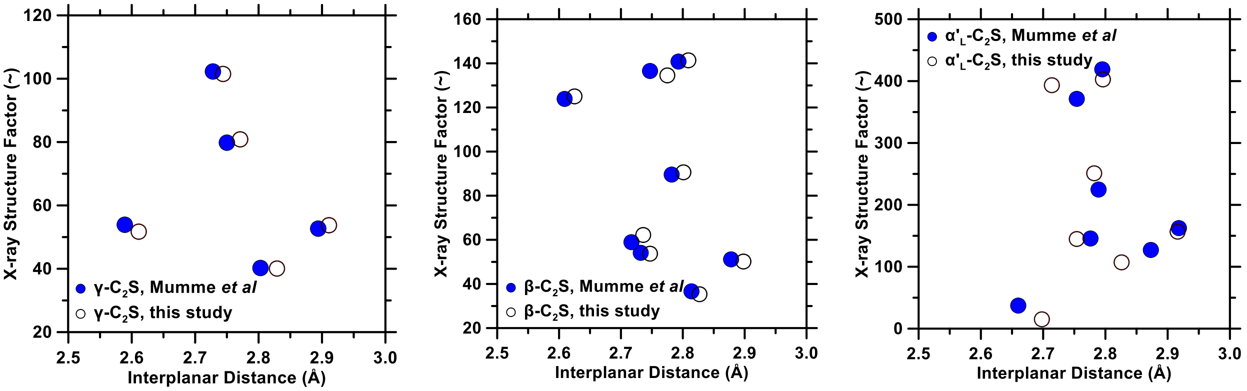

(a) ***(b)*** ***(c)***

Figure 5.2 X-ray structure factors as a function of the interplanar distance for **(a)** γ-C_2S, **(b)** β-C_2S, and **(c)** α'_L-C_2S. The blue dots represent values obtained by Mumme [94], [124] and the white dots are obtained by analysis of relaxed structures obtained herein. In XRD map, we filtered the bottom 10% value and calculate the remaining data for the x-ray structure factors. When cast in the context of x-ray diffraction patterns, the structure factor comparisons suggest that while peak positions would be nominally similar, peak intensities may show some differences especially so for γ-C_2S.

5.2.2 Relaxed Structure Geometry Analysis

Each γ- and β-C_2S unit cell comprises 4 Si, 8 Ca, and 16 O atoms; α'_L-C_2S shows by 12 Si, 24 Ca, and 48 O atoms per unit cell. All the O atoms coordinate with 4 Si atoms to form Si-O tetrahedra. On the contrary, the coordination number of the Ca atoms can assume different values.

Si-O tetrahedra comparison. Si atoms in all three polymorphs form comparable Si-O tetrahedra which show negligible, if any, differences in terms of Si-O bond lengths, bond angles, and tetrahedral volumes.

Table 5.2 Si-O bond lengths comparison across γ-, β- and α'$_L$-C_2S crystal structures

Si-O bonds \ Polymorphs	**γ-C_2S**	**β-C_2S**	**α'$_L$-C_2S**
Si-O1(Å)	1.67	1.66	1.67
Si-O2(Å)	1.66	1.66	1.65
Si-O3(Å)	1.66	1.65	1.65
Si-O4(Å)	1.64	1.62	1.63
Average bond length (Å)	1.66	1.65	1.65
Bond angle variance (deg^2)	24.07	9.93	2.24~10.21
Si-O tetrahedral volume (Å^3)	2.32	2.29	2.29~2.30

Si-O tetrahedra in the γ-C_2S unit cell are all equivalent in terms of volumes. In β-C_2S, Si-O tetrahedra are quite similar to each other and make a very tiny difference. For this reason, the Si-O tetrahedra present in γ-C_2S and β-C_2S can be taken as belonging to one kind only. The situation is different in α'$_L$-C_2S where the Si-O tetrahedra appear different from each other (Table 5.2). In fact, the 4 Si-O bond lengths in γ-C_2S are very close to each other, so as β-C_2S and α'$_L$-C_2S. The average bond lengths of γ-, β- and α'$_L$- C_2S structures are 1.658 Å, 1.649 Å, and 1.65 Å, respectively. The Si-O tetrahedral volumes of γ-, β- and α'$_L$- C_2S structures are 2.322 Å^3, 2.292 Å^3 and 2.29~2.30 Å^3, respectively. Both average bond lengths and Si-O tetrahedral volumes are very close to each other.

Ca-O polyhedral comparison. In contrast, drastic differences are expected in the coordination of the Ca atoms which coordinate as 6 fold, 7 or 8 fold, and 6, 7, and 8 fold respectively, in γ-, β-, and α'$_L$-C_2S. In γ-C_2S, although all the Ca atoms are 6-fold coordinated, Ca-O octahedra can be divided into two types (Ca1, and Ca2) according to the average Ca-O bond lengths and the volumes of the polyhedra. In β-C_2S, the different coordination states (7 and 8 fold) do not affect the average Ca-O bond lengths. In α'$_L$-C_2S – and in the calculated structure, 6, 7, and 8 coordinated Ca atoms exist in abundances of 33.3%, 16.7%, and 50%, respectively which are significantly different from those observed in the original structure (16.7%, 16.7%, and 66.6% [21] in order of increasing coordination). In such cases, Ca-O octahedra form a network by sharing edges and faces with each other. The 8-fold coordinated Ca-O polyhedral share faces forming a chain. Further details regarding the atomic coordination numbers (CN), average bond lengths, and the polyhedral volumes are reported in Tables 5.3-5.5.

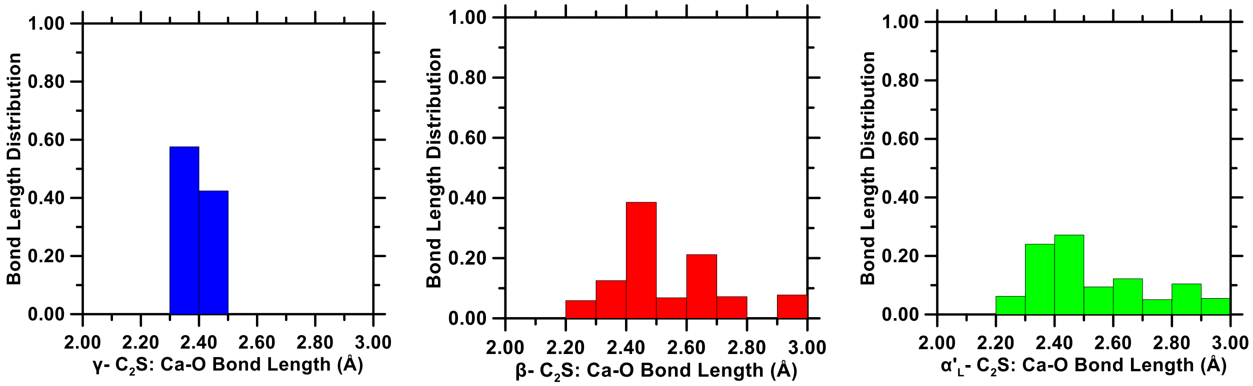

(a) *(b)* *(c)*

Figure 5.3 The bond length distributions noted for the Ca-O bond in **(a)** γ-, **(b)** β-, and **(c)** α'$_L$- C_2S polymorphs respectively.

Figures 5.4-5.6 depict the structures of the three polymorphs: (i) γ-C_2S is characterized by connected Ca-O octahedra and Si-O tetrahedra sharing edges and vertexes, (ii) β-C_2S displays a layered structure formed by Si-O tetrahedra and (iii) α'$_L$-C_2S, the lowest symmetry structure among these three polymorphs is formed by connecting numerous 6, 7-, and 8-coordinated Ca-O polyhedra and Si-O tetrahedra, where face sharing only occurs between the 8- and 6- or 8- and 7-coordinated polyhedra. While in all the three systems the Si-O bond lengths remain fixed around ≈1.6 Å, Ca-O bond lengths show significant dispersion as shown in Figure 5.3. This is in expectation with the variations in Ca-coordination noted in these systems. For example, while γ-C_2S shows an average Ca-O bond length around 2.35 Å, while in β- and α'$_L$-C_2S it ranges from 2.3 Å to 3.0 Å respectively.

The coordination nature of Ca atoms is much more complicated than that of Si-O atoms, since Ca-O polyhedra are different across the three polymorphs, and furthermore the coordination numbers can assume different values within the same crystal structure.

i) γ- C_2S case

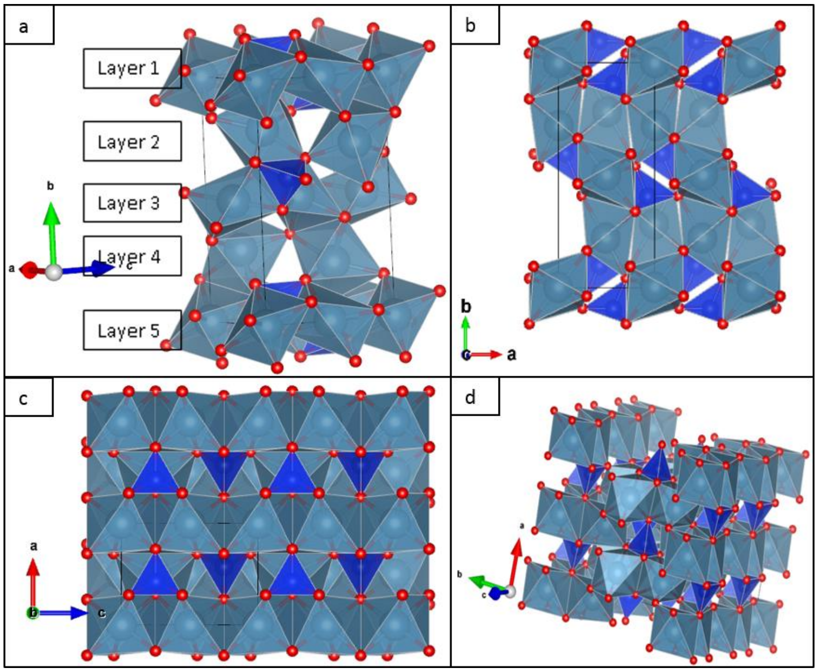

Figure 5.4 a) Five layers of γ- C_2S unit cell structure; **b)** (001) plane supercell structure; **c)** (010) plane supercell structure; **d)** perspective to emphasize the overall symmetric nature of the structure.

γ- C_2S unit cell structure consists of 4 Si-O tetrahedra and 8 Ca-O octahedra with no interstitial O atom (Fig 5.4 a-c. The γ-C_2S unit cell structure can be separated into 5 layers (Fig 5.4 a). Si-O tetrahedra exist only in layers 1, 3, and 5. Each Ca atom combines 6 O atoms and forms a Ca-O octahedron. This fact is more evident when the (001) plane is explored (Figure 5.4 b). Layer 1 repeats the structural pattern of layer 5. The composition of layer 1 is the same as that of layer 3 with the only difference lying in their orientations. Similarly, Layer 2 and layer 4 are of the same composition and of different orientations. In other words, with respect to Figure 5.4 b, when the structure is rotated rotates by 180°around the c axis, it coincides with the original structure. When the (010) plane is considered, the structure repeats itself along the *a* and the *c* axes. Every couple of Ca-O octahedra, indicated in Figure 5.4 c as #1 and #2, shares Si-O tetrahedra, indicated as #3. The Si-O tetrahedra undersurfaces, which are connected by three Ca-O octahedra vertexes, are parallel to the c axis (Figure 5.4 d implying that each Si-O tetrahedra share three edges with each of the Ca-O polyhedra.

In Layer 1, all the octahedra connect with each other by sharing edges while in Layer 2, the Ca-O octahedra connect with each other through their vertexes. Layer 1 and Layer 2 connect by edge-sharing octahedron. The orientations of the Ca-O octahedra belonging to Layer 1 and Layer 5 are the same, while Layer 3 lies opposite to them. Note that Layer 2 can be replicated by moving Layer 4 up by two layers. Each Si-O tetrahedra share three edges with three Ca-O octahedra and each O atom on these edges connect with three Ca-O octahedra and one Si-O tetrahedron. No connection is observed among the Si-O tetrahedra.

Table 5.3 Ca-O octahedral information

Ca types / **Ca-O bonds**	**Ca 1* (50% of all Ca atoms)**	**Ca2*(50% of all Ca atoms)**
Ca-O1 (Å)	2.406	2.466
Ca-O2 (Å)	2.406	2.446
Ca-O3 (Å)	2.376	2.446
Ca-O4 (Å)	2.376	2.390
Ca-O5 (Å)	2.319	2.390
Ca-O6 (Å)	2.319	2.305
Average bond length (Å)	2.367	2.407
Bond angle variance (deg^2)	201.432	174.506
Ca-O octahedron volume (Å^3)	16.248	17.309

Ca1*: Odd layers; Ca2*: Even layers.

There are two kinds of Ca atoms, Ca1 and Ca2, which are both 6-coordinated by O atoms. Ca1 atoms belong to odd layers, while Ca2 atoms belong to even layers. Structural information about the Ca octahedra are reported in Table 5.3 where the Ca-O bond lengths are listed in decreased order. Both Ca1-O and Ca2-O bond lengths are very close to each showing an averaged value of 2.367 Å and 2.407 Å, respectively. The octahedra volumes for Ca1-O and Ca2-O are 16.248 $Å^3$ and 17.309 $Å^3$, respectively corresponding to an absolute difference of 6.5%.These differences will be taken into consideration further in the project when doping position will be needed to be determined.

ii) β-C_2S case

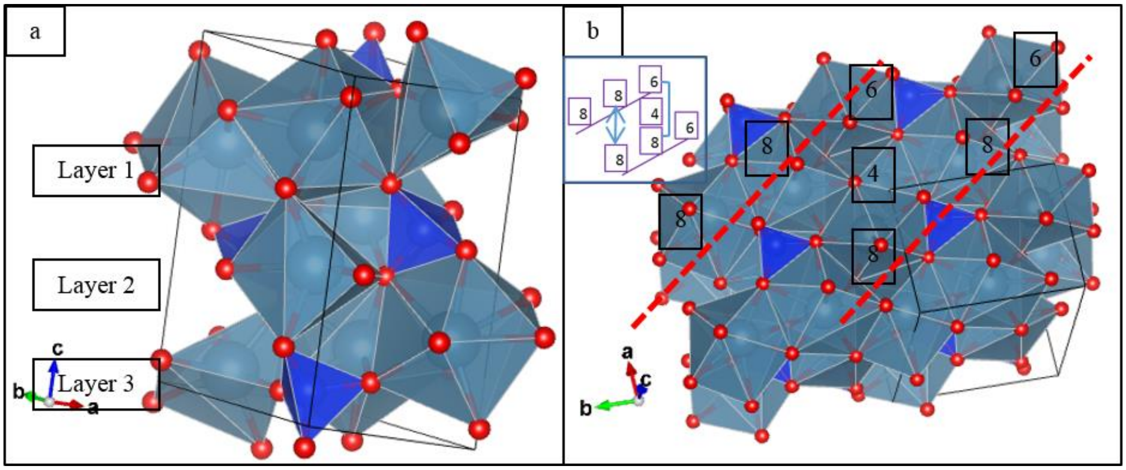

Figure 5.5 β-C_2S structure interpretation. **a)** Polyhedron layers in the β-C_2S unit cell; **b)** polyhedra connection mechanism in Layer 1 or 3, the sketch map on the left-top corner is the simplification of the polyhedra. In b), 4, 6 and 8 present the Si-O tetrahedra, the Ca-O octahedron and 8-coordinated Ca-O polyhedron. The blue arrow and fold line represent the connections between two polyhedra.

The coordination numbers of Ca atoms in the β-C_2S structure are 6 and 8. This result differs from the one reported in the literature (7 and 8). [20] This disagreement is from the bond length cutoff, however, the crystal structure agrees with the previous results. The 6- and 8-coordinated Ca atoms can be identified as Ca1 Ca2, respectively. β- C_2S unit cell structure is a monoclinic structure and its symmetry is not as high as γ- C_2S. As from Figure 5.5 a, the unit cell is formed by three polyhedral layers. While the Si-O tetrahedra evenly arrange in three layers, Ca1-O octahedra and Ca2-O polyhedra arrange as follows: i) Layer 1 → one Ca1-O octahedron and two Ca2-O polyhedra; ii) Layer 2 → two Ca1-O octahedra; iii) Layer 3 → one Ca1-O octahedron and 2 Ca2-O polyhedra. The two nearest Ca2-O polyhedra are connected to each other by face-sharing while each Ca2-O polyhedron connects with two other Ca2-O polyhedra.

Ca1-O polyhedra connect with other polyhedra by sharing edges and vertexes. In Layer 2, one Ca1-O polyhedron connects with the two nearest Ca1-O polyhedra and one Si-O tetrahedron. This is similar to what is observed for Si-O tetrahedra in Layer 1 and Layer 3 characterized by edge-sharing. One of the Si-O tetrahedra connects only with one Ca1-O and one Ca2-O polyhedron by sharing edges. The connection mechanism can be represented according to the scheme reported in Figure 5.5 b where the numbers indicate the coordination numbers. 4, 6, and 8 present the Si-O tetrahedra, the Ca-O octahedron, and an 8-coordinated Ca-O polyhedron, respectively.

Table 5.4 β-C_2S Ca-O polyhedral structural features

Ca types **Ca-O bonds**	**Ca1* (5000% of all Ca atoms)**	**Ca2* (50% of all Ca atoms)**
Ca-O1 (Å)	2.651	2.726
Ca-O2 (Å)	2.581	2.674
Ca-O3 (Å)	2.461	2.673
Ca-O4 (Å)	2.419	2.469
Ca-O5 (Å)	2.351	2.415
Ca-O6 (Å)	2.232	2.413
Ca-O7 (Å)	/	2.404
Ca-O8 (Å)	/	2.398
Average bond length (Å)	2.449	2.522
Bond angle variance (deg2)	449.888	/
Ca-O polyhedron volume (Å3)	15.479	27.864

*: Ca1 → coordination number = 6; Ca2 → coordination number = 8. Note: For beta-C_2S, if the bond maximum length is set as 2.8 Å, the coordination number is 6 and 8.

Ca atoms are evenly divided into Ca1- and Ca2-type atoms. In Table 5.4, Ca1-O and Ca2-O bond lengths are listed in decreasing orders. Ca1-O bond lengths range from 2.232 to 2.651 Å, and Ca2-O bonds range from 2.398 to 2.762 Å with an averaged bond lengths 2.449 Å and 2.522 Å, respectively. However, the volume of the Ca2-O polyhedron (27.864 Å^3) is 80% larger than that of Ca1-O (15.479 Å^3). The Ca1-O and Ca2-O polyhedra are similar to those in β-C_2S unit cell, and each Si-O tetrahedron shares 2 edges with a Ca-O polyhedron.

iii) α'$_L$- C_2S case

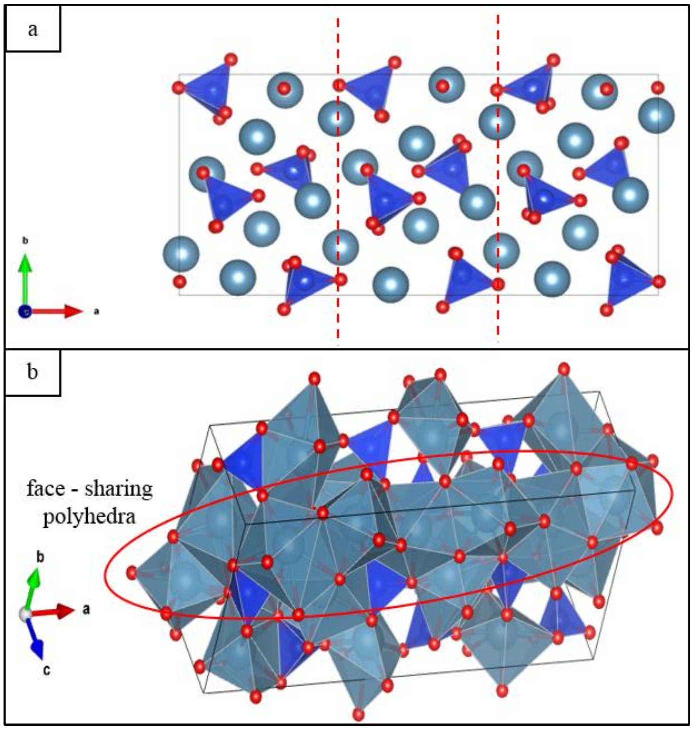

Figure 5.6 α'$_L$ -C_2S unit cell structure. **a)** (001) plane and the unit cell can be divided into three parts for analysis; **b)** Face sharing Ca-O polyhedral chain. The bond length maximum is set as 3.2 Å and the coordination numbers of Ca anion are 7 and 8.

α'$_L$- C_2S unit cell structure is more complex than γ- and β-C_2S structures because its unit cell is tripled in the c crystallographic axis (Figure 5.6 a). For this reason, it is convenient to divide α'$_L$-

C_2S unit cell into three portions along the equivalent c direction. Although the tree parts share the same chemical composition, the structure is not merely repeated. In fact, the orientations of the Si-O tetrahedra and the Ca atom positions are different (see Figure 5.6 a). Nevertheless, it should be noted that although there are some differences among the three portions of the unit cell, the corresponding Si-O tetrahedra, and Ca-O polyhedra show very similar bond lengths and volumes. For example, although the orientations of 3 Si-O tetrahedra on the top line of Figure 5.6 a) are slightly different, the bond lengths and tetrahedral volumes are the same. Also, since no major differences occur in the Ca-O polyhedra the Ca atoms can be classified in only one of the three portions of the α'_L- C_2S unit cell structure.

The Ca atoms in α'_L -C_2S are, within a 1:1 ratio, either 7- or 8-coordinated. However, Ca atoms showing the same coordination number is geometrically different as indicated in Table 5.5. Unlike γ- and β-C_2S and given its complexity, it was impossible to find a unique and efficient way of showing α'_L -C_2S unit cell. Its structure can be described as characterized by a single main Ca-O polyhedral chain consisting of eighteen Ca-O polyhedra which can be indicated as "on-chain" Ca-O polyhedra. The remaining six Ca-O polyhedra are all 7-coordinated and can be indicated as "off-chain" Ca-O polyhedra. Consequently, there are twelve 8-coordinated Ca-O polyhedra and six 7-coordinated polyhedra. The on-chain Ca-O polyhedra connect with each other only by sharing faces while the off-chain Ca-O polyhedra connect with the chain by sharing edges or vertexes. In a specific case, four of the off-chain Ca-O polyhedra connect with the chain by sharing edges and two of them by sharing vertexes. The Si-O tetrahedra invest in the interstitial space in between Ca-O polyhedra to which are connected by sharing edges and vertexes. The Si-O tetrahedra do not connect with each other. Similarly to γ -C_2S, in the α'_L -C_2S unit cell, each Si-O tetrahedral shares three edges with Ca-O polyhedra while in the β-C_2S structure, the edge-sharing number of Si-O tetrahedral is limited to two.

Table 5.5 α'_L -C_2S unit cell structure polyhedra information

Ca types **Ca-O bonds**	**Ca 1*(1/6 of all Ca atoms)**	**Ca2* (1/6 of all Ca atoms)**	**Ca3* (1/6 of all Ca atoms)**	**Ca4* (1/6 of all Ca atoms)**	**Ca5* (1/6 of all Ca atoms)**	**Ca6* (1/6 of all Ca atoms)**
Ca-O1 (Å)	3.088	2.854	3.137	2.670	2.842	2.983
Ca-O2 (Å)	2.971	2.719	2.771	2.624	2.820	2.643
Ca-O3 (Å)	2.519	2.646	2.556	2.603	2.806	2.545
Ca-O4 (Å)	2.489	2.483	2.425	2.552	2.456	2.487
Ca-O5 (Å)	2.434	2.466	2.367	2.459	2.430	2.427
Ca-O6 (Å)	2.357	2.373	2.365	2.402	2.422	2.381
Ca-O7 (Å)	2.971	2.249	2.245	2.392	2.345	2.349
Ca-O8 (Å)	/	/	/	2.380	2.340	2.336
Average bond length (Å)	2.582	2.541	2.552	2.510	2.558	2.519
Bond angle variance (deg^2)	/	/	/	/	/	/
Ca-O-polyhedron	22.868	22.147	21.946	27.347	28.323	27.191

*: Ca 1, 2, 3's coordination number is 7 and Ca 4, 5, 6's coordination number is 8.

As mentioned above, although Ca atoms in α'_L -C_2S unit cell can be divided into two types in reference to their coordination number, the Ca-O polyhedra common to the same coordination number are different (Table 5.5). For this reason, the Ca atoms can be classified according to six different kinds, indicated Ca1~6. Ca1~3 are 7-coordinated and Ca4~6 are 8-coordinated. The two classes show different variations in bond lengths. Table 5.6 lists this information in decreasing order. The Ca1~3-O bond lengths ranges are 2.971~3.088 Å, 2.249~2.854 Å, and 2.245~3.317 Å, respectively. The maximum bond length of Ca3-O is 16% bigger than that of Ca2-O; the minimum bond length of Ca1-O is 32% bigger than that of Ca3-O. Nevertheless, their average bond lengths and polyhedral volumes are quite close to each other. The Ca4~6-O bond lengths range 2.380~2.670 Å, 2.340~2.842 Å, and 2.336~2.938 Å, respectively. Unlike the 7-coordinated Ca-O polyhedra, the minimum bond lengths are quite similar to each other and the maximum bond lengths vary less. In fact, the maximum bond length of Ca6-O is roughly 122% bigger than that of Ca4-O while the average bond lengths and volumes of the 8-coordinated Ca-O polyhedra are also quite similar. The overall Ca-O average bond lengths of the 7- and 8-coordinated Ca-O polyhedra are similar, too.

iv) Summary

After the analysis of the three polymorphic structures, the following conclusions can be drawn.

a) The coordination numbers of γ-, β- and α'$_L$ -C_2S are 6, 6 & 8, and 7 & 8, respectively;

b) All the Si-O tetrahedra are similar in all three polymorphic structures;

c) In γ-, β- and α'$_L$ -C_2S structures, there are 2, 2, and 6 kinds of Ca atoms, respectively, with respect to bond lengths and Ca-O polyhedra volumes. This aspect is important for further investigation of doping sites selection;

d) γ- C_2S is the most symmetric structure, followed by β- C_2S and α'$_L$ -C_2S.

The change in coordination numbers from the γ- C_2S structure to β- C_2S and then α'$_L$ -C_2S can be at least partially explained as follows.

When lattice (equivalent) parameters are compared across the polymorphs with setting γ-C_2S as the standard, β- and α'$_L$ -C_2S result compressed in the b axis by 17% and 18%, respectively (Table 5.1). As a result, the crystal structure changes by adjusting atomic positions as well as polyhedra orientation, while the coordination number of Ca changes from 6 to 6 & 8 (β- C_2S) and 7 & 8 (α'$_L$ -C_2S).

5.3 Mechanical Properties

The mechanical behavior of materials is an essential property in materials engineering. For this reason, the determination of the elastic constants of γ-, β- and α'$_L$ -C_2S is a key task in this work. Once the elastic constants are available, the other mechanical properties, e.g. Young's modulus and Poisson's ratio, can be calculated from them. Two computational methods can be applied for the determination of the overall set of elastic constants: (i) the energy method and (ii) the stress-strain method [132] (discussed in Section 3). In this research, the latter is applied because the elastic constants can be obtained directly obtained from applied strains and corresponding stress.

5.3.1 Calculation Design

The necessary steps for the determination of the elastic constants with the stress-strain method are listed as it follows:

- Step 1: Apply optimized structures from previous parts for elastic constants calculation;
- Step 2: The calculation is designed according to the stress-strain method; by imposing the strain matrix, the calculation is divided into 6 steps corresponding to the following 6 steps×strain variations: ±1.0%, ± 0.8%, ±0.6%, ±0.4%, ±0.2%);
- Step 3: The structure is relaxed at each imposed strain;
- Step 4: A linear fit is performed for each C_{ij} and the slope is determined;
- Step 5: The mechanical moduli arising from the elastic constants are determined according to the Voigt, Reuss, and Hill averages.

In order to determine the full set of elastic constants, the following procedure was adopted. A preset deformation "e" is imposed to act on the unit cell according to the values ±1.0%, ± 0.8%, ±0.6%, ±0.4%, ±0.2% while a corresponding strain ε_i applies. Within the adopted scheme, the diagonal strain components equal to preset deformation while the off-diagonal strain components equal to half of the preset deformation. With the pre-set strains acting on the unit cells, the corresponding stress is calculated by relaxing the structures. Taking strain symmetry into consideration, the full set of elastic constants (C_{ij}) can then be easily obtained by applying the definition of elastic constants as the relation between stress and strain. Obviously, the compliance matrix (S_{ij}) can also be obtained through the inversion of the C_{ij} matrix.

a) Orthorhombic Structure

The full set of elastic constants for an orthorhombic lattice is given in the matrix as in Figure 5.7. Taking the symmetry into consideration, there are only nine independent components left: C_{11}, C_{22}, C_{33}, C_{44}, C_{55}, C_{66}, C_{12}, C_{13}, and C_{23}. The calculation can be designed following six steps:

a) $\varepsilon_1=e$, $\varepsilon_{i\neq1}=0$ to obtain C_{11}, C_{12}, and C_{13};
b) $\varepsilon_2=e$, $\varepsilon_{i\neq2}=0$ to obtain C_{22} and C_{23};
c) $\varepsilon_3=e$, $\varepsilon_{i\neq3}=0$ to obtain C_{33};
d) $\varepsilon_4=0.5e$, $\varepsilon_{i\neq4}=0$ to obtain C_{44};
e) $\varepsilon_5=0.5e$, $\varepsilon_{i\neq5}=0$ to obtain C_{55};
f) $\varepsilon_6=0.5e$, $\varepsilon_{i\neq6}=0$ to obtain C_{66}.

$$\begin{pmatrix} C_{11} & C_{12} & C_{13} & 0 & 0 & 0 \\ C_{12} & C_{22} & C_{23} & 0 & 0 & 0 \\ C_{13} & C_{23} & C_{33} & 0 & 0 & 0 \\ 0 & 0 & 0 & C_{44} & 0 & 0 \\ 0 & 0 & 0 & 0 & C_{55} & 0 \\ 0 & 0 & 0 & 0 & 0 & C_{66} \end{pmatrix}$$

Figure 5.7 Orthorhombic structure elastic constant matrix

b) Monoclinic Structure

The full set of elastic constants for a monoclinic lattice is given by the matrix reported in Figure 5.8 where thirteen independent components are present: C_{11}, C_{22}, C_{33}, C_{44}, C_{55}, C_{66}, C_{12}, C_{13}, C_{23}, C_{16}, C_{26}, and C_{36}. The calculation for this set of components can be designed following the six steps listed below:

a) $\varepsilon_1=e$, $\varepsilon_{i\neq1}=0$ to obtain C_{11}, C_{12}, C_{13}, and C_{16};
b) $\varepsilon_2=e$, $\varepsilon_{i\neq2}=0$ to obtain C_{22}, C_{23}, and C_{26};
c) $\varepsilon_3=e$, $\varepsilon_{i\neq3}=0$ to obtain C_{33} and C_{36};
d) $\varepsilon_4=0.5e$, $\varepsilon_{i\neq4}=0$ to obtain C_{44} and C_{45};
e) $\varepsilon_5=0.5e$, $\varepsilon_{i\neq5}=0$ to obtain C_{55};
f) $\varepsilon_6=0.5e$, $\varepsilon_{i\neq6}=0$ to obtain C_{66}.

$$\begin{pmatrix} C_{11} & C_{12} & C_{13} & 0 & 0 & C_{16} \\ C_{12} & C_{22} & C_{23} & 0 & 0 & C_{26} \\ C_{13} & C_{23} & C_{33} & 0 & 0 & C_{36} \\ 0 & 0 & 0 & C_{44} & 0 & 0 \\ 0 & 0 & 0 & 0 & C_{55} & 0 \\ C_{16} & C_{26} & C_{36} & 0 & 0 & C_{66} \end{pmatrix}$$

Figure 5.8 Monoclinic structure elastic constant matrix

5.3.2 Calculation Results

Before elastic constants calculation, the unit cell structures should be relaxed to ensure the remaining stresses as small as possible. The variable-cell relaxation results for unstrained structures are shown in Table 5.1. The calculation is based on preset strains imposed on the optimized structures, so the following calculations are performed at a fixed unit-cell volume. As mentioned, all the relaxation calculations were performed with the Quantum ESPRESSO package imposing thresholds on the energy and the force convergences of 10^{-5} eV, and 10^{-4} eV/bohr^3, respectively. The stress matrix can be read directly from the output file and the elastic constant matrix can be obtained as shown in Table 5.6.

Table 5.6 Elastic constants for γ-, β- and α'$_L$ -C_2S

Data / **C_{ij}**	**γ-C_2S (Orthorhombic)**		**β-C_2S (Monoclinic)**		**α'$_L$-C_2S (Orthorhombic)**	
	C_{ij} (GPa)	0.5(C_{ij}+C_{ji}) (GPa)	C_{ij} (GPa)	0.5(C_{ij}+C_{ji}) (GPa)	C_{ij} (GPa)	0.5(C_{ij}+C_{ji}) (GPa)
C_{11}	177.2		164.5		163.6	
C_{12}	60.3	60.3	47.0	46.9	51.4	51.0
C_{21}	60.2		46.9		50.6	
C_{13}	63.1	63.1	62.2	63.0	42.3	42.3
C_{31}	63.0		63.8		42.4	
C_{15}	/		-22.8	-16.7	/	
C_{51}	/		-10.7		/	
C_{22}	123.2		197.3		162.9	
C_{23}	60.7	60.6	58.8	58.8	63.8	63.8
C_{32}	60.5		58.8		63.8	
C_{25}	/		0.3	0.2	/	
C_{52}	/		0.1		/	
C_{33}	147.8		171.3		145.5	
C_{35}	/		-5.5	-7.7	/	
C_{53}	/		-10.0		/	
C_{44}	52.4		47.9		39.3	
C_{46}	/		2.2	0.7	/	
C_{64}	/		-0.7		/	
C_{55}	62.6		30.7		95.3	
C_{66}	75.2		53.7		52.6	

The values of the diagonal parameters reflect the material capability of resistance to compressive or tensile stress; the higher the value, the stiffer the material. Taking γ- C_2S as a reference, the ratios of C_{11}, C_{22} and C_{33} with respect to β- and α'$_L$ -C_2S are 1: 0.93: 0.92, 1: 1.60: 1.32, and 1:1.16: 0.98, respectively. From Table 5.1, the equivalent side lengths arising from the equivalent a, b, and c axes are 1:1.09:1.0863, 1:0.83:0.8221 and 1:1.00:1.01, respectively. The comparison of these ratios indicates that the stiffness of the materials is inversely proportional to unit cell side lengths. A shorter side length indicates the atoms in this side direction is closer to each and these atoms will form stronger bonds, which explains why the stiffness of γ- and α'_L -C_2S are inversely proportional to unit cell side lengths. However, β- C_2S structure does obey this trend because it is monoclinic structure.

Table 5.7 Comparison of elastic constants and unit cell structures

C_{ij} phase	x	C_{11} (GPa)	ratio	y	C_{22} (GPa)	ratio	z	C_{33} (GPa)	ratio
γ-C_2S	*a*	177.20	1	c	147.78	1	*b*	123.19	1.00
β-C_2S	*a*	164.54	0.93	*b*	197.34	1.60	*c*	171.26	1.16
α'_L-C_2S	*c*	145.48	0.92	*a*	163.36	1.32	*b*	162.9	0.95

Note: x, y, and z stand for equivalent *a*, *b,* and *c* direction, respectively and the symbols under x, y and z columns are the unit cell axes before transformation to their equivalent axes.

As in Table 5.7, some of the off-diagonal symmetric elastic constants vary significantly between each other. This is the case, for example, for C_{15} and C_{51}. An explanation for this result is that the β- C_2S structure is not stable under the imposed strained conditions. The negative values also indicate the structure is quite unstable under strains.

5.3.3 Calculation of Young's Modulus and Poisson's Ratio of Elastic Constants

Elastic properties play a key role in materials science and technology. The elastic tensors at any order are defined by the Taylor expansion of the elastic energy or stress in terms of the applied strain. It is reported that the elastic Young's modulus and the Poisson's ratio can also be derived from the values of C_{ij}.[129] In this study, *ElaStic* is used. *ElaStic* is a tool that is able to calculate the full second-order elastic stiffness tensor for any crystal structure from ab initio total-energy and/or stress calculations. This tool also provides the elastic compliances tensor and applies the Voigt and Reuss averaging procedure in order to obtain an evaluation of the bulk, shear, and Young moduli as well as the Poisson ratio of polycrystalline samples. In a first step, the space-group is determined. Then, a set of deformation matrices is selected, and the corresponding structure files are produced. In a next step, total-energy or stress calculations for each deformed structure are performed by a chosen density-functional theory code. The computed energies/stresses are fitted as polynomial functions of the applied strain in order to get derivatives at zero strain. The knowledge of these derivatives allows for the determination of all independent components of the elastic tensor. In this context, the accuracy of the elastic constants critically depends on the polynomial fit. Therefore, we carefully study how the order of the polynomial fit and the deformation range influence the numerical derivatives, and we propose a new approach to obtain the most reliable results. We have applied ElaStic to representative materials for each crystal system, using total energies and stresses calculated with the full-potential all-electron codes exciting and WIEN2k as well as the pseudo-potential code Quantum ESPRESSO [52]

Step 1: Voigt approach, upper limit:

$$B_V = \frac{1}{9}[(C_{11}+C_{22}+C_{33})+2(C_{12}+C_{13}+C_{23})] \tag{5.3}$$

$$G_V = \frac{1}{15}[(C_{11}+C_{22}+C_{33})-2(C_{12}+C_{13}+C_{23})+3(C_{44}+C_{55}+C_{66})] \tag{5.4}$$

Step 2: Reuss approach, lower limit:

$$B_R = [(S_{11}+S_{22}+S_{33})+2(S_{12}+S_{13}+S_{23})]^{-1} \tag{5.5}$$

$$G_R = 15[4(S_{11}+S_{22}+S_{33})-4(S_{12}+S_{13}+S_{23})+3(S_{44}+S_{55}+S_{66})]^{-1} \tag{5.6}$$

where S_{ij} are the elements of the compliance matrix.

Step 3: Hill approach, average:

$$G_H = \frac{1}{2}(G_V + G_R) \tag{5.7}$$

$$B_H = \frac{1}{2}(B_V + B_R) \tag{5.8}$$

Step 4: Young's modulus and Poisson's ratio:

$$E = \frac{9BG}{3B+G} \tag{5.9}$$

$$\nu = \frac{3B-2G}{2(3B+G)} \tag{5.10}$$

where B and G are the bulk and shear modulus, respectively.

Table 5.8 Modulus and Poisson's ratio calculation

Approaches	**Modulus**	**γ-C_2S (Orthorhombic)**	**β-C_2S (Monoclinic)**	**α'$_L$-C_2S (Orthorhombic)**
Voigt approach	B_V (GPa)	90.7	96.7	87.3
	G_v (GPa)	55.7	51.00	58.4
Reuss approach	B_R (GPa)	87.0	95.2	87.0
	G_R (GPa)	52.3	46.8	53.2
Hill approach	B_H (GPa)	88.8	96.00	87.2
	G_H (GPa)	54.0	48.9	55.8
Young's modulus	E (GPa)	134.7	125.4	138.0
Piosson's ratio	ν	0.25	0.28	0.24

Table 5.9 lists the results obtained for the bulk and the shear moduli. The different values for the modulus reflect a degree of structural anisotropy across the three polymorphs related to the

chemical composition of the different crystallographic directions. The most important factors influencing variations in Young's modulus and Poisson's ratio for the three polymorphs are considered to be the density of the materials, the Si-Si pair distances, and Si-O average bond lengths. Generally, G and E are proportional to mass density and ν is inversely proportional to mass density; B does not change a lot as mass density increases. β -C_2S, a monoclinic crystal structure, exhibits completely opposite behavior to γ- and α'$_L$ -C_2S with respect to G, B, E and ν as mass density increases.

Table 5.9 Factors relating to the mechanical properties

Phase	B_H (GPa)	G_H (GPa)	E (GPa)	ν	Mass density (g/cm^3)	MD ratio	Si-Si pair distance (Å)	Si-O average bond length (Å)
γ-C_2S	1	1	1	1	2.912	1	4.098	1.658
β-C_2S	1.0807	0.9056	0.9310	1.12	3.241	1.1130	4.148	1.649
α'$_L$-C_2S	0.9813	1.0337	1.0244	0.96	3.215	1.1041	4.217	1.65

As per discussion in section 5.3, the equivalent b axis is compressed during the transition from γ- C_2S to β-C_2S and furthermore when the α'$_L$ -C_2S structure is reached. As the equivalent b side is compressed, the Si-Si pair distances increase with a consequent increase in the density of the material and decrease in unit cell volume (Table 5.1). Such structural changes can be related to changes in the mechanical properties of the materials. The Si-O average bond length is the only factor that is not influenced a lot.

5.3.4 Summary

The stress-strain method was applied to determine the full set of elastic constants for the three C_2S polymorphs. With the calculated elastic constant the mechanical moduli and the Poisson's ratio were also derived. Diagonal elastic constants are discussed and related to changes in the lattice parameters. For γ- and α'$_L$ -C_2S which are orthorhombic lattices shear and Young's moduli are compared with respect to considerations related to the density of the material and the Si-Si pair distance; Poisson's ratio and bulk modulus are inverses proportional to mass density/ Si-Si pair distance. β -C_2S shows opposite trend to γ- and α'$_L$ -C_2S with respect to B, G, E, and ν.

The bulk (B_v), shear (G_v) and Young's moduli (E), Poisson's ratio (ν), as well as the indentation modulus (M) were calculated for the different C_2S polymorphs and are summarized in Table 5.10. Table 5.6 reports the complete list of elastic constant components for these structures. The different values of the elastic moduli reflect a degree of structural anisotropy of the three polymorphs, which indicates mechanical differences arising from the different structural configurations. The calculated Young's moduli are in good agreement with experimental data and range between 130-to-140 GPa [131]. For β-C_2S (Table 5.10), the overall set of calculated mechanical moduli also agree well with the data of Manzano et al.[35] α'$_L$-C_2S shows the largest Young's modulus (134.7 GPa) while the smallest is reported for the β- polymorph (125.4 GPa). As a general trend, β-C_2S shows inferior mechanical properties with its elastic modulus 7% and 9% smaller, and its hardness roughly 5% and 7% smaller as compared to γ-, and α'$_L$-C_2S, respectively.

The change observed in Young's modulus can be related to the compression that the *b* axis undergoes (17% change) during the transition from γ- to β-, which is even more pronounced when the α'$_L$-C_2S structure forms. As γ-C_2S is systematically compressed along the *b* direction, the Si-Si distance increases inducing an increase in density due to the reduction in the unit cell volume (see Table 1). This suggests that a density anomaly is seen in C_2S – wherein Young's modulus does not follow the evolution of density in the materials. It should be noted that the Si-O average bond length is the only structural descriptor which is not majorly affected by the compression (Table S1). On the basis of these results, one could speculate that cement's richer in belite, than another C_2S phase would be most attractive from the perspective of the grinding energy required to achieve equivalent milling, i.e., powder fineness outcomes. It is also noted that the elastic modulus of C_2S vs. C_3S is approximately 3.7% smaller – once again suggesting the practical gain, i.e., savings in grinding energy that would result if cement was richer in C_2S than C_3S. [133], [134]

Table 5.10 A tabulation of mechanical moduli, Poisson's ratio, and density of the C_2S polymorphs.

Approach	**Properties**	**γ-C_2S (Orthorhombic)**	**β-C_2S (Monoclinic)**	**β-C_2S (Manzano et al.[131])**	**β-C_2S (Exp.)**	**α'$_L$-C_2S (Orthorhombic)**
Voigt	B_V (GPa)	90.7	96.7			87.3
	G_v (GPa)	55.7	51.0			58.4
Reuss	B_R (GPa)	87.0	95.2			87.0
	G_R (GPa)	52.3	46.8			53.2
RVH	B_H (GPa)	88.8	96.0	111.0		87.2
	G_H (GPa)	54.0	48.9	53.1		55.8
Young's Modulus	E (GPa)	134.7	125.4	137.9	130-140 [131]	138.0
Poisson's ratio	ν	0.25	0.28	0.30	0.30 [135]	0.24
Ind. Modulus	M (GPa)	143.7	136.1			146.4
Density	ρ(g/cm^3)	2.912	3.241			3.215

Note: the subscript "V" means Vigot

5.4 Enthalpy of Formation

Knowledge of the enthalpy of formation can be used to establish the relative stability of the three different C_2S polymorphs. Thus, enthalpy datasets were calculated with respect to the: i) constitutive elements (ΔH_e) and ii) constitutive simple oxides (ΔH_o). The calculated results are noted in Table 5.11 and compared with experimental data. [136] In general, good agreement is seen (e.g., the enthalpy values agree within ±1% for ΔHe) and the stability of the C_2S polymorphs ranks as γ- < β- ≈ α'$_L$-C_2S – from most stable, to least stable.

Table 5.11 The enthalpy of formation of the different C_2S polymorphs calculated with respect to the constitutive elements, and simple oxides. Also shown, are comparative experimental data.

Polymorphs	ΔH_e* (kJ/mol) (exp[29])	ΔH_e (kJ/mol) (calc, this work)	ΔH_o*(kJ/mol) (exp[29])	ΔH_o (kJ/mol) (calc, this work)
γ (orthorhombic)	-2316.4	-2321.8	-135.6	-127.0
β (Larnite, monoclinic)	-2306.6	-2296.7	-125.8	-101.9
α'$_L$ (orthorhombic)	-2298.1	-2295.3	-125.2	-100.5

*: data from the literature refer to measurements carried out at 273.15 K and 1 atm.

However, the computed values for ΔH_o show poorer agreement – showing differences on the order of 6% (γ-C_2S), and 20% (β-, and α'$_L$-C_2S) vis-à-vis experimental data. Nevertheless, the ranking of phase stability remains unchanged.[103] The cohesive energy of the cohesive energies which order as 4.83 MJ/mol, 4.81 MJ/mol, and 4.80 MJ/mol for γ-, β- and α'$_L$-C_2S, respectively once again reinforces the idea that γ-C_2S is the most stable of the C_2S polymorph.

5.5 Charge Distribution and Density of States (DOS)

Charge Density Difference: Charge density maps in 2D/3D can be used to qualitatively investigate the nature of the chemical bonds between atoms. As such, charge density difference maps were obtained by subtracting each single atom charge density from the total charge density of the unit cell to gain insights regarding charge gain or loss of the atoms in the bulk (i.e., the same atoms when organized into a unit cell). Figure 5.9 shows 3D charge density difference maps for γ-, β- and α'$_L$-C_2S unit cells with the charge density isosurface set to 0.01 $e^-/Å^3$. The yellow and blue shading represent positive (gain) and negative (loss) charge densities, respectively. It can be seen that O-atoms are uniformly surrounded by large yellow areas on account of their electronegativity. On the other hand, silicon atoms are surrounded by blue areas which indicate the tendency of Si-atoms to donate charge – with a tetrahedral geometry of the charge density being noted. The charge distribution around the Ca-atoms reflects a significant charge loss indicating the ionic nature of these atoms. A comparison of charge density maps between the polymorphs shows that all three polymorphs show similar, strong Si-O bonds as indicated by the large blue areas surrounding the Si-atoms in their tetrahedral coordination.

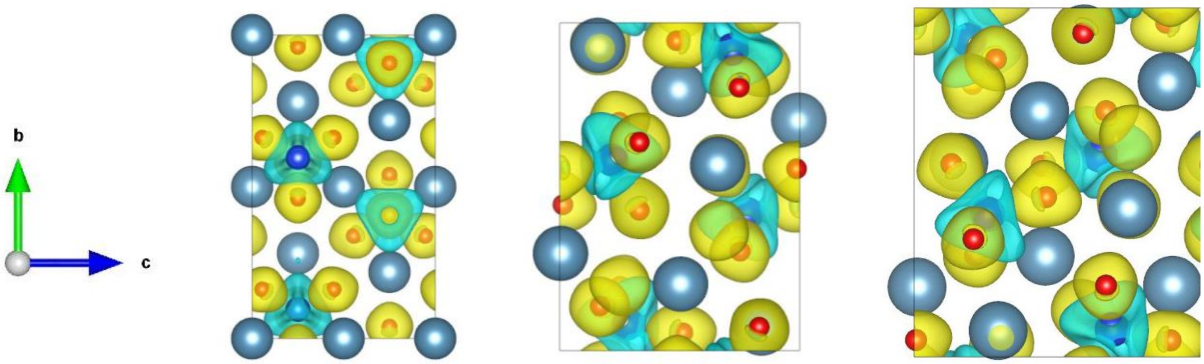

(a) **(b)** **(c)**

Figure 5.9 The 3D charge density difference maps for: **(a)** γ-C_2S, **(b)** β-C_2S, and **(c)** α'$_L$-C_2S as viewed from the "a" crystallographic direction with the isosurface level set at 0.01 $e^-/Å^3$. The yellow and blue areas represent positive and negative charge densities, respectively. The blue spheres surrounded by blue areas are Si-atoms, the red spheres surrounded by yellow areas are O-atoms and the large grey spheres indicate Ca-atoms.

To further study how electron charge density distributes between the Si- and O-atoms, the charge density difference with respect to the bond length is reported (see Figure 5.10) where the position of the O-atom is set as reference, i.e., the position of the O-atom coincides with the "0" position on the x-axis. With this reference, the Si-atom lies ≈1.65 Å apart from O-atom. Correspondingly, the Si-O-Si charge density curves indicate that the differences across the three polymorphs are negligible and that the Si-O bond distances are similar to each other. However, charge density distributions along the Si-O-Si tetrahedron pairs provide an explanation about the occurrence of pairs in the Si-O tetrahedra 3D motif which are common to the three polymorphs. The normal planes to the tetrahedron pairs lie at the midpoint of the Si-O-Si bond length, i.e., at 2.05 Å for γ-, 2.07 Å for β-, and 2.18 Å for α'_L-C_2S, for which the Si-O-Si pairs are shown in Figure 5.2-to-5.6. It should be noted that while linear charge density of the β- and γ- polymorphs are very similar, α'_L-C_2S remains dramatically different showing a biased gain in charge (from other atoms) towards the Si-atom in the range 2.4-to-3.4 Å. This may explain why α'_L-C_2S possesses different properties with respect to the other two polymorphs.

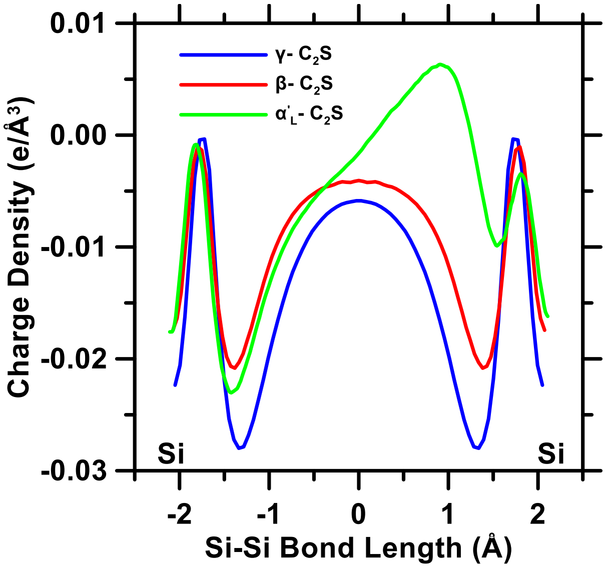

Figure 5.10 The linear charge density distribution of the different C_2S polymorphs plot as a function of the shortest Si-O-Si bonds.

Partial Density of States (PDOS), Conduction Band Maximum (CBM), and Valence Band Minimum (VBM): The concept of DOS refers to the number of states that electrons can occupy per energy interval at each energy level. Therefore a DOS map describes the electron states at different energy levels while the partial density of states (PDOS) factorizes the DOS into its electron orbitals. Since the reactivity of materials can be contextualized within the concept of a band gap, the energy range of interest lays around the Fermi energy level (set to 0 in Figure 5.11). The PDOS around the Fermi level of α'_L-C_2S is ≈10% higher than those of γ- and β- polymorphs indicating a higher electron transfer potential for α'_L relative to the other polymorphs.

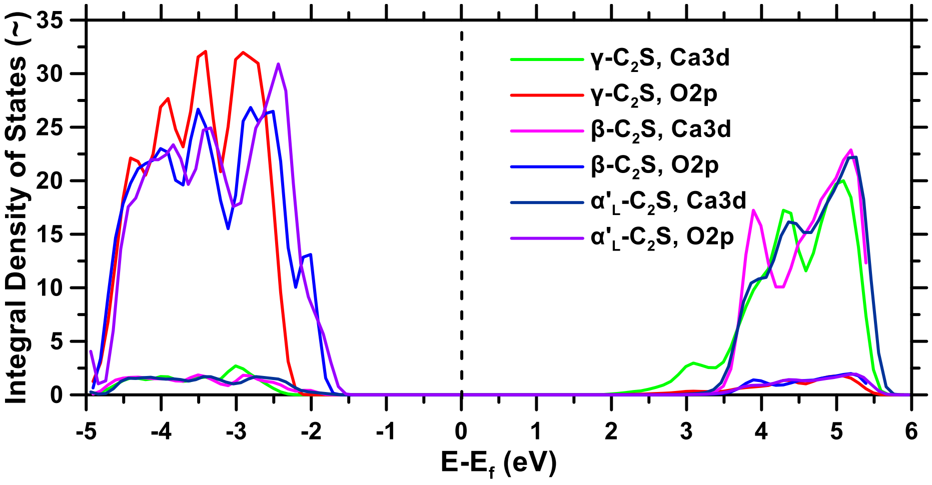

Figure 5.11 The partial density of states (PDOS) of the γ-, β-, and α'_L-C_2S polymorphs. The Fermi level is set uniformly at 0 eV.

Table 5.12 VB and CB levels around the Fermi energy.

Polymorph	**E_g by Qianqian et al (eV)** [103]	**E_g (this work) (eV)**	**VBM (eV)**	**CBM (eV)**	**E_f (eV)**
γ-C_2S	~4.3	3.8	-2.11	1.7	7.66
β-C_2S	~5	4.3	-1.6	2.77	8.7
α'_L-C_2S	~3.6	3.8	-1.3	2.55	8.5

The PDOS profiles show that the valence band (VB) is dominated by O-2p orbitals while the conduction band (CB) is dominated by Ca-3d states. In the case of α'_L-C_2S much sharper peaks than those appearing in β- and γ-C_2S are observed at both the VB and the CB. This is unexpected given that α'_L-C_2S contains three times the number of atoms present in the other two unit cells. The valence band maxima (VBM) of the polymorphs follow the trend: α'_L- < β- < γ-C_2S, while the conduction band minima (CBM) scales as γ- < α'_L- < β-C_2S. While all polymorphs are insulators with band gaps >3.0 eV, β-C_2S shows the largest band gap followed by γ- and α'_L-C_2S – in good agreement with previous studies (see Table 5.12).[103]

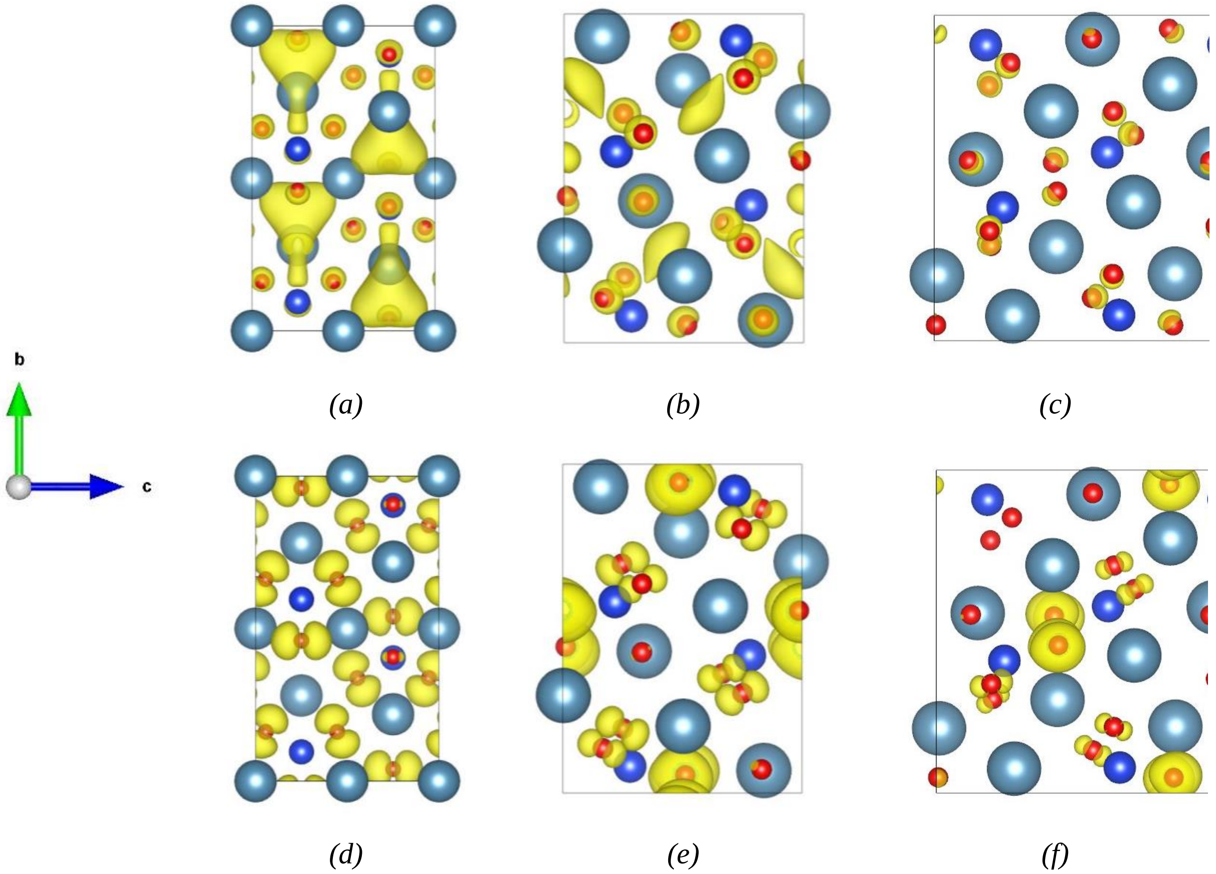

Figure 5.12 (a-to-c) Conduction band maxima (CBM) and (d-to-f) valence band minima (VBM) for γ-, β- and α'_L- C_2S polymorphs as viewed along the "*a*" crystallographic direction. The isosurface is set to 0.001 $e^-/Å^3$. Yellow and blue areas represent charge density gain and loss, respectively. The blue spheres are Si-atoms, the red spheres surrounded by yellow areas are O-atoms and the large grey spheres indicate Ca-atoms.

The partial charge density at CBM and VBM can be used to describe chemical reactivity with the VBM describing a tendency for the electrophilic attack, and the CBM governing nucleophilic attack (see Figure 5.12). According to the VBM isosurfaces, the electrons are mostly localized by O-atoms. Specifically, in γ-C_2S electrons are evenly distributed around O-atoms while in the β- and α'_L-

structures some O-atoms are less electron-negative as indicated by the unevenly distributed intensity of yellow shadings surrounding the O-atoms (see Figure 5.12 (e-f)).

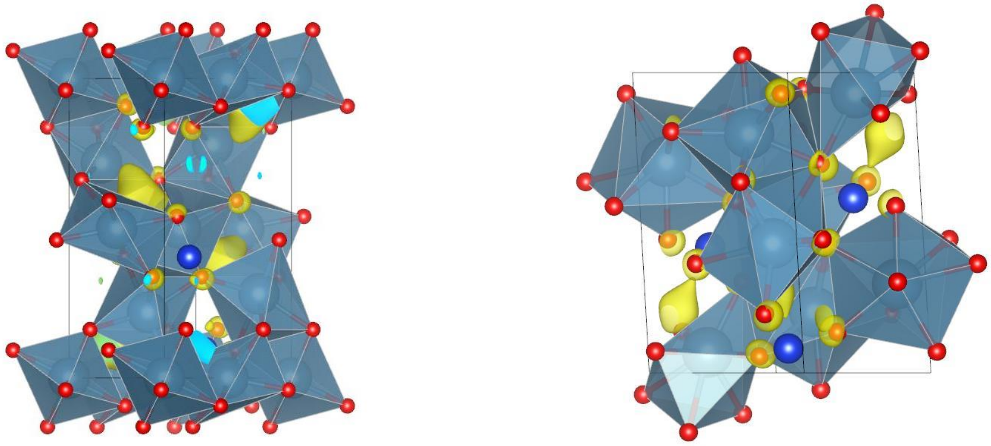

(a) CBM of γ-C_2S with Ca-O polyhedra.

(b) CBM of β-C_2S with Ca-O polyhedra.

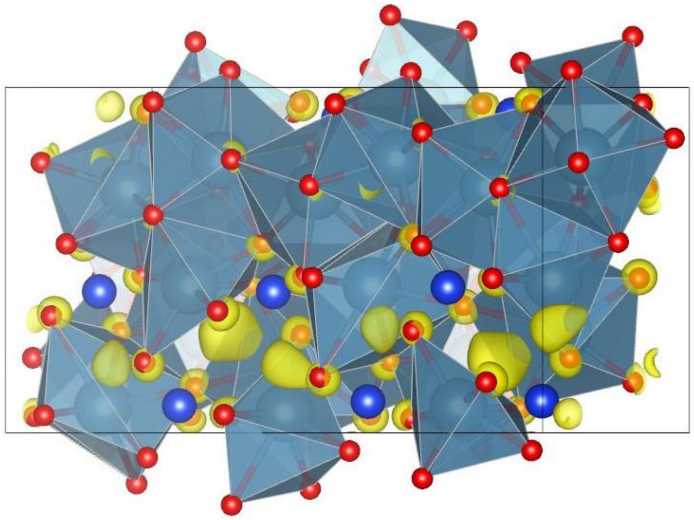

(c) CBM of α'_L-C_2S with Ca-O polyhedra.

Figure 5.13 CBM maps with Ca-O polyhedra of a) γ-C_2S, b) β-C_2S, and c) α'_L-C_2S. The red, blue, and grey spheres indicate O, Si, and Ca atoms, respectively. Yellow areas represent charge density gain. The charge distributes around O atoms, as well as Ca-O polyhedra interstitial spaces.

This suggests that the chemical reaction (e.g., with water) could occur uniformly at any site in γ-C_2S, but such reactions show a more site-specific affinity (i.e., at O-sites) in the other two polymorphs. When it comes to the CBM, the O-atoms show a slightly attractive capability with no longer electron-preferred O atoms where the charge distributes not only around O atoms but also in the interstitial spaces of belonging to the Ca-O polyhedra (Figure 5.13). For the CBM of γ- and β-C_2S, electrons distribute more substantially around the Si- and Ca-atoms, while in α'_L no significant electron localization is observed. These observations appear to indicate that β-C_2S is more reactive than the other C_2S phases; a conclusion in agreement with previous observations. The highest isosurface values for the CBM in γ-, β- and α'_L-C_2S are noted as 6.98×10^{-3} e^-/ Å^3, 8.26×10^{-3} e^-/ Å^3, and 2.59×10^{-3} e^-/ Å^3, respectively. In reference to VBM, the maximum isosurface values are 4.28×10^{-2} e^-/ Å^3, 9.25×10^{-2} e^-/ Å^3, and 4.72×10^{-2} e^-/Å^3, respectively. Since higher isosurface values can serve as an indicator of higher reactivity [36] – these quantifications, once again indicate that β-C_2S would be the most reactive of the pure C_2S polymorphs considered herein.

5.6 Summary

In this study, the property of pure and doped C_2S was investigated and compared. Starting from experimental structures, γ-, β- and α'_L-C_2S polymorphs were studied using DFT method: crystalline structures, formation enthalpies, mechanical properties, charge density difference maps, the density of states as well as VBM and CBM were determined and compared across the three pure polymorphs. Structural features, simulated XRD maps, and formation enthalpy (both from the elements and oxides) are in good agreement with experiments. In particular, enthalpies reveal the stability trend γ-C_2S > β-C_2S > α'_L-C_2S. Calculated elastic moduli are also in good agreement with experimental evidence with β-C_2S showing the smallest elastic moduli and hardness among the three polymorphs. Charge density difference distribution along the shortest Si-Si bonds show that α'$_L$-C_2S may possess different properties due to peculiar charge density distribution. Moreover, PDOS map indicates that α'$_L$-C_2S could be more reactive given its relatively small energy gap. For all three polymorphs, the density of states is dominated by O-2p states in VBM and by Ca-3d states in CBM. From CBM and VBM maps, β-C_2S reveals to be the most reactive of the polymorphs due to uneven charge localization in the VBM and charge distribution among Si and Ca atoms.

6. Doping Effect on β-C_2S

6. 1. Inspection of Mg, Al, and B Doping Effect

6.1.1 Introduction to Doped β-C_2S

As introduced previously, cement manufacture is responsible for around 7% of anthropogenic CO_2 emissions – suggesting a strong need to originate improved binder materials for use in construction with a reduced CO_2 impact. Cement clinker consists of four major phases – alite (Ca_3SiO_5, 50-70 mass %), belite (Ca_2SiO_4, 15-30 mass %), aluminate phase ($Ca_3Al_2O_6$, 5-10 mass %) and the ferrite phase ($Ca_4Al_2Fe_2O_{10}$, 5-15 mass %). Alite (impure C_3S) and belite (impure β-C_2S) constitute over 75 mass % of cement and form the primary strength contributing phases. However, belite on account of its low reactivity (e.g., only around 10% of the belite present reacts in the first 30 days of aging), only contributes appreciably to strength after 90 or more days of aging – as a result of which belite contents in cement remain small, vis-à-vis, alite. Nevertheless, β-C_2S forms at a temperature that is around 300°C lower than alite, [20] and requires one less formula unit of CaO. As a result, per unit mass, it has a CO_2 impact that is 17% smaller than alite – on account of a reduced need for CaO, and fuel consumption.[5] As such, enhancing the reactivity of belite, and further reducing its formation temperature – by the insertion of chemical impurities – is a very promising strategy to manipulate crystallochemical configurations of this phase – with a view towards synthesizing cement with increased reactive belite contents (and reduced alite contents) and thus reduced CO_2 impact.

The doped structure has been reported to potentially improve the reactivity of β-C_2S and recently computational methods have been successfully applied to address the chemical reactivity of the cementing phases. [34]–[36], [103] Wang et al.[103] applied DFT methods to investigate the relationship between the electronic structure and reactivity of α'$_L$-, β-, and γ-C_2S by examining the connections between cohesive energies, band gaps, valence band maximum (VBM) and the local density of states (LDOS). Huang et al. [133] on the other hand employed DFT methods to gain insights regarding the influence of impurities on structural, thermodynamic, mechanical, and the electronic properties of triclinic C_3S.

Sakurada et al. found that in Ba-doped β-C_2S the 7- coordinated Ca site is more stable than 8- coordinated Ca site. [34] Durgun et al. inserted Mg, Al, and Fe in β-C_2S to address their effect on CBM and VBM maps, and to explain the greater reactivity of the Al-doped species with respect to the other two doped materials.[137] The adopted doping strategy obeys to the neutral-cell concept where: (i) Two Mg atoms replace two Ca atoms; (ii) Two Al or B atoms replace one Ca and/or one Si atoms. Given the expected impurity concentration reported for Al_2O_3 and Fe_2O_3 (4~6wt%) [20], a low impurity concentration ratio is imposed. In order to fulfill this requirement (<3 wt.%), a 2×1×3 supercell (containing 168 atoms) was considered which also allows for a reasonable compromise between accuracy of the results and required computational time.

Despite significant data is available, clear evidence regarding the influences of impurities, as a function of the element type, and dosage remains difficult to assess from experiments alone. For example, while B impurities in C_2S are noted to positively influence its reactivity, [83] detailed insights into "why this is so" remain unavailable. To gain better insights, the most common dopants, i.e., Mg, Al and B, existing in β-C_2S will be taken into consideration.

The influences of impurities Mg, Al, B are examined and focus is paid to this nature of examinations because: (i) thermodynamic data, i.e., the enthalpy of formation (determined both from the elements and oxides) provides knowledge about the relative stability of the compounds; (ii) knowledge of mechanical properties is needed to optimize industrial processes such as grinding/milling operations and (iii) charge density maps, and electronic structure provide indications of the reactivity of the different C_2S structures and compositions with respect to each other. In sum, this information is relevant to understanding how compositional, and processing variations can be used to optimize C_2S, and cement reactivity.

6.1.2 Doped Crystal Structures

The optimized lattice parameters of (Mg, Al, B) doped β-C_2S structures are reported in Table 6.1 where the lattice parameters of phase pure β-C_2S are also determined on a 2×1×3 supercell to ensure consistent comparisons. Since all the foreign ions are smaller than the original cations, the doped structures would be expected to show a contraction in unit cell volume. Indeed, while Mg- and Al-doped structures show volume reductions on the order of 0.50% and 0.05%, respectively, the B-doped structure expands by around 0.10%. This behavior is related to internal structural changes, and reorganizations involving the Ca-O bonds, wherein the polyhedra cages where the cations are sited, alter following dopant insertion. In turn, B-doping is also the most effective in inducing changes in the Ca-O bond length distribution. In fact, when two Mg atoms replace two Ca atoms with coordination number of 7 and 8, the structure relaxes to form 5 and 6 coordinated Mg-O polyhedra, respectively. As a further modification, the newly formed polyhedra change from edge to vertex sharing. The situation referring to Al and B dopants where one Si site and its nearest Ca site are replaced is more complex. In fact, although both the dopants exhibit a +3 valence character, their most stable states show different configurations. While in the case of Al the Al_{Si}-O tetrahedral structure is preserved, the Al_{Ca} coordination number changes from 7 to 5 and, similarly to what observed in the Mg case, the edge-sharing structure changes into a vertex sharing one. Overall, the B-doped structure is the most interesting among the substitutions addressed herein because of the more dramatic structural modifications it undergoes with respect to the pure case. The insertion of B atoms doped into Si and Ca sites generates two B-O triangles as a consequence of increased bond lengths in the tetrahedra. For example, along with the B_{Si}-O-Si_{Ca} bonds, the B_{Si}-O bond length is 2.56 Å, while the $O_{bridging}$-B_{Ca} bond length is only 1.36 Å. The averaged bond lengths for the B_{Si}-O and B_{Ca}-O bonds forming the triangles (1.40 Å and 1.41 Å, respectively) recall those reported for B_2O_3.[138]

Table 6.1 The lattice parameters of pure and doped β-C_2S structures calculated from a (2×1×3, denotes a, b, c directions, see below) expansion of the single unit cell.

β-C_2S Variant		**a (Å)**	**b (Å)**	**c (Å)**	**β (°)**	**Unit Cell Volume(Å^3)**
Pure	Phase Pure	11.136	9.356	20.394	94.557	2118.0
Doped	Mg (0.6 at. %)	11.123	9.319	20.386	94.430	2106.7
	Al (1.2 at. %)	11.119	9.354	20.419	94.582	2116.9
	B (1.2 at. %)	11.037	9.389	20.517	94.299	2120.1

Note: All impure β-C_2S structures are doped uniformly with 2 impurity ions per supercell.

6.1.3 Linear Charge Distribution

Linear charge distribution describes how electrons distribute along the bond length. It demonstrates the bond strength among atoms. The influences of Mg, Al, and B species, inserted as foreign ions into β-C_2S are assessed in the context of their impacts on structural changes, linear charge distributions along the M_{Ca}-O-N_{Si} bonds, and phase stability as described by the enthalpy of formation. Special focus is paid to elucidate how changes in atomic bonding induced by the presence of impurities including (Mg, Al, B) – reduces phase stability, and hence the ease with which a given doped β-C_2S structure may form, i) from its constituents, or ii) dissolve when placed in contact with water.

Differences in the local structures of the doped materials can be expected to lead to changes in physicochemical properties.[139], [140] Given the computational nature of this work, and the above discussion changes in the linear charge distribution (i.e., the electron density distribution along specific chemical bonds) are investigated. The comparison is performed with respect to the linear charge distributions observed along M_{Ca}-O-N_{Si}, where the notation M_{Ca} and N_{Si} indicate the cation/site inserted at a Ca or Si site, respectively. Results are plotted in Figure 6.1 where O sites are the reference points, and negative and positive values refer to Ca and Si cation sites, respectively. Ca(7)-O-Si and Ca(8)-O-Si indicate the pure cases. Excluding the Al case, all the species exhibit a strong electron density transfer from cations to anions, indicating the presence of ionic bonds. The oscillating behavior characterizing the electron density distribution along Al_{Ca}-O indicates the covalent nature of this bond. Dramatic changes in the electron density along the B_{Ca}-O bond provide the B_{Ca} site with a substantial ionic-like behavior. The remaining M_{Ca}-O bonds show similar trends while varying in bond lengths, indicating that Mg and Al impurities do not affect Ca sites significantly. On the O-N_{Si} side, all the curves show a consistent oscillatory behavior (covalent bonds). Overall, among all the chemical bonds examined, the two extremes are represented by the O-B_{Si} whose covalency nature is much stronger than that of O-Al_{Si}.

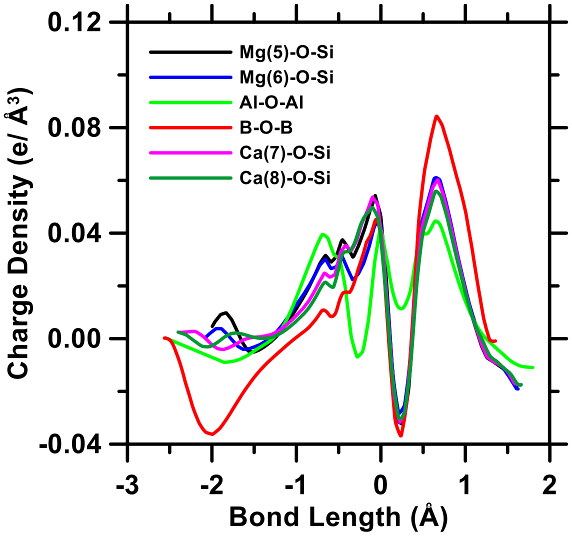

Figure 6.1 The linear charge density distribution along the MCa-O-NSi bonds. MCa and NSi represent sites occupied by Ca-atoms (left) and Si-atoms (right), respectively in the pure β-C2S structure. The numbers in parenthesis in the figure legend indicate the coordination number of atoms at a given site. The O-anion is located at the "0" position on the x-axis.

On the bases of the electron density distribution along the M_{Ca}-O-N_{Si} bond, a general comparison with respect to pure β-C_2S can be made. While Mg-doped β-C_2S does not show any evident peculiarity in terms of linear charge density distribution (this implying that its properties will substantially remain unchanged), Al- and B-doped cases are dramatically different with B exhibiting 50% more ionic behavior than the pure case, this indicating a significant potential for the material to be more solvable. Regardless their insertion sites, Al form covalent bonds with O atoms which consequently induce dramatic changes, i.e., the Ca-O ionic bond will change to Al-O covalent bond after Al substitutes Ca atom. This conclusion is in agreement with what reported by Young-Min and Seong-Hyeon [140] which indicated B and Al as the most effective dopants in enhancing hydration kinetics in β-C_2S across the series Al(+3), B(+3), P(+3), Fe(+3), S(+6), and K(+1).

6.1.4 Concentration Effect on Formation Enthalpy

Similar to pure phase formation enthalpy calculation, doped structure cases will need to take MgO, Al_2O_3, and B_2O_3 into consideration. The impurities (Mg, Al, and B) were inserted in β-C_2S because this is the technologically relevant, and impure polymorph present in ordinary Portland cement (OPC).[20] To provide a consistent comparison between the phase pure β-C_2S structure and doped structures a supercell approach was utilized wherein the basic unit cell of β-C_2S was expanded 3x in *c* direction and 2x in *a* direction. The resulting supercell contained 168 atoms. As such, either: (i) 1 or 2 Mg atoms (0.59 % or 1.19 % Mg, by mass), (ii) 2 or 4 Al atoms (1.38 % or 2.63 % Al, by mass) and (iii) 2 or 4 B atoms (0.53% or 1.07 % B, by mass) respectively were inserted in all the different doping scenarios. The doping scheme was chosen so as to ensure electroneutrality – therefore, Mg^{2+} substituted Ca^{2+} atoms randomly, since these substitutions occur with no consideration of size preference. On the other hand, Al^{3+} and B^{3+} substituted Ca^{2+} and Si^{4+} atoms such that these substitutions were carried out at the nearest (proximate) Ca-O-Si sites on account of the favored nature of such substitutions, i.e., from an energetic perspective.

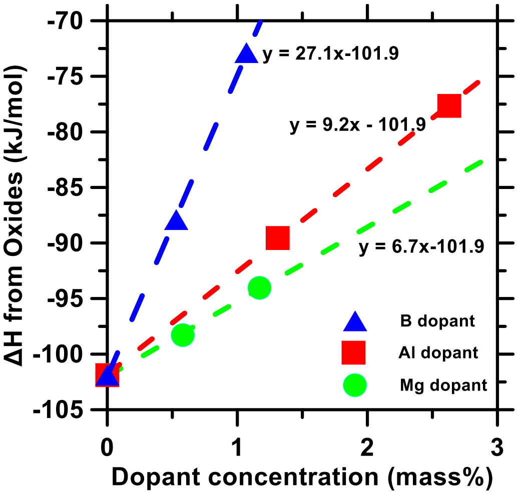

Figure 6.2 The enthalpy of formation of pure and doped β-C_2S with respect to their constituent simple oxides as a function of the impurity concentration.

The enthalpies of formation determined for the doped materials are all higher than that of β-C_2S. Moreover, for each dopant, the enthalpy increases linearly with increases in concentration with B dominating the trend (Figure 6.2). For example, while the formation enthalpy of pure β-C_2S as determined from the oxides is -101.9 kJ/mol with a 1% dopant concentrations, the enthalpies for B-, Al-, and Mg-doped materials are -74.8 kJ/mol, -92.7 kJ/mol, and -95.2 kJ/mol, respectively. These values correspond to increases of the order of 28%, 9%, and 7%, respectively. It can, therefore, be expected that these dramatic changes will have the potential for a tremendous energy saving in cement clinker manufacturing processes even taking into account the intrinsic doping limit of these materials. Figure 6.2 shows the linear trend describing the increasing energy behavior (from the oxides) as a function of the dopant concentration. Such trends are in good agreement with experimental evidence. At difference with observations obtained through the analysis of CBM and VBM, the presence of Mg seems to play a non-negligible role on the enthalpy of formation, despite being the least substantial. Among the three dopants addressed in this work, B exhibits an extraordinary effect, followed by Al, and Mg. From these observations, one can hypothesize that the B-doped material, showing such a larger formation enthalpy, can be expected to be more unstable, and be able to exhibit active properties, such as chemical higher reaction rates. In other words, this material showing higher energy will need smaller activation energy to overcome reaction barrier. Following these considerations, the hydration rates of the considered doped-materials can be ranked as B- > Al- > Mg-doped C_2S, which provide a promising evidence for further investigations.[34], [137], [140]

6.1.5 Summary and Conclusions

B, Al, and Mg atoms were considered to build the doped structure of β-C_2S. The linear charge distributions along the M_{Ca}-O-N_{Si} bond show that both Al_{Ca}-O and O-Al_{Si} have a covalent nature, as well as O-B_{Si}, at the difference with B_{Ca}-O which is strongly ionic. These results can be combined with experimental evidence to interpret the high doping efficiency of B and Al. To conclude, B dopant is proved to be very promising in decreasing β-C_2S formation enthalpy. It is claimed that higher formation enthalpy in the doped species can be an indicator of higher reactivity due to smaller energy barrier needed to be overcome during chemical reactions. However, whether the doping mechanism is in the way we calculated need to be confirmed, which will be studied in next part.

6.2 Doping of C_2S: Misfit Effect

In this section, density functional theory (DFT) simulations are carried out to systemically investigate doping in dicalcium silicate (Ca_2SiO_4: C_2S). The energetics of defect formation mechanisms for species involving Na^+, K^+, Mg^{2+}, Sr^{2+}, Al^{3+} , Fe^{3+}, B^{3+}, and Ge^{4+} dopants will be evaluated in order to find site preference for all cationic substitutions listed above. This will help to reveal to the fact that what kind of doped structure(s) is more possible to forming and what configuration(s) are more unstable (reactive). Only low dopant concentrations 0.25 mass% have been considered to avoid the clustering of dopants. Ca^{2+} and Si^{4+} sites are evaluated to find out the substituting preference for all the ions listed above. The following aspects will be investigated: i) The doping site preference, ii) the dopant size mismatch effect, and iii) doping concentration effect.

6.2.1 Introduction

Before such an approach can be applied to C_2S, however, it is necessary to elucidate mechanisms by which dopants incorporate themselves in the C_2S structure, such as charge compensation and energetically favorable defects arrangement. Indeed, changes in doping mechanism can have substantially different effects on the stability of the doped structures and the electron distributions within. Doping mechanisms for the common dopants remain only partially understood for C_2S [34], [35], [131], [141]. For example, for the cationic dopant, it is thought that such species can either substitute: (i) Ca-atoms at one of the two symmetrically unique positions, or the (ii) Si-atom which is sited in a tetrahedral arrangement. Depending on the valence state of the dopant, the charge is compensated by the formation of defects (e.g., vacancies). The vast majority of studies which have examined doping in C_2S have taken a simplistic view, for example: site preference is not considered, dopant size has not been assumed relevant, in spite of potential geometrical misfits of substituent species, and doping sites have been chosen so as to *a priori* ensure electrical charge balance of the C_2S unit cell [35], [133], [137].

To more comprehensively elucidate doping in C_2S, we systematically studied low-concentration doping mechanisms in β-C_2S (belite), the dominant phase of the C_2S present in OPC. Other C_2S polymorphs, such as the γ- and α- forms are less common [20] and hence we focus only on β-C_2S. By simulating the doped structures containing isolated defects using Density Functional Theory (DFT), we identify energetically preferred defect formation mechanisms for substitutional dopants including Na^+, K^+, Mg^{2+}, Sr^{2+}, Al^{3+}, Fe^{3+}, B^{3+}, and Ge^{4+}. All dopants investigated show significant site preference, which we find arises from different levels of local distortions around the dopant species at different cation sites. We identify a strong relationship between the defect formation enthalpy and the size mismatch between the dopant and substituted cation which we attribute to an *elastic misfit stress*. The outcomes provide guidance to assess the effects of defect formation mechanisms for other dopants, and, thereby, provide new insights to guide dopant selection for designing C_2S compositions optimized for reactivity and performance.

6.2.2 Computational Methods

To investigate doping in β-C_2S at a density functional (DFT) level, all calculations were performed using the Vienna Ab initio Simulation Package (VASP, ver. 5.3) [107], [142], a projector augmented plane wave code. The exchange-correlation potential uses the generalized gradient approximation (GGA) [114] with the Perdew-Burke-Ernzerhof (PBE) functional [114], [143] and corresponding projector augmented-wave (PAW) pseudopotentials provided in VASP [123], [144]. In the case of Ge, a particularly hard pseudopotential is selected, following recommendations from previous studies [145], so that the correct phase ordering observed in GeO_2 is reproduced. The cutoff energy of the plane-wave basis is set to 520 eV. Spin polarization is considered in all the calculations. For Fe^{3+}, we focus on the high spin state as it is found to be more stable than the low spin state, in agreement with observations in other iron compounds [146]. We note that Fe^{3+} is known to have highly correlated *d*-electrons that cannot be properly described by the standard DFT method [146], [147]. While correction schemes, such as the *Hubbard U-method* [148], can substantially improve electronic property (e.g., band structure) predictions [146], [147], they do not substantially modify the thermodynamic properties (e.g., formation enthalpy) [147]. Such corrections are therefore not applied in the present work.

To study doping mechanisms in the dilute limit, we simulate isolated, charged defects in a large supercell. The homogenous electron gas (HEG) approach is applied in the simulations to enforce the convergence of the electrostatic energy in charged, periodic systems. It is also well-known that such simulations of charged defects require large systems to ensure convergence of total energy [149]. Several correction schemes are available, but they require specific cell shapes (e.g., orthorhombic) [150], [151] or intensive computation [152]. Thus, they are impractical for investigating a large number of different defects in the considered monoclinic C_2S structure. However, the convergence behavior of such systems has been extensively investigated and is found to be predictable (i.e., the energy follows a polynomial function with respect to the size of the system) [149]. In addition, due to the electrostatic screening of the host lattice, structural relaxations can reduce the effects of defect charges [152]. As such, we analyzed convergence for different system sizes using a series of unrelaxed supercells, ranging from 1×1×1, 2×2×1, 2×2×2, to 3×3×3. For the defects considered in the present study, a 2×2×2 supercell (192 atoms) is sufficient to achieve a convergence of energy below ~0.5 eV before relaxation. As an example, Figure 6.3 shows such convergence for the case of a Si-vacancy, i.e., the defect with the highest charge considered in this study. A 1×2×2 k-mesh is adopted for sampling the reciprocal space. For each defect, a full structural relaxation is performed on the supercell, during which all the atomic positions, as well as the cell size and shape, are allowed to change. The relaxation is considered to achieve convergence when the force acting on each atom reaches a value below 0.01 eV/Å.

Once the structures containing variously isolated, charged defects are fully relaxed and associated energies obtained, we then proceed with investigating preferred defect mechanism in dilute limit, i.e., assuming the defects are isolated and non-interacting. For aliovalent dopants, doping will produce additional defects due to the need for charge compensation, e.g., Na-dopant substituting Ca-atoms would be compensated by oxygen vacancy, while B doping can involve cation vacancy (when substituting Ca), oxygen vacancies (when substituting Si), or co-substitutions. Details of different mechanisms are described in the following sections by defect equations written using Kröger-Vink notation [153]. By comparing the defect formation enthalpies associated with the possible mechanisms, we identify favorable mechanisms based on which the effects of doping are evaluated and discussed.

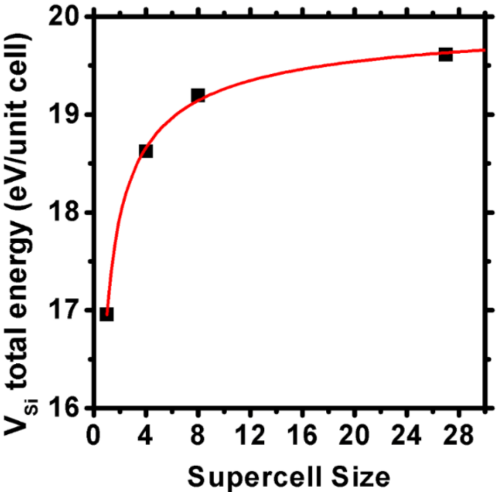

Figure 6.3 The total energy for the case of a Si-vacancy shown for different sizes of the supercell. The total energy reference is set as pure β-C2S and the data are fitted by a power law.

6.2.3 Intrinsic Defects

β-Ca_2SiO_4 has a monoclinic structure (space group P21/c; see Figure 6.4). Following relaxation, the computed lattice parameters are a = 11.149 Å, b = 13.628 Å, c = 18.758 Å and α = 90.000°, γ = 90.001°, β = 85.337°, in good agreement with experimental data (a = 11.024 Å, b = 13.516 Å, c = 18.628 Å and α = γ = 90.000°, β = 85.420° [50]).

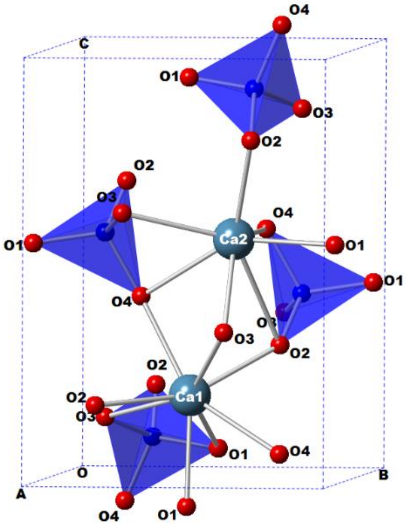

Figure 6.4 The unit cell of β-C_2S. For better visualization of the Ca-polyhedra, only one Ca1 atom and one Ca2 atom are displayed.

All the atoms in the unit cell occupy the 4e sites (site multiplicity of 4). As illustrated in Figure 6.4, the unit cell is composed of two symmetrically unique Ca (hereafter denoted as Ca1 and Ca2), one Si, and four O atoms (hereafter denoted as O1-to-O4) – as distinguished by their positions. The Ca1 and Ca2 atoms are 8-fold and 7-fold coordinated, respectively, and the Si atom is 4-fold coordinated, as in most of silicate crystals and glasses. The SiO_4 tetrahedra are separated from each other, but share corners or edges with neighboring Ca-$O_{7/8}$ polyhedra. The Ca-O polyhedra connect with each other by sharing faces or edges.

Starting from the pristine β-C_2S structure, intrinsic defects are firstly being investigated. Only vacancies are focused, i.e., the cation (in Kröger-Vink notation, $V_{Ca}^{''}$ and $V_{Si}^{''''}$) and oxygen ($V_{O}^{\bullet\bullet}$) vacancies. In previous studies, interstitial defects have been found to be highly unfavorable and thus unlikely to form in β-C_2S. [31], [154] The formation enthalpy and formation volume of all defects can be found in Table 6.2. We observe that Ca vacancies are more favorable at Ca2 sites, as their formation enthalpy is smaller by 0.53 eV with respect to Ca1 vacancies. On the other hand, O vacancies form preferentially at the O2 site, which features an enthalpy of formation 0.44 eV lower than that of the least favorable site (O3). As such, in the following, the O2 site is used for all defect calculations involving oxygen vacancies. Based on the energies associated with the most preferred defect sites, we can calculate the formation enthalpy of the so-called Schottky defects using the following defect equations:

$$C_2S \rightarrow < C_2S \cdot V_{Ca}^{''} \cdot V_O^{\cdot\cdot} > + CaO;\ \Delta H_{Ca1} = 3.11\ eV, \Delta H_{Ca2} = 2.58\ eV \tag{6.1}$$

$$C_2S \rightarrow < C_2S \cdot V_{Si}^{''} \cdot 2V_O^{\cdot\cdot} > + SiO_2;\ \Delta H\ = 6.18\ eV \tag{6.2}$$

From the calculated defect formation enthalpies, we note that Schottky defects in β-C_2S would predominately involve Ca rather than Si vacancies. Nonetheless, the energies required to create intrinsic defects in β-C_2S are fairly high (note that *kT* at 2000K is 0.17 eV). Therefore, it is very unlikely that β-C_2S would contain a large concentration of point defects without the parallel existence of extrinsic dopants, which are the focus of the following sections.

Table 6.2 The defects formation enthalpy ΔH_f (eV) and formation volume ΔV_f (A^3) for a range of defects considered

Defects Combination	ΔHf (eV)	ΔVf (Å3)	Defects Combination	ΔHf (eV)	ΔVf (Å3)
V_{Si}	31.60	75.55	VCa + VO	2.58	38.74
V_{O1}	0.17	-13.5	VSi + VO	6.18	99.69
V_{O2}	-0.27	-18.4	NaCa + VO	0.35	12.69
V_{O3}	1.18	-14.53	NaSi + VO	5.58	24.12
V_{O4}	0.17	-13.27	MgCa	0.94	3.79
V_{Ca1}	16.18	33.78	MgSi + VO	3.61	62.29
V_{Ca2}	15.64	28.80	AlCa + VCa	2.33	24.94

Note: The formation volume is calculated similarly as is the defect formation enthalpy. For example for the formation of a silicon vacancy the defect formation volume is written as: $C_2S \rightarrow < C_2S \cdot V_{Si}^{''} \cdot 2V_O^{\cdot\cdot} > + SiO_2;\ \Delta V\ = 99.69\ Å^3$.

6.2.4 Ca Substitutions

We examine β-C_2S (substitutionally) doped with Na^+, K^+, Mg^{2+}, Sr^{2+}, Al^{3+}, Fe^{3+}, B^{3+}, and Ge^{4+}, eight dopants that are common to calcium silicates cement. We investigate substitutions at the different Ca cation sites (Ca1 and Ca2 sites whose ionic radii are 1.12 Å and 1.06 Å [155], respectively, due to their different coordination numbers). The formation of interstitial defects is considered [52]. For Na^+ and K^+ dopants, Ca substitutions need to be charge-balanced by oxygen vacancies, as indicated by the following defect equations:

$$\frac{1}{2}\mathrm{Na_2O} + \frac{1}{2}\mathrm{C_2S} \rightarrow < \frac{1}{2}\mathrm{C_2S} \cdot \mathrm{Na}_{\mathrm{Ca}}^{'} \cdot \frac{1}{2}\mathrm{V}_{\mathrm{O}}^{\cdot\cdot} > + \mathrm{CaO};\ \Delta \mathrm{H}_{\mathrm{Ca1}} = 0.63\ \mathrm{eV}, \Delta \mathrm{H}_{\mathrm{Ca2}} = 0.35\ \mathrm{eV} \quad (6.3)$$

$$\frac{1}{2}\mathrm{K_2O} + \frac{1}{2}\mathrm{C_2S} \rightarrow < \frac{1}{2}\mathrm{C_2S} \cdot \mathrm{K}_{\mathrm{Ca}}^{'} \cdot \frac{1}{2}\mathrm{V}_{\mathrm{O}}^{\cdot\cdot} > + \mathrm{CaO};\ \Delta \mathrm{H}_{\mathrm{Ca1}} = 0.61\ \mathrm{eV}, \Delta \mathrm{H}_{\mathrm{Ca2}} = 0.38\ \mathrm{eV} \quad (6.4)$$

Na^+ substitutions, both at Ca1 and Ca2 sites, are associated with a relatively small defect formation enthalpy, with Ca2 sites being favored. Figures 6.5b and 6.5b show relaxed atomic positions around the Na^+ dopant. We observe that the substitution does not induce substantial distortion around the dopant. Indeed, the coordination number and the configuration of the oxygen neighbors remains similar to that of the corresponding Ca-sites in phase pure C_2S. Similarly, K^+ dopants also prefer substitution at the Ca2 site, with a slightly larger formation enthalpy. The coordination number of K^+ is 8 and 6 at Ca1 and Ca2 sites, respectively.

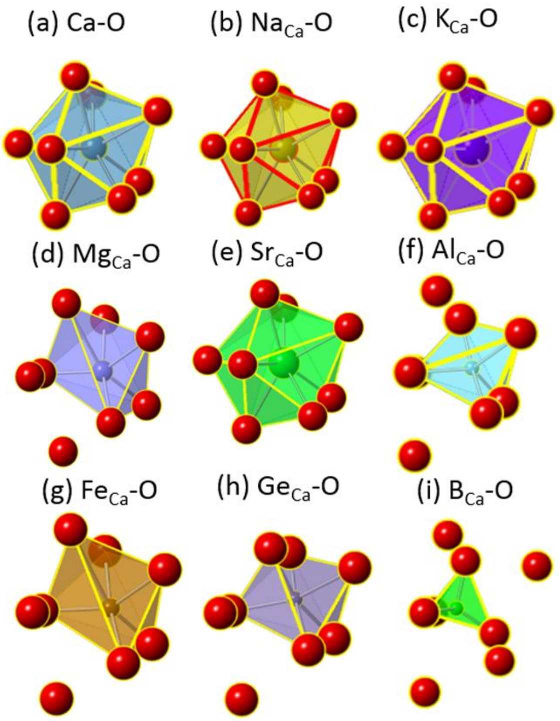

Figure 6.5 The local atomic environment around the native and dopant atoms after structural relaxation in the case of substitutions carried out at the Ca1 site.

For Mg^{2+} and Sr^{2+} dopants, the substitution of Ca-atoms is isovalent. As such, no other defects are created:

$$\mathrm{MgO} + \mathrm{C_2S} \rightarrow < \mathrm{C_2S} \cdot \mathrm{Mg_{Ca}} > + \mathrm{CaO};\ \Delta\mathrm{H_{Ca1}} = 1.14\ eV, \Delta H_{Ca2} = 0.94\ eV \tag{6.5}$$

$$\mathrm{SrO} + \mathrm{C_2S} \rightarrow < \mathrm{C_2S} \cdot \mathrm{Sr_{Ca}} > + \mathrm{CaO};\ \Delta\mathrm{H_{Ca1}} = -0.22\ eV, \Delta H_{Ca2} = -0.21\ eV \tag{6.6}$$

For Mg^{2+} ions, we find that the defect formation enthalpies, both at Ca1 and Ca2 sites, are higher than those of Na^{+} substitutions. In addition, due to the smaller ionic radius of Mg^{2+} with respect to Ca^{2+}, Mg^{2+} substitutions result in a change of the coordination number. As shown in Figures 6.5d and 6.5d, the coordination number of Mg^{2+} is 6 and 5 at the Ca1 and Ca2 sites, respectively, as compared to 8 and 7 in pure C_2S. Such changes in coordination environment cause distortions of the local structure that results in the formation of undercoordinated oxygen anions which then leads to an increase in the defect formation enthalpy. In the case of Sr^{2+}, which is a larger dopant than Ca^{2+}, the original local atomic environment is maintained following substitution, i.e., the same coordination number as Ca^{2+} (8 and 7 at the Ca1 and Ca2 site, respectively, see Figure 6.5e and 6.5e). The formation enthalpy is small and negative, which suggests that the substitution is energetically easy or even favored. This is unsurprising, as β-Sr_2SiO_4 is a stable phase and can easily form a solid solution with β-Ca_2SiO_4 [156], [157], which suggests a high solubility of Sr^{2+} in β-Ca_2SiO_4.

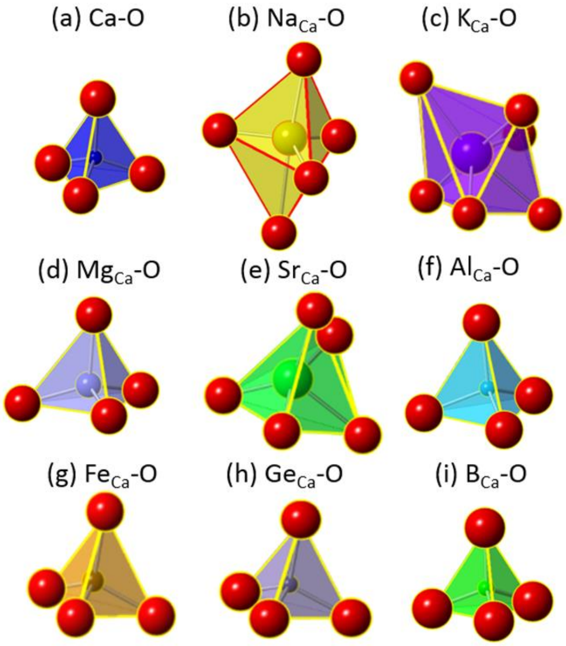

Figure 6.6 The local atomic environment around the native and dopant atoms after structural relaxation in the case of substitutions carried out at the Ca2 site.

In the case of Al^{3+} and Fe^{3+} dopants, to satisfy charge balance, Ca-atom substitutions would result in the formation of Ca or Si vacancies. We examined both mechanisms, as described by relevant defect equations (Equations 7-to-10). It should be noted that, ideally, doping with trivalent dopant can be charge balanced by two dopants simultaneously substituting one Ca^{2+} and one Si^{4+}. This mechanism, however, is found to be energetically unfavorable, as is discussed later.

$$\frac{1}{2}\mathrm{Al_2O_3} + \mathrm{C_2S} \rightarrow < \mathrm{C_2S} \cdot \mathrm{Al}_{\mathrm{Ca}}^{\cdot} \cdot \frac{1}{2}\mathrm{V}_{\mathrm{Ca}}^{''} > + \frac{3}{2}\mathrm{CaO};\ \Delta\mathrm{H}_{\mathrm{Ca1}} = 2.83\ \mathrm{eV}, \Delta\mathrm{H}_{\mathrm{Ca2}} = 2.33\ \mathrm{eV} \tag{6.7}$$

$$\frac{1}{2}\mathrm{Al_2O_3} + \mathrm{C_2S} \rightarrow < \mathrm{C_2S} \cdot \mathrm{Al}_{\mathrm{Ca}}^{\cdot} \cdot \frac{1}{2}\mathrm{V}_{\mathrm{Si}}^{\cdot\cdot} > + \frac{1}{4}\mathrm{Si}O_2 + \mathrm{CaO};\ \Delta\mathrm{H}_{\mathrm{Ca1}} = 3.08\ \mathrm{eV}, \Delta\mathrm{H}_{\mathrm{Ca2}} = 2.58\ \mathrm{eV} \tag{6.8}$$

$$\frac{1}{2}\mathrm{Fe_2O_3} + \mathrm{C_2S} \rightarrow < \mathrm{C_2S} \cdot \mathrm{Fe}_{\mathrm{Ca}}^{\cdot} \cdot \frac{1}{2}\mathrm{V}_{\mathrm{Ca}}^{''} > + \frac{3}{2}\mathrm{CaO};\ \Delta\mathrm{H}_{\mathrm{Ca1}} = 2.59\ \mathrm{eV}, \Delta\mathrm{H}_{\mathrm{Ca2}} = 2.17\ \mathrm{eV} \tag{6.9}$$

$$\frac{1}{2}\mathrm{Fe_2O_3} + \mathrm{C_2S} \rightarrow < \mathrm{C_2S} \cdot \mathrm{Fe}_{\mathrm{Ca}}^{\cdot} \cdot \frac{1}{2}\mathrm{V}_{\mathrm{Si}}^{\cdot\cdot} > + \frac{1}{4}\mathrm{Si}O_2 + \mathrm{CaO};\ \Delta\mathrm{H}_{\mathrm{Ca1}} = 2.84\ \mathrm{eV}, \Delta\mathrm{H}_{\mathrm{Ca2}} = 2.43\ \mathrm{eV} \tag{6.10}$$

For Al^{3+} dopants, the formation enthalpies are substantially higher as compared to those obtained for Na^{+} and Mg^{2+} substitutions, due to the need for charge balance that is ensured by the formation of cation vacancies. Additionally, examination of the coordination environments around Al-dopant atoms reveals significant distortions with respect to the original local structure around the Ca sites. Indeed, following substitution, the Al^{3+} dopant is four-coordinated (at the Ca2 site, see Figure 6.6f) and five coordinated (at the Ca1 site, see Figure 6.5f) depending on the substitution site. These Al-coordination numbers are common in disordered silicates, e.g., calcium aluminosilicate glasses [158]. As such, substantial rearrangements and distortions of the local atomic structure occur when Al^{3+} substitutes Ca^{2+} atoms explaining the high defect formation enthalpies. However, such distortions are unsurprising as Al-atoms are substantially smaller than Ca species.

Comparing to Al^{3+} doping, Fe^{3+} doping prefers similar doping preferences with a formation enthalpy that is about 0.2 eV lower. The coordination number of Fe^{3+} is higher than Al^{3+} (6 and 5, at Ca1 and Ca2 sites, respectively, Figures 6.5g and 6.5g). Similar to Al^{3+} and Fe^{3+} dopants, B^{3+} cations are smaller than Ca^{2+} species, so substitutions of Ca^{2+} by B^{3+} are also associated with high defect formation enthalpies, across both charge compensation mechanisms. Expectedly, B^{3+} dopants acquire coordination numbers that are commonly observed in borosilicate glasses [159] (3 at the Ca2 site and 4 at the Ca1 site, as shown in Figures 6.5i and 6.6i, respectively), which induces considerable rearrangements and distortions in the local atomic structures.

$$\frac{1}{2}\mathrm{B_2O_3} + \mathrm{C_2S} \rightarrow < \mathrm{C_2S} \cdot \mathrm{B}_{\mathrm{Ca}}^{\cdot} \cdot \frac{1}{2}\mathrm{V}_{\mathrm{Ca}}^{''} > + \frac{3}{2}\mathrm{CaO};\ \Delta\mathrm{H}_{\mathrm{Ca1}} = 3.13\ \mathrm{eV}, \Delta\mathrm{H}_{\mathrm{Ca2}} = 2.21\ \mathrm{eV} \tag{6.11}$$

$$\frac{1}{2}\mathrm{B_2O_3} + \mathrm{C_2S} \rightarrow < \mathrm{C_2S} \cdot \mathrm{B}_{\mathrm{Ca}}^{\cdot} \cdot \frac{1}{2}\mathrm{V}_{\mathrm{Si}}^{\cdot\cdot} > + \frac{1}{4}\mathrm{Si}O_2 + \mathrm{CaO};\ \Delta\mathrm{H}_{\mathrm{Ca1}} = 3.38\ \mathrm{eV}, \Delta\mathrm{H}_{\mathrm{Ca2}} = 2.46\ \mathrm{eV} \tag{6.12}$$

$$\mathrm{GeO_2} + \mathrm{C_2S} \rightarrow < \mathrm{C_2S} \cdot \mathrm{Ge}_{\mathrm{Ca}}^{\cdot\cdot} \cdot \mathrm{V}_{\mathrm{Ca}}^{''} > +2\mathrm{CaO};\ \Delta\mathrm{H}_{\mathrm{Ca1}} = 3.86\ \mathrm{eV}, \Delta\mathrm{H}_{\mathrm{Ca2}} = 3.00\ \mathrm{eV} \tag{6.13}$$

$$\mathrm{GeO_2} + \mathrm{C_2S} \rightarrow < \mathrm{C_2S} \cdot \mathrm{Ge}_{\mathrm{Ca}}^{\cdot\cdot} \cdot \frac{1}{2}\mathrm{V}_{\mathrm{Si}}^{''} > +\mathrm{CaO} + \frac{1}{2}\mathrm{Si}O_2;\ \Delta\mathrm{H}_{\mathrm{Ca1}} = 4.22\ \mathrm{eV}, \Delta\mathrm{H}_{\mathrm{Ca2}} = 3.36\ \mathrm{eV} \tag{6.14}$$

Finally, Ge^{4+} doping results in the highest defect formation enthalpy among all the substitutions at Ca sites investigated herein. Although an energy penalty is expected for such substitutions – since the smaller size of Ge^{4+} induces substantial changes in the local atomic environment (see Figure 6.5g and 3g) – we speculate that the defect formation energy is overestimated. It has been shown that the standard DFT method fails to provide realistic relative stability between GeO_2 phases [145]. Similar issues are observed in our calculations; rutile-like GeO_2 (Ge coordination number = 6) is marginally more stable (0.02 eV per GeO_2) than the quartz-like structure (Ge coordination number = 4). It is likely that the stability of Ge^{4+} substitution at the Ca sites, which produces a rutile-like local environment (coordination number of 6 and 5 at Ca1 and Ca2 sites, respectively, see Figure 6.5g and 6.6g), has been underestimated. This would contribute to the (spuriously) high defect formation enthalpies. However, such issues warrant further investigations. Overall, for all the dopants, we find that substitutions are preferred at Ca2 sites, since the associated formation enthalpies are systematically smaller than those observed for Ca1 sites (by 0.20-to-0.92 eV), except in the case of Sr^{2+}, where both sites are equally stable. This, in turn, suggests that Ca1 polyhedra are more stable than the Ca2 ones.

6.2.5 Si Substitutions

As compared to Ca substitutions, Si (ionic radius 0.26 Å [155]) substitutions are simpler as only one symmetrically unique host Si-site is available. In addition, all the considered dopants have lower or equal valence comparing with Si^{4+} and, as such, the substitution of Si-atoms can be compensated by the formation of oxygen vacancies, as described by the following defect equations:

$$\frac{1}{2}\mathrm{Na_2O} + \mathrm{C_2S} \rightarrow < \mathrm{C_2S} \cdot \mathrm{Na}_{\mathrm{Si}}^{'''} \cdot \frac{3}{2}\mathrm{V}_{\mathrm{O}}^{\cdot\cdot} > + \mathrm{SiO_2};\ \Delta\mathrm{H} = 5.58\ \mathrm{eV} \tag{6.15}$$

$$\frac{1}{2}\mathrm{K_2O} + \mathrm{C_2S} \rightarrow < \mathrm{C_2S} \cdot \mathrm{K}_{\mathrm{Si}}^{'''} \cdot \frac{3}{2}\mathrm{V}_{\mathrm{O}}^{\cdot\cdot} > + \mathrm{SiO_2};\ \Delta\mathrm{H} = 6.40\ \mathrm{eV} \tag{6.16}$$

$$\mathrm{MgO} + \mathrm{C_2S} \rightarrow < \mathrm{C_2S} \cdot \mathrm{Mg}_{\mathrm{Si}}^{''} \cdot \mathrm{V}_{\mathrm{O}}^{\cdot\cdot} > + \mathrm{SiO_2};\ \Delta\mathrm{H} = 3.61\ \mathrm{eV} \tag{6.17}$$

$$\mathrm{SrO} + \mathrm{C_2S} \rightarrow < \mathrm{C_2S} \cdot \mathrm{Sr}_{\mathrm{Si}}^{''} \cdot \mathrm{V}_{\mathrm{O}}^{\cdot\cdot} > + \mathrm{SiO_2};\ \Delta\mathrm{H} = 5.63\ \mathrm{eV} \tag{6.18}$$

$$\frac{1}{2}\mathrm{Al_2O_3} + \mathrm{C_2S} \rightarrow < \mathrm{C_2S} \cdot \mathrm{Al}_{\mathrm{Si}}^{'} \cdot \frac{1}{2}\mathrm{V}_{\mathrm{O}}^{\cdot\cdot} > + \mathrm{SiO_2};\ \Delta\mathrm{H} = 0.96\ \mathrm{eV} \tag{6.19}$$

$$\frac{1}{2}\mathrm{Fe_2O_3} + \mathrm{C_2S} \rightarrow < \mathrm{C_2S} \cdot \mathrm{Fe}_{\mathrm{Si}}^{'} \cdot \frac{1}{2}\mathrm{V}_{\mathrm{O}}^{\cdot\cdot} > + \mathrm{SiO_2};\ \Delta\mathrm{H} = 1.05\ \mathrm{eV} \tag{6.20}$$

$$\frac{1}{2}\mathrm{B_2O_3} + \mathrm{C_2S} \rightarrow < \mathrm{C_2S} \cdot \mathrm{B}_{\mathrm{Si}}^{'} \cdot \frac{1}{2}\mathrm{V}_{\mathrm{O}}^{\cdot\cdot} > + \mathrm{SiO_2};\ \Delta\mathrm{H} = 0.46\ \mathrm{eV} \tag{6.21}$$

$$\mathrm{GeO_2} + \mathrm{C_2S} \rightarrow < \mathrm{C_2S} \cdot \mathrm{Ge}_{\mathrm{Si}} > + \mathrm{SiO_2};\ \Delta\mathrm{H} = -0.93\ \mathrm{eV} \tag{6.22}$$

Among all eight dopants, the local atomic environment of $Mg2^+$, Al^{3+}, Fe^{3+}, B^{3+}, and Ge^{4+} retains a tetrahedral coordination environment – similar to the native Si^{4+}. However, substitutions involving Na^+, K^+, and Sr^{2+}, due to their larger sizes than Si^{4+}, induce noticeable distortions of the tetrahedral geometry. For example, K^+ and Sr^{2+} acquire larger coordination number of 6 and 5, respectively, while in the case of Na^+ substitution, the tetrahedron is so distorted that an additional oxygen anion moves into the vicinity of the first coordination shell of the dopant (see Figure 6.7b which shows the local atomic environment around the dopant atoms after structural relaxation, in the case of substitutions carried out at the Si site. For the four-coordinated dopants, we also observe some, albeit more subtle, structural distortions when the size is noticeably larger than Si^{4+}. For instance, in the case of Mg^{2+} substitutions, the intra-tetrahedral angles vary from 95.4° to 116.6°, significantly deviating from an ideal tetrahedron, i.e., 109.5°. Therefore, it is not surprising that substitutions by larger ions show higher defect formation enthalpies, as compared to the smaller species, such as Al^{3+}, Fe^{3+}, B^{3+}, and Ge^{4+}. Finally, we note again the magnitude of defect formation enthalpy associated with Ge^{4+} doping may be substantially overestimated as discussed above. Nonetheless, Ge^{4+} substitution at Si sites should indeed be favorable, as suggested by the experimentally observed solid solution between Ca_2SiO_4 and Ca_2GeO_4 [160].

To summarize the results, the defect formation enthalpies are plotted for each dopant in Figure 6.8. As opposed to the findings of a previous study [35], we observe that all the dopants examined herein exhibit strong site preferences. Overall, Na^+, K^+, Mg^{2+}, and Sr^{2+} impurities preferentially occupy Ca sites, whereas Al^{3+}, Fe^{3+}, Ge^{3+}, and B^{3+} substitutions are favored in Si sites. The site preference is substantial (e.g., in the case of Na^+, the difference in the defect formation enthalpy exceeds 5 eV), which suggests that unfavorable substitutions are unlikely to be observed under practical cement synthesis conditions – even under modestly non-equilibrium (i.e., kinetic controlled) conditions.

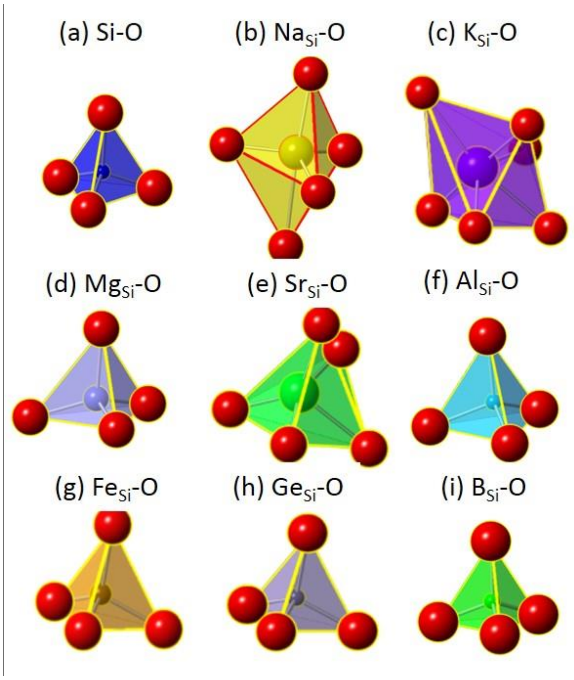

Figure 6.7 The local atomic environment around the dopant atoms after structural relaxation, in the case of substitutions, carried out at the Si site.

In the case of the trivalent dopants (Fe^{3+}, Al^{3+}, and B^{3+}), previous studies have proposed that doping occurs via co-substitution, in which two trivalent dopants simultaneously replace one Ca^{2+} and one Si^{4+}, although no energetic substantiation is offered vis-a-vis other substitution mechanisms. Here we calculate the defect formation enthalpies for two trivalent dopants:

$$\mathrm{Fe_2O_3 + C_2S \rightarrow< C_2S \cdot Fe'_{Si} \cdot Fe^{\cdot}_{Ca2} > + SiO_2 + CaO;\ \Delta H = 3.31\ eV} \tag{6.23}$$

$$\mathrm{Al_2O_3 + C_2S \rightarrow< C_2S \cdot Al'_{Si} \cdot Al^{\cdot}_{Ca2} > + SiO_2 + CaO;\ \Delta H = 2.00\ eV} \tag{6.24}$$

$$\mathrm{B_2O_3 + C_2S \rightarrow< C_2S \cdot B'_{Si} \cdot B^{\cdot}_{Ca2} > + SiO_2 + CaO;\ \Delta H = 1.38\ eV} \tag{6.25}$$

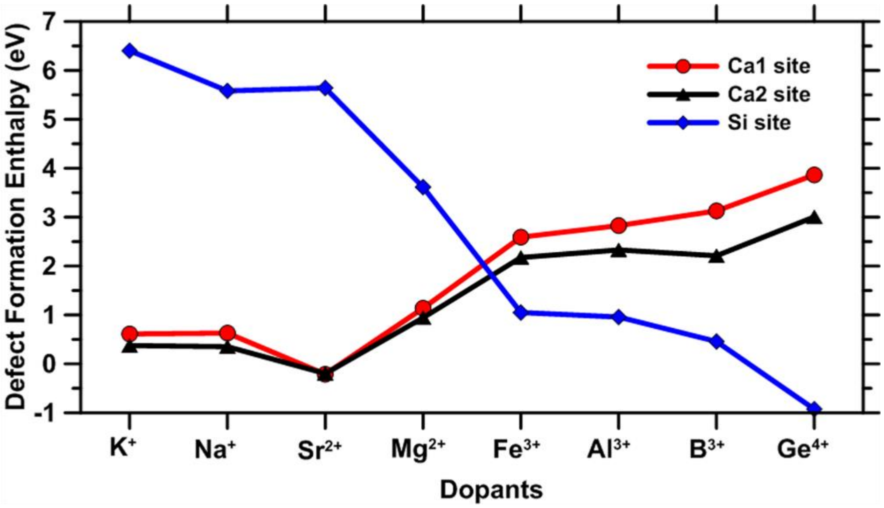

Figure 6.8 The calculated defect formation enthalpies for each dopant atom when substitutions are carried out at the two Ca or one Si site.

Examination of the above equations for Fe^{3+}, Al^{3+} and B^{3+} and the associated energetics suggests that the co-substitution mechanism assumed for trivalent dopant substitution requires additional energy on the order of 1.21 eV, 0.08 eV and 0.46 eV per pair of dopants, respectively as compared to Si substitutions that are balanced by oxygen vacancies. This suggests that the commonly assumed "co-substitution" mechanism is not energetically favorable, at least at low doping concentrations – and is thus unlikely to manifest under equilibrium or modestly non-equilibrium conditions.

6.2.6 Discussion

Charge balance ensured by oxygen vacancies that form upon aliovalent cationic substitutions is a common point defect formation mechanism observed in oxides [161]. Oxygen vacancies are known to have major effects on materials; being capable of altering mechanical properties [162], diffusion [163] and electronic structure [164]. For cementitious materials, these properties can influence hydration behavior, as suggested previously [133]. Therefore, identifying the correct doping mechanism is of primary importance to achieve the effective compositional design of the cementitious calcium silicates.

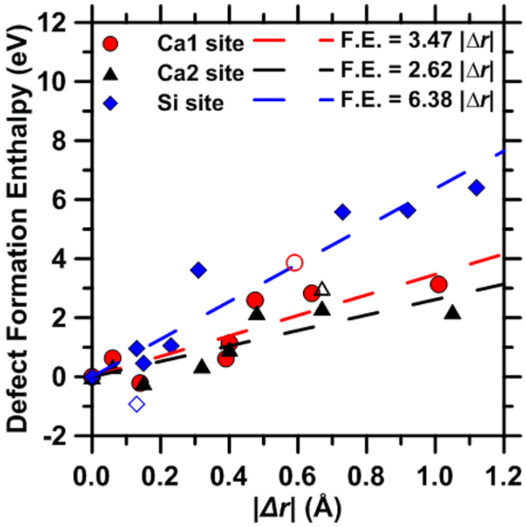

Figure 6.9 The formation enthalpies associated with the formation of specific defects as a function of the "radial size mismatch" between the dopant and the host cation. This mismatch is calculated as the absolute value of the difference in ionic radii. Linear trends emerge for each doping site, fitting parameters for which are noted in the figure. Due to uncertainties in the defect formation enthalpies for Ge (open symbols), its data is excluded from the fittings.

Upon examination of the local atomic structures around the dopant atom, we find that the energetic preference of each mechanism is associated with the extent of the local structural rearrangements that are induced by the substitution. Indeed, for the dopants featuring an ionic radius comparable to that of Ca^{2+} cations, such as Na^{+}, the original coordination structure around the Ca sites can be maintained, whereas substantial distortions are induced when they substitute Si^{4+} which is a much smaller atom. In particular, in the case of small dopants substituting Ca^{2+} species, we observe that the dopant reverts to its "natural" coordination number after structural relaxation by creating undercoordinated oxygen ions. Based on these observations, it is not surprising that these strong distortions, resulting from size mismatch, give rise to energetic penalties – that we characterize as being analogous to an ***"elastic misfit stress"*** (see Figure 6.9 and text below). This highlights the importance of selecting the proper dopant, which induces the formation of appropriate defects in doped materials. This is important for example to alter electronic structure related behaviors, e.g., hydration, since electronic properties are sensitive to the distortions in the atomic structure.

Based on the discussion above, it is clear that the size mismatch between the dopant and substituted ion (atom) is a critical factor that impacts the stability of the doped structures. Other more common parameters, e.g., the difference in valence or the so-called "field strength", i.e., the ratio of the ionic valence to the ionic radius (Z/r, unitless) do not show relevant correlations. Careful examination of Figure 6.9 shows that the defect formation enthalpy is linearly correlated with the ionic radius difference between the native species, and the substituent. Here, the ionic radii of the considered defects ranks as: K^+ (1.38 Å, 6-fold coordinated) > Sr^{2+} (1.21 Å, 7-fold coordinated) > Na^+ (1.12 Å, 7-fold coordinated) > Mg^{2+} (0.66 Å, 5-fold coordinated) > Al^{3+} (0.39 Å, 4-fold coordinated) > Fe^{3+} (0.49 Å, 4-fold coordinated) > Ge^{4+}/Al^{3+} (0.39 Å, 4-fold coordinated) > B^{3+} (0.11 Å, 4-fold coordinated). This suggests that destabilization of the doped C_2S structure has its origins in an elastic ***misfit stress*** that develops to accommodate a dimensionally mismatched atomic species. Such linear behavior has also been observed in ion-exchanged glasses, which show a volumetric expansion that results in a compressive stress that is proportional to the size, and concentration of "stuffed" (i.e., ion-exchanged) atoms [165].

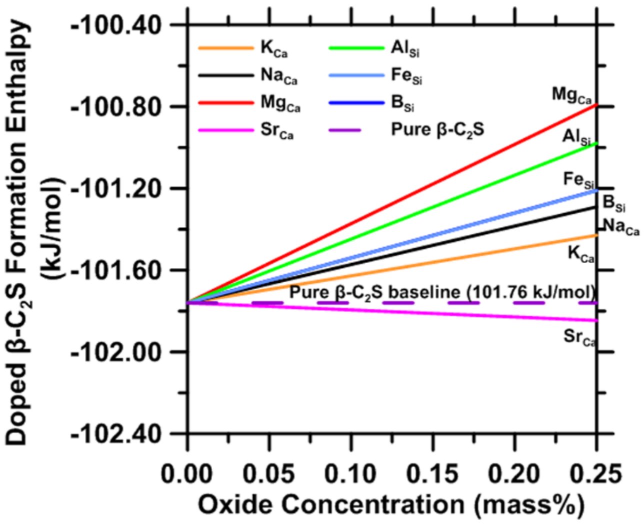

Figure 6.10 The enthalpy of formation of doped β-C_2S calculated with respect to its constituent simple oxides as a function of the dopant concentration. The values are calculated in kilojoules per mole of Ca_2SiO_4 using a conversion factor of 1 eV = 96.485 kJ/mol.

Due to the different nature of bonding, e.g., ionic vs. covalent, and the complex defect mechanisms, the defect formation enthalpy shows some variation from ideal linear behavior with an ionic size mismatch. Such variations may be partially accounted for by analyzing the real misfit strain at atomic level [159]. Nonetheless, the linear relationship noted in Figure 6.9 provides a guide to screen dopants with respect to the targeted level of destabilization. For example, it would be appropriate to identify dopants that show no preference between Ca (or more specifically the Ca2 site which is a preferred doping location) and Si sites since such doping has shown optimal enhancements in the properties of other materials [165], [166]. From the relationship presented in Figure 6.9, it can be predicted that such dopants should be characterized by $|\Delta r_{Ca}| = 2.44 \bullet |\Delta r_{Si}|$, where $|\Delta r_{Ca}|$ and $|\Delta r_{Si}|$ are the size mismatch between the dopant and Ca^{2+} and Si^{4+} species, respectively. Our structural analysis reveals that the dopants substituting Si^{4+} usually remain 4-fold coordinated, while they would relax to their native coordination numbers at the Ca-site. Taken together, this suggests that Ti^{4+} ($|\Delta r_{Si}|$ = 0.16 Å for $Ti^{4+,IV}$ whereas $|\Delta r_{Ca}|$: 0.45 Å for $Ti^{4+,VI}$) would show minimal site preferences. Finally, Figure 6.10 shows the calculated enthalpy of formation (ΔH_f at 0K, in kJ per mole of Ca_2SiO_4) of doped C_2S, with respect to its binary oxides, as a function of the dopant concentration. Expectedly, doping destabilizes the C_2S structure, with Mg^{2+} cations showing the highest destabilizing effect. Note that, we only consider low doping concentrations, where the defects are isolated and non-interacting. Indeed, dopant-dopant interactions may occur at higher doping concentrations, resulting in deviations from the linear relationship. Such defect interactions may be sensitive to the processing conditions such as synthesis temperature and cooling rate – and the solubility limits of the different dopant species. Further, high temperatures could reduce defect interactions and reduce clustering, while fast cooling may promote segregation. These mechanisms, along with other property modifications, e.g. hydration-related electronic properties, are worthy of future investigations.

6.2.7 Conclusions

We have studied defect formation in doped C_2S at a DFT level of theory. Based on the simulations, we have identified the most favorable doping mechanisms at low dopant concentrations (i.e., for isolated defects) for a series of dopants including Na^+, K^+ , Mg^{2+}, Sr^{2+}, Al^{3+} , Fe^{3+}, B^{3+}, and Ge^{4+}. We find that large dopants such as Na^+, K^+, Mg^{2+}, and Sr^{2+} prefer Ca2-site substitutions, while smaller dopants such as Al^{3+} , Fe^{3+}, B^{3+}, and Ge^{4+} favor substitution at Si sites. In all cases, the site preference is substantial (i.e., energetically) due to the considerable local atomic distortions that result when the dopant is located at an unfavorable site. Furthermore, we find that the energetic preferences, as captured by the defect formation enthalpy, are strongly correlated with the ionic size mismatch between the dopant and the substituted ion, which suggests that the destabilization of the system primarily arises from the resistance of the atomic structure to accommodate smaller or larger units (as compared to the native atoms) in the C_2S lattice. Such a correlation can be used to estimate the extent of destabilization that can be expected for other dopants, which provides critical insight into selecting proper dopants for tailoring C_2S properties via compositional design.

7. Steel Corrosion in Concrete: Mechanisms of Pitting Corrosion

7.1 General Introduction

On a macroscopic scale, corrosion has been considered to be the degradation of materials' properties because of the interaction between materials and the environments surrounding them.[47] In contrast to a macro concept of corrosion, a conventional understanding usually points corrosion to metallic materials. Almost all metallic products for engineering application are facing corrosion problems with typical examples including aluminum-magnesium alloy on aircrafts, the steel of offshore platform, as well as reinforce rebar inside concrete construction structures. According to the newest report from National Association of Corrosion Engineers (NACE), the estimated global cost from corrosion reaches 2.5 trillion U.S. dollars, which is about 3.4% of the global GDP of the year 2013. [167] Among all the metallic engineering materials, steel has been the majority metallic construction material, as a result, the corrosion of steel has been attracted increasing focus and efforts. [62], [65], [68], [77], [168]

Concrete is the most widely used artificial material in modern society construction in circumstances such as skyscrapers, bridges, highways, as well as dams. The global usage of concrete was reported to be about 25 billion tonnes per year, which was equivalent to over 3.8 tonnes per person all over the world. [169] Concrete has been well-known of its high in compression strength but low in tensile strength. To compensate this weakness, reinforced steel rebar has been embedded into concrete structures and provide the tensile strength. However, the reinforced rebar could be corroded under certain circumstances and one of the most common threats is chloride-induced corrosion which accelerates the corrosion process significantly.

Corrosion of metals can be classified into several categories based on the morphology change, nature of corrosion, as well as the environments that caused corrosion. [61] Here are several common forms of corrosion in concrete structures.

1) *General Corrosion.* General corrosion, also called uniform corrosion or overall corrosion, is one of the most common corrosion forms. The corrosion is usually induced by surface chemical/electrochemical reaction between the metal and its surrounding environment, e.g., aqueous solutions. This form of corrosion is of usually about at a constant corrosion and result in continuous losing of materials, which may lead to multiple ways of failure such as insufficient mechanical strength, leakage of liquid due to thinner container walls, cracking of wrap-up materials due to expanding volume from corrosion product, etc. In concrete structure, the theoretical corrosion rate of rebar is a very slow process because the concrete with low permeability protects the rebar very well. Besides, the high pH (>13) also provided passivation environments and protect steel from corrosion. For example, the general corrosion rate of rebar in concrete is about 0.1 μm/year. [170] It is also reported that a uniform loss of about 25 μm will enventually lead to concrete cracking. [171] However, if the concrete fails to protect the rebar, general corrosion will be accelerated significantly. [172]–[174] For example, Gonzalez et al. reported that practical general corrosion rate of rebar in concrete turned out to reach 20 μm per year which will lead to structural failure over 50 years. [172]
2) *Pitting Corrosion.* Pitting corrosion is a typical form of localized corrosion. The initiation of corrosion usually starts from the destruction of the passivation layer on the metal surface

with the early age morphology acting as the rougher surface. [175], [176] It performs in a way that at small spots the material losses at a much higher rate than the rest of surface. As a result, some local depressions of various depth and diameters will be generated in the surface of the metal surface. These holes could be isolated or close to each other, sometimes even merge into each other forming lager holes. Pitting corrosion is one of the most dangerous corrosion form because 1) it removes little amount of materials but could cause stress concentrated and failure, 2) it is difficult to detect as pits are usually covered by corrosion product and small in size, 3) it may take a long period, e.g., months or years, before pits can be found, 4) the failure caused by pits often happens in a sudden.

Pitting corrosion is extensively existing to metallic materials, especially when aggressive ions, e.g., chloride ions, are introduced. There are many opportunities for reinforcing concrete structure to get access to chloride ions. For example, in clod area, de-icing salt is vastly used to melt ice which will lead to extensive chloride-containing chemicals on concrete structures over time. When the concrete structure cracks, chloride ions could very easily reach rebar and lead to severe corrosion.[62], [177]–[179] More detailed information regarding pitting corrosion will be introduced in section 7.5.

3) *Stress Corrosion*. This corrosion phenomenon happens with the coexisting of stress applied to metal materials and exposure to the corrosive environment. With the stress, metal prefers to crack faster comparing to just exposed to aggressive solutions, meanwhile, the yield stress will be greatly decreased. [180] Stress corrosion of rebar is usually not the reason for concrete failure, instead, the failure of the bond between concrete and rebar will lead to an end of strength supply from rebar.[181]–[183] According to the report of K. Bhargava et al., when the corrosion level of rebar is of 1-to-4 % by mass loss, as long as the concrete is not cracked, the bonding between rebar and concrete will be increased and the concrete system

is safe; however, if the corrosion level exceeds this level, the concrete around the rebar cracks and strength of the concrete structure reduces significantly. [183]

4) *Galvanic Corrosion.* Different elements have different electrochemical potentials. When different elements get a touch with each other, they will form unit cells with current goes directly through their boundaries. During this process, the more active element will lose electrons and be oxidized into higher-valent state ions, while the noble element will gain electrons and be reduced to lower valent state ions. The rate of this type of corrosion depends on the potential difference between those two elements, the resistance of electron channels, as well as the area of the boundary. Galvanic corrosion could be formed in the way of macrocell and microcell corrosion in concrete, with the macrocell formed by coupling a piece of rebar with other rebar or component which is in the different electrochemical environments, and the microcell is formed by the local difference such as chemical composition variants. [174] A big influence from galvanic corrosion is the cathode-to-anode area ratio.[184] As the metallic components usually work as an anode (losing electrons), if its area is relatively small, the current flowing through this area will be enlarged causing an acceleration of the corrosion. Comparing to the concrete, the surface area of rebar is relatively smaller, and the rebar corrosion usually starts from a partially exposed metal surface, consequently, the galvanic corrosion will perform in a way of severe local corrosion which causes significant damage to concrete structures. [185], [186]

5) *Erosion Corrosion.* When the solution is flowing or being stirring as the corrosion happens, there will be two factors enhancing the corrosion process — the mechanical damage upon the metal surface and then removing the corrosion product/protective film away from the metal surface so that the corrosion will proceed on faster. This type of corrosion happens frequently in a large number of circumstances such as vessels, pipes, offshore platforms and

so on. This type of corrosion rarely happens to rebar in concrete because of the protection of concrete over.

6) *Other Corrosion Forms.* Other corrosion forms such as microorganism corrosion, high-temperature corrosion etc. are corrosion under specific environments. The reason of corrosion forms should always be considered at the specific environment. A practical corrosion behavior is usually a combination of those corrosion forms with some of them playing the dominated role.

7.2 Chemical Reactions of Corrosion

The corrosion process is an electrochemical reaction process, which needs four essential components, namely, the cathode, the anode, the outer circuit connection for electron transportation, as well as the conducting solution that allows ion migration. The metallic material usually acts as the anode, where oxidation reactions occur with metal atoms being oxidized to their higher valent states. Taking ferrous system as an example, the electrode reaction on anode size usually proceeds in the following way:

$$\mathrm{Fe} \rightarrow \mathrm{Fe}^{2+} + 2\mathrm{e}^{-} \quad (7.1)$$

Here an iron atom releases two electrons and turns to +2 valent state. Those two electrons will follow the outer circuit connection and arrive at cathode size. With the electrons on the cathode side, the reduction reaction is stimulated with water and oxygen molecules turn to hydroxyl ions. Here the cathode could be a lot of materials which are nobler than iron, e.g., platinum and silver. In water and oxygen system, the electrochemical reaction on cathode can be expressed as follows:

$$\mathrm{H_2O} + \frac{1}{2}\mathrm{O_2} + 2\mathrm{e}^{-} \rightarrow 2\mathrm{OH}^{-} \quad (7.2)$$

Inside the electrolyte, the generated hydroxyl ions migrate towards the anode and form the first step corrosion product, namely ferrous hydroxide. The reaction as:

$$Fe^{2+} + 2OH^- \rightarrow Fe(OH)_2 \quad (7.3)$$

Ferrous is an unstable state of the iron element and it tends to be oxidized into the ferric state. So the ferrous hydroxide, together with water and extra oxygen, will form the second step iron corrosion product. However, the corrosion product could be ferric hydroxide, iron oxide (magnetite, Fe_3O_4) and/or ferric oxide (hematite, Fe_2O_3). Ferric hydroxide is the brown/yellow product known as rust. Despite that the chemical composition of the oxide layer is not well agreed on, it is believed to be a mix of irons oxides and/or hydroxides. Moreover, the exact composition highly depends on the local pH values and applied electric potentials at the metal surface. [187] Here, considering water and iron only, the possible reactions are listed below:

$$4Fe(OH)_2 + O_2 + 2H_2O \rightarrow 4Fe(OH)_3 \quad (7.4)$$

$$2Fe(OH)_2 + O_2 \rightarrow Fe_2O_3 \bullet H_2O + 2H_2O$$

$$(7.5)\ 3Fe(OH)_2 + 2OH^-$$

$$2Fe_3O_4 + 2OH^- \rightarrow 3Fe_2O_3 + H_2O + 2e^- \quad (7.7)$$

$$Fe_3O_4 + OH^- + H_2O \rightarrow 3FeOOH + e^- \quad (7.8)$$

In concrete structures, the electrolyte is known as pore solution. The pH value of pore solution is usually above 13, [188], [189] and the pH value of pore solution could be decreased by carbonation process. If the pH is above 11.5 the steel is still under passivation condition with a stable γ-ferric oxyhydroxide forming on steel surface[168].

$$2Fe(OH)_2 + \frac{1}{2}O_2 \rightarrow 2\gamma - FeOOH + H_2O \quad (7.9)$$

The passivation layer on steel surface is about 5 nm thick. [190], [191] Ghods et al. used X-ray photoelectron spectroscopy (XPS) investigated the chemical composition of the passivation layer and found that the oxide layer could be distinguished into two layers. The inner part consisted of ferrous oxides and the outer part consisted of ferric oxides. The passivity and chloride-induced depassivation of carbon steel in simulated concrete pore (CP) solution (pH=13.3) was investigated using angle-resolved X-ray photoelectron spectroscopy (XPS). After full passivation, the thickness of the oxide film on steel specimens was approximately 5nm. The oxide films close to the steel substrate were mainly composed of protective Fe(II) oxides while near the free surface the film consisted mostly of Fe(III) oxides. The addition of chloride to the CP solution decreased the thickness of the oxide film and changed its stoichiometry such that near the film/substrate interface the Fe(II)/Fe(III) decreased. [172]

Cracking of concrete during the serving period is very common due to stress from shrinkage, freeze-thaw cycles, and mechanical force and so on. [192]–[194] These cracks propagate towards the in-depth direction and might eventually reach the surface of reinforced rebar. Along the in-depth direction of the crack, the exposed pore solution will be carbonated resulting in a decrease of pH value. [195]–[197] When the pH value is lower than a critical value, e.g., 11.5, [172] the pore solution stops passivating steel surface. The cracks also open channels for oxygen getting access to the steel surface, which will encourage the electrochemical reactions as listed in above equations.

7.3 Chloride Ion-induced Corrosion

Aggressive anions have been reported to be essential to initiate pitting corrosion. [198]–[200] Halide anions, i.e., Cl-, Br-, and I-, have been reported to be aggressive and most frequently found to initiate pitting corrosion. [201], [202] Chloride ion is of the most aggressive among the halide ions due to its high diffusion rate [203]–[205]; another reason for much focus on chloride ion is its wide distribution in nature such as ocean environment [206], de-icing salts [207], and earth crust [208]. Pitting corrosion occurs above a critical aggressive anion concentration. For example, a typical chloride concentration has been reported to be above 3×10^{-4} mol/L. [209]

Chloride ions could reach rebar surface either through either diffusion or a regional increase of chloride concentration. The diffusion of chloride towards the steel surface is because that there is a chloride concentration gradient, which can be described by Fick's second law.

$$\frac{\partial\varphi}{\partial \mathrm{t}} = \mathrm{D}\frac{\partial^2\varphi}{\partial^2 \mathrm{x}} \tag{7.10}$$

where φ is the concentration in dimensions, t is time, D is the diffusion coefficient in dimensions, and x is the position.

It takes long for the chloride ions diffuse to rebar surface if the concrete wraps up rebar densely. However, chloride ions could reach rebar faster through approaches such as chloride contaminated water when mixing concrete and cracks providing channels for chloride ions. As a result, the pore solution accumulates chloride ions at a much faster rate than diffusion mechanism and the corrosion will be initiated quicker.

Chloride-ion exposure has been reported to be the primary factor causing rebar corrosion. [62], [178], [210], [211] The chloride-induced corrosion reactions have been reported as following.[212]

$$4\mathrm{Fe(OH)_2} + \mathrm{Cl^-} \rightarrow 3\mathrm{Fe(OH)_2} \bullet \mathrm{Fe(OH)_2Cl} + \mathrm{e^-} \tag{7.11}$$

$$3\mathrm{Fe(OH)_2} \bullet \mathrm{Fe(OH)_2Cl} \rightarrow 4\mathrm{FeOOH} + 3\mathrm{e^-} + \mathrm{Cl^-} + 4\mathrm{H^+} \tag{7.12}$$

$$4[3\mathrm{Fe(OH)_2} \bullet \mathrm{Fe(OH)_2Cl}] \rightarrow 4[\mathrm{Fe(OH)_2} \bullet \mathrm{FeOOH}] + 3\mathrm{Cl}^- + 8\mathrm{H}^+ + 5\mathrm{e}^- \quad (7.13)$$

The $\mathrm{Fe(OH)_2} \bullet \mathrm{Fe(OH)_2Cl}$ is known as green rust phase. As can be seen from the equation 7.11-7.13, during this set of corrosion reaction chloride ions are not solidified into corrosion products and chloride ions just participate in the reaction. Moreover, as hydroxyl ions being fixed into corrosion products, protons are left and local pH value will be decreased. This increase of corrosion will furtherly prevent the passivation process and accelerate the corrosion rate.

8. Pitting Corrosion on AISI 1045 Steel Surface Enhanced by Chloride at Neutral pH

8.1 Introduction: Influences of Chloride Ions on the Initiation and Propagation of Pitting Corrosion

Among all the corrosion forms mentioned above, pitting corrosion is one of the most focused forms because of its high dangerousness and universality. The research interests have been aroused from multiple reasons, not only because pitting corrosion vastly affect metals such as iron, aluminum, magnesium, copper, nickel, tin, and so on but pitting corrosion is difficult to study despite of its threatening to metallic materials. The difficulty to study is due to a number of reasons. First, the small size of pits makes their detection challenging especially during the early stages of pitting when the pits feature diameters ≤ 20 μm and depths of only a few tens of nanometers.[213]–[218] Second, pits may be obscured by corrosion products that may form (concurrently with pits) on metallic surfaces.[216], [219], [220]

Pitting corrosion, a particularly damaging form of metallic corrosion has been a subject of research for several decades.[77], [209], [213], [214], [219], [221]–[225] Although the formation of pits consumes only a relatively small amount (mass) of material, the role of pits in serving as defect sites for crack initiation and continuing corrosion can be significant.[226], [69], [227], [228] Halide ions such as chloride (Cl^-) are well-known to accelerate the pitting corrosion of alloys such as steel.[229], [230], [224], [231]–[233] Numerous mechanisms have been proposed to explain pitting initiation, namely:[200], [221] (1) penetration, wherein Cl^- species penetrate through the passivation layer and react with the metal at the metal-oxide interface, creating vacancies. As vacancies accumulate, the passive oxide film is damaged, exposing the bare metal (or alloy) to the electrolyte;[175] (2) adsorption, which involves the sorption of aqueous Cl^- on the passivation layer, locally decreasing its thickness until the bare metal is exposed.[209], [232] Such thinning is thought to arise from the increase in the ionic conductivity of the oxide film that results in the migration of metal ions from the alloy surface through the film;[234] and, (3) film breakdown, which occurs due to the interaction of aqueous Cl^- with oxide layer defects such as grain boundaries as a result of which the passive film undergoes continuous breakdown.[235], [236] Unfortunately, in spite of extensive research, there is no general consensus as to which of these proposed mechanisms, and models dominantly control the evolution and progression of the pitting corrosion process, and at which (temporal) stages.

The three mechanisms, naming penetration mechanism, adsorption mechanism, and film breaking mechanism are introduced below and the schematic figures describing these mechanisms are shown in Figure 8.1. It should be noted that these theories are developed for pure metals, whereas for practical alloy materials, pitting initiation is often associated with a surface defect such as inclusions or second-phase grains. [200]

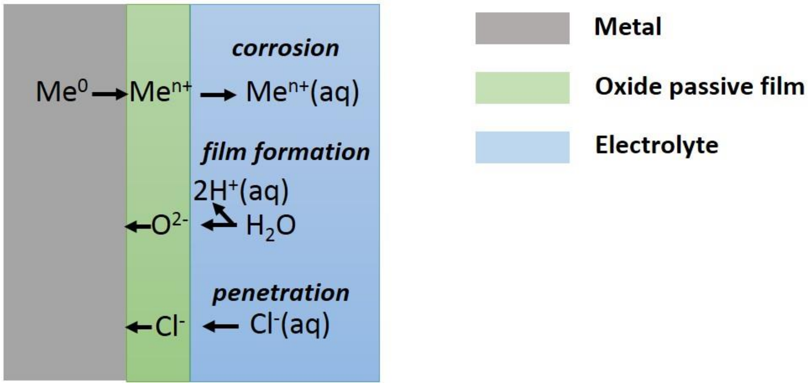

a) Penetration Mechanism

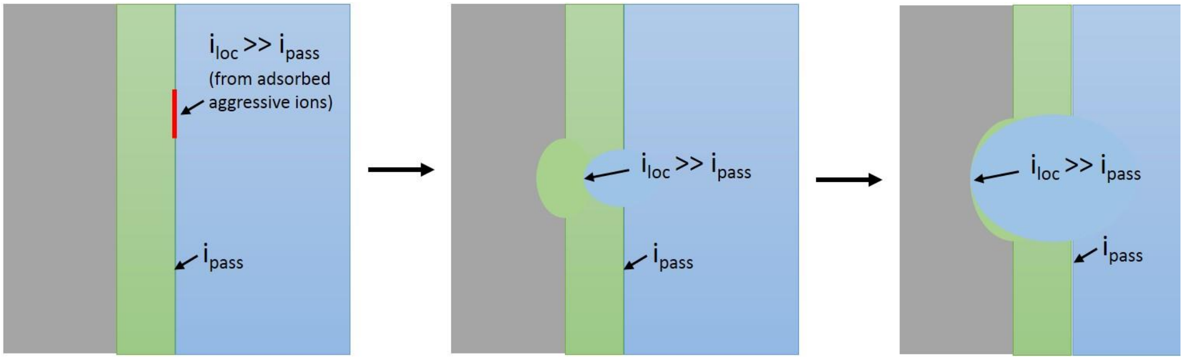

b) Adsorption Mechanism

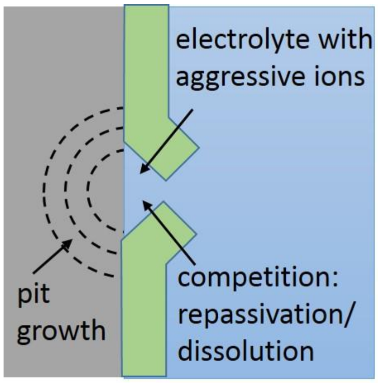

c) Film Breaking Mechanism

Figure 8.1 Schematic diagrams representing pitting corrosion initiation process by a) penetration mechanism, b) adsorption and thinning mechanism, and c) film breaking mechanism. [200]

a) Penetration mechanism

Penetration mechanism, as shown in Figure 8.1 a), correlates to the transportation of both metallic ions and aggressive anions through the metal-oxide interface, oxide film, and oxide-electrolyte interface. [200], [175], [237] The accumulated anions on the oxide-electrolyte interface and the Fe^{3+} at the metal-oxide interface form a strong electric field which drives Fe^{3+} ions migrate towards the oxide-electrolyte interface direction. [237] This is the enhanced oxide layer dissolution process by thinning of an oxide layer on the metal-oxide interface, which will eventually break down the passivation state. To neutralize the charge by migration of Fe^{3+}, the aggressive ions like Cl^- and O^{2-} will be driven towards the metal-oxide interface direction. However, these anions have larger ionic radii, so they migrate towards the metal-oxide interface direction at a lower rate comparing to Fe^{3+} ions. Experimental evidence has been reported that aggressive anions have been found in passivation layer [238] but some other studies claim no such evidence [239], [240].

A model of point-defect developed by Macdonald et al [241] gives a better explanation of penetration theory. As the vacancies formed by the migration of Fe^{3+} ions on the metal-oxide interface accumulate at the metal-oxide interface, the oxide film gets thinner. Eventually, the film breaks and pits start to initiate.

b) Adsorption Mechanism

At the energetically preferred places of the passivation film, the aggressive anions accumulate and generate large electric filed through the thickness of the film. This local concentrated electric filed will lead to i) exchange of OH^- or O^{2-} by aggressive anions with smaller ionic size to neutralized localize charge on a metal surface, ii) rapid migration rate of Fe^{3+} ions and vacancies accumulation. As the aggressive anions replace the original anions, the dissolution rate of the new compound, e.g., oxyhalide compound, is much higher than the oxide. This process is described in Figure 8.1 b).

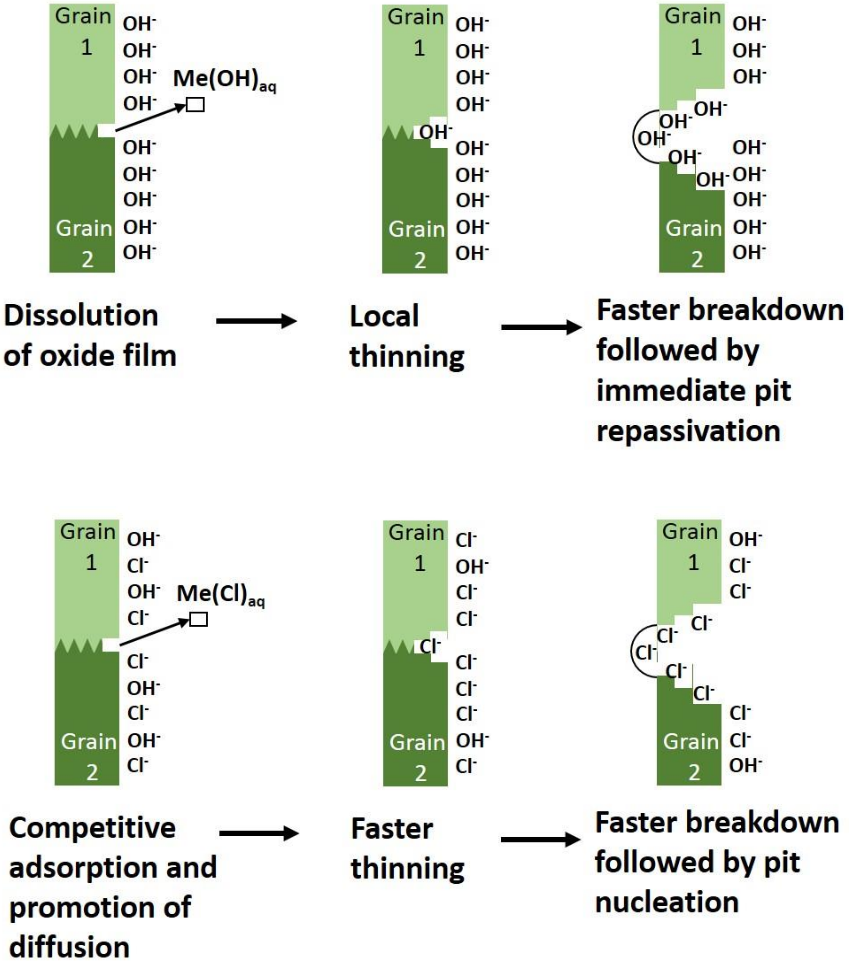

Figure 8.2 Schematic diagrams representing adsorption mechanism of pitting corrosion initiation by comparing with and without Cl- ions cases [230]

In Figure 8.2, the diagrams describe the process of passivation film breaks down by adsorption mechanism. When there is no Cl^- ion, at the energy preferable sites, OH^- ions are attracted onto oxide film due to the attraction force by Fe^{3+}. Fe^{3+} ions then migrate towards the oxide-liquid interface and form $Me(OH)_{aq}$ compound leaving vacancies at the metal-oxide interface. Due to the low migration rate of OH^- and low solubility of $Me(OH)_{aq}$, the local thinning process is in overall slow. However, when there are aggressive anions, e.g., Cl^- existing, the migration rate of Cl^-

is much faster than OH^-, moreover, the dissolution rate of $Me(Cl)_{aq}$ is higher than $Me(OH)_{aq}$. Both effects lead to a faster passivation film thinning process, as a result, the localized pitting corrosion occurs rapidly.

The accumulation of aggressive ions in aqueous solution is necessary for forming stable pitting corrosion. [221] At the beginning, the passivation layer on metal surface protect metal from corrosion, however, as the corrosive ions species adsorb and accumulate on the passivation film, the film will break down. Moreover, those corrosive ions prevent passivation layer from re-forming. As a result, continuous corrosion proceeds on and stable pits may grow and propagate.

c) Film Breaking Mechanism

This mechanism fit for the scenario when there is surface defect such as a crack in the metal surface oxide film and aggressive anions exist in the electrolyte, see Figure 8.1 c). The aggressive anions contact directly with bare metal surface and corrosion reaction proceeds rapidly. Moreover, when sufficient aggressive anions accumulate on the surface defects to balance the local charge, these ions will prevent repassivation from bare metal. Strehblow stressed that in stationary measurement, film breaking mechanism could be more favorable due to the introduced stress by local potential difference and the corresponding passivation layer break-down. [237]

The existing of chloride ions in surface defect will encourage the film break-down. The basic concept is the same to film breaking mechanism introduced above, when there is defect such as a crack in metal surface oxide film the anions will contact with the bare metal surface. But the OH- ions are large in size and have little possibility to migrate to the bare metal surface, so the film collapse is finally caused by the accumulation of vacancies after Fe^{3+} migration, as shown in Figure 8.3 a). If there are aggressive anions in the aqueous solution, they migrate to the bare metal surface much faster and easier and form corrosion product. As the corrosion product expands, eventually the oxide film fails to withhold the expansion and breaks with the more bare metal surface exposed to the electrolyte.

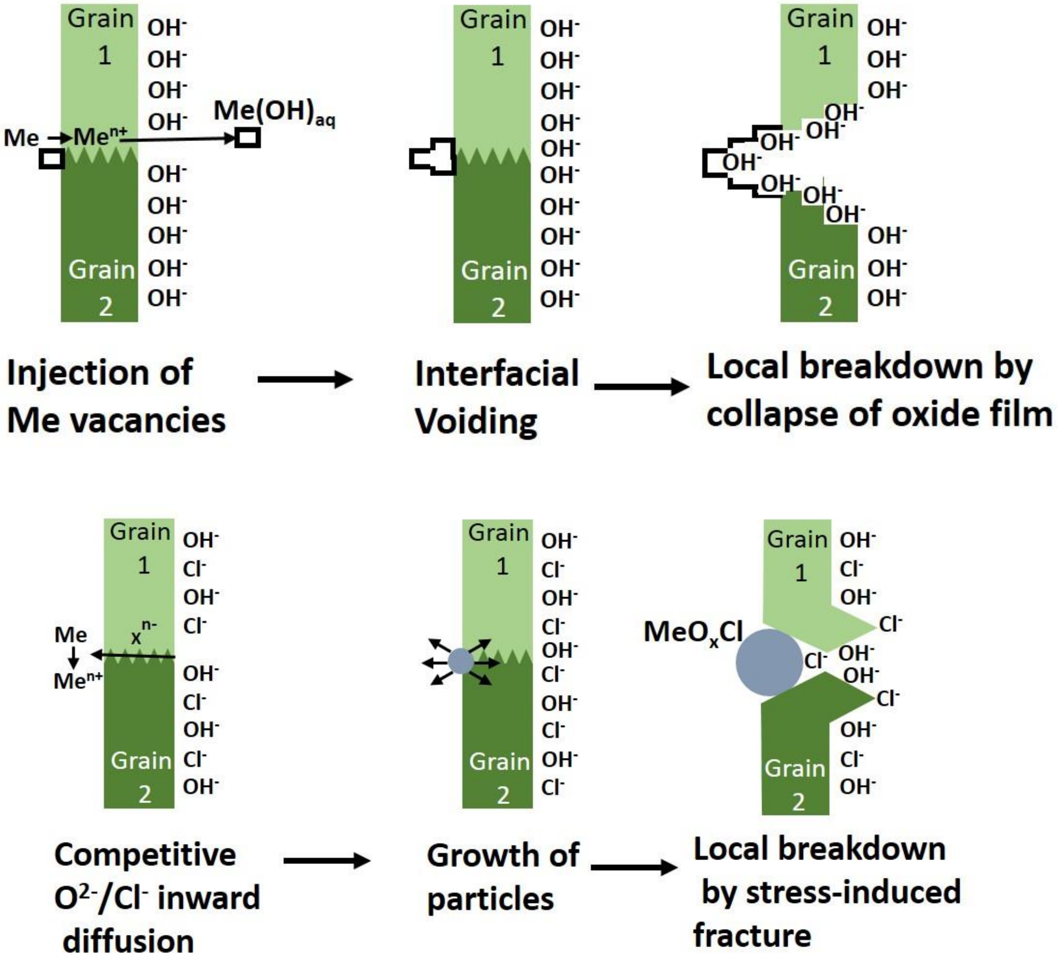

Figure 8.3 Schematic diagrams representing film breaking mechanism of pitting corrosion initiation by comparing with and without Cl- ions cases [230]

Brustein et al detected the pitting propagation on type 304L steel surface in chloride-containing and chloride free solutions.[242] They applied electrochemical approach and measured the electric current change of the metal sample to observe the pitting current. To their recognition, the pitting process could be taken as four steps including pit nucleation, embryonic pit formation, metastable pit formation, and stable pit formation. These steps were told from the corrosion current peaks over time. They compared the corrosion currents of type 304L steel in chloride free and chloride-containing solutions and found that 1) without chloride ions the current-time curve is a smooth decaying curve, indicating a passivation process, and 2) in the solution of 25 mM HCl and 75 mM $HClO_4$ with 0.2 V potential applied, not only the overall corrosion current was increased but there were a few current abrupt increase in that curve, meaning that both the general corrosion and pitting corrosion were encouraged. Besides, they also found for type 304L steel in 25 mM HCl and 75 mM $HClO_4$ solution with 0.2 V potential applied, the pitting nucleation started within 1 second. This study provided direct evidence of pitting corrosion periods by telling the corrosion current change over time; it also demonstrated the repassivation phenomenon in the chloride-free environment as well as the stimulation effect from chloride ions.

Despite measuring the pitting carrion current can provide the elucidation of pitting periods, it is lack of evidence of the reason of pitting, e.g., what initiates pitting? To address this problem, many studies have been conducted to reveal this fact.

It is well-known that second phase in steel is one the most important agent to trigger the pitting corrosion initiation. [77], [243]–[247] For example, Mary et al found that pitting corrosion started at the MnS inclusion dissolution.[77] They applied focused ion beam/secondary ion mass spectroscopy (FIB/SIMS) to measure the chemical composition around a MnS particle in type 316F stainless steel surface. It is found that at the edge of a MnS particle, the Cr content is at very low concentration hence it would not protect steel from corrosion, and the Cr/Fe mass ratio is more than 60% lower than that in the bulk material. At the distance away from the MnS particle edge, the Cr/Fe ratio increased and eventually it reached the bulk material ratio level at about 800 nm away from the edge. David et al. applied the high resolution scanning electrochemical/photoelectrochemical microscopy (SECM) and atomic force microscopy (AFM) to observe the trigger mechanism of pitting corrosion on type 316F stainless steel. [214] They captured the 3-dimensional image of a defined steel area and tracked the surface change around MnS inclusions with respect to local current and height evolution. They concluded that the pitting corrosion initiated resulted from the fast dissolution of sulfide inclusion where chloride ions concentrated by electromigration.

To summarize the previous studies regarding pitting corrosion mechanism, the pitting corrosion is usually initiated at surface defect especially second phase inclusions such as sulfide particles. While electrochemical studies may be widely applied to examine pitting – these approaches only assess bulk ("average") behavior – without being able to resolve microscale features.[221], [237], [248]–[251] More recently however, electrochemical scanning tunneling microscopy (ECSTM) has been used to study oxide layer removal and pitting initiation on metal surfaces,[252], [253] while atomic force microscopy (AFM)[254] has been utilized to observe the morphology of single pits. These techniques have provided valuable insights into pit growth without invoking any assumptions regarding the active area of pitting sites or regarding current densities of single pits.[200] However these methods offer very limited visualization as for example, ECSTM can only probe a small field of view (FOV) on the order of a few square microns, and AFM is unable to image sharp and deep pits (> 10 μm) due to its limited vertical range.

Previous studies either focused on the pitting initiation around a single or several pits with a determination of chemical composition or a track of geometry evolution. Electrochemical methods were generally used to test the overall performance of pitting corrosion and distinguish the pitting corrosion periods without knowing the detailed change of pits. In recent studies, SECM, AFM, and

ECSTM have been applied to observe the pitting propagation process over time, but with these methods 1) pit depth could not be accurately measured due to technical limitations, 2) sufficient pits were not available for reliable statistics, and 3) external force or current might be applied when measuring which influenced the pitting corrosion rate.

Based on the knowledge from previous studies, the preferred pitting initiation sites and chemistry have known, and I will be focusing the observation of the process of pitting initiation and propagation and the hidden information in that process. In this thesis, to overcome the limitations discussed above, vertical scanning interferometry (VSI) is used for the first time to study the initiation and development of pitting corrosion on AISI 1045 steel surfaces. In brief, VSI uses the interference of light having short coherence lengths to assess surface heights without external influences to pitting corrosion. As such, a vertical range of up to a few millimeters that can be sampled at nanometer resolution, in combination with up to the sub-micron lateral resolution, allows for the detection of pits from their nucleation until maturity. Furthermore, to acquire statistically valid data, multiple images can be tiled to generate composite images that represent sample areas of up to tens of square millimeters. These capabilities enable observations of pit nucleation and propagation, at an unparalleled resolution over representative surface areas. As such, this study unambiguously elucidates new insights into the kinetics and mechanisms of pitting corrosion in medium carbon steels, and the effects of aqueous Cl^- species on amplifying corrosion activity, at the nanoscale.

8.2 Materials and Methods

8.2.1. Materials and Sample Preparation

Commercially available AISI 1045 steel was sectioned into coupons with dimensions of 1.7 cm × 0.8 cm × 1.7 cm (length × width × height) using a low-speed precision saw (Buehler, IsoMet 1000). This medium-carbon steel features a nominal composition in mass % of: C (0.43-0.50%), P (0-0.04%), Mn (0.60-0.90%), S (0-0.05%), Si (0.15-0.30%), and Fe (98.21-98.85%). Polytetrafluoroethylene (PTFE) which is well-known to be inert in corrosive solutions,[255]–[257] was used as the reference material for VSI imaging as noted below. In addition, PTFE is hydrophobic – therefore it resists the deposition of corrosion products on its surfaces. Coupons of PTFE were sectioned and embedded adjacent to the steel sample in an epoxy 'puck' (see Figure 8.4a) to facilitate handling. After curing the resin for at least 10 hours at ambient temperature, the hardened puck was progressively polished using 400-, 600-, 800-, and 1,200-grit sandpaper and 6-, 3-, 1-, ¼-µm diamond pastes. The polished sample was cleaned by ultrasonication in ethanol for 2 minutes and then dried in a stream of ultrahigh purity (UHP) nitrogen gas.

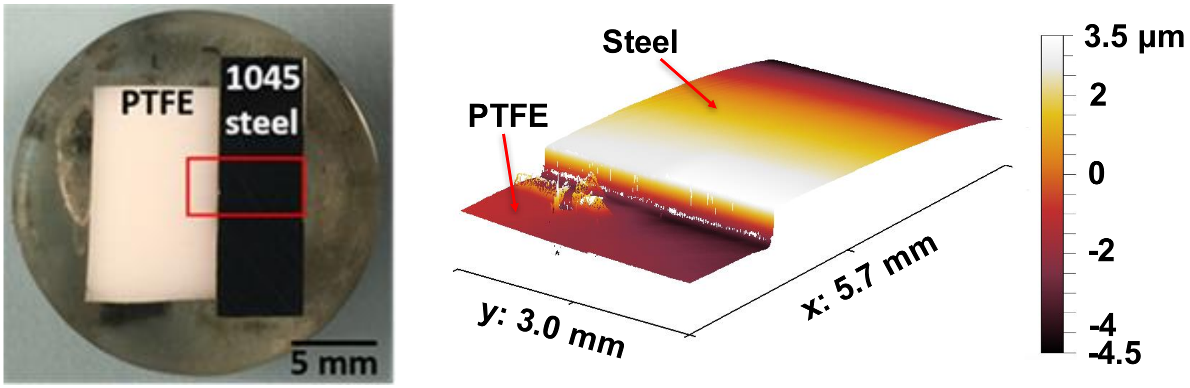

(a) (b)

Figure 8.4 (a) An image of the plane-polished epoxy "puck" in which the PTFE and AISI 1045 steel coupons were embedded, and, **(b)** A representative VSI image of the reference (PTFE) and steel samples that are embedded beside each other.

8.2.2. Vertical Scanning Interferometry (VSI)

The evolution of the steel surface's morphology during corrosion was monitored using VSI (NewView 8200, Zygo Corporation), see Figure 8.5. To enable imaging of large corroding areas, a 5× Mirau objective (numerical aperture, N.A. = 0.13) was used which offers a lateral resolution (i.e., pixel size) of 1.63 μm in the x and y directions. The nominal vertical resolution is on the order of 2 nm. With this configuration, the field of view of each VSI image is 1.7 mm × 1.7 mm and can be expanded by merging ("tiling") multiple images that are imaged along a grid (e.g., a grid comprised of A × B images consists of A.B images that are taken sequentially). Tiled areas consisting of the steel and reference surfaces, and having nominal dimensions on the order of 5.7 mm × 3.0 mm, were examined (see Figure 1b). The observable surface area of the steel is on the order of 10.7 mm^2 and consists of 4.03×10^6 pixels. This large imaging area allows for the observation of hundreds of corrosion pits simultaneously.

Figure 8.5 Photo of VSI instrument (NewView 8200, Zygo Corporation)

To initiate corrosion, the polished planar sample surface was immersed in 70 mL of either: (i) 18 MΩ cm deionized (DI) water, or, (ii) 100 mM NaCl solution, which was prepared by adding ACS reagent grade NaCl to 18 MΩ cm DI water. The measured pH of this solution was 5.8 and the reaction temperature was 25 ± 3°C. The corrosive solution (70 ml) contacted a surface with a nominal area of 17 mm × 8 mm resulting in a surface (solid)-to-volume (liquid) ratio of 0.002 mm^{-1}

(S/V).[258] The sample was periodically removed from the solution and dried with a nitrogen gas stream prior to surface topography characterization. Corrosion activity was assessed periodically for up to 10 hours in DI water, and 3.5 hours in 100 mM NaCl solution, at which time the steel surface was almost completely covered by (visible) corrosion products.

Surface topography data (i.e., in the form of three-dimensional (3D) images) acquired by VSI were processed and analyzed using MATLAB©. The analysis was carried out using bespoke scripts that performed the following operations: (1) 3D images of a given (imaging) area that were acquired at different reaction times were aligned; (2) corrosion pit sites were identified; and (3) the geometry (i.e., radius, depth, and aspect ratio) of the pits was characterized, all as a function of contact time with the reaction solution. If a given pixel location did not contain height data, such data was retrieved by interpolation from a 4th order function fitted to the known (local topography) data. To align the 3D images, the PTFE reference was marked with a sharp tool (Figure 8.5). Then, an area of an arbitrary size enclosing the *mark* was cropped from the 3D image and then converted into a 2D grayscale image. This 2D image was then aligned with that collected at t = 0 using an image-registration algorithm that only permitted translation and rigid rotation within the *x-y* plane. It should be noted that since the sample was mounted on a stable (resin) substrate, out-of-plane corrections, such as rotations in the *x-z* or *y-z* plane (i.e., tilting), were generally not necessary after the in-plane alignment. The image-registration algorithm produced a 2D transformation matrix, which was then applied to the entire 3D image. Aligning the 3D surface topography using the reference mark enabled precise identification of transient and newly formed features on the steel surface as corrosion evolved. In addition to lateral alignment, the 3D images were also aligned vertically (in the *z*-coordinate) by matching the average heights of equivalent areas on the PTFE reference at t = 0 and at later times (see Figure 8.6).

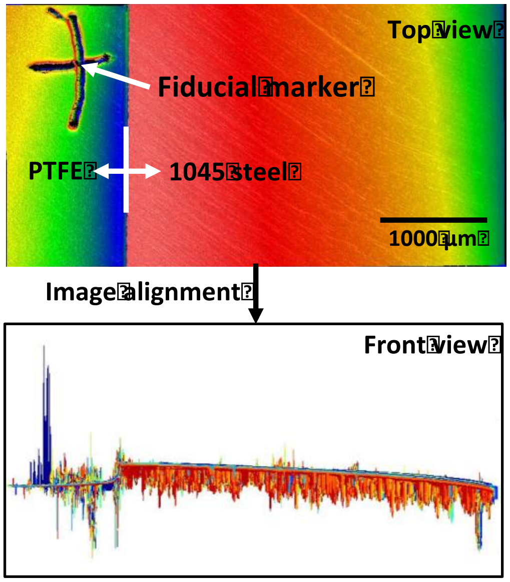

Figure 8.6 An illustration of the VSI 3D image alignment method. **(top)** A fiducial mark placed on the reference PTFE surface is used to align all VSI 3D images to the t_0 image. **(bottom)** An example wherein 50 (3D) images are aligned using this method.

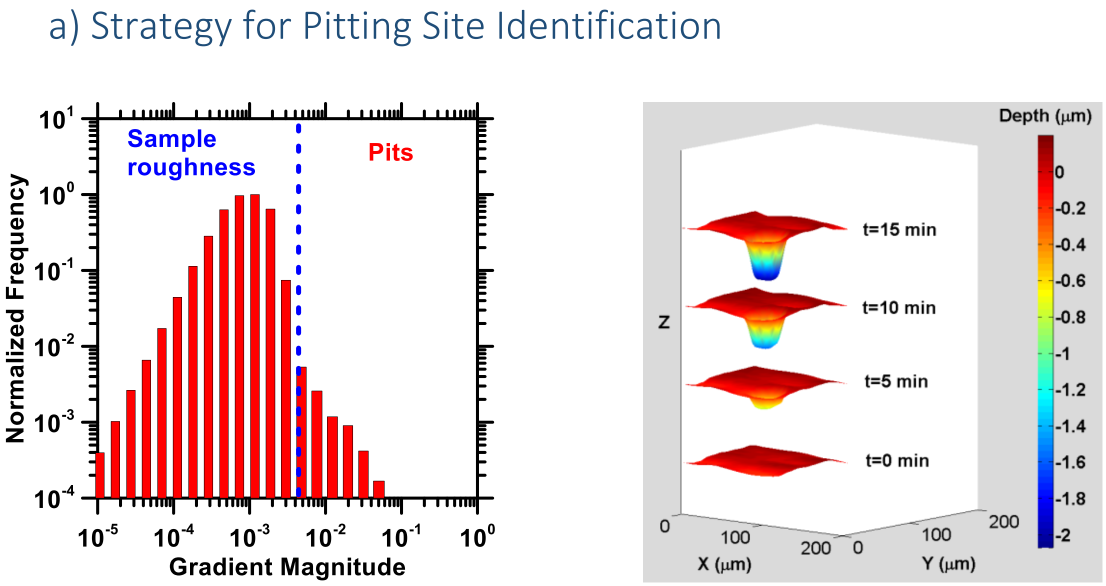

(a) (b)

Figure 8.7 (a) The methodology for identifying pitting sites on the sample surface. In general, pits are differentiated from the sample's roughness as the top 1% of the gradient values shown by the dashed blue line, and **(b)** An illustration of pit growth on AISI 1045 steel in 100 mM NaCl. From the bottom to the top, the diagram shows time evolution after 0 min, 5 min, 10 min, and 15 min of solution exposure. After 15 min, the pit depth reached 2 µm.

Although general topographical features could be readily identified from the unprocessed 3D images (e.g., the average height of the steel surface relative to that of the inert reference), identifying transient and fine-scale features such as pitting sites require additional effort. Such pit identification was accomplished in two steps. First, each pixel located on a 3D image was classified as either a part of a pit or not, based on the magnitude of its gradient (i.e., slope in 2-dimensions, $\sqrt{(\frac{\partial z}{\partial x})^2 + (\frac{\partial z}{\partial y})^2}$, where z is the height of each pixel) compared to a threshold value. The threshold for gradient-based identification of pits was selected based on the distribution of gradients in each image (e.g., see Figure 2a). A typical value of such a threshold is 1%, i.e., if the maximum gradient frequency distribution in a VSI image is F, then only pixels with a gradient magnitude below $0.01F$ are considered to be non-pitting sites, while pixels with a gradient magnitude greater than $0.01F$ are identified as pits (Figure 8.7 a).

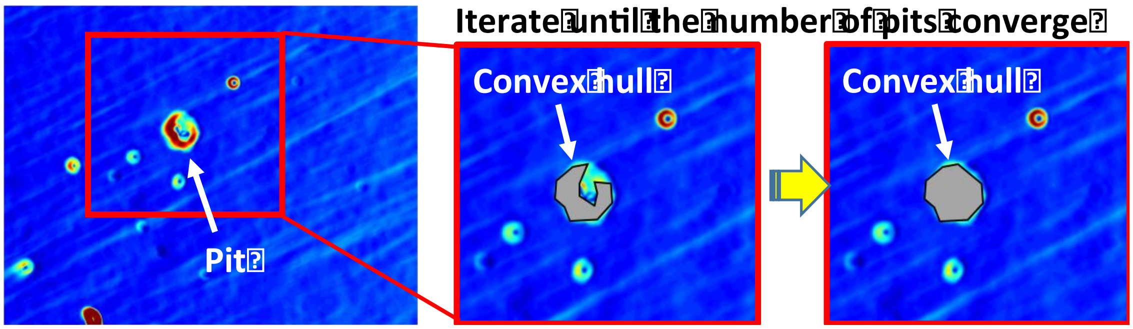

Figure 8.8 An illustration of the pit identification process using the convex hull method. **(left)** A gradient map of the steel surface showing a pit to be identified. **(middle)** A 2D convex hull is drawn on the target pit. Initially, the convex hull may not be able to completely identify a pit. **(right)** The convex hull algorithm is iterated until the number of pits converges to a stable value to ensure that the convex hull covers the specific pit completely.

It is recognized that pits could also be identified based on an absolute height change with respect to the initial surface. However, such methods are ineffective in distinguishing localized height decreases (i.e., pit formation) from uniform surface retreat (i.e., dissolution of the alloy). In contrast, the use of a local gradient-based method allows for pits to be identified based solely on their geometrical characteristics, and the gradient of their proximate surroundings. However, since the gradient method exploits the idea that the walls of the pit are expected to be high-slope features, it tends to ignore the region at the bottom of a pit, which typically has a relatively lower gradient. Thus, to ensure that a pit was identified in its entirety, a convex hull algorithm was implemented (Figure 8.8). First, all neighboring pixels initially identified as belonging to pits (e.g., pixels at the walls of the pits) were grouped.[259] Then, a 2D convex hull was drawn around each group of pixels, based on their x and y coordinates, to indicate an area that is a potential pitting site. Based on overlaps in areas belonging to different potential pitting sites, the grouping of points was iteratively updated. A new convex hull was then drawn around points belonging to two overlapping areas, hence consolidating the areas into one pit. This process was performed iteratively until the number of pits converged to a stable value. Each pit was then assigned a unique identifier for further analyses.

b) Characterizing Pit Geometry, Transience, and Surface Evolutions

Once pitting sites were identified, analyses were carried out to characterize pit nucleation and growth. To establish the baseline surface used to correct for tilt and curvature, first, a 4th order polynomial was fitted to the 3D image excluding all identified pits, to capture the surface curvature (Figure 8.8). The roughness of the steel surface without the pits, R_{rms}, is calculated with respect to this baseline surface as: $R_{rms} = \sqrt{\frac{\sum_{i=1}^{n} dz^2}{n}}$, where n is the number of data points, and dz is the distance to the baseline surface. The depth of each pit was defined as the distance between the lowest point in the pit and the baseline surface (Figure 8.9). On the other hand, the pit radius was calculated from the measured pit area, assuming that the pits can be roughly circumscribed by a circle. By analyzing overlapping pits (i.e., the same pitting sites) in time-spaced surface topographies, the nucleation and growth process of each pit can be studied. This permits quantification of the pit density as a function of time, and the evaluation of pit growth rates, while being able to distinguish existing from new pits at each time interval.

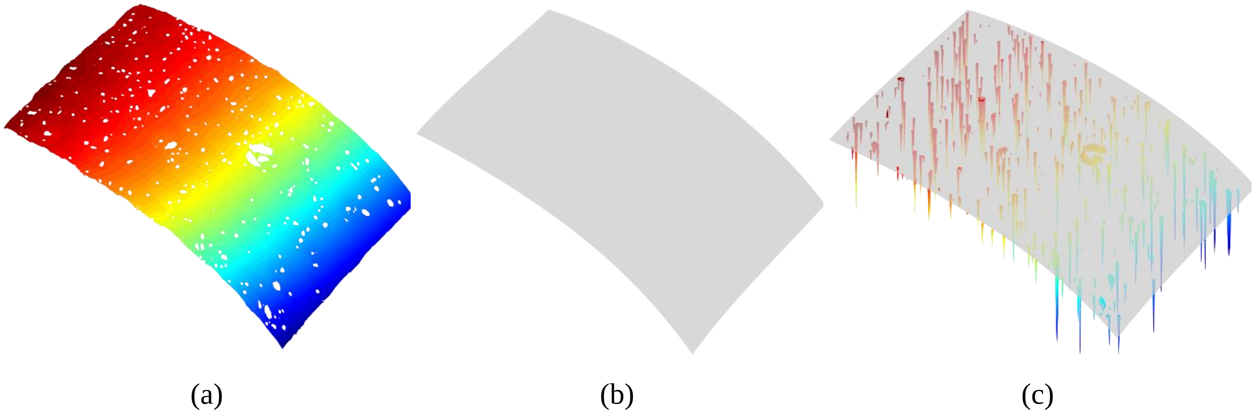

Figure 8.9 An illustration of the method employed to calculate pit depth. (a) A VSI image of the non-pitting area of the sample surface. Note that the pits have been removed from the data. A fourth-order polynomial is fitted (a) to determine the baseline surface, (b), from which pit depths are obtained, as shown in (c).

8.3 Results and Discussion

8.3.1. Spatially Heterogeneous Pitting Corrosion on AISI 1045 Steel Surfaces

Careful examination of 3D topography data acquired using VSI reveals the highly non-uniform, i.e., heterogeneous, the progress of corrosion in both DI water and 100 mM NaCl solutions. To quantitatively examine the heterogeneity of corrosion processes, the height difference was calculated pixel-by-pixel relative to the unreacted t_0 surface, across each time-spaced FOV. The frequency distribution of height differences was then monitored over time as shown in Figure 8.40. It should be noted that negative and positive height differences indicate either the (net) removal from or the deposition of material on to the surface, respectively. As corrosion proceeds, distinct changes in these distributions become evident. Expectedly, at t_0, the distribution was characterized by a sharp peak centered at 0 μm. This 'peak' persisted even at later times indicating that the majority of the surface featured a largely uniform, unchanging topography across the FOV and that only localized domains on the surface (i.e., encompassing less than 1% of all pixels) showed substantial changes characteristic of pitting corrosion.[200]

The surface height evolutions in DI water and in 100 mM NaCl solutions are distinct (Figure 8.40). For example, in DI water, corrosion is associated with the deepening of localized pits, as suggested by the emergence of the 'low-frequency tail' shown in Figure 8.40(a). The largest surface retreat measured, which affected approximately 0.001% of all pixels (i.e., 40 pixels), was about 10 μm after 10.17 h of reaction (Figure 8.40a). In the presence of 100 mM NaCl on the other hand, pitting (e.g., see Figure 2b) resulted in a surface height decrease (mass removal) of up to 5 μm and the development of a secondary peak centered at around -2 μm after only 0.33 h of solution contact (Figures 8.7b, 8.7d). In time, this secondary peak became indistinguishable from the initial peak, suggesting that generally, pitting evolved to be undifferentiated from the overall surface retreat, which was on the order of 0.7 μm after 3.67 h (see red arrows in Figures 8.7b, 8.7d). As a result, the entire steel surface became uniformly and extensively pitted, as illustrated in the VSI images below. Importantly, the amount of mass loss and the rate of mass (height) decrease are substantially higher in the presence of aqueous Cl^- than in DI water.

Pitting is accompanied by the deposition of corrosion products. In DI water, simultaneous to pitting, a broadly homogeneous height increase of about 3 μm was observed over around 0.1% of the imaging area, suggesting the growth of a surface layer composed of corrosion products. This is likely because the samples were not rinsed prior to imaging of the surface. As a result, corrosion products may have remained on the surface. For carbon steels exposed in water, based on previous studies, and our observations, μRaman spectroscopy, and energy dispersive x-ray spectroscopy (SEM-EDS) have both identified the corrosion products as consisting of lepidocrocite (γ-FeOOH), goethite (α-FeOOH), and the iron oxides hematite (Fe_2O_3) and magnetite (Fe_3O_4).[260], [261]

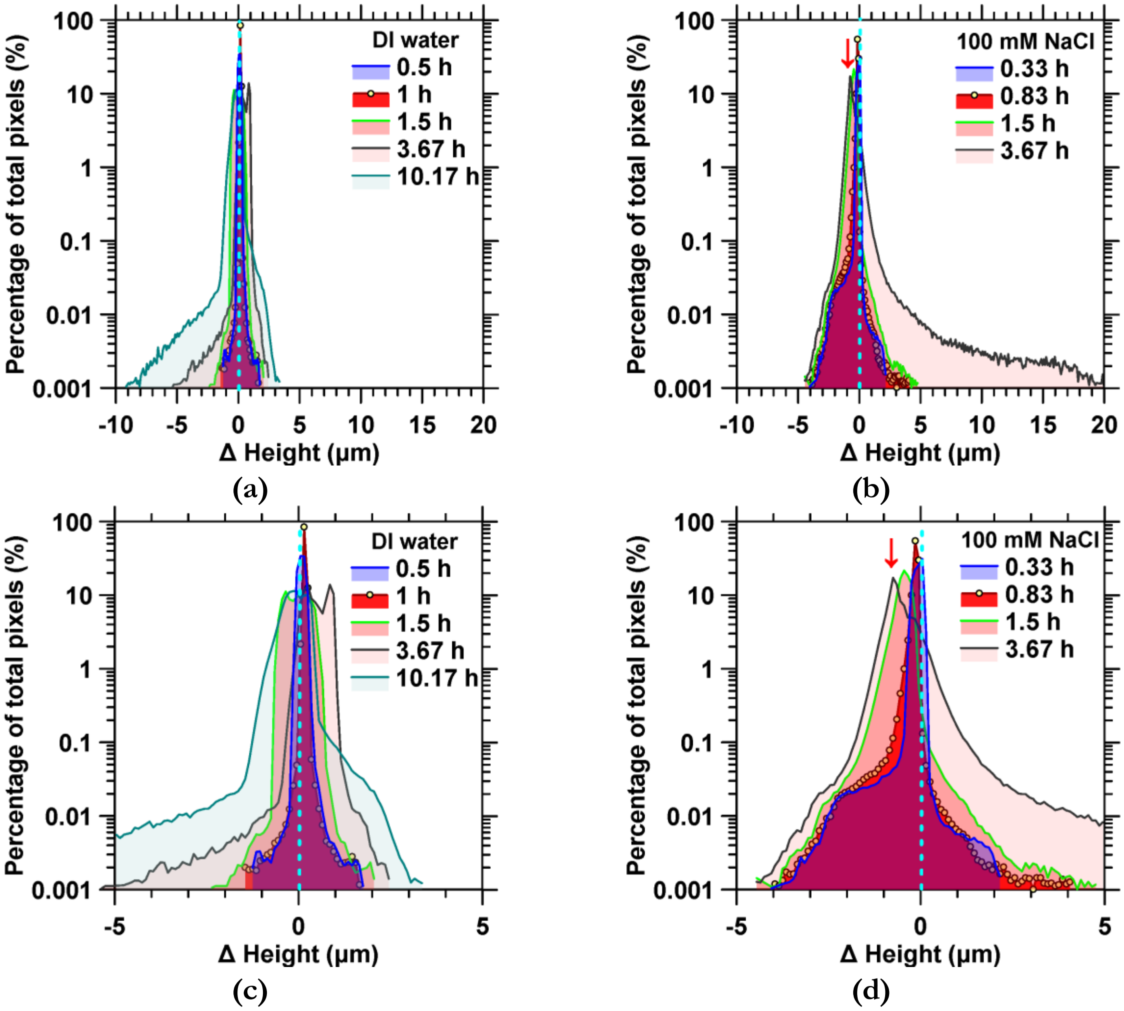

Figure 8.40 Representative frequency diagrams showing the distribution of height differences across different pixel locations for AISI 1045 steel reacting with: **(a)** DI water, and **(b)** 100 mM NaCl solution. The height difference is calculated by subtracting the heights at a given *(x,y)* location at the respective times indicated in the legend from that at $t = 0$ h. As such, negative height differences indicate mass loss (e.g., pit formation and surface roughening), and positive height differences indicate the deposition of corrosion products. **(c)** and **(d)** are the distributions over the height range of -5 to 5 μm, showing in more detail the respective height distributions in **(a)** and **(b)**.

On the other hand, upon exposure to 100 mM NaCl, the frequency distribution of steel surface heights features a long tail signifying a height increase of as much as 25 μm after 3.67 h of solution exposure (Figure 8.40b). This indicates the substantial formation of corrosion products on 1045 steel reacting with Cl^--containing solutions, consistent with previous observations, e.g., using Electronic Speckle Pattern Interferometry (ESPI).[262] In addition to the iron oxides and hydroxides noted above, akaganeite (β-FeOOH) has been detected by μRaman spectroscopy as corrosion product in steels exposed to Cl^-.[263]–[265] Indeed, compositional data acquired using SEM-EDS indicates the presence of lepidocrocite and akageneite on AISI 1045 steel exposed to both 10 mM and 100 mM NaCl after 24 hours of contact time (see Figure 8.41). It should be noted that the observed height increases in the presence of Cl^- are also localized, with a small fraction of the surface (0.02 % of the pixels) showing an increase of 10 to 20 μm. The specific surficial features that are associated with these distributions are further discussed below.

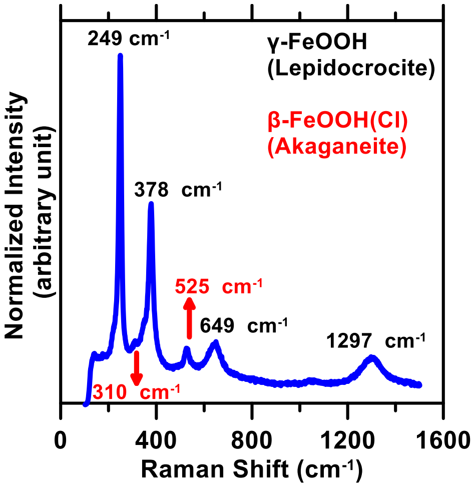

(a)

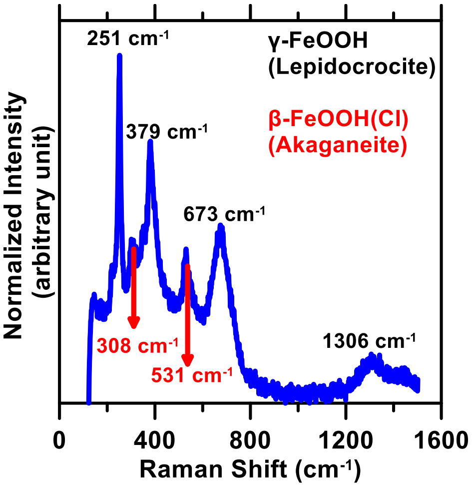

(b)

Figure 8.41 Raman spectra of AISI 1045 steel surfaces reacted for 24 hours with **(a)** 10 mM NaCl, and **(b)** 100 mM NaCl solutions. In both cases, lepidocrocite (γ-FeOOH) (labeled with black text) and akaganeite (β-FeOOH(Cl)) (labeled with red text) are detected, consistent with previous observations.[263]–[265]

The highly localized nature of corrosion reactions is highlighted in the following VSI images that represent large fields of view of 1000 μm × 1000 μm (see Figures 8.9, 8.10). For clarity, surface topography data are presented alongside its corresponding gradient map, which aids in the identification of high-slope features such as pitting sites (see Figures 8.9e-h and Figures 8.10e-h). In general, in both DI water and 100 mM NaCl solution, pits nucleated as the surface roughened. While pit formation and surface roughening progressed in a similar manner in both DI water and NaCl solution, expectedly, the progress of reactions is highly accelerated in the latter case. In DI water, an initial period of up to around 1.67 h is characterized by the absence of significant changes in surface morphology (Figures 8.9a). Afterwards, pit nucleation is accompanied by substantial surface roughening in the vicinity of pitting sites (e.g., see Figures 8.9b-c and 8.9f-g). Based on stochastic modeling, it has been proposed that this initial nucleation period represents the time required to establish a critical local acidic pH that induces pitting.[75] Such pit nucleation is further provoked by the induction of a passive dissolution current that triggers local instabilities in the alloy's (surface) microstructure.[75] As corrosion continues, new pits form preferentially within the initially roughened/destabilized area (e.g., see Figures 8.9d, 8.9h) in the shape of a "circular basin"; likely due to the localized rupture and weakening of the passivation layer in these zones. The formation of these circular basins, which have depths between 100-200 nm with respect to the non-pitted surface, is postulated to be on account of an (effective) $1/r^2$ scaling in the corrosion current density that radiates from the geometric center of the circular basin(s) to un-roughened (uncorroded) locations on the steel surface. This process of pit nucleation, roughening and basin formation around pitting sites, and pit growth and proliferation continues until the steel surface shows evident discoloration characteristic of 'rusting'.

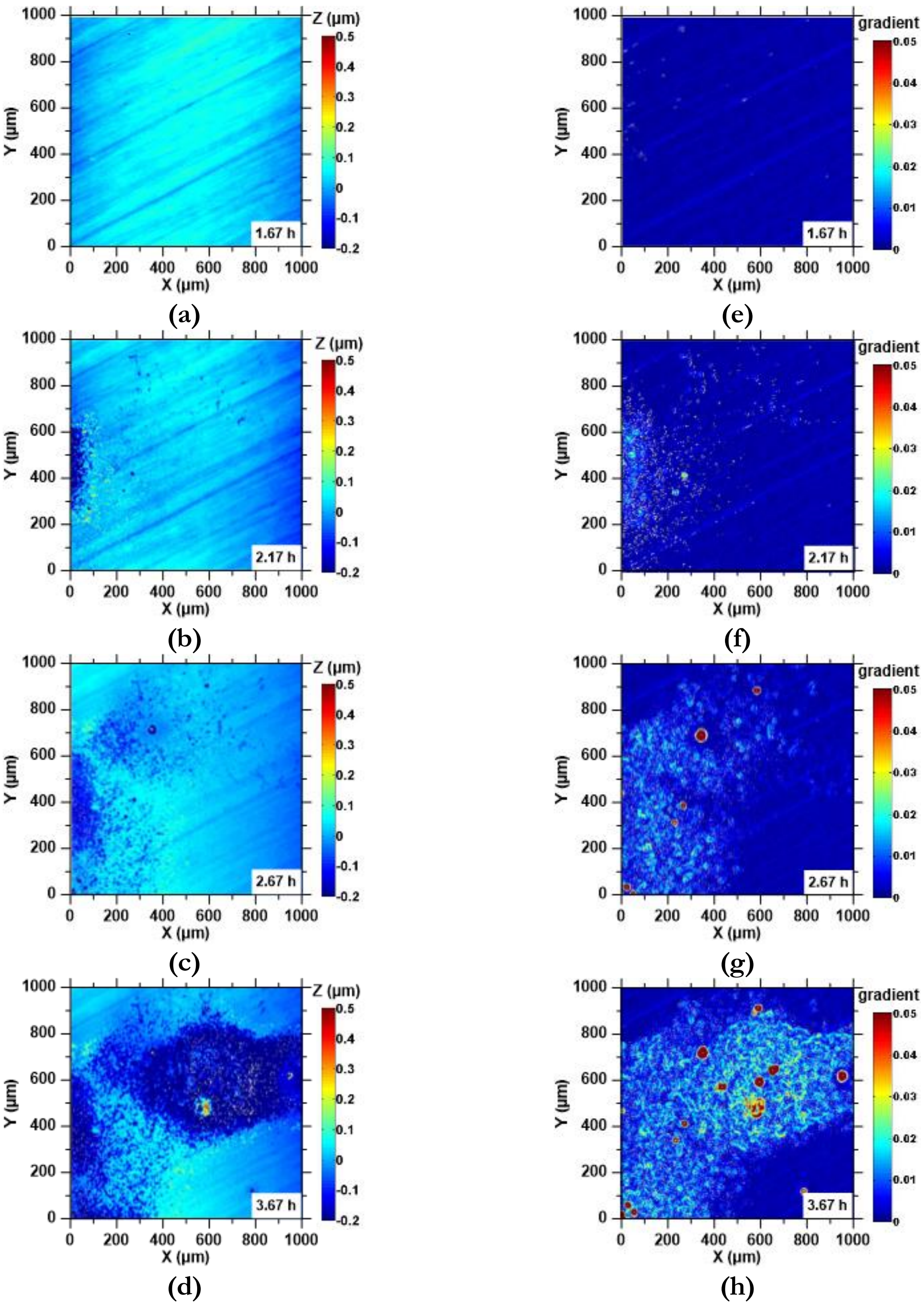

Figure 8.42 Representative illustrations of the height evolution of the steel surface following exposure to DI water after **(a)** 1.67 h, **(b)** 2.17 h, **(c)** 2.67 h, and **(d)** 3.67 h. The corresponding gradient maps are shown in: **(e)** to **(h)**, respectively. Pitting sites were not evident until t = 1.67 h, as shown in **(a)** and **(e)**. After this time, pits nucleate as shown in **(b, f)**, and then continue to grow with concurrent surface roughening **(c, d, g, h)**. New pits formed around initially stabilized pits that are often isolated as evident in **(c)** and **(g)**.

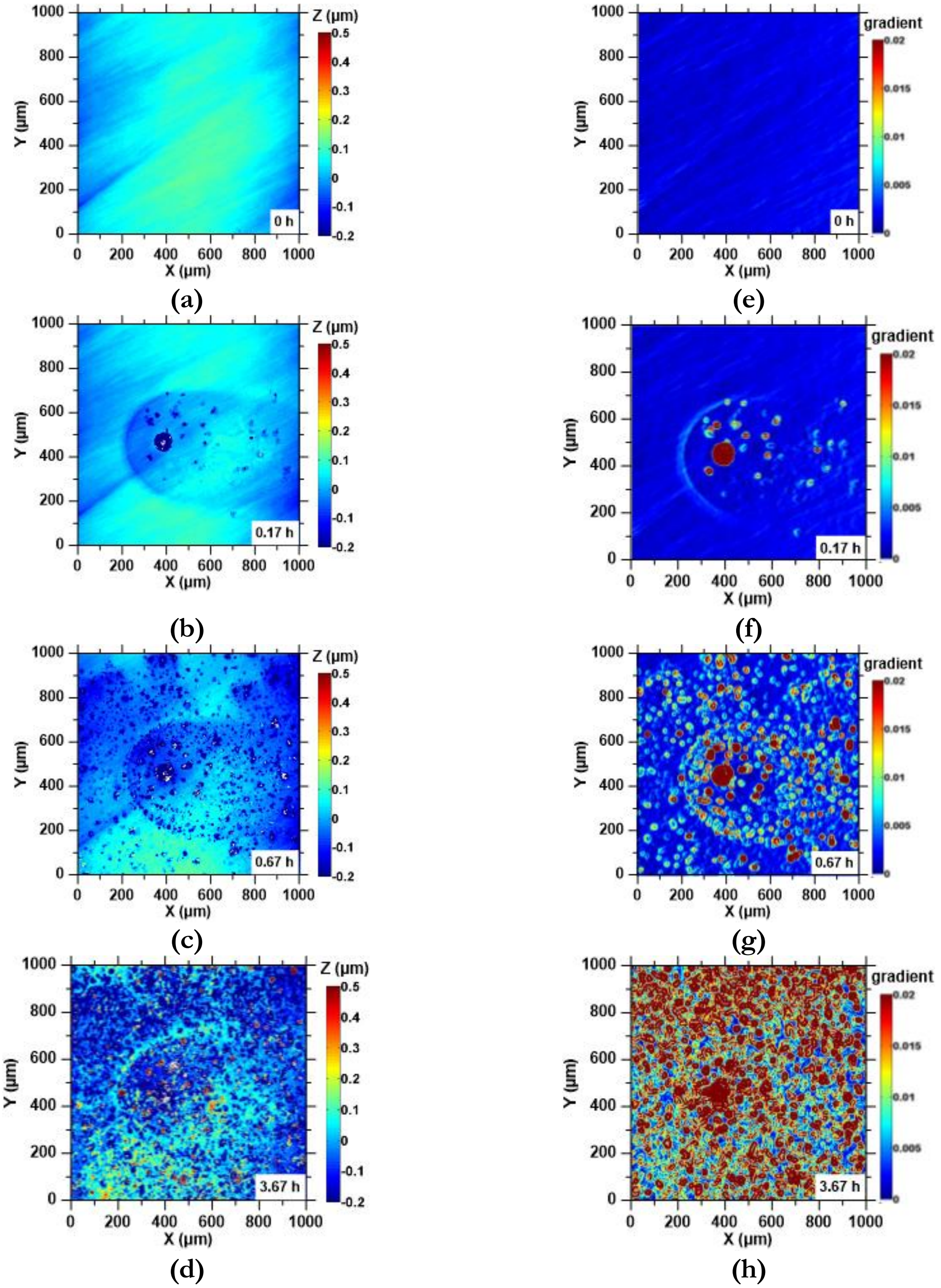

(a) (e)

(b) (f)

(c) (g)

(d) (h)

Figure 8.43 Representative illustrations of the height evolution of the steel surface following exposure to 100 mM NaCl for: **(a)** 0 h, **(b)** 0.17 h, **(c)** 0.67 h, and **(d)** 3.67 h. The corresponding gradient maps are shown in **(e)** to **(h)**, respectively. The end of the "dormant period" is marked by the development of circular basins around an initially formed isolated pit **(b, f)**. Significant pit nucleation and growth are observed within these basins initially, after which pit formation proceeds near-uniformly across the entire surface **(d, h)**.

Corrosion dynamics remain broadly unchanged in steel exposed to 100 mM NaCl solution, as shown in Figure 8.43. Expectedly, corrosion proceeds much faster in the presence of aqueous Cl^- with a considerable shortening in the time to pit nucleation, basin formation, and pit (and basin) growth. For example, within 0.17 hours of exposure, distinct circular basins with depths on the order of 100-to-200 nm are observed around the initially formed isolated pits (see Figure 5b), indicative of local section loss ("thinning").[200] Circular basins of a similar morphology have been previously observed in mild (low-carbon) steels exposed to Cl^--containing alkaline solutions.[266], [267] Once again, new pits nucleate within these basins (Figures 8.10b, 8.10f), and in addition, homogeneous pitting is observed outside the basin regions after longer periods of Cl^- exposure (Figures 8.10c, 8.10g). This nature of near-uniform surface pitting was not observed with DI water even after 10 hours of exposure although it is possible that such uniform pitting may indeed emerge after DI water exposure for greatly extended time periods. Consequently, and in time, the corroded steel surface consisted of overlapping (coalescent) basins that can be several hundreds of microns in diameter and ranging from 10s-to-100s of nanometers in depth (see Figure 8.42d and Figure 8.44) over the time-scales as examined in this study.

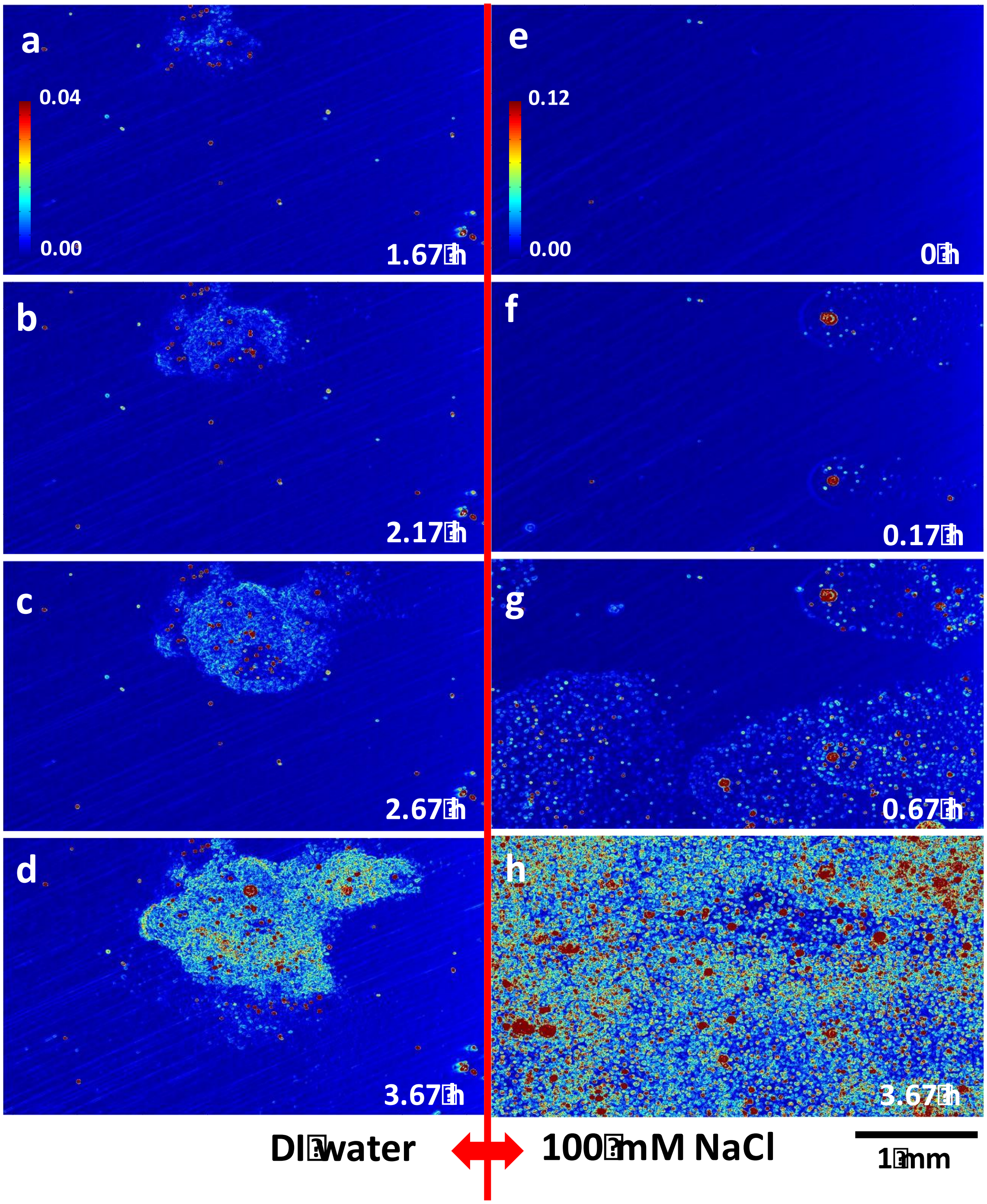

Figure 8.44 Gradient maps of corroding 1045 steel surfaces showing circular basins formed in **(a-d)** deionized water, and **(e-h)** 100 mM NaCl solution. These roughened circular basins are depassivated regions in which pits preferentially nucleate. As corrosion proceeded, the basins expand and eventually coalesce covering the entire FOV, and in time, the sample surface.

8.3.2. Identifying the Different Stages in Pit Nucleation and Growth

The evolution of pitting was assessed by quantifying pitting parameters including the: (i) pit density (i.e., the total number of pits per unit area) which includes identification of transient pits, those that may be masked due to deposition of corrosion products, and newly formed and growing pits (Figure 12), (ii) average depth and radius of pits present in the field-of-view (see Figures 8.13a, 8.13b), and, (iii) average pit aspect ratio (see Figures 8.13c, 8.13d).

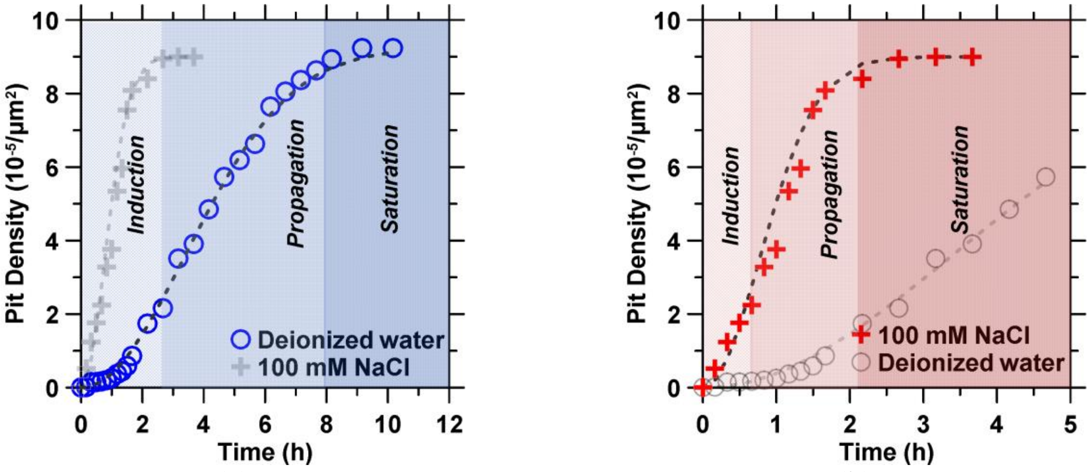

(a) (b)

Figure 8.45 The pit density for steel surfaces reacting with: **(a)** DI water, and **(b)** 100 mM NaCl solution as a function of time. The respective best-fit curves obtained by fitting a modified second-order Avrami equation are shown by dashed lines. The shaded regions indicate the periods of induction, propagation, and saturation of pitting corrosion.

Analysis of the pit parameters reveals three distinct stages of corrosion: (1) an *induction* (or dormant) period when the surface undergoes negligible topographical changes, (2) a *propagation* period that is characterized by a rapid increase in the pit density, and (3) a *saturation* period wherein the rate of pitting shows an asymptotic plateau (see Figure 8.45).[200], [242], [268] The time evolution of the pit density data which suggests the susceptibility for pit nucleation and corrosion rates,[269] can be described by a modified Avrami equation which is representative of a two-dimensional nucleation and growth process,[270] as given by $N = b\left(1 - e^{-at^2}\right)$, where N and t are the pit density and time, and *a* and *b* are fitting parameters, respectively (Table 1). The maximum rate of increase in the (areal) density of pitting sites, r_{max}, can be written as: $r_{max} = \sqrt{\frac{2a}{e}}b$. The times denoting the end of the induction and propagation periods, t_{ind} and t_{prop}, respectively, are obtained by determining the saddle points from the third derivative of the 2D-Avrami equation (see Figure 8.45 and Table 8.1).

Table 8.1 The best-fit parameters of the modified second-order Avrami equation that was fitted to the pit density data shown in Figure 6.

Solutions	Parameters					
	a^* (/h^2)	**b^{**} (-)**	**R^2**	**r_{max} §(/h)**	**t_{ind} † (h)**	**t_{prop} ‡ (h)**
Deionized water	0.043	923.32	1.00	164.24	2.53	7.96
100 mM NaCl	0.670	899.60	0.99	631.65	0.64	2.02

*, ** fitting parameters
§ maximum rate of increase in the pit density
† time at the end of induction period
‡ time at the end of propagation period

The periods of induction, propagation, and saturation determined from the pit density evolution also delineate the evolution of the pit geometry as shown in Figure 8.46. For instance, the beginning of the induction period in DI water is characterized by a stable average pit depth and radius, and thus, aspect ratio (Figures 8.13a, 8.13c). Later, during the propagation and saturation periods, the pit depth increases continuously, whereas the pit radius remained largely constant – suggesting the deepening of existing pits, without the nucleation of any new ones. A marked contrast with the 100 mM NaCl solution was observed. Therein, the average pit depth increased steadily in both induction and saturation periods (Figure 8.46b). On the other hand, the average pit radius transitioned from being initially stable (induction), to decreasing progressively during propagation due to the continual emergence of new and smaller pits (e.g., see Figures 8.10d, 8.10h) achieving a stable value in the saturation regime. Indeed, the propagation period is characterized by the rapid nucleation of small and shallow pits, resulting in a constant average pit depth despite the deepening of existing pits. It has been proposed that pits initiate and become stable when they exceed a critical dimension, i.e., wherein local potential gradients are maintained.[75] In support of this idea, for example, in both DI water and 100 mM NaCl solutions, the critical radius of pits having depths distinguishable from the surface roughness is around 4 μm. In addition to the pitting parameters, the root means square (RMS) surface roughness of the non-pitted regions also increased with time (see Figure 8.47). Thus, in contrast to the pit density (see Figure 8.45), a final saturation period was not observed for either pit depths or surface roughness indicating the persistence of corrosion reactions as shown in Figure 8.46 and Figure 8.47.

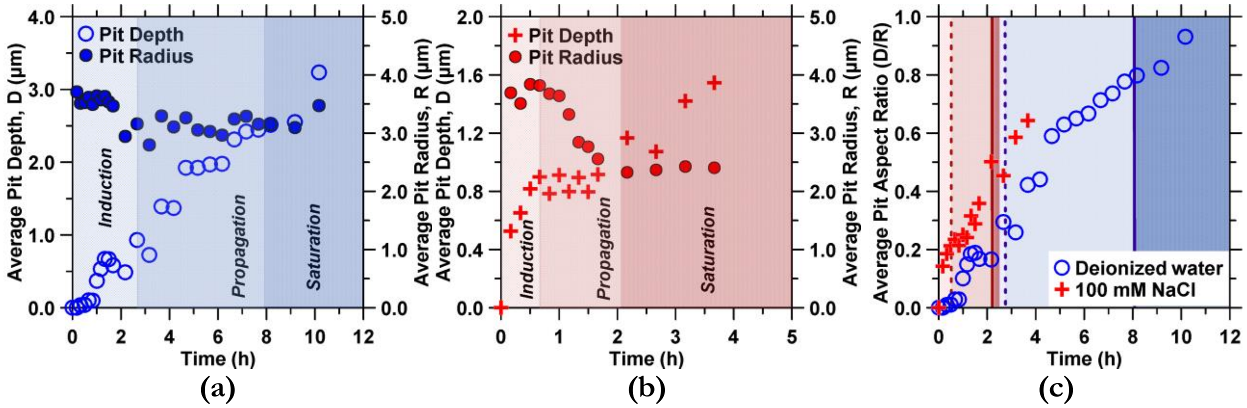

Figure 8.46 The evolution of the pit geometry following exposure to (a) DI water and (b) 100 mM NaCl solution. The average depths, D (open circles in (a), red crosses in (b)) and radii, R (closed circles in (a) and (b)) are plotted on the primary and secondary y-axis, respectively. (c) The average pit aspect ratios (i.e., AR = pit depth/pit radius, or D/R, unitless) are also given for DI water and 100 mM NaCl solutions. The shaded regions indicate the periods of induction, propagation, and saturation. The dashed and solid lines in (c) indicate the end of the induction and propagation periods, respectively, in both DI water and 100 mM NaCl.

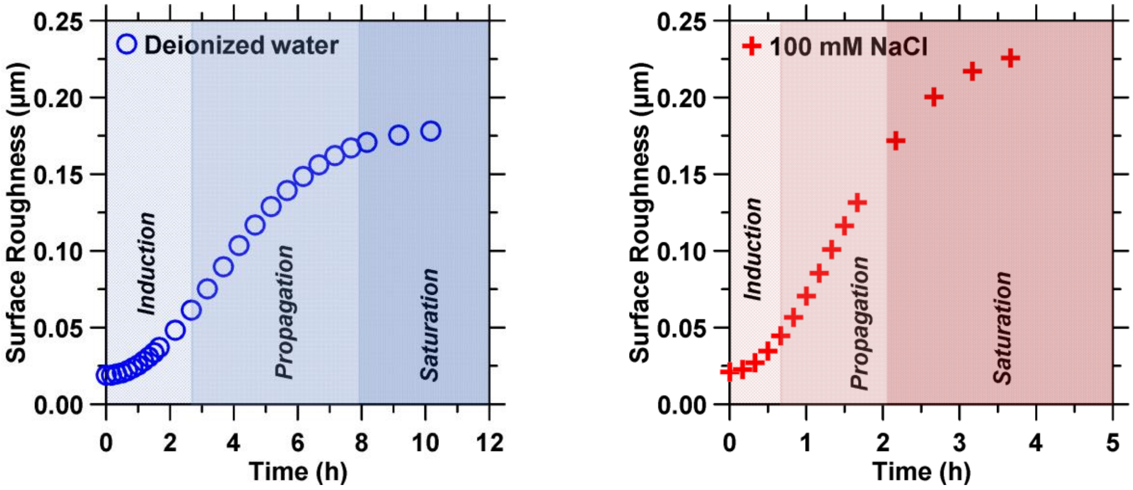

(a) **(b)**

Figure 8.47 The RMS surface roughness evolution in non-pitting zones as a function of time in AISI 1045 steel reacted with **(a)** DI water and **(b)** 100 mM NaCl solution. The shaded regions indicate the periods of induction, propagation, and saturation.

8.4 New Insights into Pitting Corrosion and its Morphological Evolutions

From the discussion above, it is clear that pitting corrosion of AISI 1045 steel is highly heterogeneous (Figures 8.9-8.10), and proceeds in multiple steps (see Figure 8.45). During the induction period, the formation of pits (i.e., *induction pits*) and the associated increase in surface roughness evolve slowly. The induction period in steel corrosion is widely thought to result from the presence of a passivation layer that is presumed to be composed of iron oxides having a thickness of ≤ 20 nm.[200], [221], [251], [253], [254], [271] It is important to highlight that induction pits catalyze corrosion in their vicinity, leading to the formation of roughened shallow basins with an RMS roughness that is around a factor of 10 higher than the passivated regions (Figures 8.9c, 8.10b). On account of their substantial depth (> 100 nm), these basin regions are expected to be depassivated since the surface retreat in these zones is much larger than the typical thickness of a passivated oxide layer. Hence, the formation of these basins clearly marks passivity breakdown; a process that precedes and is distinct from pitting itself.[200] The presence of a potential difference, i.e., from the bottom of a pit, to the surface of the circular basins, results in the deepening of propagation pits and sustained corrosion via a roughening-pitting process. In contrast, the area outside these basin regions exhibits limited pitting, particularly in the case of DI water, and at small exposure times, even in the presence of chloride ions.

Cl^- ions significantly accelerate steel corrosion,[230]–[232] as manifested by the following: (a) an enhanced tendency for roughened depassivated basins to develop, (b) nucleation of pits within, as well as outside the depassivated basin regions, and, (c) aggressive autocatalytic pitting corrosion. These observations can be understood by consideration of the two distinct processes discussed above: the breakdown of the passivation film, and pit nucleation and growth. Numerous studies have suggested that passivity loss in the presence of Cl^- ions occur via mechanisms including (1) penetration,[175] (2) adsorption,[209], [232] and (3) film breakdown.[235], [236] As such, local thinning which results in the formation of depassivated basin regions is observed both in the presence or absence of Cl^-, but it is substantially accelerated when Cl^- ions are present.[230] The heightened adsorption of Cl^- in localized domains is expected to cause local dissolution and thinning by producing ionic point defects and regions of high local current density. This is consistent with the shortened induction period that is observed when Cl^- ions are introduced as compared to DI water. On the other hand, the penetration of Cl^- into the oxide film would result in a contaminated film, which has a higher ionic conductivity than the pristine film. The observation of pit nucleation outside the locally thinned depassivated basin regions supports the hypothesis that the penetration of Cl^- ions are another, but the less important mechanism by which pitting occurs. This is based on the observation that, initially, the pit density outside the depassivated basins is far lower, than within the basin regions. It should be noted that uniformly distributed pitting occurred only at later times, consistent with an initial period of minimal corrosion in these regions. This implies a characteristic time that is associated with the penetration of the passivation layer by Cl^- species to a critical depth, as a function of the local solution and solid (passive film) thickness and composition. Finally, we did not observe an explicit film-rupture/peeling mechanism which is also expected to be a precursor to the onset of pitting corrosion. However, since this mechanism implies a dependence on grain or scratch geometry, i.e., where the film may undergo continuous breakage and repair, and potential inhibition of repassivation due to the adsorption of Cl^- species, more detailed investigations of alloy microstructure and measurements of localized pit nucleation rates are necessary to better understand the role of film rupture, if any, on passivity breakdown.

The origin of the induction pits whose formation marks localized passivation breakdown, merits further consideration. For example, induction pits are expected to arise at defect sites, e.g., near-surface voids or embedded secondary-phase particles, which are weakly passivated or thermodynamically unstable (vis-à-vis the bulk alloy), [209], [230], [200] and therefore can serve as nucleation sites for pit formation, once depassivated. Indeed, our SEM-EDS analysis reveals that induction pits typically feature high concentrations of sulfur and manganese, whose abundances generally decrease as the pits grow (e.g., see Figure 8.48). This observation supports the idea that pits may originate – although not exclusively – from the dissolution of manganese sulfide (MnS) inclusions which form in steel during quenching. [272] These inclusions which display a high chemical affinity for oxygen and water, can rapidly solubilize, leaving behind pits that grow to be greater than 20 μm in diameter. [273] More problematically, halide/Cl^- ions are known to preferentially adsorb at such inclusion sites. [274]

In general, it is observed that after passivity is lost at the end of the induction period, pitting dramatically accelerates. It is important to note that the propagation pits tend to deepen despite the accumulation of corrosion products on the surface (see Figure 8.40b). This implies that the rate of formation of corrosion products or salt films [275] in the vicinity of, or within the pits may be important in controlling their growth; especially when pit growth occurs under diffusion control.

[200], [276]–[280] In general, the microenvironment within the pit is characterized by low pH (<2) and high ionic concentrations, particularly Cl$^-$, which facilitate corrosion by encouraging the dissolution of Fe, [276] improving charge transfer and increasing the (apparent) solubility of Fe^{2+} due to its complexation with Cl$^-$ which promotes corrosion. [281]–[283] In water, the anodic reaction is given by $Fe \rightarrow Fe^{2+} + 2e^-$, which generally occurs within the pits, whereas the cathodic reactions are given by: $2H_2O + 2e^- \rightarrow H_2 + 2(OH^-)$, which occurs in weakly acidic and neutral solutions, and $\frac{1}{2}O_2 + H_2O + 2e^- \rightarrow 2(OH^-)$, which is limited by oxygen diffusion, and which may not occur within the pit. Expectedly, local acidification in the microenvironment arises from chemical, electropotential, and geometrical gradients within and around the pit sites. [75]

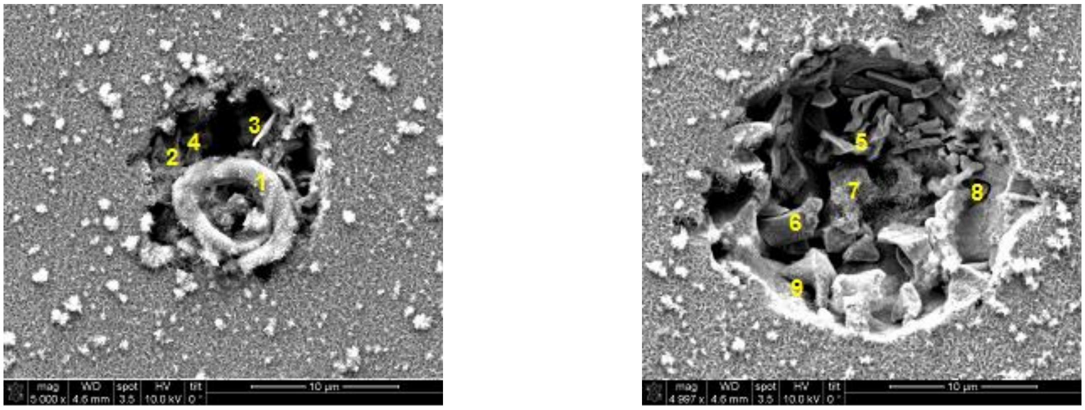

(a) **(b)**

Figure 8.48 SEM micrographs of a representative induction pit on AISI 1045 steel reacting with 100 mM NaCl for: (a) 0.08 h, and (b) 3.3 h, showing radial expansion with time. In (a), sample areas labeled 1 to 4 have the following Mn and S contents: 0.12%, 2.31%, 22.12%, and 17.28%, and 0.04%, 0.15%, 0.10%, and 0%, respectively, as measured by SEM-EDS (in mass %). At longer reaction times, in (b), sample areas labeled 5 to 9 have the following Mn and S contents: 2.23%, 5.01%, 2.80%, 2.75%, and 1.29%, and 0.08%, 0.14%, 0.01%, 0.22%, and 0.01%, respectively (in mass %). The relatively high concentrations of Mn and S are consistent with the presence of a MnS inclusion at this pitting site.

The high concentrations of Fe^{2+} cations in dissolution zones result in the migration of Cl$^-$ ions towards the anodic region in the bottom of the pit to maintain electrical neutrality. This promotes acidification within the pits, [284] for example via reactions including but not restricted to: $FeCl_2 + 2H_2O \rightarrow Fe(OH)_2 + 2HCl$ and $2Fe(OH)_2 + 2H_2O \rightarrow 2Fe(OH)_3 + 2H^+ + 2e^-$. Therefore, as corrosion within a pit progresses, the pH decreases locally, and the cathodic proton reduction reaction occurs: $2H^+ + 2e^- \rightarrow H_2$. The net corrosion process within the pit can then be described by:$Fe + 2H^+ \rightarrow Fe^{2+} + H_2$. It is important to note that the complexation of Fe^{2+} with Cl^- may enhance the transport of the former away from the pits, so that corrosion continues. The decrease in pH promotes the migration of Cl^- ions into the pit, [262] giving rise to an autocatalytic process that continues so long as Fe dissolution is sustained. In addition, the formation and breakdown of passive films can be described by the following equations: $Fe + H_2O \rightarrow Fe_2O_3 + 3H_2$, which describes film formation, and $Fe_2O_3 + 6H^+ \rightarrow 2Fe^{3+} + 3H_2O$, which describes film dissolution. Thus, high Cl^- concentrations and low(er) pH levels would inhibit film formation as also predicted from Pourbaix diagrams. [285], [286] The presence of pit occlusions limits the transport of reaction products to the solution, consequently maintaining the highly aggressive environment within the pit, and furthering dissolution so long as a supply of oxygen is maintained. [77], [200] Therefore, in addition to accelerating the loss of passivation, Cl^- enhances corrosion by sustaining autocatalytic pitting by maintaining acidity and preventing repassivation. Notably, it has been shown from cyclic polarization measurements that at $[Cl^-]/[OH^-] > 1$, and across a range of concentrations of $[Cl^-]$, passivity cannot be maintained, and that localized corrosion is eventually replaced by active general corrosion. [266] This is only aided by the fact that as Fe-hydroxide precipitates near the alloy surface, the local $[Cl^-]/[OH^-]$ further increases due to the local depletion of $[OH^-]$ species, further enhancing corrosion rates.[287]

8.5 Summary and Conclusions

The corrosion of AISI 1045 steel in DI water and 100 mM NaCl solutions was elucidated by direct, nanoscale observations of reacting surface topographies using vertical scanning interferometry (VSI). Our findings highlight that corrosion is a heterogeneous process that is preceded by film breakdown and then proceeds by pitting, whose progress can be characterized by three stages, namely, induction, propagation, and saturation, based on the rates of pit nucleation and growth. It is highlighted that induction pits form at sites that are likely occupied by MnS (or another secondary phase) inclusions or at surface defects. The formation of these pits destabilizes the passive film due to processes including dissolution, and when Cl^- ions are present by the heightened adsorption, and penetration of Cl^- species. These processes cause surface roughening and the formation of shallow basins in the vicinity of the pit, resulting in local thinning, and eventually loss of the passive film. Initially, the depassivated region is occupied by shallow pits, which are indistinguishable from surface roughness. These shallow pits may either repassivate (i.e., transient pits) or continue to grow (propagation pits). If the pit grows up to a critical value herein identified to be an effective 'circular' radius on the order of 4 μm, repassivation will not occur, and the pit would continue to grow in depth. Eventually, the pit density reaches a maximum and saturates as most of the alloy surface becomes covered with pits. Significantly, pitting is observed to be autocatalytic, i.e., although a saturation in pit density is observed, pit depths continued to increase over time. This autocatalytic nature of pitting is ensured by the maintenance of aggressive local pit microenvironments. Although similar to DI water exposure in a broad sense, the addition of NaCl substantially accelerated pitting corrosion by reducing the induction time and by increasing the rate of pit nucleation and growth. Taken together, these results indicate that Cl^- ions enhance corrosion by promoting the breakdown of protective oxide films that are expected to be present on steel surfaces, and by assisting in maintaining aggressive pitting microenvironments due to processes including Cl^- adsorption (primary) and penetration (secondary). The outcomes of this study provide direct evidence that pitting is the dominant form of corrosion in 1045 steel, and is fundamental to the onset and progression of such degradation. Importantly, we demonstrate how detailed surface morphology characterization and quantifications from VSI imaging can provide new insights into better understanding electrochemical processes such as corrosion, and carefully examining potential mechanisms (e.g., film breakdown, Cl^- adsorption and penetration, etc.) which control the time-dependent evolution of such deleterious reactions.

9. Summary and Conclusions

9.1 Summary of the Thesis

The objective of this research was to improve the sustainability of reinforced concrete. Cement and steel rebar has been taken into consideration because 1) the reactivity of *belite* can be potentially improved via doping method and 2) the chloride-induced pitting corrosion is widely existing and need efforts in understanding the initiation and propagation process. For cement research, DFT simulation method has been applied to investigate the properties of C_2S polymorphs and doping effects in β- C_2S; for steel corrosion research, VSI has been applied to observe the pitting initiation and evolution process over time at the nanoscale and both chloride-free and chloride-containing environments have been considered. Here is the detail work has been conducted.

Cement Research

For pure C_2S simulation, γ-, β- and α'_L-C_2S polymorphs have been investigated with the following propertied calculated:

- The crystal structures of three polymorphs have been fully relaxed with high accuracy parameter setting-up
- Lattice parameters, bond lengths, bond angles, as well as unit cell volumes of the three polymorphs have been compared to reported experimental/computational data
- Mechanical properties of three polymorphs have been calculated using stress-strain calculation method, with the mechanical coefficient matrix, Young's modulus, bulk modulus, indentation modulus, Poisson's ratio calculated and compared to reported data
- Formation enthalpy of three polymorphs has been calculated

- 3-dimensional charge distribution as well as charge distribution along atomic bonds have been calculated and analyzed
- Density of States (DOS) of three polymorphs have been calculated
- Conduction band minimum (CBM) and valence band maximum (VBM) have been calculated

Doping effect with several commonly existing foreign ions has been investigated on the β-C_2S crystal structure which is the primary phase of *belite*. Firstly, Mg^{2+}, Al^{3+}, and B^{3+} have been considered to study the potential of instability from an electronic scale point of view.

- Mg^{2+}, Al^{3+}, and B^{3+} have been doped into β- C_2S and investigate the crystal structure property change for the searching of most reactive structure;
- Doped structure have been relaxed to configure the final crystal structures, and the lattice parameters have been determined
- Linear charge density along dopant-oxygen-silicon/dopant has been calculated to justify the bond-forming preferences
- The formation enthalpy as a function of doping concentration has been calculated to determine the optimal dopant(s)

A series of dopants, namely Na^{+}, K^{+}, Mg^{2+}, Sr^{2+}, Al^{3+} , Fe^{3+}, B^{3+}, and Ge^{4+} have been doped into β-C_2S for the particular purpose of checking ionic size misfit effect.

- Intrinsic vacancy formation energy on Ca1/2 and Si sites have been calculated
- Preferential doping geometries for all 8 dopants have been determined according to defect formation enthalpy
- Defect formation enthalpy with respect to ionic size misfit has been determined

- Stability of doped structure with respect to doping concentration for all 8 foreign ions have been calculated

  Steel Research

Pitting corrosion on AISI 1045 steel surface have been studied.

- Pitting initiation and propagation processes of AISI 1045 steel have been for the first time studied using VSI to reveal the nature of nanoscale;
- Investigated items include pit density, average pith depth, aspect ratio of pits, and surface height change distribution;
- Both chloride-free and chloride-containing (100 mM) conditions have been studied

9.2 Conclusions

The following conclusions are drawn from the analysis and results in previous chapters.

1. For the C_2S study, the simulated lattice parameters for γ-, β- and α'_L-C_2S agree well with experimental data. Si-O tetrahedral in the three C_2S phase are the same and the difference of derives from the configuration of Si-O tetrahedral and Ca-O polyhedral.
2. Judging from the (partial) density of states for γ-, β- and α'_L-C_2S, the chemical reactivity could be ranked in the sequence of α'_L- > β- > γ- C_2S, and this result agrees with experiments and other simulation work. The simulated Young's modules indicate the mechanical property ranks in the order of α'_L- > γ- > β-C_2S.
3. B^{3+}, Al^{3+}, and Mg^{2+} ions have been doped into β-C_2S. In this doping, a Mg^{2+} ion replaces a Ca^{2+} ion; two B^{3+}/Al^{3+} ions replacing a Ca^{2+} ion and a Si^{4+} ion to balance the charge. With this doping approach, the same mass concentration B reduces the formation enthalpy the

least, following by Al. This indicated B doped structure has the highest enthalpy and potentially the most reactive one, and this conclusion agrees with the experimental result.

4. B^{3+}, Al^{3+}, and Mg^{2+} ions have been doped to Si and Ca sites. The calculating from the defect formation enthalpy, the coordination number of B^{3+}, Al^{3+}, and Mg^{2+} are 4, 5, and 7 respectively. It proves that the stability of introduced defects in β-C_2S strongly correlates to the ionic size difference between foreign ions and the original ions.
5. Ca1 site and Ca2 site are of 8- and 7- coordinated with oxygen atoms, respectively. By checking the vacancy formation enthalpy, it is found Ca2 site needs less energy to form vacancy defect than the Ca1 site. This proves that if a dopant would go to a Ca site then the Ca2 site will be optimal.
6. Telling from the substitution defect formation enthalpy over Na^+, K^+, Mg^{2+}, Sr^{2+}, Al^{3+} , Fe^{3+}, B^{3+}, and Ge^{4+} dopants, it is found that Na^+, K^+, Mg^{2+}, and Sr^{2+} ions prefer Ca2 site while Al^{3+} , Fe^{3+}, B^{3+}, and Ge^{4+} ions will be more stable at Si sites.
7. Over checking the ionic size misfit effect with the 8 dopants, the primary factor determining the substitution preference turns out to be ionic size mismatch. The smaller the ionic radii difference between a dopant and the ion being replaced, the more stable the substitution defect will be.
8. In order to use the calculated results to guide industrial production, doping concentration effect as a function of stability has been checked. At the same doping concentration (oxide mass%), the instability of doped structure is ranking in sequence of $Mg^{2+} > Al^{3+} > Fe^{3+} > (B^{3+} \approx Na^+) > K^+ > Sr^{2+}$. Ge^{4+} is found to have negative formation enthalpy when substituting Si atoms indicating this is a strong endothermal process. As a result, the Ge^{4+} doped structure is more stable than original β-C_2S structure.

9. For 1045 steel pitting corrosion study, observing from the pit density, average pit depth, as well as surface height change frequency distribution data, 100 mM NaCl accelerates pitting corrosion significantly with respect of pitting initiation time, pit density and pit depth quantity.
10. The pit density data follows second order parabolic fitting trend. The pitting evolution process consists of induction, propagation, and saturation periods. This is different from the results with electrochemical study methods such as characteristic pitting current, where pitting evolution process is considered including only initiation and propagation process. The difference results from the merging of pits in the later period.
11. Once pits initiate, they remove the passivation layer around them and encourage more pits forming within the depassivated zone until pits spread all over the metal surface.
12. In this study, adsorption mechanism is the dominated type to break down passivation state and penetration, as well as film breakdown mechanisms, are less important.

Cement and steel rebar are two of the most significant materials influencing the sustainability of reinforced concrete structure. Based on the conclusions, the sustainability of reinforced concrete can be potentially improved following the findings in this thesis.

Firstly, the "green" cement has been designed with the basic idea improving the reactivity of *belite*. Since it is difficult to design crystal using experimental method, simulation method has been applied to provide theoretical guidance. The simulation has been conducted obeying the energy minimization rule (lowest formation enthalpy) to obtain the most reliable *belite* structures. Especially, the ionic misfit effect has been developed for unknown doping struct

ure prediction, which fills the gap of doped *belite* structure design. Potential future work with the present knowledge includes 1) simulation work of other dopants to find optimized structure(s), 2) synthesis the optimal crystal structure(s) as simulated, 3) try out the reactivity of the structure(s) as well as 4) the strength testing of such hydrated cement.

The study of pitting corrosion of steel aims at providing scientific evidence to help the design of corrosion prevention. The pitting nucleation and propagation process has attracted a lot of research efforts but with limited understanding. In this work, the pitting corrosion has been studied 1) without external applications, e.g., applied potential so the corrosion process occurs of its nature, and 2) of both high resolution and sufficient field of view to give both accurate and statistic results. On knowing the pitting evolution process and the role chloride ions play, future work could be conducted to design corrosion-protecting research, including factors of pH, chloride ion concentration, protective ions such as nitrate, and so on.

Appendices

MATLAB code for VSI 3D image data analysis

Code 1: Document Format Covert (for Windows Operating System)

Python Code

```
def tic():
   #Homemade version of matlab tic and toc functions
   import time
   global startTime_for_tictoc
   startTime_for_tictoc = time.time()

def toc():
   import time
   if 'startTime_for_tictoc' in globals():
      print ("Elapsed time is"  + str(time.time() - startTime_for_tictoc) + " seconds.")
   else:
      print ("Toc: start time not set")


def process_xyz(filename):
          tic()
          f=open(filename,'r')
          for i in range(0,7):
                    f.readline()

          l=f.readline().split()
          resol=l[6]
          print(resol)
          l=f.readline().split()
          while(l[0]!='#'):
                    l=f.readline().split()
          wfilename='processed_'+filename
          w=open(wfilename,'w')
          while(1):
                    l=f.readline().split()
                    if not l:
                              break
                    if(len(l)==4):
                              w.write(l[0]+' '+l[1]+' NaN\n')
                    elif(len(l)==3):
                              w.write(' '.join(str(x) for x in l)+'\n')
          f.close()
          w.close()
          toc()
```

```
name=['t','t','t']
# name is the time moment when 3D image data is aquired
for n in name:
        filename='t'+n+'.xyz'
        print(filename)
        process_xyz(filename)
```

MATLAB Code

```
clc; clear all;
t=[20 30:30:120 180:60:720];
% time when 3D images are captured
fname=cell(1,length(t));
for k=1:length(t)
    tic;
     fname{k}=['pos1_t',num2str(t(k)),'.xyz']

    temp=fname{k};
    fd=fopen(temp);
    for n=1:7
    fgetl(fd);
    end
    line8=textscan(fgetl(fd),'%f');
    resol=line8{1}(7);

    frewind(fd);
    coor=textscan(fd,'%f%f%s%s','HeaderLines',14);

    fclose(fd);
    ff=coor{3};
    ff=strrep(ff,'No','999999');
    l=length(ff);
    fff=zeros(l,1);
    for m=1:l
       fff(m,1)=str2num(ff{m});
    end

    data=[coor{1},coor{2},fff];

    data(data==999999)=NaN;
    x=data(:,1)*resol*1e6;
    y=data(:,2)*resol*1e6;
    z=data(:,3);

    nx=max(data(:,2)+1);
    ny=max(data(:,1)+1);
    X=reshape(x,ny,nx)';
    Y=reshape(y,ny,nx)';
```

```
    Z=reshape(z,ny,nx)';
    save(['t',num2str(t(k))], 'X','Y','Z','resol');
    toc;
end
```

Code 2: 3D Image Alignment and Rotation

```
clc; clear all;
close all;

fall=figure;
hold on;
view([0 1 0]);
axis square;
% daspect([ 1 1 1]);

t=[0 3]
alignt=zeros(2,2,length(t));
CCC=jet(length(t));
fname=cell(1,length(t));
for i =1:length(t)
    fname{i}=['t',num2str(t(i))];
    disp(fname{i});
load(fname{i});
nx=size(X,2);
ny=size(X,1);
f2=figure;
hold on;
mesh(X,Y,Z);
view([0 0 1]);
zoom=ginput(2);
xlim(sort(zoom(:,1)));
ylim(sort(zoom(:,2)));
% axis ratios
daspect([ 1 1 0.01]);
%colorbar;

title(['t',num2str(t(i))]);
% store two reference points coordinates into alignt matrix
alignt(:,:,i)=ginput(2);
figure(f2);
% show the selected two points on image
plot3(alignt(:,1,i),alignt(:,2,i),[0 0],'or')
title(['t',num2str(t(i))]);

xyAL=[reshape(X,[],1),reshape(Y,[],1)];

v1=alignt(2,:,1)-alignt(1,:,1);
vi=alignt(2,:,i)-alignt(1,:,i);

xyAL=xyAL-repmat(alignt(1,:,i)+alignt(1,:,1),size(xyAL,1),1);
cosv=vi*v1'/norm(vi)/norm(v1);
```

```
        fprintf('rotate by %5.1f degree\n',rad2deg(acos(cosv)));
        R=[cosv -(1-cosv^2); 1-cosv^2 cosv];
        xyAL=(R*[xyAL(:,1)';xyAL(:,2)'])';

        figure(fall);
        mesh(reshape(xyAL(:,1),nx,ny),reshape(xyAL(:,2),nx,ny),reshape(Z,nx,ny),'EdgeColor',CCC(i,:),'Face
Color','none');
        %colorbar;
        XAL=reshape(xyAL(:,1),ny,nx);
        YAL=reshape(xyAL(:,2),ny,nx);
        ZAL=Z;
        save([fname{i},'AL'], 'XAL','YAL','ZAL');
        end
        save(['alignmat',num2str(t(2)),'to',num2str(t(end))],'alignt','t');

        figure(fall);
        legend(fname);
```

Code 3: Pit Identification

```
        clear,clc;

        grdpit=0.999; % percent
        t=[0 3 6 12 24 48 72 96 120 144 168];
        fname=cell(1,length(t));
        for k =1:length(t)
            tic;
            fname{k}=['t',num2str(t(k))];
            % disp(fname{i});
            load(fname{k});

            nx=size(Z,2);
            ny=size(Z,1);
            idnan=isnan(Z);

Z=reshape(griddata(X(~idnan),Y(~idnan),Z(~idnan),reshape(X,[],1),reshape(Y,[],1),'natural'),ny,nx);

            if k==1
                idx=3600:size(Z,2)-100;
                idy=100:size(Z,1)-100;

                figure;
                surf(Z,'EdgeColor','none','FaceAlpha',0.4)
                view([0 0 1]);
                hold on;
                surf(idx,idy,Z(idy,idx),'LineStyle','none')
            end

            nsmooth=5;
            h=fspecial('disk',nsmooth);
```

```
Zs=filter2(h,Z(idy,idx));
Zs=Zs(nsmooth+1:end-nsmooth,nsmooth+1:end-nsmooth);
Xs=X(idy,idx);
Xs=Xs(nsmooth+1:end-nsmooth,nsmooth+1:end-nsmooth);
Ys=Y(idy,idx);
Ys=Ys(nsmooth+1:end-nsmooth,nsmooth+1:end-nsmooth);
coors=[reshape(Xs,[],1),reshape(Ys,[],1),reshape(Zs,[],1)];
indall=1:size(Xs,1)*size(Xs,2);

[FX,FY]=gradient(Zs,Xs(1,2)-Xs(1,1),Ys(2,1)-Ys(1,1));
FF=sqrt(FX.^2+FY.^2);
grd=reshape(FF,1,[]);
bins=linspace(min(grd),max(grd),100);
freq=histc(grd,bins);
[MX,ind]=max(freq);
[~,Ihm]=find(freq<MX*(1-grdpit),1,'first');
FFm=(bins(Ihm)+bins(Ihm+1))/2;

figure;
semilogy(bins,freq)
hold on;
yplot=ylim;
line([FFm,FFm],yplot,'Color','r')

ispitg=FF>FFm;
coorsp=[Xs(ispitg),Ys(ispitg),zeros(length(Xs(ispitg)),1)];
tempind=reshape(indall,size(Xs,1),size(Xs,2));
indpall=tempind(ispitg);
gID=group_nbr(coorsp,coorsp,(Xs(1,2)-Xs(1,1))*8);

figure;
surf(Xs,Ys,FF,'LineStyle','none')
caxis([0 FFm]);
view([0 0 -1])
whitebg('w')
title(fname{k})
hold on;

toc
tic;

pits=cell(max(gID),1);
for i=1:max(gID)
    if sum(gID==i)==1
        pits{i}=[];
    else
        tempcoorsp=coorsp(gID==i,1:2);
        temp=tempcoorsp(2:end,:)-repmat(tempcoorsp(1,:),size(tempcoorsp,1)-1,1);
        ptemp=cart2pol(temp(:,1),temp(:,2));
        if abs(sum(ptemp-ptemp(1)))<1e-5
            pits{i}=[];
        else
```

```
                indpp=indpall(gID==i);
                pits{i}=indpp(convhull(coorsp(gID==i,1:2)));
                ispitg(inpolygon(coors(:,1),coors(:,2),coors(pits{i},1),coors(pits{i},2)))=1;
%                   plot(coors(pits{i},1),coors(pits{i},2),'-ok','LineWidth',5);
%                   text(coors(pits{i}(1),1),coors(pits{i}(1),2),num2str(i),'FontSize',20,'FontWeight','bold');
            end
        end
    end
    pits(cellfun(@isempty,pits))=[];
%       plot(coors(ispitg,1),coors(ispitg,2),'ob','LineWidth',3);

    coorsp=[Xs(ispitg),Ys(ispitg),zeros(length(Xs(ispitg)),1)];
    tempind=reshape(indall,size(Xs,1),size(Xs,2));
    indpall=tempind(ispitg);
    gID_new=group_nbr(coorsp,coorsp,(Xs(1,2)-Xs(1,1))*10);
    while max(gID_new)~=max(gID)

        gID=gID_new;

        %       figure;
%           surf(Xs,Ys,FF,'LineStyle','none')
        caxis([0 FFm]);
        view([0 0 -1])
        whitebg('w')
        hold on;

        pits=cell(max(gID),1);
        for i=1:max(gID)
            if sum(gID==i)==1
                pits{i}=[];
            else
                tempcoorsp=coorsp(gID==i,1:2);
                temp=tempcoorsp(2:end,:)-repmat(tempcoorsp(1,:),size(tempcoorsp,1)-1,1);
                ptemp=cart2pol(temp(:,1),temp(:,2));
                if abs(sum(ptemp-ptemp(1)))<1e-5
                    pits{i}=[];
                else
                    indpp=indpall(gID==i);
                    pits{i}=indpp(convhull(coorsp(gID==i,1:2)));
                    ispitg(inpolygon(coors(:,1),coors(:,2),coors(pits{i},1),coors(pits{i},2)))=1;
%                       plot(coors(pits{i},1),coors(pits{i},2),'-ok','LineWidth',5);
                end
            end
        end
        pits(cellfun(@isempty,pits))=[];
%           plot(coors(ispitg,1),coors(ispitg,2),'ob','LineWidth',3);

        coorsp=[Xs(ispitg),Ys(ispitg),zeros(length(Xs(ispitg)),1)];
        tempind=reshape(indall,size(Xs,1),size(Xs,2));
        indpall=tempind(ispitg);
        gID_new=group_nbr(coorsp,coorsp,(Xs(1,2)-Xs(1,1))*10);
    end
```

```
        toc

    %           [polyx,polyy]=poly2cw(coorsp(pitedge,1),coorsp(pitedge,2));
    %           =indall(inpolygon(coors,coors,polyx,polyy))';
    %
%     figure;
%     mesh(Xs,Ys,FF,'FaceColor','none');
%     % quiver(Xs,Ys,FX,FY)
%     hold on;
%     plot3(Xs(ispitg),Ys(ispitg),FF(ispitg),'o')

    % save ([fname{i},'pit'],'pits');
    % save ([fname{i},'pixcoor'], 'Xs','Ys','Zs');

    fprintf('After %d minutes, there are %d pits\n ', t(k),length(pits));
    save ([fname{k},'pit'], 'Xs','Ys','Zs','FF','pits','ispitg');

end
```

Code 4: Pit Selection and Analysis

4.1 Pits Filter

```
%% delet pits that are smaller than a certain size
clc; clear;
LateralRes=1.63;
pixarea=LateralRes^2; % in square microns
limit=1;
min_pit=limit^2;
creteria= ceil(min_pit/pixarea);
t=[0 3 6 12 24:24:168];
nop_filter=zeros(length(t),2);
for k=1:length(t)
    tic;
    load(['t',num2str(t(k)),'pit']);
    nop=0;
    for i=1:length(pits)
        pitlength=length(cell2mat(pits(i)));
        if pitlength >= creteria
        nop=nop+1;
        end
    end
    fprintf('At %d minutes there are %d pits',t(k),nop);
    toc;
    nop_filter(k,1)=t(k);
    nop_filter(k,2)=nop;
%     save(['t',num2str(t(k)),'pit_filtered'],'nop')
    save('nopfiltered','nop_filter');
```

```
end
figure(); hold on;
 plot(nop_filter(:,1),nop_filter(:,2)-nop_filter(1,2),'-o');
[p,S]=polyfit(nop_filter(:,1),nop_filter(:,2)-nop_filter(1,2),2);
x=t;
y=polyval(p,x);
plot(x,y,'--g');
 title(['Regognization limit is set as ',num2str(limit),' um']);
 legend('NOP','Fitting');
 xlabel('Time/min');
 ylabel('NOP');
```

4.2 Pit Analysis—pit area, number of pits, pit depth

```
% Delete pits smaller than 300 pixels (as the lateral resolution now is 0.163 micron)
% Find the center of pits and then calculate the nearest/farthest pixels
% find all pit pixel coordinates
% find the center of a pit
% find the max and min distance pixels from pit center
clear,clc;

t=[0 3 6 12 24:24:168];
vsi0_parameters;

npit=zeros(1,length(t));
pitarea=zeros(1,length(t));
Rrms=zeros(1,length(t));
Rrms_np=zeros(1,length(t));
Rrms44_np=zeros(1,length(t));
H=zeros(1,length(t));
H_np=zeros(1,length(t));
%%
for k =1:length(t)
    tic;
    load(['t',num2str(t(k))]);
    xind=1:size(X,2);
    xref=xind(X(1,:)>lxref & X(1,:)<hxref);
    yind=1:size(Y,1);
    yref=yind(Y(:,1)>lyref & Y(:,1)<hyref);
    Zref=Z(yref,xref);
    Href=mean(Zref(~isnan(Zref)));

    load(['t',num2str(t(k)),'pit']);
    npit(k)=length(pits);
    pitarea(k)=sum(sum(ispitg))/size(ispitg,1)/size(ispitg,2);

    SR=fit([Xs(~ispitg) Ys(~ispitg)], Zs(~ispitg), 'poly44');
    ddd=Zs(~ispitg)-SR(Xs(~ispitg),Ys(~ispitg));
    Rrms44_np(k)=sqrt(mean(ddd.^2));
```

```
    H(k)=mean(mean(Zs))-Href;
    [n,~,p]=affine_fit([Xs,Ys,Zs]);
    ddd=(Xs-p(1))*n(1)+(Ys-p(2))*n(2)+(Zs-p(3))*n(3);
    Rrms(k)=sqrt(sum(sum(ddd.^2))/size(ddd,1)/size(ddd,2));

    H_np(k)=mean(Zs(~ispitg))-Href;
    [n,~,p]=affine_fit([Xs(~ispitg),Ys(~ispitg),Zs(~ispitg)]);
    ddd=(Xs-p(1))*n(1)+(Ys-p(2))*n(2)+(Zs-p(3))*n(3);
    Rrms_np(k)=sqrt(sum(ddd(~ispitg).^2)/sum(sum(ispitg)));

    pitedge =pits;
    allpitscoor=[Xs(ispitg),Ys(ispitg),Zs(ispitg)];
    pitcoor=cell(length(pitedge),1);
    center=zeros(length(pitedge),3);
    dist=cell(length(pitedge),1);
    mdist=zeros(length(pitedge),2);
    Apits=zeros(length(pitedge),1);
    Hpits_edge=zeros(length(pitedge),1);
    Hpits_fit=zeros(length(pitedge),1);
    X=reshape(Xs,[],1);
    Y=reshape(Ys,[],1);
    Z=reshape(Zs,[],1);

    for j=1:length(pitedge)

        indtemp=inpolygon(allpitscoor(:,1),allpitscoor(:,2),X(pitedge{j}),Y(pitedge{j}));
        pitcoor{j}=allpitscoor(indtemp,:);
        allpitscoor(indtemp,:)=[];

        center(j,:)=mean([X(pitedge{j}) Y(pitedge{j}) Z(pitedge{j})]);
        [K,temp]=convhull([X(pitedge{j}) Y(pitedge{j})]);
        Apits(j)=temp;
        % distance in XY plane from edge pit center
        dist{j}=sqrt((X(pitedge{j})-center(j,1)).^2+(Y(pitedge{j})-center(j,2)).^2);
        mdist(j,:)=[max(dist{j}),min(dist{j})];
    end
    for j=1:length(pitedge)

        Htemp=center(j,3)-pitcoor{j}(:,3);
        [~,ind]=max(abs(Htemp));
        Hpits_edge(j)=Htemp(ind);

        Htemp=SR(center(j,1:2))-pitcoor{j}(:,3);
        [~,ind]=max(abs(Htemp));
        Hpits_fit(j)=Htemp(ind);
    end

%     figure;
%     quickscatter3(X,Y,Z,1000,'.')
% set(gca,'FontSize',16,'DataAspectRatio',[1 1 0.002]);

    save(['t',num2str(t(k)),'dist'],'center','dist','mdist','pitcoor','pits','Apits','Hpits_edge','Hpits_fit');
```

```
    fprintf('%d minutes  ',t(k));
    fprintf('%d pits\n',length(pitedge));
    toc;
end
save surf_ana t pitarea Rrms Rrms_np npit H H_np Rrms44_np;

% to plot out the pit and its center
% figure; hold on;
% plot3(pitcoor{1}(:,1),pitcoor{1}(:,2),pitcoor{1}(:,3),'rb')
% plot3(center(1,1),center(1,2),center(1,3),'sr')
```

Code 5: Pit Geometry Visualization

```
%% Track the evolution of pit geometry over time

clear,clc;

t=[0:10:100 130:30:490 550:60:610]';
fname=cell(1,length(t));

vsi0_parameters;

load pit_geometry;

pitID=cell(2,1);
m=1;
Inewpit=1:size(center_all{1},1);
for k=1:length(devpit)
    for j=1:length(Inewpit)
        pitID{m}=[k,Inewpit(j)];
        m=m+1;
    end
    Inewpit=setdiff(1:size(center_all{k+1},1),devpit{k});
end
for j=1:length(Inewpit)
    pitID{m}=[k+1,Inewpit(j)];
    m=m+1;
end

IDcoalesce=cell(size(pitID));
ifcoalesce=cell(size(pitID));
for k=1:length(pitID)
    while pitID{k}(end,1)<=length(devpit) && devpit{pitID{k}(end,1)}(pitID{k}(end,2))~=0
        pitID{k}=[pitID{k}; pitID{k}(end,1)+1, devpit{pitID{k}(end,1)}(pitID{k}(end,2))];
    end

    ifcoalesce{k}=zeros(size(pitID{k},1),1);
    l=1;
    for j=1:size(pitID{k},1)
        if pitID{k}(j,1)<length(devpit)
```

```
            ind=1:length(devpit{pitID{k}(j,1)});
            ID=ind(devpit{pitID{k}(j,1)}~=0 &
devpit{pitID{k}(j,1)}==devpit{pitID{k}(j,1)}(pitID{k}(j,2)));
            if length(ID)>1
                ifcoalesce{k}(j)=1;
                IDcoalesce{k}(l)={ID};
            end
            l=l+1;
        end
    end
end

pitHh=cell(size(pitID));
pitAa=cell(size(pitID));
pitARar=cell(size(pitID));
pitdt=zeros(size(pitID));
iniH=zeros(size(pitID));
finH=zeros(size(pitID));
dHdt=zeros(size(pitID));
rdHdt=zeros(size(pitID));
dArdt=zeros(size(pitID));
ind=1:length(pitID);

% figure;
% hold on;
[nrow,~]=cellfun(@size,pitID);
for k=ind(nrow>=3)
    pitHh{k}=zeros(size(pitID{k}));
    pitHh{k}(:,1)=t(pitID{k}(:,1))'-t(pitID{k}(1,1));
    pitAa{k}=zerclear,clc;

t=[0:10:100 130:30:490 550:60:610]';
fname=cell(1,length(t));

vsi0_parameters;

load pit_geometry;

pitID=cell(2,1);
m=1;
Inewpit=1:size(center_all{1},1);
for k=1:length(devpit)
    for j=1:length(Inewpit)
        pitID{m}=[k,Inewpit(j)];
        m=m+1;
    end
    Inewpit=setdiff(1:size(center_all{k+1},1),devpit{k});
end
for j=1:length(Inewpit)
    pitID{m}=[k+1,Inewpit(j)];
    m=m+1;
end
```

```
    IDcoalesce=cell(size(pitID));
    ifcoalesce=cell(size(pitID));
    for k=1:length(pitID)
        while pitID{k}(end,1)<=length(devpit) && devpit{pitID{k}(end,1)}(pitID{k}(end,2))~=0
            pitID{k}=[pitID{k}; pitID{k}(end,1)+1, devpit{pitID{k}(end,1)}(pitID{k}(end,2))];
        end

        ifcoalesce{k}=zeros(size(pitID{k},1),1);
        l=1;
        for j=1:size(pitID{k},1)
            if pitID{k}(j,1)<length(devpit)
                ind=1:length(devpit{pitID{k}(j,1)});
                ID=ind(devpit{pitID{k}(j,1)}~=0 &
devpit{pitID{k}(j,1)}==devpit{pitID{k}(j,1)}(pitID{k}(j,2)));
                if length(ID)>1
                    ifcoalesce{k}(j)=1;
                    IDcoalesce{k}(l)={ID};
                end
                l=l+1;
            end
        end
    end

    pitHh=cell(size(pitID));
    pitAa=cell(size(pitID));
    pitARar=cell(size(pitID));
    pitdt=zeros(size(pitID));
    iniH=zeros(size(pitID));
    finH=zeros(size(pitID));
    dHdt=zeros(size(pitID));
    rdHdt=zeros(size(pitID));
    dArdt=zeros(size(pitID));
    ind=1:length(pitID);

    figure;
    hold on;
    [nrow,~]=cellfun(@size,pitID);
    for k=ind(nrow>=3)
        pitHh{k}=zeros(size(pitID{k}));
        pitHh{k}(:,1)=t(pitID{k}(:,1))'-t(pitID{k}(1,1));
        pitAa{k}=zeros(size(pitID{k}));
        pitAa{k}(:,1)=t(pitID{k}(:,1))'-t(pitID{k}(1,1));
        pitARar{k}=zeros(size(pitID{k}));
        pitARar{k}(:,1)=t(pitID{k}(:,1))'-t(pitID{k}(1,1));
        for j=1:size(pitHh{k},1)
            pitHh{k}(j,2)=Hpits_all{pitID{k}(j,1)}(pitID{k}(j,2));
            pitAa{k}(j,2)=Apits_all{pitID{k}(j,1)}(pitID{k}(j,2));
            pitARar{k}(j,2)=pitHh{k}(j,2)/sqrt(pitAa{k}(j,2)/pi);
        end
        pitdt(k)=pitHh{k}(end,1)-pitHh{k}(1,1);
        iniH(k)=pitHh{k}(1,2);
```

```
    finH(k)=pitHh{k}(end,2);
    [pp,S]=polyfit(pitHh{k}(:,1),pitHh{k}(:,2),1);
    dHdt(k)=pp(1);
    rdHdt(k)=S.normr;
    pp=polyfit(pitARar{k}(:,1),pitARar{k}(:,2),1);
    dArdt(k)=pp(1);

        plot(pitARar{k}(:,1),pitARar{k}(:,2))
end

npfit=2;
l=1;
dHdt=[0 0 0];
for k=ind(nrow>=npfit*2+1)
    for j=npfit+1:length(pitHh{k}(:,1))-npfit
        [pp,S]=polyfit(pitHh{k}(j-npfit:j+npfit,1),pitHh{k}(j-npfit:j+npfit,2),1);
        dHdt(l,:)=[pitHh{k}(j,1),pp(1),S.normr];
        l=l+1;
    end
    plot(pitHh{k}(:,1),pitHh{k}(:,2),'-o')
end

xbins=linspace(min(dHdt),max(dHdt),20);
freq=histc(dHdt,xbins);
figure;
bar(xbins+(diff(xbins(1:2))/2),log10(freq))

load surf_ana;
for i=1:length(Hpits_all)
    xbins=linspace(min(Hpits_all{i}),max(Hpits_all{i}),20);
    freq=histc(Hpits_all{i},xbins);
    figure;
    hold on;
    bar(xbins+(diff(xbins(1:2))/2),(freq));
    xlim([0 0.9]);
    yrange=ylim;
    line([Rrms44_np(i) Rrms44_np(i)],yrange);

    pause;
end

avgH=zeros(length(Hpits_all),1);
npits_real=zeros(length(Hpits_all),1);
for i=1:length(Hpits_all)
    isreal=Hpits_all{i}>Rrms44_np(i)*2;
    avgH(i)=mean(Hpits_all{i}(isreal));
    npits_real(i)=sum(isreal);
end
figure;
plot(t,avgH,'-o');
figure;
plot(t,npits_real,'-o');
```

```
save pit_H t avgH npits_real;

f1=figure;
f2=figure;
for k=ind(nrow>1)
    if pitID{k}(1,1)+size(pitID{k},1)-1>length(t)-1
        figure(f1);
        plot(pitHh{k}(:,1),pitHh{k}(:,2),'-o');
        hold on;
        plot(pitHh{k}(:,1),Rrms44_np(pitID{k}(1:end,1)),'-ro');
        line([pitHh{k}(1,1) pitHh{k}(end,1)],[Rrms44_np(pitID{k}(1,1)),Rrms44_np(pitID{k}(1,1))],'Color','b');
        line([pitHh{k}(1,1) pitHh{k}(end,1)],[Rrms44_np(pitID{k}(end,1)),Rrms44_np(pitID{k}(end,1))],'Color','r');
        hold off;

        figure(f2);
        plot(pitHh{k}(:,1),pitAa{k}(:,2),'-o');
        pause;
    end
end

figure;
plot(finH(pitdt>30 & rdHdt<0.08),dHdt(pitdt>30 & rdHdt<0.08),'o')
hist(dHdt(pitdt>240),200)
f1=figure;
f2=figure;
for k=ind(nrow>8)
    if pitID{k}(1,1)>1
        figure(f1);
        plot(pitHh{k}(:,1),pitHh{k}(:,2),'-o');
        figure(f2);
        plot(pitHh{k}(:,1),pitAa{k}(:,2),'-o');
    pause;
    end
end

%% Aspect ratio

save aspect t pitARar pitAa pitHh pitID pitdt rdHdt;
```

Code 6: Surface Height Distribution

```
clc,clear;

t=[0 5 10 20 30:30:120 180:60:720];
tic;
load t0AL;
xsmp=[ 3000 8000];
ysmp=[0 3400];
```

```
    issmp=XAL>xsmp(1) & XAL<xsmp(2) & YAL>ysmp(1) & YAL<ysmp(2) & ~isnan(XAL) &
~isnan(YAL) & ~isnan(ZAL);
    [n,~,p]=affine_fit([XAL(issmp),YAL(issmp),ZAL(issmp)]);
    ddd0=(XAL-p(1))*n(1)+(YAL-p(2))*n(2)+(ZAL-p(3))*n(3);

    load t0ALpit;
    xref=[ 3000 8000];
    yref=[0 3400];
    isref=XAL>xref(1) & XAL<xref(2) & YAL>yref(1) & YAL<yref(2) & ~isnan(XAL) & ~isnan(YAL)
& ~isnan(ZAL);
    base0=mean(ddd0(isref));
    ddd0=ddd0-base0;

    i=1;
    nx=size(XAL,2);
    ny=size(XAL,1);

    f2=figure;
    hold on;
    mesh(XAL,YAL,ddd0);
    view([0 0 1]);
    zoom=ginput(2);
    xlim(sort(zoom(:,1)));
    ylim(sort(zoom(:,2)));
    % axis ratios
    daspect([ 1 1 0.01]);
    % store two reference points coordinates into alignt matrix
    alignt(:,:,i)=ginput(2);
    figure(f2);
    % show the selected two points on image
    plot3(alignt(:,1,i),alignt(:,2,i),[0 0],'or')
    title(['t',num2str(t(i))]);

    xyAL=[reshape(XAL,[],1),reshape(YAL,[],1)];

    v1=alignt(2,:,1)-alignt(1,:,1);
    vi=alignt(2,:,i)-alignt(1,:,i);

    % shift
    xyAL=xyAL-repmat(alignt(1,:,i)+alignt(1,:,1),size(xyAL,1),1);
    % rotate
    cosv=vi*v1'/norm(vi)/norm(v1);
    fprintf('rotate by %5.1f degree\n',rad2deg(acos(cosv)));
    R=[cosv -(1-cosv^2); 1-cosv^2 cosv];
    xyAL0=(R*[xyAL(:,1)';xyAL(:,2)'])';

    nsmooth=5;
    h=fspecial('disk',nsmooth);
    ddd0=filter2(h,ddd0);

    toc;
    % fs=figure;
```

```
    % hold on;
    % surf(XAL,YAL,ddd0,'LineStyle','none','FaceAlpha',1);
    % plot3(XAL(isref),YAL(isref),ZAL(isref),'.')

    % dz=0.306706;
    for i =2:length(t)
        % disp(fname{i});
        tic;
        t(i)
        load(['t',num2str(t(i)),'AL'])
        issmp=XAL>xsmp(1) & XAL<xsmp(2) & YAL>ysmp(1) & YAL<ysmp(2) & ~isnan(XAL) &
~isnan(YAL) & ~isnan(ZAL);
        [n,~,p]=affine_fit([XAL(issmp),YAL(issmp),ZAL(issmp)]);
        ddd=(XAL-p(1))*n(1)+(YAL-p(2))*n(2)+(ZAL-p(3))*n(3);

        load(['t',num2str(t(i)),'ALpit'])
        isref=XAL>xref(1) & XAL<xref(2) & YAL>yref(1) & YAL<yref(2) & ~isnan(XAL) &
~isnan(YAL) & ~isnan(ZAL);
        base=mean(ddd(isref));
        ddd=ddd-base;

        f2=figure;
        hold on;
        mesh(XAL,YAL,ddd);
        view([0 0 1]);
        zoom=ginput(2);
        xlim(sort(zoom(:,1)));
        ylim(sort(zoom(:,2)));
        % axis ratios
        daspect([ 1 1 0.01]);
        % store two reference points coordinates into alignt matrix
        alignt(:,:,i)=ginput(2);
        figure(f2);
        % show the selected two points on image, *********** setting [0 0] ?
        plot3(alignt(:,1,i),alignt(:,2,i),[0 0],'or')
        title(['t',num2str(t(i))]);

        xyAL=[reshape(XAL,[],1),reshape(YAL,[],1)];

        v1=alignt(2,:,1)-alignt(1,:,1);
        vi=alignt(2,:,i)-alignt(1,:,i);

        % shift
        xyAL=xyAL-repmat(alignt(1,:,i)+alignt(1,:,1),size(xyAL,1),1);
        % rotate
        cosv=vi*v1'/norm(vi)/norm(v1);
        fprintf('rotate by %5.1f degree\n',rad2deg(acos(cosv)));
        R=[cosv -(1-cosv^2); 1-cosv^2 cosv];
        xyAL=(R*[xyAL(:,1)';xyAL(:,2)'])';

        nx=size(XAL,2);
        ny=size(XAL,1);
```

```
    XAL=reshape(xyAL(:,1),ny,nx);
    YAL=reshape(xyAL(:,2),ny,nx);

    ddd=filter2(h,ddd);
    Fs=scatteredInterpolant(xyAL(:,1),xyAL(:,2),reshape(ddd,[],1));
    ddd=reshape(Fs(xyAL0(:,1),xyAL0(:,2)),ny,nx);

    %     figure(fs);
    %     surf(XAL,YAL,ddd,'LineStyle','none');
    %     diff(isnan(diff))=[];
    ds=((ddd(issmp)-ddd0(issmp))/t(i)*1000);
    % logds=log10(ds);
    logds=ds;
    X=linspace(min(min(logds)),max(max(logds)),100);
    Y=histc(reshape(logds,[],1),X);
    figure
    hold on;
    plot(X,Y);
    title(['t',num2str(t(i))]);
    save(['freq_t',num2str(t(i))],'X','Y')
    toc;
end
```

Code 7: Sample Surface Height Change Over Time

```
clc,clear;
idy=3000:8000;
idx=100:3400;
idyref=50:2050;
idxref=1100:3100;
load t0AL;
figure();
mesh(XAL,YAL,ZAL);% image in real size
view([0 0 1]);
 figure;
 surf(ZAL,'EdgeColor','none','FaceAlpha',0.4)
 view([0 0 1]);
 hold on;
 surf(idy,idx,ZAL(idx,idy),'LineStyle','none'); % the area under obvervation
 hold off;
z0=zeros(length(idx),length(idy));
z0=ZAL(idx,idy);


t=[0 5 10 20 30:30:120 180:60:720];
h_change=zeros(length(t),2);
for k=1:length(t)
    tic;
    t(k)
```

```
load(['t',num2str(t(k)),'AL'])
% out-plane rotate
cosa=0;
cosb=0;
ref=ZAL(idxref,idyref);
%% calculate the rotation angles of out-planes, say x-z and y-z planes
% note: on x-axis, the increaments are in idyref (data columns)

% x-z plane, rotate around y axis
%     [cosa sina
%     -sina cosa]
   for i=idxref
   start_point=[XAL(i,min(idyref)) ZAL(i,min(idyref))];
   end_point=[XAL(i,max(idyref)) ZAL(i,max(idyref))];
   end_proj=[XAL(i,max(idyref)) ZAL(i,min(idyref))];
   v1= end_point -start_point; % vector in real
   v2=end_proj-start_point; % projection vector of v1
   cosa=v1*v2'/norm(v1)/norm(v2)+cosa; % the angel between v1 and v2 , cosine
   end
   cosa_avg=cosa/length(idxref);
%     Ry=[cosa_avg sqrt(1-(cosa_avg)^2);-sqrt(1-(cosa_avg)^2) cosa];

% y-z plane, rotate around x
%     [cosb -sinb
%      sinb cosb]
   for j=idyref
   start_point=[YAL(min(idxref),i) ZAL(min(idxref),i)];
   end_piont=[YAL(max(idxref),i) ZAL(max(idxref),i)];
   end_proj=[YAL(max(idxref),i) ZAL(min(idxref),i)];
   v1=end_point-start_point; % vector in real
   v2=end_proj - start_point; % projection vector of v1
   cosb=v1*v2'/norm(v1)/norm(v2)+cosb; % the angel between v1 and v2 , cosine
   end
   cosb_avg=cosb/length(idyref);
%     Rx=[cosb_avg -sqrt(1-(cosb_avg)^2);sqrt(1-(cosb_avg)^2) cosb];

%% out-plane rotation

refX=reshape(XAL(idxref,idyref),[],1);
refY=reshape(YAL(idxref,idyref),[],1);
refZ=reshape(ZAL(idxref,idyref),[],1);

zref_rot=zeros(length(refZ),1);
zref_rot=-sqrt(1-(cosa_avg)^2)*refX(:)+cosa_avg*refZ(:); % x-z plane rotation
zref_rot=sqrt(1-(cosb_avg)^2)*refY(:)+cosb_avg*refZ(:); % y-z plane rotation

samX=reshape(XAL(idx,idy),[],1);
samY=reshape(YAL(idx,idy),[],1);
samZ=reshape(ZAL(idx,idy),[],1);

zt_rot=zeros(length(samZ),1);
zt_rot=-sqrt(1-(cosa_avg)^2)*samX(:)+cosa_avg*samZ(:); % x-z plane rotation
```

```
zt_rot=sqrt(1-(cosb_avg)^2)*samY(:)+cosb_avg*samZ(:); % y-z plane rotation

% diff=(zt-z0)/(t/60);
delta_H=mean(mean(zt_rot(~isnan(zt_rot))))-mean(mean(zref_rot(~isnan(zref_rot))));

h_change(k,1)=t(k);
h_change(k,2)=delta_H;

toc;
end
save('h_change_ref_rot','h_change');
figure();
plot(h_change(:,1),h_change(:,2)-h_change(1,2),'-*');
xlabel('Time/min');
ylabel('Average Height Change/micron');
title('1045 steel corrosion in 0.01 M NaOH solution');
```

Code 8: Sample Surface Height Profile Evolution

```
clear,clc;

ifline=1;

t=[130 160 220];
fname=cell(1,length(t));

vsi0_parameters;

% initial plot
k=2;
fname{k}=['t',num2str(t(k))];

load([fname{k},'AL']);
xind=1:size(XAL,2);
xref=xind(XAL(1,:)>lxref & XAL(1,:)<hxref);
yind=1:size(YAL,1);
yref=yind(YAL(:,1)>lyref & YAL(:,1)<hyref);

figure;
hold on;
surf(XAL,YAL,ZAL,'LineStyle','none','FaceAlpha',0.5);
surf(XAL(yref,xref),YAL(yref,xref),ZAL(yref,xref),'LineStyle','none');

load([fname{k},'ALpit']);
% grdpit=0.99; % percent
indall=1:size(Xs,1)*size(Xs,2);
grd=reshape(FF,1,[]);
bins=linspace(min(grd),max(grd),100);
freq=histc(grd,bins);
[MX,ind]=max(freq);
```

```
        [~,Ihm]=find(freq<MX*(1-grdpit),1,'first');
        FFm=(bins(Ihm)+bins(Ihm+1))/2;

        surf(Xs,Ys,FF,'LineStyle','none','FaceAlpha',0.9);
        caxis([0 FFm]);
        view([0 0 1]);
        whitebg('w');
        title(['ini, ',fname{k}]);

        pregion=sort(ginput(2));

        xshift=pregion(2,1)-pregion(1,1)+100;

          if ifline==1
            xlim([pregion(1,1) pregion(2,1)]);
            ylim([pregion(1,2) pregion(2,2)]);
            pline=ginput(2);

            fline=figure;
            hold on;
          end

        f3d=figure;
        hold on;
        l=0;
        frames=[1:1:length(t)];
        CCC=jet(length(frames));
        for k=1:length(frames)
          fname{k}=['t',num2str(t(frames(k)))];

          load([fname{k},'AL']);
          refZ=ZAL(yref,xref);

          xind=1:size(XAL,2);
          xrange=xind(XAL(1,:)>pregion(1,1) & XAL(1,:)<pregion(2,1));
          yind=1:size(YAL,1);
          yrange=yind(YAL(:,1)>pregion(1,2) & YAL(:,1)<pregion(2,2));

          [FX,FY]=gradient(ZAL(yrange,xrange),XAL(1,2)-XAL(1,1),YAL(2,1)-YAL(1,1));
          thy=atan(mean(FX(~isnan(FX))));
          thx=-atan(mean(FY(~isnan(FY))));
          FF=sqrt(FX.^2+FY.^2);


coors=[reshape(XAL(yrange,xrange),[],1),reshape(YAL(yrange,xrange),[],1),reshape(ZAL(yrange,xrange),[],1)]';
          Rx=[1      0    0
            0  cos(thx) -sin(thx)
            0  sin(thx)  cos(thx)];
          Ry=[cos(thy) 0 sin(thy)
            0       1    0
            -sin(thy) 0 cos(thy)];
          coorsr=Ry*Rx*coors;
```

```
      %     [~,Iorig]=max(coorsr(3,:));
        Iorig=1;

        Xr=reshape(coorsr(1,:),length(yrange),length(xrange))-coorsr(1,Iorig);
        Yr=reshape(coorsr(2,:),length(yrange),length(xrange))-coorsr(2,Iorig);
        Zr=reshape(coorsr(3,:),length(yrange),length(xrange))-coorsr(3,Iorig);

        load([fname{k},'ALpit']);
        xind=1:size(Xs,2);
        xrange=xind(Xs(1,:)>pregion(1,1) & Xs(1,:)<pregion(2,1));
        yind=1:size(Ys,1);
        yrange=yind(Ys(:,1)>pregion(1,2) & Ys(:,1)<pregion(2,2));
        Xr=Xs(yrange,xrange);
        Yr=Ys(yrange,xrange);
        Zr=Zs(yrange,xrange)-mean(mean(refZ(~isnan(refZ))));

        figure(f3d);
         figure;
         colorbar;
         view([1 1 6]);
         caxis([0 0.1]);
         set(gca,'FontWeight','bold','fontsize',14);
         xlabel('X (um)','fontsize',14);
         ylabel('Y (um)','fontsize',14);
         zlabel('Gradient','fontsize',14);
         axis([-200,1000,-200,1000,0,0.1]);
          surf(Xr+zshift*(j-1),Yr,Zr,(Zr-cmin)/(cmax-cmin),'LineStyle','none');
          text(min(min(Xr))-20,min(min(Yr))-20,min(min(Zr+zshift*(j-1)))+zshift*0.6,['t=',num2str(t(j)),'
min'],'FontSize',16,'FontWeight','bold');

        surf(Xr+xshift*l,Yr,Zr,'LineStyle','none');
        text(min(min(Xr))+xshift*l-20,min(min(Yr))-20,min(min(Zr)),['t=',num2str(t(frames(k))),'
min'],'FontSize',16,'FontWeight','bold');

        surf(Xr,Yr,FF,'LineStyle','none');
        text(min(min(Xr))-20,min(min(Yr))-20,min(min(Zr)),['t=',num2str(t(frames(k))),'
min'],'FontSize',16,'FontWeight','bold');

        if ifline==1
          [~,temp1]=min(abs(XAL(1,xrange)-pline(1,1)));
          [~,temp2]=min(abs(XAL(1,xrange)-pline(2,1)));
          idxline=[temp1 temp2];
          [~,temp1]=min(abs(YAL(yrange,1)-pline(1,2)));
          [~,temp2]=min(abs(YAL(yrange,1)-pline(2,2)));
          idyline=[temp1 temp2];

          xrline=linspace(Xr(idyline(1),idxline(1)), Xr(idyline(2),idxline(2)),200);
          yrline=linspace(Yr(idyline(1),idxline(1)), Yr(idyline(2),idxline(2)),200);

          idnan=isnan(Zr);
          Finterp=scatteredInterpolant(Xr(~idnan),Yr(~idnan),Zr(~idnan));
```

```
            zrline=Finterp(xrline,yrline);
            figure(f3d);
            plot3(xrline+xshift*l,yrline,zrline);


            figure(fline);
            plot(sqrt((xrline-xrline(1)).^2+(yrline-yrline(1)).^2),zrline,'Color',CCC(k,:));



          end
          l=l+1;
        end
        figure(f3d);
        % caxis([cmin, cmax]);
        shading interp;
        whitebg('k');
        view([0 1 0]);
        set(gca,'FontSize',16,'DataAspectRatio',[1 1 0.002]);
        % set(gca,'ZTick',[],'FontSize',16,'DataAspectRatio',[1 1 0.002]);
        xlabel('X (\mum)','FontSize',16,'FontWeight','bold');
        ylabel('Y (\mum)','FontSize',16,'FontWeight','bold');
        zlabel('Z','FontSize',16,'FontWeight','bold');
        hcb=colorbar('FontSize',16,'FontWeight','bold');
        title(hcb,'Depth (\mum)','FontSize',16,'FontWeight','bold');
           view([1 1 6]);
           caxis([0 0.1]);
           set(gca,'FontWeight','bold','fontsize',14);
           xlabel('X (um)','fontsize',14);
           ylabel('Y (um)','fontsize',14);
           zlabel('Gradient','fontsize',14);
           axis([-200,1000,-200,1000,0,0.1]);
          %     surf(Xr+zshift*(j-1),Yr,Zr,(Zr-cmin)/(cmax-cmin),'LineStyle','none');
          %     text(min(min(Xr))-20,min(min(Yr))-20,min(min(Zr+zshift*(j-1)))+zshift*0.6,['t=',num2str(t(j)),' min'],'FontSize',16,'FontWeight','bold');

        %     surf(Xr+xshift*l,Yr,Zr,'LineStyle','none');
        %     text(min(min(Xr))+xshift*l-20,min(min(Yr))-20,min(min(Zr)),['t=',num2str(t(frames(k))),' min'],'FontSize',16,'FontWeight','bold');

          surf(Xr,Yr,FF,'LineStyle','none');
          text(min(min(Xr))-20,min(min(Yr))-20,min(min(Zr)),['t=',num2str(t(frames(k))),' min'],'FontSize',16,'FontWeight','bold');

          if ifline==1
            [~,temp1]=min(abs(XAL(1,xrange)-pline(1,1)));
            [~,temp2]=min(abs(XAL(1,xrange)-pline(2,1)));
            idxline=[temp1 temp2];
            [~,temp1]=min(abs(YAL(yrange,1)-pline(1,2)));
            [~,temp2]=min(abs(YAL(yrange,1)-pline(2,2)));
            idyline=[temp1 temp2];
```

```
        xrline=linspace(Xr(idyline(1),idxline(1)), Xr(idyline(2),idxline(2)),200);
        yrline=linspace(Yr(idyline(1),idxline(1)), Yr(idyline(2),idxline(2)),200);

        idnan=isnan(Zr);
        Finterp=scatteredInterpolant(Xr(~idnan),Yr(~idnan),Zr(~idnan));
        zrline=Finterp(xrline,yrline);
        figure(f3d);
        plot3(xrline+xshift*l,yrline,zrline);


        figure(fline);
        plot(sqrt((xrline-xrline(1)).^2+(yrline-yrline(1)).^2),zrline,'Color',CCC(k,:));



    end
    l=l+1;
end
figure(f3d);
% caxis([cmin, cmax]);
shading interp;
whitebg('k');
view([0 1 0]);
set(gca,'FontSize',16,'DataAspectRatio',[1 1 0.002]);
% set(gca,'ZTick',[],'FontSize',16,'DataAspectRatio',[1 1 0.002]);
xlabel('X (\mum)','FontSize',16,'FontWeight','bold');
ylabel('Y (\mum)','FontSize',16,'FontWeight','bold');
zlabel('Z','FontSize',16,'FontWeight','bold');
hcb=colorbar('FontSize',16,'FontWeight','bold');
title(hcb,'Depth (\mum)','FontSize',16,'FontWeight','bold');
```

Code 9: Gradient Map Visualization

```
clear,clc;

grdpit=0.99; % percent
 t=[0 5 10 20 30:30:120 180:60:720];

fname=cell(1,length(t));
for k =1:length(t)
    tic;
    fname{k}=['t',num2str(t(k)),'AL'];
    % disp(fname{i});
    load(fname{k});

    nx=size(ZAL,2);
    ny=size(ZAL,1);
    idnan=isnan(ZAL);
```

```
ZAL=reshape(griddata(XAL(~idnan),YAL(~idnan),ZAL(~idnan),reshape(XAL,[],1),reshape(YAL,[],1),'natur
al'),ny,nx);

            if k==1
               pregion=[3000 -250;4000 750];
               xind=1:size(XAL,2);
               idx=xind(XAL(1,:)>pregion(1,1) & XAL(1,:)<pregion(2,1));
               yind=1:size(YAL,1);
               idy=yind(YAL(:,1)>pregion(1,2) & YAL(:,1)<pregion(2,2));


               figure;
               surf(ZAL,'EdgeColor','none','FaceAlpha',0.4)
               view([0 0 1]);
               hold on;
               surf(idx,idy,ZAL(idy,idx),'LineStyle','none')
            end

            nsmooth=5;
            h=fspecial('disk',nsmooth);
            Zs=filter2(h,ZAL(idy,idx));
            Zs=Zs(nsmooth+1:end-nsmooth,nsmooth+1:end-nsmooth);
            Xs=XAL(idy,idx);
            Xs=Xs(nsmooth+1:end-nsmooth,nsmooth+1:end-nsmooth);
            Ys=YAL(idy,idx);
            Ys=Ys(nsmooth+1:end-nsmooth,nsmooth+1:end-nsmooth);
            coors=[reshape(Xs,[],1),reshape(Ys,[],1),reshape(Zs,[],1)];
            indall=1:size(Xs,1)*size(Xs,2);

            [FX,FY]=gradient(Zs,Xs(1,2)-Xs(1,1),Ys(2,1)-Ys(1,1));
            FF=sqrt(FX.^2+FY.^2);
            grd=reshape(FF,1,[]);
            bins=linspace(min(grd),max(grd),100);
            freq=histc(grd,bins);
            [MX,ind]=max(freq);
            [~,Ihm]=find(freq<MX*(1-grdpit),1,'first');
            FFm=(bins(Ihm)+bins(Ihm+1))/2;
             Xs=Xs-min(min(Xs));
             Ys=Ys-min(min(Ys));
            figure;
            semilogy(bins,freq)
            hold on;
            yplot=ylim;
            line([FFm,FFm],yplot,'Color','r')

            ispitg=FF>FFm;
            coorsp=[Xs(ispitg),Ys(ispitg),zeros(length(Xs(ispitg)),1)];
            tempind=reshape(indall,size(Xs,1),size(Xs,2));
            indpall=tempind(ispitg);
            gID=group_nbr(coorsp,coorsp,(Xs(1,2)-Xs(1,1))*8);
```

```
    figure;
    surf(Xs,Ys,FF,'LineStyle','none')
    caxis([0 FFm]);
%       view([0 0 1])
      view([1 1 6]);
      caxis([0 0.01]);
      set(gca,'FontWeight','bold','fontsize',14);
      xlabel('X (um)','fontsize',14);
      ylabel('Y (um)','fontsize',14);
      zlabel('Gradient','fontsize',14);
    whitebg('w')
    title(fname{k})

    hold on;

    toc
    tic;

    pits=cell(max(gID),1);
    for i=1:max(gID)
        if sum(gID==i)==1
            pits{i}=[];
        else
            tempcoorsp=coorsp(gID==i,1:2);
            temp=tempcoorsp(2:end,:)-repmat(tempcoorsp(1,:),size(tempcoorsp,1)-1,1);
            ptemp=cart2pol(temp(:,1),temp(:,2));
            if abs(sum(ptemp-ptemp(1)))<1e-5
                pits{i}=[];
            else
                indpp=indpall(gID==i);
                pits{i}=indpp(convhull(coorsp(gID==i,1:2)));
                ispitg(inpolygon(coors(:,1),coors(:,2),coors(pits{i},1),coors(pits{i},2)))=1;
%                   plot(coors(pits{i},1),coors(pits{i},2),'-ok','LineWidth',5);
%                   text(coors(pits{i}(1),1),coors(pits{i}(1),2),num2str(i),'FontSize',20,'FontWeight','bold');
            end
        end
    end
    pits(cellfun(@isempty,pits))=[];
%       plot(coors(ispitg,1),coors(ispitg,2),'ob','LineWidth',3);

    coorsp=[Xs(ispitg),Ys(ispitg),zeros(length(Xs(ispitg)),1)];
    tempind=reshape(indall,size(Xs,1),size(Xs,2));
    indpall=tempind(ispitg);
    gID_new=group_nbr(coorsp,coorsp,(Xs(1,2)-Xs(1,1))*10);
    while max(gID_new)~=max(gID)

        gID=gID_new;

        %       figure;
%           surf(Xs,Ys,FF,'LineStyle','none')
        caxis([0 FFm]);
        view([0 0 -1])
```

```
        whitebg('w')
        hold on;

        pits=cell(max(gID),1);
        for i=1:max(gID)
            if sum(gID==i)==1
                pits{i}=[];
            else
                tempcoorsp=coorsp(gID==i,1:2);
                temp=tempcoorsp(2:end,:)-repmat(tempcoorsp(1,:),size(tempcoorsp,1)-1,1);
                ptemp=cart2pol(temp(:,1),temp(:,2));
                if abs(sum(ptemp-ptemp(1)))<1e-5
                    pits{i}=[];
                else
                    indpp=indpall(gID==i);
                    pits{i}=indpp(convhull(coorsp(gID==i,1:2)));
                    ispitg(inpolygon(coors(:,1),coors(:,2),coors(pits{i},1),coors(pits{i},2)))=1;
%                       plot(coors(pits{i},1),coors(pits{i},2),'-ok','LineWidth',5);
                end
            end
        end
        pits(cellfun(@isempty,pits))=[];
%           plot(coors(ispitg,1),coors(ispitg,2),'ob','LineWidth',3);

        coorsp=[Xs(ispitg),Ys(ispitg),zeros(length(Xs(ispitg)),1)];
        tempind=reshape(indall,size(Xs,1),size(Xs,2));
        indpall=tempind(ispitg);
        gID_new=group_nbr(coorsp,coorsp,(Xs(1,2)-Xs(1,1))*10);
    end
        toc


                [polyx,polyy]=poly2cw(coorsp(pitedge,1),coorsp(pitedge,2));
                =indall(inpolygon(coors,coors,polyx,polyy))';

    figure;
    mesh(Xs,Ys,FF,'FaceColor','none');
    % quiver(Xs,Ys,FX,FY)
    hold on;
    plot3(Xs(ispitg),Ys(ispitg),FF(ispitg),'o')

    save ([fname{i},'pit'],'pits');
    save ([fname{i},'pixcoor'], 'Xs','Ys','Zs');

    fprintf('After %d minutes, there are %d pits\n ', t(k),length(pits));
    save ([fname{k},'pit'], 'Xs','Ys','Zs','FF','pits','ispitg');

end
```

Code 10: Embedded Functions

10.1 affine_fit

```
function [n,V,p] = affine_fit(X)

   p = mean(X,1);

   R = bsxfun(@minus,X,p);
   [V,D] = eig(R'*R);
   n = V(:,1);
   V = V(:,2:end);
End
```

10.2 Group_nbr

```
function gID=group_nbr(coorr,coors,cutoff)

[CN,Nlist]=CNcal_vsi(coorr,coors,cutoff,1);
gID=zeros(size(CN));

ind=1:length(gID);
l=1;
for j=1:size(CN,1)
   if gID(j)==0
      ctrID=j;
      while gID(ctrID)~=l
         gID(ctrID)=l;
         nbr=unique(cell2mat(Nlist(ctrID)));
         gID(nbr)=l;
         indtemp=ind(unique(cell2mat(Nlist(nbr))));
         ctrID=indtemp(gID(unique(cell2mat(Nlist(nbr))))~=l);
%           ctrID=nbr(gID(nbr)~=l);
      end
      l=l+1;
   end
end
```

References

[1] P. K. Mehta, "CONCRETE. STRUCTURE, PROPERTIES AND MATERIALS," 1986.

[2] J. G. MacGregor, *REINFORCED CONCRETE: MECHANICS AND DESIGN. SECOND EDITION*. 1992.

[3] D. L. Summerbell, C. Y. Barlow, and J. M. Cullen, "Potential reduction of carbon emissions by performance improvement: A cement industry case study," *J. Clean. Prod.*, vol. 135, no. Supplement C, pp. 1327–1339, Nov. 2016.

[4] E. Benhelal, G. Zahedi, E. Shamsaei, and A. Bahadori, "Global strategies and potentials to curb CO2 emissions in cement industry," *J. Clean. Prod.*, vol. 51, no. Supplement C, pp. 142–161, Jul. 2013.

[5] L. Barcelo, J. Kline, G. Walenta, and E. Gartner, "Cement and carbon emissions," *Mater. Struct.*, vol. 47, no. 6, pp. 1055–1065, Jun. 2014.

[6] Y. Dosho, "Development of a Sustainable Concrete Waste Recycling System," *J. Adv. Concr. Technol.*, vol. 5, no. 1, pp. 27–42, 2007.

[7] R. Dhir and T. Dyer, *Concrete in the Service of Mankind: Concrete for environment protection and enhancement*. CRC Press, 1996.

[8] N. Fonseca, J. de Brito, and L. Evangelista, "The influence of curing conditions on the mechanical performance of concrete made with recycled concrete waste," *Cem. Concr. Compos.*, vol. 33, no. 6, pp. 637–643, Jul. 2011.

[9] Park Young-Ji and Ang Alfredo H.-S., "Mechanistic Seismic Damage Model for Reinforced Concrete," *J. Struct. Eng.*, vol. 111, no. 4, pp. 722–739, Apr. 1985.

[10] R. Park and T. Paulay, *Reinforced Concrete Structures*. John Wiley & Sons, 1975.

[11] I. H. E. Nilsson and A. Losberg, "Reinforced Concrete Corners and Joints Subjected to Bending Moment," *J. Struct. Div.*, vol. 102, no. 6, pp. 1229–1254, 1976.

[12] J. Rootzén and F. Johnsson, "Managing the costs of CO2 abatement in the cement industry," *Clim. Policy*, vol. 17, no. 6, pp. 781–800, Aug. 2017.

[13] R. Kajaste and M. Hurme, "Cement industry greenhouse gas emissions – management options and abatement cost," *J. Clean. Prod.*, vol. 112, no. Part 5, pp. 4041–4052, Jan. 2016.

[14] P. Friedlingstein *et al.*, "Update on CO_2 emissions," *Nat. Geosci.*, vol. 3, no. 12, p. ngeo1022, Nov. 2010.

[15] G. P. Peters, G. Marland, C. L. Quéré, T. Boden, J. G. Canadell, and M. R. Raupach, "Rapid growth in CO_2 emissions after the 2008–2009 global financial crisis," *Nat. Clim. Change*, vol. 2, no. 1, p. nclimate1332, Dec. 2011.

[16] S. A. Abdul-Wahab, G. A. Al-Rawas, S. Ali, and H. Al-Dhamri, "Assessment of greenhouse CO2 emissions associated with the cement manufacturing process," *Environ. Forensics*, vol. 17, no. 4, pp. 338–354, Oct. 2016.

[17] N. Mahasenan, S. Smith, and K. Humphreys, *The cement industry and global climate change: Current and potential future cement industry CO2 emissions*. Amsterdam: Elsevier Science Bv, 2003.

[18] A. Wolter, “INFLUENCE OF THE KILN SYSTEM ON THE CLINKER PROPERTIES.,” vol. 37, pp. 327–329, Oct. 1985.

[19] L. J. Hanle, K. R. Jayaraman, and J. S. Smith, *CO2 emissions profile of the US cement industry*. 2004.

[20] H. F. W. Taylor, *Cement Chemistry*. Thomas Telford, 1997.

[21] M. Georgescu, J. Tipan, A. Badanoiu, D. Crisan, and I. Dragan, “Highly reactive dicalcium silicate synthesised by hydrothermal processing,” *Cem. Concr. Compos.*, vol. 22, no. 5, pp. 315–319, Oct. 2000.

[22] N. B. Singh, S. Rai, and N. Singh, “Highly Reactive β-Dicalcium Silicate,” *J. Am. Ceram. Soc.*, vol. 85, no. 9, pp. 2171–2176, Sep. 2002.

[23] D. Kantro and C. Weise, “Hydration of Various Beta-Dicalcium Silicate Preparations,” *J. Am. Ceram. Soc.*, vol. 62, no. 11–1, pp. 621–626, 1979.

[24] J. S. Romano, P. D. Marcato, and F. A. Rodrigues, “Synthesis and characterization of manganese oxide-doped dicalcium silicates obtained from rice hull ash,” *Powder Technol.*, vol. 178, no. 1, pp. 5–9, Sep. 2007.

[25] P. Fierens and J. Tirlocq, “Nature and concentration effect of stabilizing elements of beta-dicalcium silicate on its hydration rate,” *Cem. Concr. Res.*, vol. 13, no. 2, pp. 267–276, Mar. 1983.

[26] F. Xiuji, L. Shizong, and S. Dexun, “Research of positron annihilation and hydration of doped β-C2S,” *Cem. Concr. Res.*, vol. 17, no. 4, pp. 532–538, Jul. 1987.

[27] N. S. Gajbhiye and N. B. Singh, “Microwave assisted preparation of Fe3+ doped β-dicalcium silicate by sol–gel method,” *Mater. Res. Bull.*, vol. 45, no. 8, pp. 933–938, Aug. 2010.

[28] A. Ghose, S. Chopra, and J. F. Young, “Microstructural characterization of doped dicalcium silicate polymorphs,” *J. Mater. Sci.*, vol. 18, no. 10, pp. 2905–2914, Oct. 1983.

[29] I. P. Saraswat, V. K. Matthur, and S. C. Ahluwalia, “Effect of alkaline earth metal dopants on the thermal decomposition of the CaCO3-SiO2 system: Part II. Formation of dicalcium silicate,” *Thermochim. Acta*, vol. 95, no. 1, pp. 201–211, Nov. 1985.

[30] K. Fukuda, I. Maki, S. Ito, and S. Ikeda, “Structure Change in Strontium Oxide-Doped Dicalcium Silicates,” *J. Am. Ceram. Soc.*, vol. 79, no. 10, pp. 2577–2581, Oct. 1996.

[31] A. Cuesta, E. R. Losilla, M. A. G. Aranda, J. Sanz, and Á. G. De la Torre, “Reactive belite stabilization mechanisms by boron-bearing dopants,” *Cem. Concr. Res.*, vol. 42, no. 4, pp. 598–606, Apr. 2012.

[32] L. Bonafous, C. Bessada, D. Massiot, J.-P. Coutures, B. L. Holland, and P. Colombet, “29Si MAS NMR Study of Dicalcium Silicate: The Structural Influence of Sulfate and Alumina Stabilizers,” *J. Am. Ceram. Soc.*, vol. 78, no. 10, pp. 2603–2608, Oct. 1995.

[33] C.-J. Chan, W. M. Kriven, and J. F. Young, “Analytical Electron Microscopic Studies of Doped Dicalcium Silicates,” *J. Am. Ceram. Soc.*, vol. 71, no. 9, pp. 713–719, Sep. 1988.

[34] R. Sakurada, H. Mizuseki, and A. Singh, “First-Principle Study on Structural Stability of Ba-Doped Belite,” *37th Conf. Our World Concr. Struct.*, pp. 29–31, 2012.

[35] H. Manzano, E. Durgun, M. J. A. Qomi, F.-J. Ulm, R. J. M. Pellenq, and J. C. Grossman, “Impact of Chemical Impurities on the Crystalline Cement Clinker Phases Determined by Atomistic Simulations,” *Cryst. Growth Des.*, vol. 11, no. 7, pp. 2964–2972, Jul. 2011.

[36] E. Durgun, H. Manzano, R. J. M. Pellenq, and J. C. Grossman, “Understanding and Controlling the Reactivity of the Calcium Silicate phases from First Principles,” *Chem. Mater.*, vol. 24, no. 7, pp. 1262–1267, Apr. 2012.

[37] B. Erzar and P. Forquin, “An Experimental Method to Determine the Tensile Strength of Concrete at High Rates of Strain,” *Exp. Mech.*, vol. 50, no. 7, pp. 941–955, Sep. 2010.

[38] Y. B. Lu and Q. M. Li, “About the dynamic uniaxial tensile strength of concrete-like materials,” *Int. J. Impact Eng.*, vol. 38, no. 4, pp. 171–180, Apr. 2011.

[39] H. W. Reinhardt, “Strain Rate Effects on the Tensile Strength of Concrete as Predicted by Thermodynamic and Fracture Mechanics Models,” *MRS Online Proc. Libr. Arch.*, vol. 64, ed 1985.

[40] Mander J. B., Priestley M. J. N., and Park R., “Theoretical Stress-Strain Model for Confined Concrete,” *J. Struct. Eng.*, vol. 114, no. 8, pp. 1804–1826, Aug. 1988.

[41] J. Gao, W. Sun, and K. Morino, “Mechanical properties of steel fiber-reinforced, high-strength, lightweight concrete,” *Cem. Concr. Compos.*, vol. 19, no. 4, pp. 307–313, Jan. 1997.

[42] S. Ahmad, “Reinforcement corrosion in concrete structures, its monitoring and service life prediction—a review,” *Cem. Concr. Compos.*, vol. 25, no. 4, pp. 459–471, May 2003.

[43] A. Bentur, N. Berke, and S. Diamond, *Steel Corrosion in Concrete: Fundamentals and civil engineering practice*. CRC Press, 1997.

[44] S. E. Hussain, Rasheeduzzafar, A. Al-Musallam, and A. S. Al-Gahtani, “Factors affecting threshold chloride for reinforcement corrosion in concrete,” *Cem. Concr. Res.*, vol. 25, no. 7, pp. 1543–1555, Oct. 1995.

[45] S. Hong, H. Wiggenhauser, R. Helmerich, B. Dong, P. Dong, and F. Xing, “Long-term monitoring of reinforcement corrosion in concrete using ground penetrating radar,” *Corros. Sci.*, vol. 114, no. Supplement C, pp. 123–132, Jan. 2017.

[46] “NACE study estimates global corrosion cost at $2.5 trillion annually.” [Online]. Available: https://inspectioneering.com/news/2016-03-08/5202/nace-study-estimates-global-cost-of-corrosion-at-25-trillion-ann. [Accessed: 04-Nov-2017].

[47] B. A. Shaw and R. G. Kelly, “What is Corrosion?,” *Electrochem. Soc. Interface*, vol. 15, no. 1, p. 24, 2006.

[48] S. Kobayashi, R. Kobayashi, and T. Watanabe, “Control of grain boundary connectivity based on fractal analysis for improvement of intergranular corrosion resistance in SUS316L austenitic stainless steel,” *Acta Mater.*, vol. 102, no. Supplement C, pp. 397–405, Jan. 2016.

[49] A. Abbasi Aghuy, M. Zakeri, M. H. Moayed, and M. Mazinani, “Effect of grain size on pitting corrosion of 304L austenitic stainless steel,” *Corros. Sci.*, vol. 94, pp. 368–376, May 2015.

[50] E. Martinez-Lombardia *et al.*, “In Situ Scanning Tunneling Microscopy Study of Grain-Dependent Corrosion on Microcrystalline Copper,” *J. Phys. Chem. C*, vol. 118, no. 44, pp. 25421–25428, Nov. 2014.

[51] X. Zhou *et al.*, “Grain-stored energy and the propagation of intergranular corrosion in AA2xxx aluminium alloys,” *Surf. Interface Anal.*, vol. 45, no. 10, pp. 1543–1547, Oct. 2013.

[52] D. a Koleva, Y. Gonzalez-Garcia, H. M. Jonkers, and L. Polerecky, “Micro-Biologically Induced Steel Corrosion and Corrosion Control in Simulated Marine Environment: Steel Electrochemical Response and Micro-Organisms Viability within Cathodic Protection Application,” *Meet. Abstr.*, vol. MA2016-02, no. 13, pp. 1316–1316, Sep. 2016.

[53] M. A. Paez, “Corrosion of an Aluminum Alloy (AA2024) Influenced By Microorganisms of a Bacterial Consortium,” *Meet. Abstr.*, vol. MA2016-01, no. 15, pp. 937–937, Apr. 2016.

[54] K. Alasvand Zarasvand and V. R. Rai, “Microorganisms: Induction and inhibition of corrosion in metals,” *Int. Biodeterior. Biodegrad.*, vol. 87, no. Supplement C, pp. 66–74, Feb. 2014.

[55] S. A. Umoren and M. M. Solomon, “Effect of halide ions on the corrosion inhibition efficiency of different organic species – A review,” *J. Ind. Eng. Chem.*, vol. 21, no. Supplement C, pp. 81–100, Jan. 2015.

[56] Y. Qiang, S. Zhang, L. Guo, X. Zheng, B. Xiang, and S. Chen, “Experimental and theoretical studies of four allyl imidazolium-based ionic liquids as green inhibitors for copper corrosion in sulfuric acid,” *Corros. Sci.*, vol. 119, no. Supplement C, pp. 68–78, May 2017.

[57] D. Bankiewicz, S. Enestam, P. Yrjas, and M. Hupa, “Experimental studies of Zn and Pb induced high temperature corrosion of two commercial boiler steels,” *Fuel Process. Technol.*, vol. 105, no. Supplement C, pp. 89–97, Jan. 2013.

[58] Z. Li, F. Sun, Y. Shi, F. Li, and L. Ma, “Experimental study and mechanism analysis on low temperature corrosion of coal fired boiler heating surface,” *Appl. Therm. Eng.*, vol. 80, no. Supplement C, pp. 355–361, Apr. 2015.

[59] J. Lehmusto, B.-J. Skrifvars, P. Yrjas, and M. Hupa, “Comparison of potassium chloride and potassium carbonate with respect to their tendency to cause high temperature corrosion of stainless 304L steel,” *Fuel Process. Technol.*, vol. 105, no. Supplement C, pp. 98–105, Jan. 2013.

[60] J. Priss, H. Rojacz, I. Klevtsov, A. Dedov, H. Winkelmann, and E. Badisch, “High temperature corrosion of boiler steels in hydrochloric atmosphere under oil shale ashes,” *Corros. Sci.*, vol. 82, no. Supplement C, pp. 36–44, May 2014.

[61] M. G. Fontana, *Corrosion Engineering*. Tata McGraw-Hill, 2005.

[62] S. Mundra, M. Criado, S. A. Bernal, and J. L. Provis, “Chloride-induced corrosion of steel rebars in simulated pore solutions of alkali-activated concretes,” *Cem. Concr. Res.*, vol. 100, no. 10.1016/j.cemconres.2017.08.006, pp. 385–397, Oct. 2017.

[63] P. Combrade and F. Vaillant, “Corrosion of nickel alloys and stainless steels in polluted or confined PWR environments,” *Tech. Ing. Genie Nucleaire*, vol. BN3756, p. BN3756.1-BN3756.30, 2014.

[64] D. NIU and C. SUN, “Study on Interaction of Concrete Carbonation and Chloride Corrosion,” *J. Chin. Ceram. Soc.*, vol. 41, no. 8, pp. 1094–1099, Aug. 2013.

[65] S. Groff, M. Yen, and P. Lin, “Detecting Chloride Corrosion of Carbon Steel,” *2013 IPFW Stud. Res. Creat. Endeavor Symp.*, Apr. 2013.

[66] S. Palle, B. Howell, T. Hopwood, and B. Meade, “Evaluation of Deterioration of Structural Concrete Due to Chloride Intrusion and Other Damaging Mechanisms,” *Ky. Transp. Cent. Res. Rep.*, Sep. 2015.

[67] Z. Yang, H. Fischer, and R. Polder, “Synthesis and characterization of modified hydrotalcites and their ion exchange characteristics in chloride-rich simulated concrete pore solution,” *Cem. Concr. Compos.*, vol. 47, no. Supplement C, pp. 87–93, Mar. 2014.

[68] C. G. Berrocal, K. Lundgren, and I. Löfgren, “INFLUENCE OF STEEL FIBRES ON CORROSION OF REINFORCEMENT IN CONCRETE IN CHLORIDE ENVIRONMENTS: A REVIEW,” in *Chalmers Publication Library (CPL)*, 2013.

[69] S. I. Rokhlin, J.-Y. Kim, H. Nagy, and B. Zoofan, “Effect of pitting corrosion on fatigue crack initiation and fatigue life,” *Eng. Fract. Mech.*, vol. 62, no. 4–5, pp. 425–444, Mar. 1999.

[70] D. Starosvetsky, O. Khaselev, J. Starosvetsky, R. Armon, and J. Yahalom, “Effect of iron exposure in SRB media on pitting initiation,” *Corros. Sci.*, vol. 42, no. 2, pp. 345–359, Feb. 2000.

[71] A. Valor, F. Caleyo, L. Alfonso, D. Rivas, and J. M. Hallen, “Stochastic modeling of pitting corrosion: A new model for initiation and growth of multiple corrosion pits,” *Corros. Sci.*, vol. 49, no. 2, pp. 559–579, Feb. 2007.

[72] C. Liu, Q. Bi, A. Leyland, and A. Matthews, “An electrochemical impedance spectroscopy study of the corrosion behaviour of PVD coated steels in 0.5 N NaCl aqueous solution: Part II.: EIS interpretation of corrosion behaviour,” *Corros. Sci.*, vol. 45, no. 6, pp. 1257–1273, Jun. 2003.

[73] K. C. Emregül and A. A. Aksüt, “The effect of sodium molybdate on the pitting corrosion of aluminum,” *Corros. Sci.*, vol. 45, no. 11, pp. 2415–2433, Nov. 2003.

[74] Z. Szklarska-Smialowska, “Pitting corrosion of aluminum,” *Corros. Sci.*, vol. 41, no. 9, pp. 1743–1767, Aug. 1999.

[75] D. E. Williams, C. Westcott, and M. Fleischmann, “Stochastic Models of Pitting Corrosion of Stainless Steels II . Measurement and Interpretation of Data at Constant Potential,” *J. Electrochem. Soc.*, vol. 132, no. 8, pp. 1804–1811, Aug. 1985.

[76] R. A. Cottis, “4 - Electrochemical noise for corrosion monitoring,” in *Techniques for Corrosion Monitoring*, L. Yang, Ed. Woodhead Publishing, 2008, pp. 86–110.

[77] M. P. Ryan, D. E. Williams, R. J. Chater, B. M. Hutton, and D. S. McPhail, “Why stainless steel corrodes,” *Nature*, vol. 415, no. 6873, pp. 770–774, Feb. 2002.

[78] S. Papavinasam, “3 - Electrochemical polarization techniques for corrosion monitoring,” in *Techniques for Corrosion Monitoring*, L. Yang, Ed. Woodhead Publishing, 2008, pp. 49–85.

[79] P. Shukla, “7 - Thermodynamics of corrosion and potentiometric methods for measuring localized corrosion,” in *Techniques for Corrosion Monitoring*, L. Yang, Ed. Woodhead Publishing, 2008, pp. 156–186.

[80] C. S. Brossia, “11 - Electrical resistance techniques,” in *Techniques for Corrosion Monitoring*, L. Yang, Ed. Woodhead Publishing, 2008, pp. 277–292.

[81] M. A. Amin, “Metastable and stable pitting events on Al induced by chlorate and perchlorate anions—Polarization, XPS and SEM studies,” *Electrochimica Acta*, vol. 54, no. 6, pp. 1857–1863, Feb. 2009.

[82] S. Pournazari, D. M. Maijer, and E. Asselin, “FIB/SEM Study of Pitting and Intergranular Corrosion in an Al-Cu Alloy,” *CORROSION*, vol. 73, no. 8, pp. 927–941, Mar. 2017.

[83] J. Izquierdo, A. Eifert, R. M. Souto, and C. Kranz, “Simultaneous pit generation and visualization of pit topography using combined atomic force–scanning electrochemical microscopy,” *Electrochem. Commun.*, vol. 51, no. Supplement C, pp. 15–18, Feb. 2015.

[84] K. Kowal, J. DeLuccia, J. Y. Josefowicz, C. Laird, and G. C. Farrington, “In Situ Atomic Force Microscopy Observations of the Corrosion Behavior of Aluminum-Copper Alloys,” *J. Electrochem. Soc.*, vol. 143, no. 8, pp. 2471–2481, Aug. 1996.

[85] R. M. Rynders, C.-H. Paik, R. Ke, and R. C. Alkire, “Use of In Situ Atomic Force Microscopy to Image Corrosion at Inclusions,” *J. Electrochem. Soc.*, vol. 141, no. 6, pp. 1439–1445, Jun. 1994.

[86] P. Leblanc and G. S. Frankel, “A Study of Corrosion and Pitting Initiation of AA2024-T3 Using Atomic Force Microscopy,” *J. Electrochem. Soc.*, vol. 149, no. 6, pp. B239–B247, Jun. 2002.

[87] X. Shi *et al.*, “Microstructure and Pitting Corrosion Behavior of Plasma-Sprayed Fe-Si Nanocomposite Coating,” *J. Therm. Spray Technol.*, vol. 25, no. 5, pp. 1079–1086, Jun. 2016.

[88] W. Liu, F. Cao, Y. Xia, L. Chang, and J. Zhang, “Localized Corrosion of Magnesium Alloys in NaCl Solutions Explored by Scanning Electrochemical Microscopy in Feedback Mode,” *Electrochimica Acta*, vol. 132, no. Supplement C, pp. 377–388, Jun. 2014.

[89] A. K. Yagati, J. Min, and J.-W. Choi, “Electrochemical Scanning Tunneling Microscopy (ECSTM) – From Theory to Future Applications,” 2014.

[90] A. Chiba, I. Muto, Y. Sugawara, and N. Hara, “Effect of atmospheric aging on dissolution of MnS inclusions and pitting initiation process in type 304 stainless steel,” *Corros. Sci.*, vol. 106, no. Supplement C, pp. 25–34, May 2016.

[91] T. Ohtsuka, A. Nishikata, M. Sakairi, and K. Fushimi, “Micro-electrochemical Approach for Corrosion Study,” in *Electrochemistry for Corrosion Fundamentals*, Springer, Singapore, 2018, pp. 97–116.

[92] F. M. Lea and T. W. Parker, “The Quaternary System CaO-Al2O3-SiO2-Fe2O3 in Relation to Cement Technology.”

[93] J. H. Welch and W. Gutt, “Tricalcium Silicate and Its Stability Within the System CaO-SiO2,” *J. Am. Ceram. Soc.*, vol. 42, no. 1, pp. 11–15, Jan. 1959.

[94] W. G. Mumme, R. J. Hill, G. Bushnell-Wye, and E. R. Segnit, “Rietveld crystal structure refinements, crystal chemistry and calculated powder diffraction data for the polymorphs of dicalcium silicate and related phases,” 1995.

[95] C. J. Chan, W. M. Kriven, and J. F. Young, “Physical Stabilization of the β→γ Transformation in Dicalcium Silicate,” *J. Am. Ceram. Soc.*, vol. 75, no. 6, pp. 1621–1627, Jun. 1992.

[96] E. R. Gobechiya, N. A. Yamnova, A. E. Zadov, and V. M. Gazeev, “Calcio-olivine γ-Ca2SiO4: I. Rietveld refinement of the crystal structure,” *Crystallogr. Rep.*, vol. 53, no. 3, pp. 404–408, May 2008.

[97] Y. J. Kim, I. Nettleship, and W. M. Kriven, “Phase Transformations in Dicalcium Silicate: II, TEM Studies of Crystallography, Microstructure, and Mechanisms,” *J. Am. Ceram. Soc.*, vol. 75, no. 9, pp. 2407–2419, Sep. 1992.

[98] H. Saalfeld, “X-Ray Investigation of Single-Crystals of Beta-Ca2sio4 (larnite) at High-Temperatures,” *Am. Mineral.*, vol. 60, no. 9–10, pp. 824–827, 1975.

[99] J. N. Maycock and M. McCarty, “Crystal lattice defects in di-calcium silicate,” *Cem. Concr. Res.*, vol. 3, no. 6, pp. 701–713, Nov. 1973.

[100] K. Fujii and W. Kondo, “Rate and Mechanism of Hydration of β-Dicalcium Silicate,” *J. Am. Ceram. Soc.*, vol. 62, no. 3–4, pp. 161–167, Mar. 1979.

[101] K. Sasaki, H. Ishida, Y. Okada, and T. Mitsuda, “Highly Reactive β-Dicalcium Silicate: V, Influence of Specific Surface Area on Hydration,” *J. Am. Ceram. Soc.*, vol. 76, no. 4, pp. 870–874, Apr. 1993.

[102] J. Li, C. Y. Zhou, and Y. J. Yang, “Effects of Foreign Ions on Minerals of High Belite-Calcium Sulfoaluminate Cement,” *Mater. Sci. Forum*, vol. 743–744, pp. 239–244, 2013.

[103] Q. Wang *et al.*, “Relation between reactivity and electronic structure for α’L-, β- and γ-dicalcium silicate: A first-principles study,” *Cem. Concr. Res.*, vol. 57, no. Supplement C, pp. 28–32, Mar. 2014.

[104] P. Giannozzi *et al.*, “QUANTUM ESPRESSO: a modular and open-source software project for quantum simulations of materials.,” *J. Phys. Condens. Matter Inst. Phys. J.*, vol. 21, no. 39, pp. 395502–395502, Sep. 2009.

[105] S. E. Koonin and D. C. Meredith, “Computational physics : FORTRAN version,” *CERN Document Server*, 1990. [Online]. Available: http://cds.cern.ch/record/208294. [Accessed: 23-Oct-2017].

[106] P. Barnes and J. Bensted, *Structure and Performance of Cements, Second Edition*. CRC Press, 2002.

[107] G. Kresse and J. Furthmüller, “Efficient iterative schemes for ab initio total-energy calculations using a plane-wave basis set,” *Phys. Rev. B*, vol. 54, no. 16, pp. 11169–11186, Oct. 1996.

[108] S. J. Clark *et al.*, “First principles methods using CASTEP,” *Z. Für Krist. - Cryst. Mater.*, vol. 220, no. 5/6, pp. 567–570, 2009.

[109] M. Born and R. Oppenheimer, “Zur Quantentheorie der Molekeln,” *Ann. Phys.*, vol. 389, no. 20, pp. 457–484, Jan. 1927.

[110] Y. K. Pan, “Molecular quantum mechanics: An introduction to quantum chemistry (Atkins, P.W.),” *J. Chem. Educ.*, vol. 48, no. 4, p. A294, Apr. 1971.

[111] P. W. Atkins and R. S. Friedman, *Molecular Quantum Mechanics*. OUP Oxford, 2011.

[112] W. Kohn and L. J. Sham, “Self-Consistent Equations Including Exchange and Correlation Effects,” *Phys. Rev.*, vol. 140, no. 4A, pp. A1133–A1138, Nov. 1965.

[113] A. D. Becke, “A new mixing of Hartree–Fock and local density-functional theories,” *J. Chem. Phys.*, vol. 98, no. 2, pp. 1372–1377, Jan. 1993.

[114] J. P. Perdew, K. Burke, and M. Ernzerhof, “Generalized Gradient Approximation Made Simple,” *Phys. Rev. Lett.*, vol. 77, no. 18, pp. 3865–3868, Oct. 1996.

[115] A. D. Becke, “Density-functional exchange-energy approximation with correct asymptotic behavior,” *Phys. Rev. A*, vol. 38, no. 6, pp. 3098–3100, Sep. 1988.

[116] J. P. Perdew and Y. Wang, “Pair-distribution function and its coupling-constant average for the spin-polarized electron gas,” *Phys. Rev. B*, vol. 46, no. 20, pp. 12947–12954, Nov. 1992.

[117] C. Lee, W. Yang, and R. G. Parr, “Development of the Colle-Salvetti correlation-energy formula into a functional of the electron density,” *Phys. Rev. B*, vol. 37, no. 2, pp. 785–789, Jan. 1988.

[118] A. D. Becke, “Density-functional thermochemistry. III. The role of exact exchange,” *J. Chem. Phys.*, vol. 98, no. 7, pp. 5648–5652, Apr. 1993.

[119] K. K and J. Kd, “Comparison of Density-Functional and Mp2 Calculations on the Water Monomer and Dimer,” *J. Phys. Chem.*, vol. 98, no. 40, pp. 10089–10094, 1994.

[120] D. Fj, F. Jw, S. Pj, and F. Mj, “Ab-Initio Calculation of Vibrational Absorption and Circular-Dichroism Spectra Using Density-Functional Force-Fields - A Comparison of Local, Nonlocal, and Hybrid Density Functionals,” *J. Phys. Chem.*, vol. 99, no. 46, pp. 16883–16902, 1995.

[121] D. R. Hamann, M. Schlüter, and C. Chiang, “Norm-Conserving Pseudopotentials,” *Phys. Rev. Lett.*, vol. 43, no. 20, pp. 1494–1497, Nov. 1979.

[122] D. Vanderbilt, "Soft self-consistent pseudopotentials in a generalized eigenvalue formalism," *Phys. Rev. B*, vol. 41, no. 11, pp. 7892–7895, Apr. 1990.

[123] P. E. Blöchl, "Projector augmented-wave method," *Phys. Rev. B*, vol. 50, no. 24, pp. 17953–17979, Dec. 1994.

[124] W. G. Mumme, L. M. D. Cranswick, and B. C. Chakoumakos, "Rietveld crystal structure refinements from high temperature neutron powder diffraction data for the polymorphs of dicalcium silicate," 1996.

[125] C. Feigl, S. P. Russo, and A. S. Barnard, "A comparative density functional theory investigation of the mechanical and energetic properties of ZnS," *Mol. Simul.*, vol. 37, no. 4, pp. 321–333, Apr. 2011.

[126] N. Pantha, K. Belbase, and N. P. Adhikari, "First-principles study of the interaction of hydrogen molecular on Na-adsorbed graphene," *Appl. Nanosci.*, vol. 5, no. 4, pp. 393–402, Apr. 2015.

[127] C. Froese Fischer, "General Hartree-Fock program," *Comput. Phys. Commun.*, vol. 43, no. 3, pp. 355–365, Feb. 1987.

[128] R. Fletcher and R. Fletcher, "The Theory of Constrained Optimization," in *Practical Methods of Optimization*, John Wiley & Sons, Ltd, 2000, pp. 195–228.

[129] R. Golesorkhtabar, P. Pavone, J. Spitaler, P. Puschnig, and C. Draxl, "ElaStic: A tool for calculating second-order elastic constants from first principles," *Comput. Phys. Commun.*, vol. 184, no. 8, pp. 1861–1873, Aug. 2013.

[130] Z. Wu, E. Zhao, H. Xiang, X. Hao, X. Liu, and J. Meng, "Crystal structures and elastic properties of superhard IrN2 and IrN3 from first principles," *Phys. Rev. B*, vol. 76, p. 054115, 2007.

[131] H. Manzano, J. S. Dolado, and A. Ayuela, "Elastic properties of the main species present in Portland cement pastes," *Acta Mater.*, vol. 57, no. 5, pp. 1666–1674, Mar. 2009.

[132] M. Caro, S. Schulz, and E. O'Reilly, "Comparison of stress and total energy methods for calculation of elastic properties of semiconductors," *J. Phys. Condens. Matter*, vol. 25, no. 2, pp. 1–13, 2013.

[133] J. Huang, L. Valenzano, T. V. Singh, R. Pandey, and G. Sant, "Influence of (Al, Fe, Mg) Impurities on Triclinic Ca3SiO5: Interpretations from DFT Calculations," *Cryst. Growth Des.*, vol. 14, no. 5, pp. 2158–2171, May 2014.

[134] K. Velez, S. Maximilien, D. Damidot, G. Fantozzi, and F. Sorrentino, "Determination by nanoindentation of elastic modulus and hardness of pure constituents of Portland cement clinker," *Cem. Concr. Res.*, vol. 31, no. 4, pp. 555–561, Apr. 2001.

[135] W. C. Oliver and G. M. Pharr, "An improved technique for determining hardness and elastic modulus using load and displacement sensing indentation experiments," *J. Mater. Res.*, vol. 7, no. 6, pp. 1564–1583, Jun. 1992.

[136] J. Haas, G. Robinson, and B. Hemingway, "Thermodynamic Tabulations for Selected Phases in the System Cao-Al2o3-Sio2-H2o at 101.325 Kpa (1 Atm) Between 273.15 and 1800-K," *J. Phys. Chem. Ref. Data*, vol. 10, no. 3, pp. 575–669, 1981.

[137] E. Durgun, H. Manzano, R. J. M. Pellenq, and J. C. Grossman, "Understanding and Controlling the Reactivity of the Calcium Silicate phases from First Principles," *Chem. Mater.*, vol. 24, no. 7, pp. 1262–1267, Apr. 2012.

[138] S. L. Strong and R. Kaplow, “The structure of crystalline B2O3,” *Acta Crystallogr. B*, vol. 24, no. 8, pp. 1032–1036, Aug. 1968.

[139] G.-C. Lai, T. Nojiri, and K. Nakano, “Studies of the stability of β-Ca2SiO4 doped by minor ions,” *Cem. Concr. Res.*, vol. 22, no. 5, pp. 743–754, Sep. 1992.

[140] Y.-M. Kim and S.-H. Hong, “Influence of Minor Ions on the Stability and Hydration Rates of β-Dicalcium Silicate,” *J. Am. Ceram. Soc.*, vol. 87, no. 5, pp. 900–905, May 2004.

[141] E. Durgun, H. Manzano, P. V. Kumar, and J. C. Grossman, “The Characterization, Stability, and Reactivity of Synthetic Calcium Silicate Surfaces from First Principles,” *J. Phys. Chem. C*, vol. 118, no. 28, pp. 15214–15219, Jul. 2014.

[142] G. Kresse and J. Furthmüller, “Efficiency of ab-initio total energy calculations for metals and semiconductors using a plane-wave basis set,” *Comput. Mater. Sci.*, vol. 6, no. 1, pp. 15–50, Jul. 1996.

[143] A. T. Lech, C. L. Turner, R. Mohammadi, S. H. Tolbert, and R. B. Kaner, “Structure of superhard tungsten tetraboride: A missing link between MB2 and MB12 higher borides,” *Proc. Natl. Acad. Sci.*, vol. 112, no. 11, pp. 3223–3228, Mar. 2015.

[144] G. Kresse and D. Joubert, “From ultrasoft pseudopotentials to the projector augmented-wave method,” *Phys. Rev. B*, vol. 59, no. 3, pp. 1758–1775, Jan. 1999.

[145] V. L. Deringer, M. Lumeij, R. P. Stoffel, and R. Dronskowski, “Ab initio study of the high-temperature phase transition in crystalline GeO2,” *J. Comput. Chem.*, vol. 34, no. 27, pp. 2320–2326, Oct. 2013.

[146] D. B. Ghosh and S. de Gironcoli, “A new look on the nature of high-spin to low-spin transition in Fe2O3,” *Condens. Matter*, May 2009.

[147] G. Rollmann, A. Rohrbach, P. Entel, and J. Hafner, “First-principles calculation of the structure and magnetic phases of hematite,” *Phys. Rev. B*, vol. 69, no. 16, p. 165107, Apr. 2004.

[148] A. I. Liechtenstein, V. I. Anisimov, and J. Zaanen, “Density-functional theory and strong interactions: Orbital ordering in Mott-Hubbard insulators,” *Phys. Rev. B*, vol. 52, no. 8, pp. R5467–R5470, Aug. 1995.

[149] H.-P. Komsa, T. T. Rantala, and A. Pasquarello, “Finite-size supercell correction schemes for charged defect calculations,” *Phys. Rev. B*, vol. 86, no. 4, p. 045112, Jul. 2012.

[150] G. Makov and M. C. Payne, “Periodic boundary conditions in ab initio calculations,” *Phys. Rev. B*, vol. 51, no. 7, pp. 4014–4022, Feb. 1995.

[151] J. Neugebauer and M. Scheffler, “Adsorbate-substrate and adsorbate-adsorbate interactions of Na and K adlayers on Al(111),” *Phys. Rev. B*, vol. 46, no. 24, pp. 16067–16080, Dec. 1992.

[152] N. D. M. Hine, K. Frensch, W. M. C. Foulkes, and M. W. Finnis, “Supercell size scaling of density functional theory formation energies of charged defects,” *Phys. Rev. B*, vol. 79, no. 2, p. 024112, Jan. 2009.

[153] F. A. Kröger and H. J. Vink, “Relations between the Concentrations of Imperfections in Crystalline Solids,” in *Solid State Physics*, vol. 3, Supplement C vols., F. Seitz and D. Turnbull, Eds. Academic Press, 1956, pp. 307–435.

[154] K. Suzuki, S. Ito, T. Nishikawa, and I. Shinno, “Effect of Na, K and Fe on the formation of α- and β-Ca2SiO4,” *Cem. Concr. Res.*, vol. 16, no. 6, pp. 885–892, Nov. 1986.

[155] R. D. Shannon, “Revised effective ionic radii and systematic studies of interatomic distances in halides and chalcogenides,” *Acta Crystallogr. A*, vol. 32, no. 5, pp. 751–767, Sep. 1976.

[156] T. L. Barry, “Fluorescence of Eu2+-Activated Phases in Binary Alkaline Earth Orthosilicate Systems,” *J. Electrochem. Soc.*, vol. 115, no. 11, pp. 1181–1184, Nov. 1968.

[157] S. Lee, S.-H. Hong, and Y. J. Kim, “Synthesis and Luminescent Properties of (Sr,M)2Si(O1−xNx)4:Eu2+ (M: Mg2+, Ca2+, Ba2+),” *J. Electrochem. Soc.*, vol. 159, no. 5, pp. J163–J167, Jan. 2012.

[158] M. Bauchy, “Structural, vibrational, and elastic properties of a calcium aluminosilicate glass from molecular dynamics simulations: The role of the potential,” *J. Chem. Phys.*, vol. 141, no. 2, p. 024507, Jul. 2014.

[159] M. M. Smedskjaer, J. C. Mauro, R. E. Youngman, C. L. Hogue, M. Potuzak, and Y. Yue, “Topological Principles of Borosilicate Glass Chemistry,” *J. Phys. Chem. B*, vol. 115, no. 44, pp. 12930–12946, Nov. 2011.

[160] W. EYSEL and T. HAHN, “Polymorphism and solid solution of Ca2GeO4 and Ca2SiO4,” *Z. Für Krist. - Cryst. Mater.*, vol. 131, no. 1–6, pp. 322–341, 2015.

[161] F. Agulló-López, C. R. A. Catlow, and P. D. Townsend, *Point defects in materials*. London; San Diego: Academic Press, 1988.

[162] M. Greenberg, E. Wachtel, I. Lubomirsky, J. Fleig, and J. Maier, “Elasticity of Solids with a Large Concentration of Point Defects,” *Adv. Funct. Mater.*, vol. 16, no. 1, pp. 48–52, Jan. 2006.

[163] K. D. Kreuer, T. Dippel, Y. M. Baikov, and J. Maier, “Water solubility, proton and oxygen diffusion in acceptor doped BaCeO3: A single crystal analysis,” *Solid State Ion.*, vol. 86–88, no. Part 1, pp. 613–620, Jul. 1996.

[164] M. V. Ganduglia-Pirovano, A. Hofmann, and J. Sauer, “Oxygen vacancies in transition metal and rare earth oxides: Current state of understanding and remaining challenges,” *Surf. Sci. Rep.*, vol. 62, no. 6, pp. 219–270, Jun. 2007.

[165] B. Wang, R. J. Lewis, and A. N. Cormack, “Computer simulations of large-scale defect clustering and nanodomain structure in gadolinia-doped ceria,” *Acta Mater.*, vol. 59, no. 5, pp. 2035–2045, Mar. 2011.

[166] M. O. Zacate, L. Minervini, D. J. Bradfield, R. W. Grimes, and K. E. Sickafus, “Defect cluster formation in M2O3-doped cubic ZrO2,” *Solid State Ion.*, vol. 128, no. 1, pp. 243–254, Feb. 2000.

[167] “ASSESSMENT OF THE GLOBAL COST OF CORROSION.” [Online]. Available: http://impact.nace.org/economic-impact.aspx. [Accessed: 04-Nov-2017].

[168] G. J. Verbeck, “Mechanisms of Corrosion of Steel in Concrete,” *Spec. Publ.*, vol. 49, pp. 21–38, Jan. 1975.

[169] CSI, “Recycling Concrete (Full Report),” 2009. .

[170] L. Xing, “Evaluation of multiple corrosion protection systems and corrosion inhibitors for reinforced concrete bridge decks,” D.Eng., 2010.

[171] D. W. Pfeifer, “HIGH PERFORMANCE CONCRETE AND REINFORCING STEEL WITH A 100-YEAR SERVICE LIFE,” *PCI J.*, vol. 45, no. 3, Jun. 2000.

[172] J. A. González, C. Andrade, C. Alonso, and S. Feliu, “Comparison of rates of general corrosion and maximum pitting penetration on concrete embedded steel reinforcement,” *Cem. Concr. Res.*, vol. 25, no. 2, pp. 257–264, Feb. 1995.

[173] J. A. González, S. Feliú, P. Rodríguez, E. Ramírez, C. Alonso, and C. Andrade, “Some questions on the corrosion of steel in concrete—Part I: when, how and how much steel corrodes,” *Mater. Struct.*, vol. 29, no. 1, p. 40, Jan. 1996.

[174] B. Elsener, “Macrocell corrosion of steel in concrete – implications for corrosion monitoring,” *Cem. Concr. Compos.*, vol. 24, no. 1, pp. 65–72, Feb. 2002.

[175] T. P. Hoar, D. C. Mears, and G. P. Rothwell, “The relationships between anodic passivity, brightening and pitting,” *Corros. Sci.*, vol. 5, no. 4, pp. 279–289, Jan. 1965.

[176] G. S. Frankel and N. Sridhar, “Understanding localized corrosion,” *Mater. Today*, vol. 11, no. 10, pp. 38–44, Oct. 2008.

[177] D. L. Spellman and R. F. Stratfull, “CHLORIDES AND BRIDGE DECK DETERIORATION,” Nov. 1969.

[178] C. L. Page, N. R. Short, and W. R. Holden, “The influence of different cements on chloride-induced corrosion of reinforcing steel,” *Cem. Concr. Res.*, vol. 16, no. 1, pp. 79–86, Jan. 1986.

[179] X. Shi, L. Fay, Z. Yang, T. A. Nguyen, and Y. Liu, “Corrosion of Deicers to Metals in Transportation Infrastructure: Introduction and Recent Developments,” *Corros. Rev.*, vol. 27, no. 1–2, pp. 23–52, 2011.

[180] A. Bhattacharya, “Stress corrosion cracking of duplex stainless steels in caustic solutions,” Ph.D., 2008.

[181] Y. Zhao, J. Yu, and W. Jin, “Damage analysis and cracking model of reinforced concrete structures with rebar corrosion,” *Corros. Sci.*, vol. 53, no. 10, pp. 3388–3397, Oct. 2011.

[182] J. Hou, X. Fu, and D. D. L. Chung, “Improving both bond strength and corrosion resistance of steel rebar in concrete by water immersion or sand blasting of rebar,” *Cem. Concr. Res.*, vol. 27, no. 5, pp. 679–684, May 1997.

[183] K. Bhargava, A. K. Ghosh, Y. Mori, and S. Ramanujam, “Corrosion-induced bond strength degradation in reinforced concrete—Analytical and empirical models,” *Nucl. Eng. Des.*, vol. 237, no. 11, pp. 1140–1157, Jun. 2007.

[184] C. Arya and P. R. W. Vassie, “Influence of cathode-to-anode area ratio and separation distance on galvanic corrosion currents of steel in concrete containing chlorides,” *Cem. Concr. Res.*, vol. 25, no. 5, pp. 989–998, Jul. 1995.

[185] A. Nasser, A. Clément, S. Laurens, and A. Castel, “Influence of steel–concrete interface condition on galvanic corrosion currents in carbonated concrete,” *Corros. Sci.*, vol. 52, no. 9, pp. 2878–2890, Sep. 2010.

[186] S. Dong, B. Zhao, C. Lin, R. Du, R. Hu, and G. X. Zhang, “Corrosion behavior of epoxy/zinc duplex coated rebar embedded in concrete in ocean environment,” *Constr. Build. Mater.*, vol. 28, no. 1, pp. 72–78, Mar. 2012.

[187] I. Galan and F. P. Glasser, “Chloride in cement,” *Adv. Cem. Res.*, vol. 27, no. 2, pp. 63–97, Feb. 2015.

[188] H. B. Gunay, O. B. Isgor, and P. Ghods, “Kinetics of Passivation and Chloride-Induced Depassivation of Iron in Simulated Concrete Pore Solutions Using Electrochemical Quartz Crystal Nanobalance,” *CORROSION*, vol. 71, no. 5, pp. 615–627, Dec. 2014.

[189] A. Vollpracht, B. Lothenbach, R. Snellings, and J. Haufe, “The pore solution of blended cements: a review,” *Mater. Struct.*, vol. 49, no. 8, pp. 3341–3367, Aug. 2016.

[190] J. E. Castle and C. R. Clayton, “The use of in the x-ray photo-electron spectroscopy analyses of passive layers on stainless steel,” *Corros. Sci.*, vol. 17, no. 1, pp. 7–26, Jan. 1977.

[191] P. Ghods, O. Burkan Isgor, F. Bensebaa, and D. Kingston, “Angle-resolved XPS study of carbon steel passivity and chloride-induced depassivation in simulated concrete pore solution,” *Corros. Sci.*, vol. 58, no. Supplement C, pp. 159–167, May 2012.

[192] M. F. Kaplan, “Crack Propagation and the Fracture of Concrete,” *J. Proc.*, vol. 58, no. 11, pp. 591–610, Nov. 1961.

[193] G. Song, H. Gu, Y. L. Mo, T. T. C. Hsu, and H. Dhonde, “Concrete structural health monitoring using embedded piezoceramic transducers,” *Smart Mater. Struct.*, vol. 16, no. 4, p. 959, 2007.

[194] V. C. Li, H. Stang, and H. Krenchel, “Micromechanics of crack bridging in fibre-reinforced concrete,” *Mater. Struct.*, vol. 26, no. 8, pp. 486–494, Oct. 1993.

[195] D. J. Anstice, C. L. Page, and M. M. Page, “The pore solution phase of carbonated cement pastes,” *Cem. Concr. Res.*, vol. 35, no. 2, pp. 377–383, Feb. 2005.

[196] V. T. Ngala and C. L. Page, “EFFECTS OF CARBONATION ON PORE STRUCTURE AND DIFFUSIONAL PROPERTIES OF HYDRATED CEMENT PASTES,” *Cem. Concr. Res.*, vol. 27, no. 7, pp. 995–1007, Jul. 1997.

[197] B. Huet, V. L’Hostis, F. Miserque, and H. Idrissi, “Electrochemical behavior of mild steel in concrete: Influence of pH and carbonate content of concrete pore solution,” *Electrochimica Acta*, vol. 51, no. 1, pp. 172–180, Oct. 2005.

[198] B. Kabanov, R. Burstein, and A. Frumkin, “Kinetics of electrode processes on the iron electrode,” *Discuss. Faraday Soc.*, vol. 1, pp. 259–269, 1947.

[199] M. A. Streicher, “Pitting Corrosion of 18Cr-8Ni Stainless Steel,” *J. Electrochem. Soc.*, vol. 103, no. 7, pp. 375–390, Jul. 1956.

[200] G. S. Frankel, “Pitting Corrosion of Metals A Review of the Critical Factors,” *J. Electrochem. Soc.*, vol. 145, no. 6, pp. 2186–2198, Jun. 1998.

[201] F. H. Assaf, S. S. Abd El-Rehiem, and A. M. Zaky, “Pitting corrosion of zinc in neutral halide solutions,” *Mater. Chem. Phys.*, vol. 58, no. 1, pp. 58–63, Feb. 1999.

[202] N. D. Greene and M. G. Fontana, “A Critical Analysis of Pitting Corrosion,” *CORROSION*, vol. 15, no. 1, pp. 41–47, Jan. 1959.

[203] C. L. Page, N. R. Short, and A. El Tarras, “Diffusion of chloride ions in hardened cement pastes,” *Cem. Concr. Res.*, vol. 11, no. 3, pp. 395–406, May 1981.

[204] N. Gowripalan, V. Sirivivatnanon, and C. C. Lim, “Chloride diffusivity of concrete cracked in flexure,” *Cem. Concr. Res.*, vol. 30, no. 5, pp. 725–730, May 2000.

[205] C. Andrade, “Calculation of chloride diffusion coefficients in concrete from ionic migration measurements,” *Cem. Concr. Res.*, vol. 23, no. 3, pp. 724–742, May 1993.

[206] D. R. Kester, I. W. Duedall, D. N. Connors, and R. M. Pytkowicz, “Preparation of Artificial Seawater,” *Limnol. Oceanogr.*, vol. 12, no. 1, pp. 176–179, Apr. 1967.

[207] E.-L. Thunqvist, “Regional increase of mean chloride concentration in water due to the application of deicing salt,” *Sci. Total Environ.*, vol. 325, no. 1, pp. 29–37, Jun. 2004.

[208] K. K. Turekian and K. H. Wedepohl, “Distribution of the Elements in Some Major Units of the Earth’s Crust,” *GSA Bull.*, vol. 72, no. 2, pp. 175–192, Feb. 1961.

[209] J. M. Kolotyrkin, “Pitting Corrosion of Metals,” *CORROSION*, vol. 19, no. 8, p. 261t–268t, Aug. 1963.

[210] Y. Liu and R. E. Weyers, “Modeling the Time-to-Corrosion Cracking in Chloride Contaminated Reinforced Concrete Structures,” *Mater. J.*, vol. 95, no. 6, pp. 675–680, Nov. 1998.

[211] K. A. T. Vu and M. G. Stewart, “Structural reliability of concrete bridges including improved chloride-induced corrosion models,” *Struct. Saf.*, vol. 22, no. 4, pp. 313–333, Jan. 2000.

[212] P. Refait and J.-M. R. Génin, “The oxidation of ferrous hydroxide in chloride-containing aqueous media and pourbaix diagrams of green rust one,” *Corros. Sci.*, vol. 34, no. 5, pp. 797–819, May 1993.

[213] P. C. Pistorius and G. T. Burstein, “Metastable Pitting Corrosion of Stainless Steel and the Transition to Stability,” *Philos. Trans. R. Soc. Lond. Math. Phys. Eng. Sci.*, vol. 341, no. 1662, pp. 531–559, Dec. 1992.

[214] D. E. Williams, T. F. Mohiuddin, and Y. Y. Zhu, “Elucidation of a Trigger Mechanism for Pitting Corrosion of Stainless Steels Using Submicron Resolution Scanning Electrochemical and Photoelectrochemical Microscopy,” *J. Electrochem. Soc.*, vol. 145, no. 8, pp. 2664–2672, Aug. 1998.

[215] H. W. Pickering and R. P. Frankenthal, “On the Mechanism of Localized Corrosion of Iron and Stainless Steel I . Electrochemical Studies,” *J. Electrochem. Soc.*, vol. 119, no. 10, pp. 1297–1304, Oct. 1972.

[216] G. S. Frankel, L. Stockert, F. Hunkeler, and H. Boehni, “Metastable Pitting of Stainless Steel,” *CORROSION*, vol. 43, no. 7, pp. 429–436, Jul. 1987.

[217] R. P. Frankenthal and H. W. Pickering, “On the Mechanism of Localized Corrosion of Iron and Stainless Steel II . Morphological Studies,” *J. Electrochem. Soc.*, vol. 119, no. 10, pp. 1304–1310, Oct. 1972.

[218] P. M. Natishan and E. McCafferty, “The Mechanism of Blister Formation and Rupture in the Pitting of Ion-Implanted Aluminum,” *J. Electrochem. Soc.*, vol. 136, no. 1, pp. 53–58, Jan. 1989.

[219] N. J. Laycock, S. P. White, J. S. Noh, P. T. Wilson, and R. C. Newman, “Perforated Covers for Propagating Pits,” *J. Electrochem. Soc.*, vol. 145, no. 4, pp. 1101–1108, Apr. 1998.

[220] P. Ernst, N. J. Laycock, M. H. Moayed, and R. C. Newman, “The mechanism of lacy cover formation in pitting,” *Corros. Sci.*, vol. 39, no. 6, pp. 1133–1136, Jun. 1997.

[221] H.-H. Strehblow, “Nucleation and Repassivation of Corrosion Pits for Pitting on Iron and Nickel,” *Mater. Corros.*, vol. 27, no. 11, pp. 792–799, Nov. 1976.

[222] R. C. Newman, H. S. Isaacs, and B. Alman, “Effects of Sulfur Compounds on the Pitting Behavior of Type 304 Stainless Steel in Near-Neutral Chloride Solutions,” *CORROSION*, vol. 38, no. 5, pp. 261–265, May 1982.

[223] R. C. Alkire and K. P. Wong, “The corrosion of single pits on stainless steel in acidic chloride solution,” *Corros. Sci.*, vol. 28, no. 4, pp. 411–421, Jan. 1988.

[224] P. C. Pistorius and G. T. Burstein, “Growth of corrosion pits on stainless steel in chloride solution containing dilute sulphate,” *Corros. Sci.*, vol. 33, no. 12, pp. 1885–1897, Dec. 1992.

[225] J. R. Scully, N. D. Budiansky, Y. Tiwary, A. S. Mikhailov, and J. L. Hudson, “An alternate explanation for the abrupt current increase at the pitting potential,” *Corros. Sci.*, vol. 50, no. 2, pp. 316–324, Feb. 2008.

[226] T. C. Lindley, P. Mcintyre, and P. J. Trant, “Fatigue-crack initiation at corrosion pits,” *Met. Technol.*, vol. 9, no. 1, pp. 135–142, Jan. 1982.

[227] Dolley, Lee, and Wei, “The effect of pitting corrosion on fatigue life,” *Fatigue Fract. Eng. Mater. Struct.*, vol. 23, no. 7, pp. 555–560, Jul. 2000.

[228] R. Pérez-Mora, T. Palin-Luc, C. Bathias, and P. C. Paris, “Very high cycle fatigue of a high strength steel under sea water corrosion: A strong corrosion and mechanical damage coupling,” *Int. J. Fatigue*, vol. 74, pp. 156–165, May 2015.

[229] S. J. Kim and S. G. Hong, “A study on pitting initiation mechanism of super-austenitic stainless steel weld in chloride environment,” *J. Mater. Res.*, vol. 31, no. 21, pp. 3345–3351, Nov. 2016.

[230] P. Marcus, V. Maurice, and H.-H. Strehblow, “Localized corrosion (pitting): A model of passivity breakdown including the role of the oxide layer nanostructure,” *Corros. Sci.*, vol. 50, no. 9, pp. 2698–2704, Sep. 2008.

[231] H. Boehni, “Breakdown of passivity and localized corrosion processes,” *Langmuir*, vol. 3, no. 6, pp. 924–930, Nov. 1987.

[232] T. P. Hoar and W. R. Jacob, “Breakdown of Passivity of Stainless Steel by Halide Ions,” *Nature*, vol. 216, no. 5122, pp. 1299–1301, Dec. 1967.

[233] D. de la Fuente *et al.*, “Corrosion mechanisms of mild steel in chloride-rich atmospheres,” *Mater. Corros.*, vol. 67, no. 3, pp. 227–238, Mar. 2016.

[234] V. Cicek, *Corrosion Engineering and Cathodic Protection Handbook: With an Extensive Question and Answer Section*. John Wiley & Sons, 2017.

[235] N. Sato, “A theory for breakdown of anodic oxide films on metals,” *Electrochimica Acta*, vol. 16, no. 10, pp. 1683–1692, Oct. 1971.

[236] N. Sato, K. Kudo, and T. Noda, “The anodic oxide film on iron in neutral solution,” *Electrochimica Acta*, vol. 16, no. 11, pp. 1909–1921, Nov. 1971.

[237] H.-H. Strehblow, “Breakdown of passivity and localized corrosion: Theoretical concepts and fundamental experimental results,” *Mater. Corros.*, vol. 35, no. 10, pp. 437–448, Oct. 1984.

[238] P. Marcus and J.-M. Herbelin, “The entry of chloride ions into passive films on nickel studied by spectroscopic (ESCA) and nuclear (36Cl radiotracer) methods,” *Corros. Sci.*, vol. 34, no. 7, pp. 1123–1145, Jul. 1993.

[239] J. A. Bardwell, B. MacDougall, and G. I. Sproule, “Use of SIMS to Investigate the Induction Stage in the Pitting of Iron,” *J. Electrochem. Soc.*, vol. 136, no. 5, pp. 1331–1336, May 1989.

[240] P. Marcus, *Corrosion Mechanisms in Theory and Practice, Third Edition*. CRC Press, 2011.

[241] C. Y. Chao, L. F. Lin, and D. D. Macdonald, “A Point Defect Model for Anodic Passive Films I . Film Growth Kinetics,” *J. Electrochem. Soc.*, vol. 128, no. 6, pp. 1187–1194, Jun. 1981.

[242] G. T. Burstein, C. Liu, R. M. Souto, and S. P. Vines, “Origins of pitting corrosion,” *Corros. Eng. Sci. Technol.*, vol. 39, no. 1, pp. 25–30, Mar. 2004.

[243] G. Wranglén, “Review article on the influence of sulphide inclusions on the corrodibility of Fe and steel,” *Corros. Sci.*, vol. 9, no. 8, pp. 585–602, Jan. 1969.

[244] Z. Szklarska-Smialowska, “Influence of Sulfide Inclusions on the Pitting Corrosion of Steels,” *CORROSION*, vol. 28, no. 10, pp. 388–396, Oct. 1972.

[245] D. E. Williams and Y. Y. Zhu, “Explanation for Initiation of Pitting Corrosion of Stainless Steels at Sulfide Inclusions,” *J. Electrochem. Soc.*, vol. 147, no. 5, pp. 1763–1766, May 2000.

[246] M. Smialowski, Z. Szklarska-Smialowska, M. Rychcik, and A. Szummer, “Effect of sulphide inclusions in a commercial stainless steel on the nucleation of corrosion pits,” *Corros. Sci.*, vol. 9, no. 2, pp. 123–125, Jan. 1969.

[247] G. S. Eklund, “Initiation of Pitting at Sulfide Inclusions in Stainless Steel,” *J. Electrochem. Soc.*, vol. 121, no. 4, pp. 467–473, Apr. 1974.

[248] H. S. Isaacs, “The localized breakdown and repair of passive surfaces during pitting,” *Corros. Sci.*, vol. 29, no. 2, pp. 313–323, Jan. 1989.

[249] M. P. Ryan, N. J. Laycock, H. S. Isaacs, and R. C. Newman, “Corrosion Pits in Thin Films of Stainless Steel,” *J. Electrochem. Soc.*, vol. 146, no. 1, pp. 91–97, Jan. 1999.

[250] H. Böhni, “Localized Corrosion of Passive Metals,” in *Uhlig’s Corrosion Handbook*, R. W. Revie, Ed. John Wiley & Sons, Inc., 2011, pp. 157–169.

[251] J. Soltis, “Passivity breakdown, pit initiation and propagation of pits in metallic materials – Review,” *Corros. Sci.*, vol. 90, pp. 5–22, Jan. 2015.

[252] J. Kunze, V. Maurice, L. H. Klein, H.-H. Strehblow, and P. Marcus, “In situ STM study of the effect of chlorides on the initial stages of anodic oxidation of Cu(111) in alkaline solutions,” *Electrochimica Acta*, vol. 48, no. 9, pp. 1157–1167, Apr. 2003.

[253] T. Massoud, V. Maurice, L. H. Klein, and P. Marcus, “Nanoscale Morphology and Atomic Structure of Passive Films on Stainless Steel,” *J. Electrochem. Soc.*, vol. 160, no. 6, pp. C232–C238, Jan. 2013.

[254] T. Massoud, V. Maurice, L. H. Klein, A. Seyeux, and P. Marcus, “Nanostructure and local properties of oxide layers grown on stainless steel in simulated pressurized water reactor environment,” *Corros. Sci.*, vol. 84, pp. 198–203, Jul. 2014.

[255] C. A. Sperati and H. W. Starkweather, “Fluorine-containing polymers. II. Polytetrafluoroethylene,” in *Fortschritte Der Hochpolymeren-Forschung*, Springer, Berlin, Heidelberg, 1961, pp. 465–495.

[256] R. G. Chaudhuri and S. Paria, “Dynamic contact angles on PTFE surface by aqueous surfactant solution in the absence and presence of electrolytes,” *J. Colloid Interface Sci.*, vol. 337, no. 2, pp. 555–562, Sep. 2009.

[257] J. D. Miller, S. Veeramasuneni, J. Drelich, M. R. Yalamanchili, and G. Yamauchi, “Effect of roughness as determined by atomic force microscopy on the wetting properties of PTFE thin films,” *Polym. Eng. Sci.*, vol. 36, no. 14, pp. 1849–1855, Jul. 1996.

[258] I. Pignatelli, A. Kumar, R. Alizadeh, Y. Le Pape, M. Bauchy, and G. Sant, “A dissolution-precipitation mechanism is at the origin of concrete creep in moist environments,” *J. Chem. Phys.*, vol. 145, no. 5, p. 054701, Aug. 2016.

[259] C. B. Barber, D. P. Dobkin, and H. Huhdanpaa, “The Quickhull Algorithm for Convex Hulls,” *ACM Trans Math Softw*, vol. 22, no. 4, pp. 469–483, Dec. 1996.

[260] X. Nie, X. Li, C. Du, Y. Huang, and H. Du, “Characterization of corrosion products formed on the surface of carbon steel by Raman spectroscopy,” *J. Raman Spectrosc.*, vol. 40, no. 1, pp. 76–79, Jan. 2009.

[261] D. Dwivedi, K. Lepková, and T. Becker, “Carbon steel corrosion: a review of key surface properties and characterization methods,” *RSC Adv.*, vol. 7, no. 8, pp. 4580–4610, 2017.

[262] M. F. Wang, X. G. Li, N. Du, Y. Z. Huang, and A. Korsunsky, “Direct evidence of initial pitting corrosion,” *Electrochem. Commun.*, vol. 10, no. 7, pp. 1000–1004, Jul. 2008.

[263] K. Asami and M. Kikuchi, “In-depth distribution of rusts on a plain carbon steel and weathering steels exposed to coastal–industrial atmosphere for 17 years,” *Corros. Sci.*, vol. 45, no. 11, pp. 2671–2688, Nov. 2003.

[264] C. Rémazeilles and P. Refait, “On the formation of β-FeOOH (akaganéite) in chloride-containing environments,” *Corros. Sci.*, vol. 49, no. 2, pp. 844–857, Feb. 2007.

[265] S. Li and L. H. Hihara, “A Micro-Raman Spectroscopic Study of Marine Atmospheric Corrosion of Carbon Steel: The Effect of Akaganeite,” *J. Electrochem. Soc.*, vol. 162, no. 9, pp. C495–C502, Jan. 2015.

[266] M. Saremi and E. Mahallati, “A study on chloride-induced depassivation of mild steel in simulated concrete pore solution,” *Cem. Concr. Res.*, vol. 32, no. 12, pp. 1915–1921, Dec. 2002.

[267] S. A. Karrab, M. A. Doheim, M. S. Aboraia, and S. M. Ahmed, “Study of Cavitation Erosion Pits on 1045 Carbon Steel Surface in Corrosive Waters,” *J. Tribol.*, vol. 134, no. 1, pp. 011602-011602-6, Feb. 2012.

[268] G. T. Burstein, P. C. Pistorius, and S. P. Mattin, “The nucleation and growth of corrosion pits on stainless steel,” *Corros. Sci.*, vol. 35, no. 1, pp. 57–62, Jan. 1993.

[269] C. Punckt *et al.*, “Sudden Onset of Pitting Corrosion on Stainless Steel as a Critical Phenomenon,” *Science*, vol. 305, no. 5687, pp. 1133–1136, Aug. 2004.

[270] M. Avrami, “Kinetics of Phase Change. II Transformation-Time Relations for Random Distribution of Nuclei,” *J. Chem. Phys.*, vol. 8, no. 2, pp. 212–224, Feb. 1940.

[271] J. A. Bardwell, B. MacDougall, and G. I. Sproule, “Use of SIMS to Investigate the Induction Stage in the Pitting of Iron,” *J. Electrochem. Soc.*, vol. 136, no. 5, pp. 1331–1336, May 1989.

[272] V. Rudnev, D. Loveless, and R. L. Cook, *Handbook of Induction Heating, Second Edition*. CRC Press, 2017.

[273] C. H. Paik, H. S. White, and R. C. Alkire, “Scanning Electrochemical Microscopy Detection of Dissolved Sulfur Species from Inclusions in Stainless Steel,” *J. Electrochem. Soc.*, vol. 147, no. 11, pp. 4120–4124, Nov. 2000.

[274] B. Lin, R. Hu, C. Ye, Y. Li, and C. Lin, “A study on the initiation of pitting corrosion in carbon steel in chloride-containing media using scanning electrochemical probes,” *Electrochimica Acta*, vol. 55, no. 22, pp. 6542–6545, Sep. 2010.

[275] T. R. Beck and R. C. Alkire, “Occurrence of Salt Films during Initiation and Growth of Corrosion Pits,” *J. Electrochem. Soc.*, vol. 126, no. 10, pp. 1662–1666, Oct. 1979.

[276] J. Galvele, “Transport processes in passivity breakdown—II. Full hydrolysis of the metal ions,” *Corros. Sci.*, vol. 21, no. 8, pp. 551–579, Jan. 1981.

[277] H. S. Isaacs and G. Kissel, “Surface Preparation and Pit Propagation in Stainless Steels,” *J. Electrochem. Soc.*, vol. 119, no. 12, pp. 1628–1632, Dec. 1972.

[278] H. S. Isaacs, “The Behavior of Resistive Layers in the Localized Corrosion of Stainless Steel,” *J. Electrochem. Soc.*, vol. 120, no. 11, pp. 1456–1462, Nov. 1973.

[279] S. Scheiner and C. Hellmich, “Stable pitting corrosion of stainless steel as diffusion-controlled dissolution process with a sharp moving electrode boundary,” *Corros. Sci.*, vol. 49, no. 2, pp. 319–346, Feb. 2007.

[280] S. Scheiner and C. Hellmich, “Finite Volume model for diffusion- and activation-controlled pitting corrosion of stainless steel,” *Comput. Methods Appl. Mech. Eng.*, vol. 198, no. 37–40, pp. 2898–2910, Aug. 2009.

[281] R. C. Newman and H. S. Isaacs, “Diffusion-Coupled Active Dissolution in the Localized Corrosion of Stainless Steels,” *J. Electrochem. Soc.*, vol. 130, no. 7, pp. 1621–1624, Jul. 1983.

[282] G. T. Gaudet *et al.*, “Mass transfer and electrochemical kinetic interactions in localized pitting corrosion,” *AIChE J.*, vol. 32, no. 6, pp. 949–958, Jun. 1986.

[283] X. Liu and F. J. Millero, “The solubility of iron hydroxide in sodium chloride solutions,” *Geochim. Cosmochim. Acta*, vol. 63, no. 19, pp. 3487–3497, Oct. 1999.

[284] J. Mankowski and Z. Szklarska-Smialowska, “Studies on accumulation of chloride ions in pits growing during anodic polarization,” *Corros. Sci.*, vol. 15, no. 6, pp. 493–501, Jan. 1975.

[285] T. Misawa, “The thermodynamic consideration for Fe-H2O system at 25°C,” *Corros. Sci.*, vol. 13, no. 9, pp. 659–676, Jan. 1973.

[286] S. Kesavan, T. A. Mozhi, and B. E. Wilde, “Technical Note: Potential-pH Diagrams for the Fe-Cl−-H2O System at 25 to 150 C,” *CORROSION*, vol. 45, no. 3, pp. 213–215, Mar. 1989.

[287] K. Karadakis, V. J. Azad, P. Ghods, and O. B. Isgor, “Numerical Investigation of the Role of Mill Scale Crevices on the Corrosion Initiation of Carbon Steel Reinforcement in Concrete,” *J. Electrochem. Soc.*, vol. 163, no. 6, pp. C306–C315, Jan. 2016.